HUNTING FOR WATER WITH MCS

Ramin Lolachi

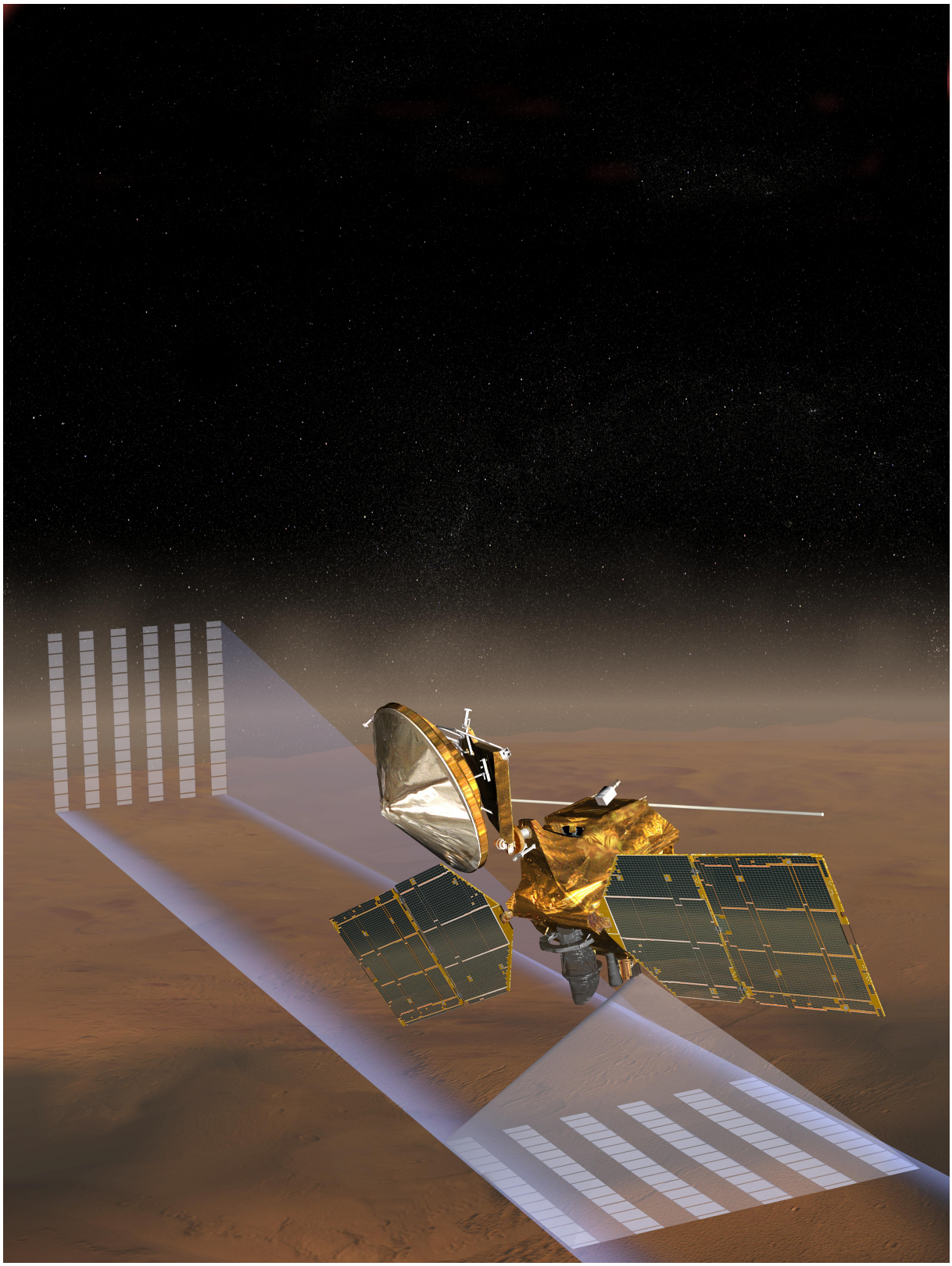
Lady Margaret Hall

Atmospheric, Oceanic and Planetary Physics

University of Oxford

Hilary 2019

DPhil Thesis



MCS | Mars Climate Sounder in action on Mars Reconnaissance Orbiter.

COURTESY NASA/JPL-CALTECH.

University of Oxford



A thesis submitted for the degree of Doctor of Philosophy at the University of Oxford

HUNTING FOR WATER WITH MCS

ASSESSING THE RETRIEVABILITY OF WATER VAPOUR WITH MARS CLIMATE SOUNDER

Ramin Lolachi

Lady Margaret Hall

Atmospheric, Oceanic and Planetary Physics

Hilary Term 2019

Hilary Term, 2019

Atmospheric, Oceanic and Planetary Physics

Department of Physics

University of Oxford

HUNTING FOR WATER WITH MCS

Assessing the Retrievability of Water Vapour with Mars Climate Sounder

This thesis is submitted to the Department of Physics, Division of Mathematical and Physical Sciences, University of Oxford, in full fulfilment of the requirements for the degree **Doctor of Philosophy**. This thesis, its analysis and conclusions, are entirely my own, except where otherwise stated.

Word Count $\approx$ 66,000

Page Count = 255

Ramin Lolachi

Lady Margaret Hall, Oxford

Abstract

Mars Climate Sounder (MCS) is an infrared radiometer aboard NASA's Mars Reconnaissance Orbiter (MRO) launched in August 2005 and designed to characterize the temporal and spatial variation of temperature, dust and water profiles. MCS has nine spectral channels in the range 0.3–50 μm. An original goal of the mission was retrieval of vertical water profiles. This was to be done using two spectrally co-located channels (centred at 42 μm)—a narrow channel (B3), which was mainly sensitive to dust, and a broader overlapping channel (B2) sensitive to both dust and water. This has been severely compromised by the fact that the B2 and B3 filters did not meet their specification, with a much wider than expected spectral response.

This thesis is split into three parts attempting to assess the current ability of MCS to retrieve water vapour. In the first part, work was done assessing the ramifications on the water vapour sensitivity of the B3-B2 pair and the B2 channel alone through extensive simulation work. The B3-B2 pair were found to have a drastically reduced sensitivity to water vapour that was further reduced by the presence of dust and low temperatures. Radiance residuals of B2 from MCS observations showed that a water vapour signal is present in the channel. Simulations of MCS radiances and retrieval of synthetic observations revealed that the accuracy of water vapour retrievals is sensitive to the choice of aerosol particle size and that in the presence of moderate aerosol opacity (dust and water ice), aerosol radiance contribution in B2 is falsely misinterpreted as water vapour.

In the second part, work was done measuring the spectral response of the B3 filter in order to understand the process behind the spectral broadening in the B-channels. It was thought that random forward scattering of out-of-bandpass radiation by the mesh filter may be the cause of the widening. Using a custom-made jig and FTIR spectrometer, measurements were taken at several filter-detector separation distances. No change in the B3 response FWHM was observed as the distance was varied.

In the final part, a two-stage retrieval method was applied to MCS observations for MY28 northern hemisphere summer (L_s=111–173°). Nightside vertical profiles of water vapour were retrieved for the first time showing interaction with the aphelion cloud belt directly. Possible interaction between dust and water cycles was seen. Retrieval results compared favourably with observations by others for both column abundances and vertical profiles. Of particular note was good agreement with results from Clancy et al. (2017) using vertical water profiles derived from CRISM retrievals of 1.27 μm $O_2(^1\Delta_g)$ dayglow. A number of spurious retrievals were seen and these are attributed to the aerosol model choice problem seen in the simulations.

Acknowledgements

ἄνδρα μοι ἔννεπε, μοῦσα, πολύτροπον, ὃς μάλα πολλὰ
πλάγχθη, ἐπεὶ Τροίης ἱερὸν πτολίεθρον ἔπερσεν:
πολλῶν δ' ἀνθρώπων ἴδεν ἄστεα καὶ νόον ἔγνω,
πολλὰ δ' ὅ γ' ἐν πόντῳ πάθεν ἄλγεα ὃν κατὰ θυμόν,
ἀρνύμενος ἥν τε ψυχὴν καὶ νόστον ἑταίρων.

Sing to me of the man, Muse, the man of twists and turns driven time and again off course,
once he had plundered the hallowed heights of Troy.
Many cities of men he saw and learned their minds,
many pains he suffered, heartsick on the open sea,
fighting to save his life and bring his comrades home.

—HOMER, *The Odyssey*

It has been a long journey and I cannot believe that I have finally made it to the end. There are so many people to thank and I am sure I shall forget some of them, but if that is you—thank you very much! I would like to start by thanking my long-suffering supervisor, Pat Irwin, who managed to find time for me, championed and supported me through this adventure from start to finish (including reading all the draft manuscripts for this work). I would also like to thank the rest of the Oxford planetary crew for the lessons learned both academically and otherwise, including the infamous Friday group lunches. For the administrators: the inimitable Sarah Harrington, Monika Porada, Lucy Li and Andrea Simpson for dealing with all my administration woes, smoothing things out and finding me money in unexpected places. From the MCS team a big thank you to Armin Kleinböhl and David Kass for help with technical elements of MCS observations.

The work presented here was funded by the Science and Technology Facilities Council in the UK, and the Mars Reconnaissance Orbiter mission is a NASA/JPL endeavour.

Some special mentions include Hugh Mortimer for all the time spent reading the drafts of my laboratory work chapter and also for giving me the occasional kick up the backside or word of encouragement when things were tough. To my wonderful officemates, Jo Eberhardt and

Jaemin Lee, for keeping things lively and never boring. To great friends at AOPP: Benjamin Grandey, Luis Millán, Amrita Shravat, Rosalind West and Corwin Wright.

I would also like to thank my family and friends. My parents, Susan and Homayoon, for supporting me in this endeavour emotionally, financially and logistically. My grandparents, who sadly have not lived to see this day—my grandmother Beatrice McKever for her love, warmth and support even during the time of her failing health. My grandfather, Desmond McKever, who even though he never saw me start this work, set me on the path, lighting the spark that flamed into my passion for astronomy and planetary science. To my wonderful friends Anne and Elizabeth Venner for believing that I could make it this far. To Tom Judge, Ben Ward, Daniel Wright and my church bible study group for frequently listening to my woes and praying for me, and in Daniel's case also for checking the Greek in the thesis epigrams. To my darling Carissa, for her love, who put up with my stress and angst, pushed me, consoled me and chided me over the line.

Finally, to the one who calls the stars by name, who created Mars and me, and gave me the desire and ability to explore the worlds of his wondrous creation.

For my parents, in memory of my grandparents and for the one who got me through it all.

Contents

Declaration iv

Abstract v

Acknowledgements vii

1 Introduction: Water Vapour in the Martian Atmosphere 1
- 1.1 History of Water on Mars . . . 5
- 1.2 Current Martian Water Reservoirs . . . 7
- 1.3 Water Vapour Observations . . . 10
  - 1.3.1 Seasonal/Interannual Variation . . . 10
  - 1.3.2 Spatial Distribution . . . 16
  - 1.3.3 Vertical Distribution . . . 17
  - 1.3.4 Diurnal Variation . . . 21
- 1.4 Thesis Outline . . . 23

2 Mars Climate Sounder and Mars Reconnaissance Orbiter 24
- 2.1 Description of MRO Spacecraft . . . 24
- 2.2 MCS: Instrument Overview . . . 26
  - 2.2.1 Optics and Mechanisms . . . 30
  - 2.2.2 Focal Plane Assembly and Detectors . . . 32
  - 2.2.3 Observation Strategy, Cycle and Viewing Modes . . . 34
  - 2.2.4 Observational Coverage . . . 36
  - 2.2.5 In-Flight Calibration . . . 37
- 2.3 Detection of Water Vapour and Problems . . . 38
  - 2.3.1 The Water Vapour Channels B3 and B2 . . . 38
  - 2.3.2 Extended FOV Wings . . . 39
  - 2.3.3 Elevation Slew-Impairment . . . 40
- 2.4 Data Pipeline . . . 40
  - 2.4.1 FOV Rotation and Averaging . . . 41

3 Radiative Transfer Modelling 44
- 3.1 Molecular Spectroscopy . . . 44
- 3.2 The Radiative Transfer Equation . . . 45
  - 3.2.1 Limb Viewing . . . 50
- 3.3 Calculating Transmission . . . 51
  - 3.3.1 Sources of Opacity . . . 53
  - 3.3.2 Line-by-Line Models . . . 61

3.3.3 Correlated-k Models . . . 63
3.3.4 Scattering Tests . . . 69
3.3.5 Assumption of Local Thermodynamic Equilibrium . . . 78
3.4 Martian Reference Atmosphere . . . 79

4 Retrieval Theory **84**
4.1 What is Retrieval Theory? . . . 84
4.2 The Forward Model . . . 86
4.3 Exact Solutions . . . 86
4.4 Least Squares . . . 88
4.5 Linear Optimal Estimation . . . 89
4.6 Non-Linear Optimal Estimation and NEMESIS . . . 91
4.6.1 Errors . . . 94
4.6.2 Tuning . . . 97
4.6.3 Functional Derivatives, Vertical Sensitivity and Multi-Stage Retrievals . . . 97
4.7 L2 Retrievals . . . 101
4.7.1 L2 Modified Chahine Method . . . 101
4.7.2 Comparison of L2 Method with Optimal Estimation . . . 103

5 Sensitivity Studies I: Radiance Effects **104**
5.1 Ratio Sensitivity Simulations in Limb Viewing . . . 104
5.1.1 Simulation and Data Processing . . . 105
5.1.2 Results and Discussion . . . 107
5.2 B3/B2 Scatter Plots of Observed & Simulated Radiances . . . 108
5.2.1 Data, Processing and Simulation . . . 109
5.2.2 Results and Discussion . . . 109
5.3 B3/B2 Scatter Sensitivity Simulations . . . 110
5.3.1 Simulation Procedure . . . 112
5.3.2 Results and Discussion . . . 114
5.4 B2 Radiance Residuals for Water Vapour . . . 120
5.4.1 Observations . . . 121
5.4.2 Retrieval and Residual Method . . . 122
5.4.3 Results . . . 124
5.4.4 Conclusions . . . 130
5.5 Effect of Dust/Ice Particle Size on B2 radiances . . . 130
5.5.1 Simulation Procedure . . . 131
5.5.2 Results and Discussion . . . 135
5.6 Summary . . . 139

6 Sensitivity Studies II: Effect of Aerosol Size on Retrievals **140**
6.1 Method . . . 141
6.1.1 Synthetic Measurement Creation . . . 141
6.1.2 Retrieval of Synthetics . . . 143
6.2 Results . . . 145
6.2.1 Dust Series: First Stage . . . 145
6.2.2 Dust Series: Second Stage (Water) . . . 147
6.2.3 Water Ice Series: First Stage . . . 151
6.2.4 Water Ice Series: Second Stage (Water) . . . 154
6.3 Using Covariance Matrices to Assess Aerosol Size Sensitivity . . . 159
6.4 Conclusions . . . 162
6.5 Sensitivity Summary: Implications for Water Vapour Retrievals . . . 163

7 Characterizing the Spectral Passband of B3 **165**
7.1 Experimental Set-Up & Strategy . . . 168
7.2 Data Treatment & Uncertainties . . . 173
7.3 Results . . . 175
7.4 Discussions & Conclusions . . . 178

8 Retrievals **179**
8.1 Observations . . . 179
8.2 Method . . . 180
8.2.1 A Priori . . . 180
8.2.2 Retrieval Procedure . . . 180
8.2.3 Detector Selection and Dummy B1 . . . 181
8.3 Results . . . 183
8.3.1 Retrieval Quality and Coverage . . . 183
8.3.2 First Stage Retrieval Results . . . 186
8.3.3 Second Stage Retrieval Results . . . 191
8.3.4 Column Abundances . . . 191
8.3.5 Vertical Profiles & Comparison with CRISM Results . . . 196
8.3.6 Comparison with SPICAM Results . . . 204
8.4 Conclusions . . . 214

9 Conclusions and Future Work **218**
9.1 Conclusions . . . 218
9.1.1 Sensitivity Studies . . . 218
9.1.2 Characterizing the Spectral Passband of B3 . . . 220
9.1.3 Retrievals . . . 221
9.2 Future Work . . . 224
9.2.1 Sensitivity Studies . . . 224
9.2.2 Characterizing the Spectral Passband of B3 . . . 224
9.2.3 Retrievals of Water Vapour . . . 225
9.3 Summary . . . 228

Bibliography **229**

1

Introduction: Water Vapour in the Martian Atmosphere

Mars has captivated the imagination of the human race for thousands of years, starting with naked eye observations of its baleful red glow and confusing retrograde motion. This fascination grew further still after Galileo pointed a telescope at the red planet over 400 years ago (Sheehan, 1996). It did not take observers long to start speculating about this other world and what it contained. Belief about water on Mars goes back to long before the space age, when in the 17th and 18th centuries the astronomers Huygens, Cassini and Herschel monitored the advance and retreat of the polar ice (now known to be CO_2 ice over a water ice layer) and saw signs of clouds (Sheehan, 1996). They attributed their observations to being caused by water.

In the 19th century these ideas came to a head when the Italian astronomer Giovanni Schiaparelli claimed that he had observed long networks of straight lines on the surface, which he dubbed 'canali'. By this stage the significant and seasonally changeable dark areas of Mars observable through a telescope visually, were interpreted as being due to vegetation and bodies of water. He believed the lines were naturally-formed channels carrying water across the surface of the planet (Sheehan, 1996; Read & Lewis, 2004). Initially, when his work was translated into English, 'canali' was mistranslated into 'canal' (implying artificial construction) rather than 'channel' (natural origin).

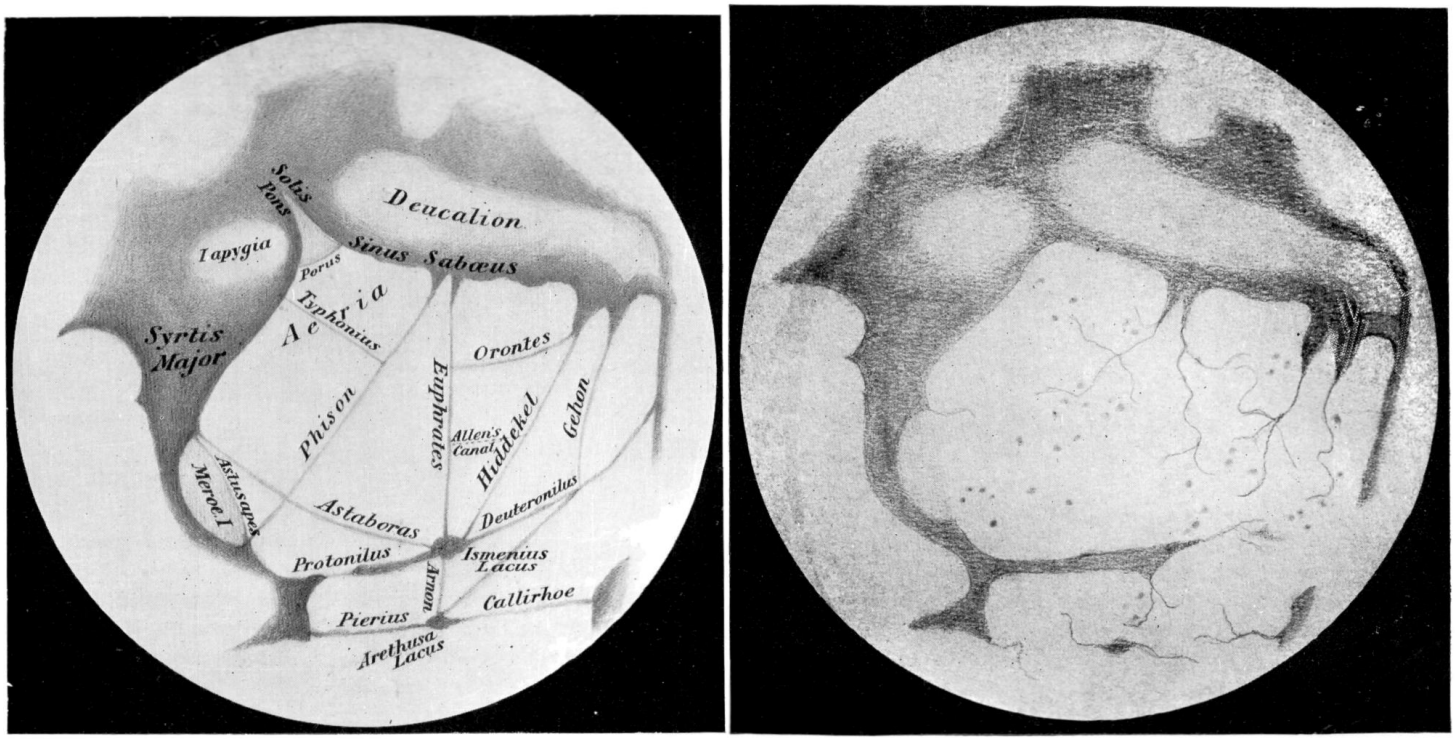


Figure 1.1 | Figure reproduced from Evans & Maunder (1903), *MNRAS*, showing **(Left)** Map of Martian canals believed to have been observed at the time. **(Right)** A drawing of Mars based on the map used in the experiment, where the canal lines have been replaced with dots. The students were asked to draw from this at different distances.
Credit: Public domain.

The observations of Schiaparelli led the now infamous US businessman and astronomer Percival Lowell to declare that these networks were the work of intelligent life on Mars, irrigation canals for farming Martians. This belief in Mars and its canals captured the public imagination and persisted into the early 20th century. By this stage though doubts had started to arise as an increasing number of astronomers including E. E. Barnard failed to observe them (Sheehan, 1996). Further evidence against the canals came from the results of an experiment conducted with the aid of schoolboys from the Royal Greenwich Hospital school in Evans & Maunder (1903). The students, who were unaware of what they were drawing, were asked to observe from various distances and draw from a small disk containing an image of Mars* with minute dot-like markings in place of the canal lines (see Fig. 1.1). As distance increased the likelihood of the dots being mistaken for lines increased. The results showed that at the limit of visibility, fine details like dots can be integrated into lines—the canals of Mars were an optical illusion.

Any hopes of finding water or vegetation on the surface were finally quashed by the advent of the space age. Starting with Mariner 4 in July 1965, space probes revealed Mars to be the

*Based on contemporary maps/drawings of Mars as viewed by eye through observatory telescopes.

cold desert world we know today. However, in 1971 Mariner 9 arrived at Mars and amazed everyone with its observations revealing a diverse geology. The topography of Mars was shown to have a regional dichotomy, roughly following the hemispheres of the planet. The southern hemisphere features ancient heavily cratered highlands while the northern hemisphere features younger vast low lying plains and volcanic features. A zoo of eclectic geological features were revealed including the largest shield volcano in the Solar System, Olympus Mons, which stands at a majestic 27 km and the Valles Marineris, which at more than 4,000 km long, 200 km wide and up to 7 km deep dwarfs the Earth's Grand Canyon. The most intriguing find was geomorphic evidence that indicated that liquid water had flowed on the surface of Mars and that there may have even been rainfall. This came in the form of the valley networks and massive outflow channels, discussed in more detail in the next section. Since the findings of Mariner 9, the evidence for past water on the surface of the planet has increased including indications of ancient crater lakes and even an ancient ocean (Grotzinger et al., 2015; Perron et al., 2007).

A brief summary of Mars' planetary and atmospheric parameters is given in Tbl. 1.1. The Mars of today is cold (with surface temperatures as low as 140 K) and dry–the closest terrestrial analogue being the dry valleys of Antarctica (Read & Lewis, 2007; Summerhayes & Beeching, 2007). The atmosphere is almost pure CO_2 (making up about 95%) with a very low surface pressure of $<$610 Pa ($\sim$6 mbar), over a hundred times less than that here on Earth. The value of 610 Pa is significant as it is near the triple point of water. As Mars' ambient surface pressure is mostly below this value it means that if water vapour is cooled below its condensation temperature it sublimes as solid ice rather than condensing as liquid water. Similarly if ice on the surface is heated it directly sublimes as vapour (Read & Lewis, 2004).

When combining the geomorphic evidence described above of an early 'wet' Mars with the known current dry climate of the planet a paradox arises—where has all the water gone? The difficulty is that liquid water is not stable on the Martian surface in the current climate (see above). Stabilization processes suggested have included a previous warmer climate with increased pressure, water with increased salinity (which changes the sublimation/freezing temperatures of the water (Haberle, 2001)) or a flow of meltwater at the base of glaciers in 'tubes' enclosed by the ground below and the glacier above (Read & Lewis, 2004). Current reservoirs/forms for water on Mars include layers of water ice underneath the CO_2 ice at the polar caps (Bibring et al., 2004), sub-surface ice in the regolith (Boynton et al., 2002; Smith et al., 2009b), water vapour

Table 1.1 | Planetary and atmospheric parameter comparison for Mars and Earth.

Credit: Material from Read & Lewis (2004), 'The Martian Climate Revisited: Atmosphere and Environment of a Desert Planet', published 2004, Praxis Publishing Ltd. Reproduced with permission of SNCSC.

	Earth	Mars
Mean orbital radius (10^{11} m)	1.50	2.29
Distance from Sun (AU)	0.98–1.02	1.38–1.67
Orbital eccentricity	0.017	0.093
L_s of perihelion	281°	251°
Planetary obliquity	23.93°	25.19°
Solar day, sol (s)	86,400	88,775
Year length (sol)	365.24	668.6
Equatorial radius (10^6 m)	6.378	3.396
Surface gravity, g (m s^{-1})	9.81	3.72
Surface pressure (Pa)	101,300	600 (variable)
Atmospheric constituents (molar ratio)	N_2 (77%)	CO_2 (95%)
	O_2 (21%)	N_2 (2.7%)
	H_2O (1%)	Ar (1.6%)
	Ar_2 (0.9%)	O_2 (0.13%)
Equilibrium temperature, T_e (K)	256	210
Scale height, $H_p = RT_e/g$ (km)	7.5	10.8
Surface temperature (K)	230–315	140–300

in the air (Spinrad et al., 1963), glaciers (Holt et al., 2008) and possibly even sub-glacial lakes! (Orosei et al., 2018). But even taking all of these sources together does not fully account for the water budget required for an early 'wet' Mars. The answer to this 'missing water' problem must be sought in Martian climate change.

The mechanism behind the evolution of Mars' climate to its current conditions seems to be atmospheric loss caused by a combination of solar wind and radiation. Observations from MAVEN, Hubble and Mars Express all record gases escaping from the Martian atmosphere (Chaffin et al., 2014; Clarke et al., 2014; Jakosky et al., 2017). Photodissociation of water molecules in the lower atmosphere leads to hydrogen escape by sputtering at the exobase leading to loss of global water inventory (Krasnopolsky et al., 2002; Clarke et al., 2014; Jakosky et al., 2017). Loss of both CO_2 and water over time has transformed Mars from its warmer and wetter ancient counterpart to the cold barren desert world of the present.

Before moving on we would like to give the reader some terminology that is used extensively throughout this thesis. These are precipitable microns (pr. µm), Areocentric longitude and the Mars Year (MY). Water is measured in units of precipitable microns, a unit of column abundance where 1 pr. µm=10^{-4} g cm^{-2} of water=3.35×10^{18} cm^{-2} of water molecules. The Areocentric longitude, L_s, is the longitude of the Sun along Mars' ecliptic. Similar to terrestrial seasons, the L_s system is reckoned directly from the Sun's ascending node or Martian northern Spring Equinox position, where L_s=0°. Each season is separated by 90° from the next, e.g. vernal

Table 1.2 | Mars geological timescale.

Credit: Material from Read & Lewis (2004), 'The Martian Climate Revisited: Atmosphere and Environment of a Desert Planet', published 2004, Praxis Publishing Ltd. Reproduced with permission of SNCSC.

Epoch	Time before present Gyr
Noachian	4.6–3.5
Hesperian	3.5–1.8
Amazonian	1.8–*present*

equinox (L_s=0°), summer solstice (L_s=90°), autumn equinox (L_s=180°), and winter solstice (L_s=270°) in the northern hemisphere of Mars and reversed for the southern hemisphere (Beish, 2007). Related to L_s is the concept of Mars Year (MY). One MY is defined as the length of time between vernal equinoxes on Mars where the beginning of MY1 is arbitrarily defined as April 11, 1955 (Clancy et al., 2000).

1.1 History of Water on Mars

The most obvious signs of Mars' watery past are the river valleys and the massive outflow channels on the planet's surface (Baker, 2001). The valleys tend to be only a few kilometres in width and are mainly located in the highlands of the southern hemisphere. They are estimated to be Noachian (see Tbl. 1.2) in age and are generally found in dendritic branching networks that highly resemble river valley networks on Earth (Read & Lewis, 2004). Up until recently it was thought that the valley networks and branching were not dense enough (not enough branches/stream channels for a given area) to have been formed by precipitation with surface run-off. The work of Carr (1995, 1996) proposed an alternative mechanism: the valleys formed via the process of mass wasting (a process whereby soil and surface materials are transported downhill by the action of gravity) rather than fluvially (i.e. produced by the action of a stream or river). Subsequent results such as those of Stepinski & Luo (2009) have overturned this. Searching through topographic data with a semi-automated procedure they found that the the number of valleys and density of branching are significantly higher and do in fact support formation via precipitation and surface run-off.

The outflow channels are quite different in character to the valley networks. They are much larger, with widths of several to tens of kilometres (up to 25 km) and depths ranging from hundreds of metres to kilometres. The flows that formed them must have involved ocean-current

sized amounts of water. Unlike the valley networks they do not branch but instead have a single point of origin. It is thought that the flows that carved the channels were caused by transient 'catastrophic flooding' events thought to have started in the early Noachian continuing through to the late Hesperian and early Amazonian period, though mostly Hesperian. These could be caused by the release of massive amounts of ground-water by volcanic activity, impacts or a combination. Alternatively they could have been formed by the draining of massive lakes, that formed in the valleys at higher topographical levels, onto the northern plains. See Carr (1995), Carr (1996), Baker (2001) and Read & Lewis (2004) for further details of what was summarised here.

Further evidence for rivers on Mars comes in the form of inverted relief, where the former riverbed is preserved, rising above the surrounding terrain which has been eroded (Malin et al., 2010). This is because the riverbed becomes resistant to erosion, perhaps by cementation. Subsequently it may be buried and exposed as the softer material around it erodes to reveal the bed. Examples have been found across Mars (Newsom et al., 2010; Malin et al., 2010; Morgan et al., 2014).

Many of the proposed river and streambeds also terminate in features that resemble river deltas (di Achille & Hynek, 2010). They are widespread over Mars (Irwin et al., 2005), often found at the edge of craters or basins which seem to have been filled with water forming lakes. Many are also found clustered around the conjectured northern ocean shoreline (di Achille & Hynek, 2010). There is strong evidence (topography, mineralogical, stratigraphy) of palaeolakes of various types around Mars (Cabrol & Grin, 2010). Examples of features which are believed to have formerly held lakes include impact craters such as the Gale Crater (Grotzinger et al., 2015), the impact basins Hellas and Argyre (Cabrol & Grin, 2010; Hiesinger & Head, 2002), the Vallas Marineris (Cabrol & Grin, 2010) and the Eridania Lake basin—potentially larger than the Caspian Sea (Michalski et al., 2017).

An ongoing controversial topic of Martian water history is that of that of an ocean covering the northern plains of the planet (Parker et al., 1989; 1993; Baker, 1991). It is thought that during the Hesperian epoch the largest outflow channels formed with water due to a 'catastrophic flooding' event. The water then flowed out of the channels and flooded the northern plains forming a transient ocean. The first evidence suggesting such an ocean came from 'palaeo-shorelines' (i.e. remains of what had once been the shorelines of an ocean) identified by Parker et al. (1989; 1993). Further evidence comes from deltas clustered at the alleged shorelines (see

above). The status of these geological features as shorelines has been challenged (Carr & Head, 2003) as it has been shown that in places the shorelines do not follow equipotentials, deviating by several kilometres in some locations. Perron et al. (2007) proposed that 'true polar wander' may have caused deformation to the the shorelines, a phenomenon where a planet reorients in relation to its spin axis, caused by significant mass redistribution. The reorientation causes a change in rotational potential resulting in topographic crustal deformation—addressing the equipotential deviations.

Independent evidence in the form of an enhanced D/H ratio comes from work done by Villanueva et al. (2015). As water is lost from Mars by atmospheric loss processes (see previous section), there is an enhancement in the D/H ratio as deuterium is heavier than hydrogen and so less likely to escape. Their results implied an ocean covering 20% of the Martian surface. In Rodriguez et al. (2016) landforms in the shoreline regions were presented as evidence of two tsunamis induced by asteroid impacts (30 km craters) perhaps a few million years apart and suggested that tsunamis played a large part in shaping coastal topography. Measurements using the MARSIS radar on Mars Express by Mouginot et al. (2012) showed that the dielectric constant within the shorelines was similar to those of low-sedimentary deposits (laid down by water), large deposits of ground ice (from ocean water seeping and freezing into the surface) or a combination.

Geochemical evidence for past surface water flows comes from analysis of evaporite salts found on the surface at Meridiani Planum by the Opportunity rover. The analysis of the deposits suggests that acidic ground-water in conjunction with a fluctuating water table level caused evaporating pools that were transient and shallow in nature occurring in the Noachian (Baker, 2007; Squyres et al., 2004; 2006).

1.2 Current Martian Water Reservoirs

The most visible reservoirs for water on Mars today are the polar caps which are believed to hold water ice trapped beneath thin layers of CO_2, known as the CO_2 seasonal cap (Read & Lewis, 2004; Bibring et al. 2004). When these layers sublime a residual water ice is cap is revealed and as the temperature continues to increase, large amounts of water vapour are then released into the atmosphere (Kieffer et al., 1976; Read & Lewis, 2004; Haberle & Jakosky, 1990; Jakosky & Farmer, 1982). This process tends to be the dominant one at the north pole which is warmer

than the equivalent south pole where ice is believed to stay locked at lower temperatures, caused by CO_2 ice cold trapping with temperatures around 145 K (Haberle et al., 2017). This means the residual water ice cap at this pole is rarely uncovered. The northern ice cap, about half the size of the Greenland ice cap on Earth, remains intact throughout the summer. It has a volume of around 1.2–1.7 $\times 10^6$ km^3 and a typical thickness of 3–4 km (Zuber et al., 1998). It was Kieffer et. al. (1976) using the Viking Infrared Thermal Mapper (IRTM) that discovered that the caps had some water in them in the form of the residual ice caps and were not entirely composed of CO_2, shown by the fact that the measured surface temperatures were too high. Further evidence of water ice in the caps came from Picardi et al. (2005) who used measurements from the MARSIS radar instrument aboard Mars Reconnaissance Orbiter (MRO). The polar caps are split into of layers known as the Polar Layered Deposits (PLD). These layers act as a record of past Martian climate that contain varying admixtures of dust and ice. The results of Picardi et al. (2005) gave evidence that the PLD at the north pole are composed of almost pure water ice with dust fractions of only a few percent. Later observations by Plaut et al. (2007) showed the same situation for the south pole.

The southern CO_2 cap normally does not fully sublime (see above). There have been exceptions to this with the ground-based observations of Barker (1970) and Tull (1970) suggesting in some southern summers the CO_2 cap fully sublimes and exposes the residual water ice cap. Most years the only residual water ice seen will be that at the edge of the caps during southern summer. Using results from THEMIS (Thermal Emission Imaging System) and TES (Thermal Emission Spectrometer), both aboard Mars Odyssey, Titus et al. (2002) showed evidence for water ice at the fringes of the south polar cap. Follow up work was done by Bibring et al. (2004) who used the Visible and Infrared Mineralogical Mapping Spectrometer (OMEGA) on Mars Express to map both CO_2 and water ice, the results of which were in agreement with Titus et al. (2002).

The other major reservoir of water on Mars is believed to be ice contained beneath the surface in the Martian regolith. Water can enter the regolith layer via pores and cracks becoming adsorbed onto the soil in the first few centimetres over short timescales of hours/days (Read & Lewis, 2004). Over seasonal timescales this can increase to tens of centimetres and over longer interannual/geological timescales water could potentially reach metre to kilometre scales. Evidence for widespread subsurface ice comes from comes from hydrogen abundance mapping done by Boynton et al. (2002) with the Gamma Ray Spectrometer (GRS) on Mars Odyssey (see

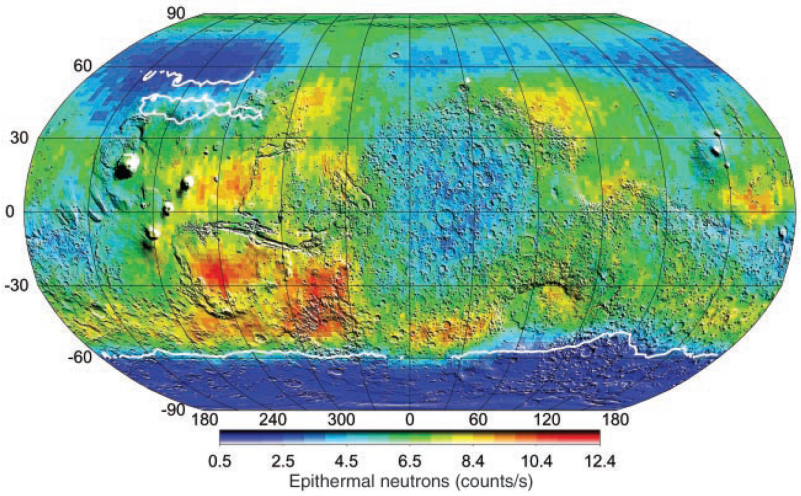


Figure 1.2 | Map of epithermal neutron flux from the Neutron Spectrometer of Mars Odyssey's GRS. Low epithermal flux is indicative of high hydrogen concentration. Contours (in white) are shown of the regions where water ice is predicted to be stable at 80 cm depth (no predictions were made poleward of 60° latitude because no data on thermal inertia were available). Note the correlation between regions of predicted ice stability and the low epithermal flux. The only exception is the small closed region of predicted ice stability, which is not observed in the epithermal neutron flux.

Credit: Boynton et al. (2002), 'Distribution of Hydrogen in the Near Surface of Mars: Evidence for Subsurface Ice Deposits'. Science, 297, 81–85. Reprinted with permission from AAAS.

Fig. 1.2). GRS worked by using epithermal neutrons to sample hydrogen, presumed to be in the form of water ice, to depths of a few metres. An ice-rich layer was found, at depths of 60 cm beneath the surface at 60°S and getting to within 30 cm at 75°S. Subsurface ice was estimated to constitute 15–35% of the observed subsurface layer by mass which was estimated to be enough for a global ocean 0.5–1.5 km deep. Bandfield (2007) made similar maps using THEMIS. This has been further corroborated by the in situ observations of subsurface water ice by Phoenix (Smith et al., 2009b).

Evidence for interaction between atmospheric water vapour and the regolith comes from a combination of models and in situ observations. Early regolith modelling was done by Zent et al. (1993) and Houben (1999) and then further developed by Böttger et al. (2005). Surface observations of relative humidity from Curiosity and Phoenix often coupled with modelling have given further proof of this process (Steele et al., 2016; Savijärvi et al., 2016; Zent et al., 2016). The modelled diurnal exchanges of water are generally small with amounts $\leq$1 pr. µm (corresponding to $\sim$10% of the typical atmospheric water column. These amounts are still enough to contribute to the formation of fogs on the surface. Over seasonal timescales the amount adsorbed or desorbed can go up to values of 10–20 pr. µm between solstice and equinox (Zent et al., 1993; Read & Lewis, 2004).

In addition to the above two major water reservoirs are some minor sources: glaciers and ice-filled craters. Evidence has mounted for glacier-like features: a prominent example being features known as lobate debris aprons being shown to contain almost pure water ice covered with an insulating layer of rocks (Holt et al., 2008; Plaut et al., 2009). A more recent find has been the ice-filled north polar impact crater Korolev (Brothers & Holt, 2016). Despite being south of the ice stability line, the ice in the crater seems to be stable year around as the crater behaves as a cold trap. Radar analysis has showed that its layering is similar to that of the north PLD. It is believed to have formed at the same time but independently of the PLD.

1.3 Water Vapour Observations

1.3.1 Seasonal/Interannual Variation

Water vapour on Mars was initially detected by Spinrad et al. (1963) at the Mount Wilson observatory. Detailed monitoring of atmospheric water vapour was first achieved by the Mars Atmospheric Water Detector (MAWD) aboard Viking 1/2 (Jakosky & Farmer, 1982) in the 1970s (MY12–13). Continuous observations from orbit resumed with almost unbroken coverage in the 1990s starting with the Thermal Emission Spectrometer (TES; MY24–27) on Mars Global Surveyor (Smith, 2002; 2004) which has since been joined and replaced by a host of other instruments. These include the Visible and Infrared Mineralogical Mapping Spectrometer (OMEGA), Ultraviolet and Infrared Atmospheric Spectrometer (SPICAM), Planetary Fourier Spectrometer (PFS) instruments aboard Mars Express (MY27–31 and beyond; Fedorova et al., 2006; Fouchet et al., 2007; Tschimmel et al. 2008; Maltagliati et al., 2011b; Trokhimovskiy et al., 2015), the Compact Reconnaissance Imaging Spectrometer for Mars (CRISM) on Mars Reconnaissance Orbiter (MRO) (Smith et al., 2009a; 2018; Toigo et al., 2013) and most recently the Atmospheric Chemistry Suite (ACS) and Nadir Occultation for Mars Discovery spectrometer suite (NOMAD) aboard ExoMars Trace Gas Orbiter (TGO) (Vandaele et al., 2019). Supporting coverage has come from landers/rovers on the surface (Titov et al., 1999; Smith et al., 2006; 2009b; Harri et al., 2014; McConnochie et al., 2018), Earth-based observatories (Schorn et al., 1969; Tull, 1970; Barker 1976; Sprague et al., 2006; Krasnopolsky et al., 2015) and Earth-orbiting satellites (Biver et al., 2005).

Monitoring of Mars over several Martian years has shown that the behaviour of water vapour is stable, repeatable and seasonally dependent (see Figs. 1.4 & 1.5). The atmosphere contains

an annual average column abundance of 10–15 pr. µm. A schematic of the seasonal progression is given in Fig. 1.3. Starting in late northern hemisphere spring (L_s=30°) water vapour sublimes into the northern atmosphere at the edge of the northern polar cap (70–80°N) as the CO_2 ice layer sublimes and reveals water ice beneath (Kieffer et al., 1976; Haberle & Jakosksky, 1990). This increases to a maximum in the early summer (L_s=100–120°) of 50–70 pr. µm. During the solstitial period a cross-equatorial Hadley cell forms reaching into the mid-latitudes. Horizontal mixing linked with planetary waves bring water from higher latitudes to the edge of the Hadley cell allowing it to be transported equatorward by the atmospheric circulation (Haberle et al., 2017; Richardson and Wilson, 2002). Further south away from the pole, the column abundance decreases, with a value of 20–25 pr. µm in the mid-latitudes and decreasing to 5 pr. µm at lower southern latitudes. As the year progresses (after L_s=130°) the northern maximum decreases and moves southwards towards the tropics and equator. As temperatures drop and the poles refreeze the abundance in the region falls to 5–10 pr. µm in the approach to the autumnal equinox (L_s=160–170°). From L_s=170–210° the maximum in the northern tropics is driven by an equinoctial circulation, where the Hadley cell has split in two at the equator, giving weak meridional transport. After this period a northwards cross-equatorial Hadley cell develops keeping water levels in the tropics relatively high until the beginning of the next Martian year.

During southern hemisphere spring the process seen at the north pole is repeated as the southern pole sublimes releasing water vapour into the atmosphere. The column abundance of the southern maximum however is about half that of its northern counterpart at 20–30 pr. µm. The reason for the dichotomy between the summer maxima at the poles is believed to be due to the the different stabilities of the CO_2 seasonal cap at each pole, with the south pole being more stable than the north (James et al., 2005; 2007). If the seasonal cap is more stable, then the residual water ice cap beneath is never exposed or has much less exposure leading to lower observed abundances of water vapour (as there is less sublimation). The greater stability of the southern cap seems somewhat counter-intuitive given the increased insolation during southern summer—due to the extreme eccentricity of Mars' orbit with southern summer corresponding to the perihelion. The explanation is that the southern cap albedo is sufficiently high to preserve the stability of the CO_2 cap (James et al., 2005; 2007; Titov, 2002). The orbital characteristics just described may aid stability due to the fact that though the southern summer has higher insolation it is shorter than northern summer. Also the southern winters tend to be colder and longer than their northern counterparts. This may lead to less CO_2 ice being sublimated in the

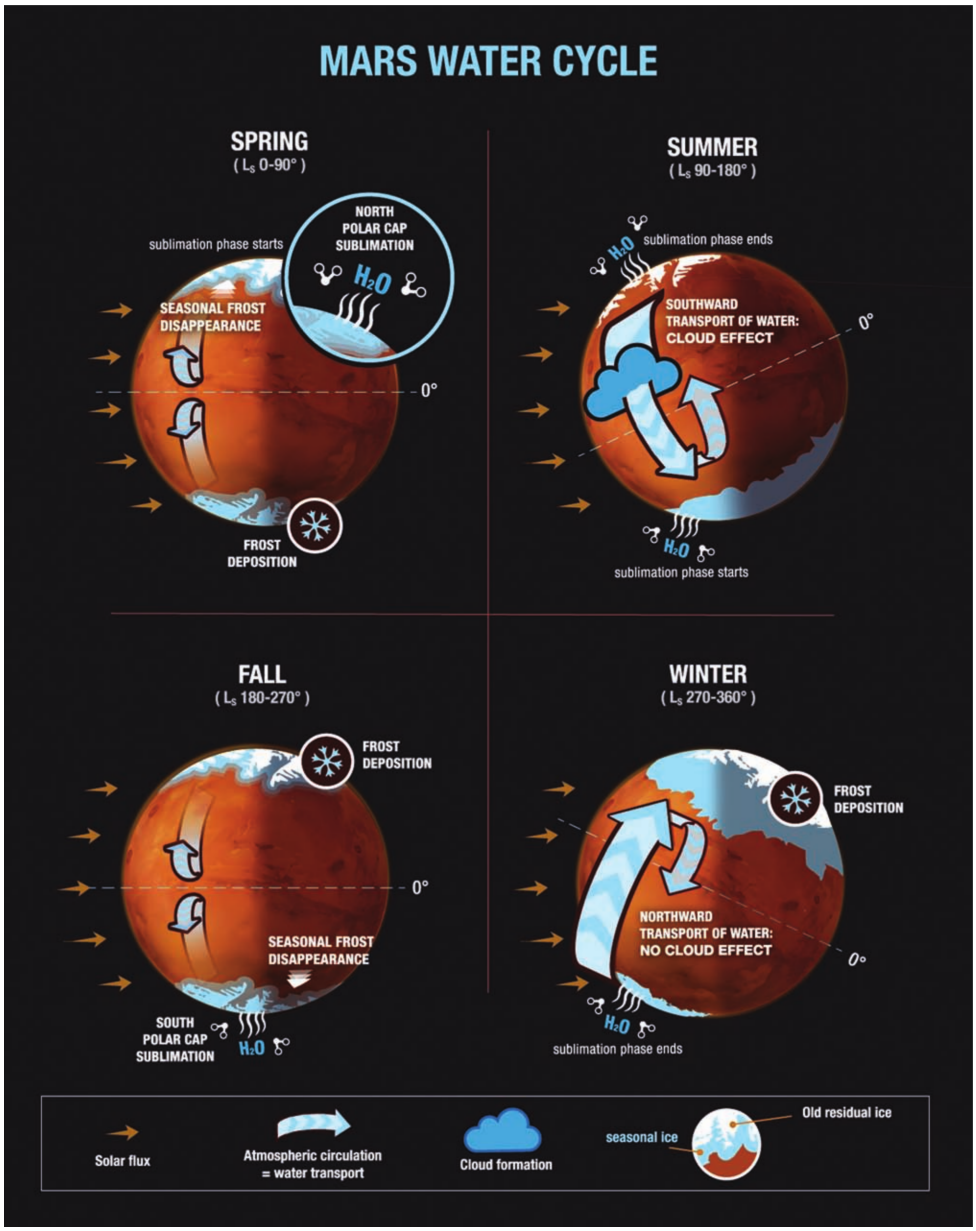


Figure 1.3 | Seasonal progression of the present Mars water cycle illustrating the exchange of water between surface and atmospheric reservoirs. A cross-equatorial Hadley cell is seen during solstitial periods. During equinoctial periods the Hadley cell splits in two at the equator with weak meridional transport. "Cloud effect" refers to the formation of the aphelion cloud belt during northern summer.

Credit: Reproduced from Haberle et al. (2017), 'The atmosphere and climate of Mars', © Cambridge University Press 2017. Reproduced with permission of The Licensor through PLSclear.

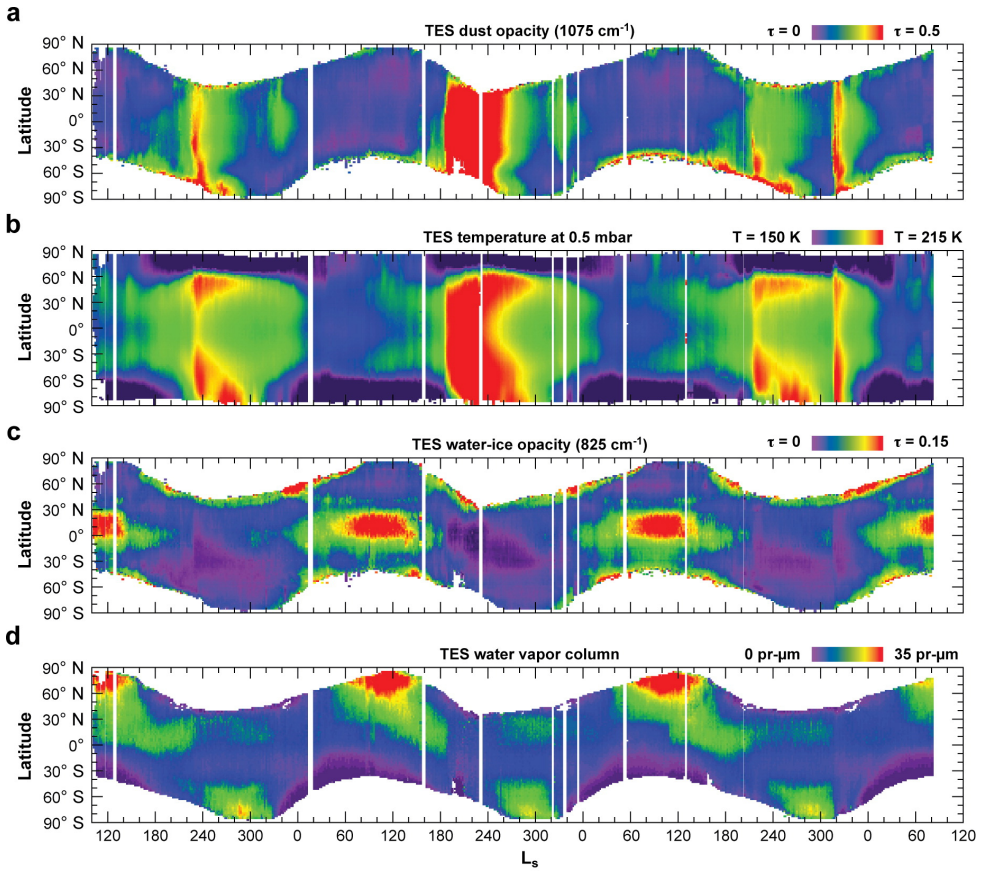


Figure 1.4 | An overview of TES atmospheric daytime nadir observations showing the seasonal and latitudinal variation of **(a)** dust optical depth (at a wavelength of 9 μm), **(b)** atmospheric temperatures (K) at 0.5 mbar (∼25 km), **(c)** water ice optical depth (at a wavelength of 12 μm), and **(d)** water vapour column abundance (precipitable microns). Data gaps (white vertical bands) were caused by spacecraft anomalies and solar conjunction. Note global dust storm and lack of northern tropics maximum at L_s=180° onwards near centre of figure.

Credit: Republished with permission of Annual Reviews, Inc., from 'Spacecraft Observations of the Martian Atmosphere', Annual Review of Earth and Planetary Sciences, 36, Smith, 2008; permission conveyed through Copyright Clearance Center, Inc.

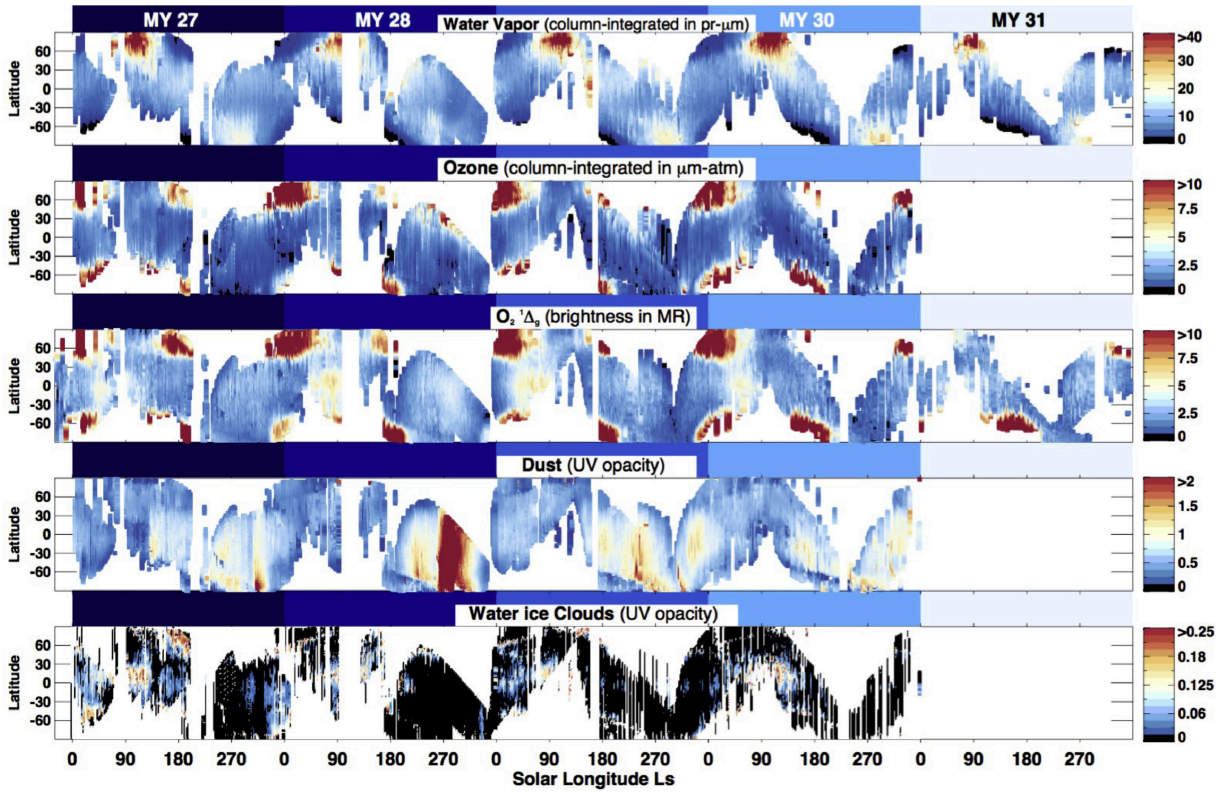


Figure 1.5 | SPICAM nadir observations showing seasonal and latitudinal variation of dust opacity, water ice opacity and water vapour column abundance. Aerosol opacity measured using the UV channel at 250 nm. Note global dust storm and reduced southern hemisphere maximum in MY28 at L_s=270°.

Credit: Reproduced from Montmessin et al. (2017), Icarus. Attribution-NonCommercial-NoDerivatives 4.0 International (CC BY-NC-ND 4.0)(https://creativecommons.org/licenses/by-nc-nd/4.0/).

summer and hence a more stable seasonal cap.

Despite strong qualitative agreement between different datasets there has been variation in absolute quantities. A representative diagnostic for this variation is the strength of the northern summer maximum: an initial value of about 100 pr. µm was found for MAWD (Jakosky & Farmer, 1982) and TES (Smith, 2002; 2004). These abundances decreased significantly after reanalysis. For MAWD there was a general reduction of 50% (Fedorova et al., 2010) with summer maximum dropping to 50–60 pr. µm, caused by updating spectral line parameters. For TES retrievals a reduction of 30% was seen (Fouchet et al., 2007; Smith, 2008) after correcting for a bias caused by the choice of a lower spectral resolution mode in much of the dataset. There have also been problems with disagreement between the various instruments on Mars Express, which take their observations simultaneously. Since then agreement has been much improved (Trokhimovskiy et al., 2015), with all in the 50–70 pr. µm range. The remaining variations have been attributed to differences in retrieval procedure and specific effects in the instruments' respective spectral bands (Korablev et al., 2006; Maltagliati et al., 2011b; Trokhimovskiy et al., 2015). For CRISM (MY28–33) a value of 50 pr. µm has been found (Smith et al., 2009a; 2018).

Apart from the variation between instruments there are also real interannual changes, though these are fairly modest (Smith 2008; Smith et al., 2018; Trokhimovskiy et al., 2015). The most variable part of the cycle is southern hemisphere summer and its associated maximum. In MAWD data this maximum is almost non-existent, though this is likely an observation effect whereby dust masks the lower atmosphere, shortening the optical path leading to reduced column abundance (Fedorova et al., 2004; 2010). In TES, SPICAM and CRISM data a real variation in abundance up to 20% is seen. A prominent example is that of the southern summer of MY28 as shown in Fig. 1.5, when a global dust storm occurred at the same time as a significant low in the southern summer maximum (10 pr. µm lower than normal). This was independently observed by SPICAM and CRISM (Smith et al., 2018; Trokhimovskiy et al., 2015). Proposed explanations for this decrease are either the dust storm shading the surface leading to surface cooling and increased regolith adsorption or the temperature profile becoming isothermal, blocking convection between the boundary layer and general circulation cell (Trokhimovskiy et al., 2015). A similar example of a reduction is seen in the vanishing of the northern autumnal tropics maximum during the dust storm in Fig. 1.4.

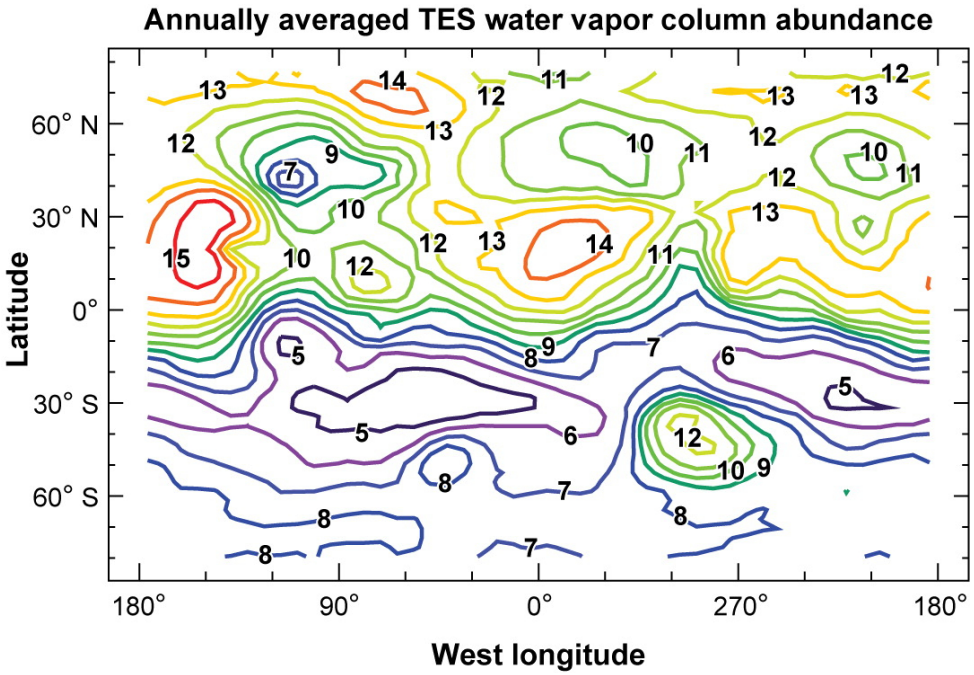


Figure 1.6 | Map showing the spatial distribution of the annually averaged water vapour column abundance (in pr. μm) as observed by TES.

Credit: Republished with permission of Annual Reviews, Inc., from 'Spacecraft Observations of the Martian Atmosphere', Annual Review of Earth and Planetary Sciences, 36, Smith, 2008; permission conveyed through Copyright Clearance Center, Inc.

1.3.2 Spatial Distribution

To the first order spatial variation in the water vapour column abundance is inversely proportional to topography (Smith, 2002; 2008) as can be seen in Fig. 1.6. For example, the Hellas basin (low region; 45°S, 290°W) shows relatively large column abundance while the surrounding southern highlands, show relatively low abundances. This inverse correlation implies that the water vapour mixing ratio is constant or a relatively weak function of altitude in the lowest scale height or two, where most of the mass of the atmosphere lies.

A major feature of the annually averaged spatial distribution is the band of increased water vapour in the 10°S–40°N band. This region remains relatively wet year-round compared to the regions lying further north and south (Smith, 2008). These regions have lower averages due to the strong seasonal variations noted in the previous sections.

There is also a strong positive correlation between albedo and water vapour column abundance (i.e. high albedo regions have high water vapour content) at low latitudes with an anti-correlation in thermal inertia (Jakosky & Farmer, 1982; Rosenqvist et al., 1992; Smith, 2002; Smith et al., 2009a; Toigo et al., 2013). Albedo, thermal inertia and surface pressure (topography) are all linked by moderate correlations and anti-correlations to each other, meaning it

is hard to pick one effect out from the rest. Each of them has direct relations with average and diurnal variation of subsurface temperature, the pore and grain size of the regolith and to the circulation patterns of the atmosphere. These can in turn influence the transport of water vapour and its adsorption and desorption into the regolith. It was noted by Smith (2002) that the albedo-water (and thermal inertia with water) relationship may well change at higher latitudes, possibly even changing sign. It is likely that albedo, thermal inertia and topography will contribute to the longitudinal variation of water vapour.

1.3.3 Vertical Distribution

To understand the behaviour of water vapour more fully in the atmosphere it is important to understand its vertical distribution. At a basic level this can be done by examining the condensation levels for water vapour along with their seasonal variation (see Fig. 1.7). This variation can be seen in results from TES, OMEGA and SPICAM (Smith, 2002; Maltagliati et al., 2011b; Montmessin et al., 2017). Between L_s=0° and 180° the atmosphere is relatively cool and so the condensation level is low (around 10–20 km), as the planet nears perihelion (currently at L_s=251°) the atmospheric temperature rises and so accordingly does the condensation level to over 40 km. This rising and falling of the condensation level has an effect on water vapour transport around the planet. During the warmer perihelion season, when the condensation level is high, water vapour can be transported from south to north via the Hadley circulation without condensing. Near aphelion the condensation level is lower and water vapour cannot be transported via the Hadley circulation without condensing leading to the creation of the water ice aphelion cloud belt (See Fig. 1.3; the belt can be seen in water ice plots Figs. 1.4 & 1.5 around L_s=90°). This could explain the relative maximum observed at low northerly latitudes during the autumn and winter, and the much larger latitudinal gradient in water vapour in the northern summer as compared to the southern summer (Clancy et al., 1996; Smith, 2002).

For further detail, observation of the vertical profile of water vapour itself are necessary. The first direct measurements were made by the Phobos/Auguste experiment, which used solar occultation orbiting geometry to retrieve vertical profiles of water vapour for the Martian atmosphere (Rodin et al., 1997; Krasnopolsky, 1991). An averaged vertical water profile from Rodin et al. (1991) is given in Fig. 1.8. The profile shows very dry atmospheric conditions above ∼30 km with the mixing ratio dropping down as low as 3 ± 2 ppm. Below 30 km (which is the condensation level) it seems to show a fairly constant mixing ratio down to the bottom of

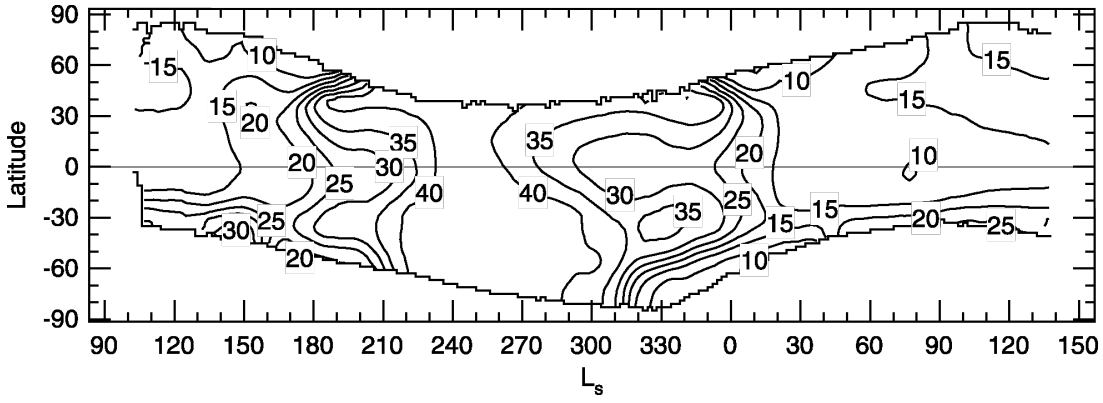


Figure 1.7 | The height in km above the surface of the water condensation level as a function of L_s and latitude from TES. Contour levels higher than 40 km above the surface are not shown. The solid lines bounding the contours on the top and bottom represent the latitude extent of where results exist.

Credit: Reproduced from Smith (2002), 'The annual cycle of water vapor on Mars as observed by the Thermal Emission Spectrometer'. Journal of Geophysical Research (Planets), 107, 25–1. Copyright 2002 by the American Geophysical Union (0148-0227/02/2001JE001522$09.00).

the observed altitude range at 10 km. A very steep increase in the water vapour mixing ratio can be seen just below the condensation level of the atmosphere (i.e. just below 30 km) to the constant mixing ratio seen below with a scale height of 2.5 km. Rodin et al. (1991) say this can be explained by the formation of clouds between 20 km and 30 km.

Until recently it was assumed that water vapour had a simple vertical structure—constant to condensation level with rapid drop-off above, but recent results from SPICAM and CRISM have shown this not to be the case (Fedorova et al., 2009; Malatagliati et al., 2011a; 2013; Clancy et al., 2017; Fedorova et al., 2018). With these two instruments extensive observation of the seasonal evolution of vertical water vapour profile has become possible (with the hope that Mars Climate Sounder can add to these results). In line with expectations during the late northern spring and early summer the vertical extent of water vapour is mainly limited to lower altitudes in line with the low condensation levels at this time of year, as the season progresses into southern spring and summer and the condensation levels rise the water vapour altitude range increases as well (Maltagliati et al., 2013). The surprising finds from these new vertical profile measures have been the observation of extensive supersaturation, detached layers of water, transport to higher altitudes, a variable correlation with dust aerosol and at times highly variable vertical profiles changing on the order of days. Examples of SPICAM and CRISM vertical profiles are given in Chapter 8 in Figs 8.12, 8.17, 8.18, 8.20–8.23 and 8.26–8.30 where they are used for comparison with MCS retrievals.

Extensive supersaturation in the atmosphere was first reported by Malatagliati et al. (2011a) (see Figs 8.17 & 8.18) and has since been corroborated by further SPICAM results and CRISM

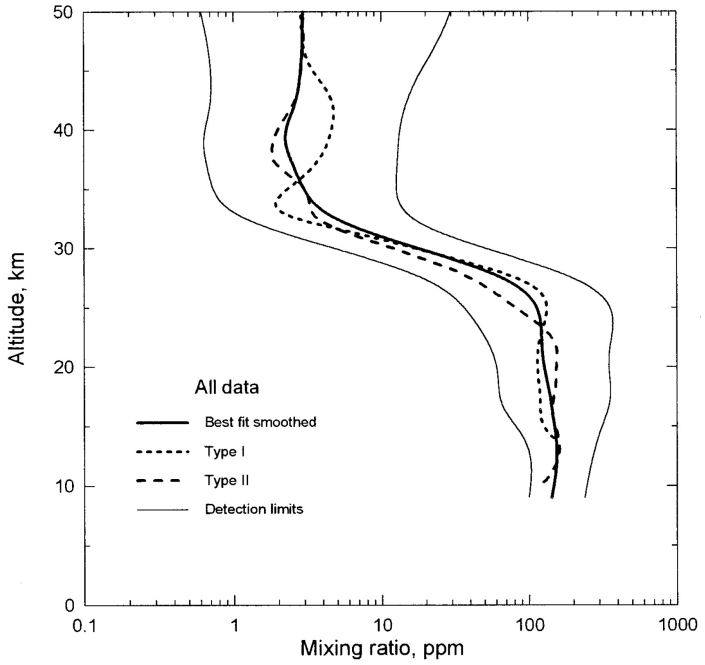


Figure 1.8 | Averaged vertical water profile from solar occultation measurements made in the Auguste experiment. The data has been convolved with a Gaussian field-of-view function that has a 4 km half-width. Separate profiles of types I (referring to lowest sounded tangent altitude being ∼20 km) and II (referring to lowest sounded tangent altitude being ∼10 km) are shown for comparison. Errors are represented by the two thin curves on either side of the main curve.

Credit: Reprinted from Icarus, 125, Rodin et al. (1997), 'Vertical Distribution of Water in the Near-Equatorial Troposphere of Mars: Water Vapor and Clouds', 212–229, Copyright (1997), with permission from Elsevier.

data. Using aphelion season MY29 (northern spring/summer, L_s=60–120°) observations they consistently found mixing ratios in excess of saturation above the condensation level (∼15 km at that time of year), in the 20–50 km region of the atmosphere with saturation ratios exceeding 10. Cases of supersaturation were found in both northern and southern hemispheres of Mars. They proposed that supersaturation was likely brought about by lack of condensation nuclei (which had been scavenged by ice clouds) at levels above the condensation level or a slowing of condensation due to the lower pressures of the middle atmosphere. Supersaturation seems strongest in the mid-latitudes during northern spring.

Along with supersaturation another startling find has been the variety and highly changeable nature of the vertical profile distributions and shapes. When looking at short timescales, on the order of days, it was seen that the vertical distribution of water vapour varies rapidly. This is in contrast to the more stable and steady behaviour shown by the longer term seasonal column abundance measurements from nadir observations discussed earlier (Maltagliati et al., 2013). The vertical profiles seem to incorporate the well understood long term stable repeatable seasonal changes along with highly variable features being superimposed. Southern spring (L_s=200–250°) is one of the most vertically dynamic periods in contrast with its featureless nadir observed steady column abundances. The variable nature of vertical profiles is attributed to a strong "synchronisation" with aerosol behaviour, although the correlation is neither simple nor systematic. One example of this link is the appearance of detached layers in profiles of both dust

and water vapour. Figures in §8.3.6 shows this and the other characteristic types of correlation observed.

The most abrupt variations observed appear in the form of "surges" where the water vapour in the atmosphere increases dramatically over the course of a few days. It was suggested that these were caused by perturbations in the lower atmosphere bringing up significant quantities of dust and water. The persistence of high abundances of water and dust at these levels after these perturbation events seems to suggest that there is interaction between the two species, rather than their just being passive tracers of atmospheric circulation. They cite the increased frequency of detached layers as evidence of this. In several retrievals aerosol and water vapour layers appear to be connected. In results from the first campaign a water layer is often observed a few kilometres below the aerosol one. They suggest that this could be formed by the evaporation of water precipitated from the cloud above by deposition.

There seems then to be a contradiction between nadir observed stability and the high variability of vertical profiles. Maltagliati et al. (2013) resolve this apparent contradiction by explaining that in the nadir, observations are more sensitive to the lower atmosphere which contains the bulk of the water in an atmospheric column. The high water concentrations seen in the Martian middle atmosphere around 50–70 km are negligible with respect to the total column abundance and that there is not an efficient link between the lower atmosphere and the higher atmospheric layers. It seems that the only time the link works more efficiently is during one of the "surge" episodes mentioned earlier.

Further evidence of the aerosol-water link came from Fedorova et al. (2018) who analysed SPICAM observations of MY28 (L_s=255–300°) including the 2007 global dust storm. In their observations they noted that during the dust storm water vapour was seen to be transported to much higher altitudes than usual for that season (comparing their results with MY32 SPICAM profiles).

In the northern hemisphere, they observed an order of magnitude increase in water vapour density in the 60–80 km height range from L_s=268–285°. During the dust storm, water vapour reached heights of 80 km with a mixing ratio $\geq$200 ppm. Two maxima were observed with largest water densities being detected at latitudes higher than 60°N during L_s=269–275°. Interestingly, this did not directly coincide with the aerosol loading but with a temperature maximum. Consequently, it was thought instead that it was related to adiabatic heating in the downwelling branch of the meridional circulation, that was intensified during the storm, transporting wa-

ter vapour from the southern hemisphere to high northern latitudes. The other maximum did coincide with high dust loading at middle northern latitudes. Comparisons with observations from the same season during MY32 (a quiet year with no global dust storm) showed that water vapour was only at 50 ppm at 60 km.

In the southern hemisphere, water vapour transport to higher altitudes was seen to be a more repeatable event, being seen in MY28 and MY32 observations. However, there was still an enhancement of the water vapour density during the dust storm. In MY28 there was an increase of 4–5 with a mixing ratio of >100 ppm correlating well with the vertical aerosol extension, whilst in MY32 a factor of 2–3 with a mixing ratio of >100 ppm was observed.

Fedorova et al. (2018) proposed that this high altitude water vapour could be a source of extra hydrogen escape after photodissociation by near-UV sunlight helping to explain increased hydrogen coronal emission observed by the Hubble Space Telescope (Clarke et al., 2014) and SPICAM UV spectrometer (Chaffin et al., 2014).

Further evidence of high altitude water vapour increases due to dust storms have been seen in early results from the ACS and NOMAD instruments aboard ExoMars Trace Gas orbiter (Vandaele et al., 2019). They monitored the vertical water vapour distribution prior to and during the onset of the MY34 global dust storm (starting at $L_s \approx 185°$, 30 May 2018). Large abundance increases at 40–80 km were observed during the storm. Increases by a factor of of 4–5 were seen and sometimes even larger, in line with what was seen by Fedorova et al. (2018). Elevated abundances above 40 km of up to 250 ppm were seen at northern mid-latitudes and 100 ppm at southern mid-latitudes. Smaller increases up to about 40 ppm were seen at high northern and summer latitudes.

1.3.4 Diurnal Variation

Results for diurnal variation are fewer and less extensive than those for seasonal and interannual cases, but the list is growing. The first major review collecting knowledge of diurnal results together was presented in Titov (2002): for ground-based observations (Sprague et al., 1996; 2006), ISM/Phobos (Rosenqvist et al., 1992), IMP/Pathfinder (Titov et al., 1999) and IRIS/Mariner-9 (Formisano et al., 2001; Ignatiev et al., 2001). These different sets of results are compared in Fig. 1.9.

A consistent pattern is revealed: a low abundance in the morning that increases monotonically until somewhere between 12h and 14h (local solar time) and then monotonically decreases.

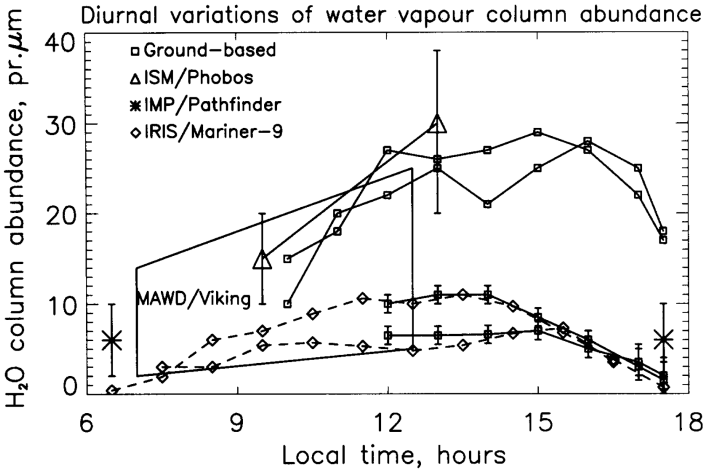


Figure 1.9 | Diurnal variations of the atmospheric water vapour column abundance.

Credit: Reprinted from Icarus, 29, Titov (2002), 'Water vapour in the atmosphere of Mars', 183–191, Copyright (2002), with permission from Elsevier.

This correlates well with the diurnal change in temperature, so at the hottest part of the day the most water vapour is in the atmosphere. Changes between the night-time minima and daytime maxima are in the 10–20 pr. µm range. The major difference between the instruments is in their respective amplitudes. Some ground-based observations and all IRIS observations give much smaller changes than the curves for ISM or the other ground-based changes. The discrepancies are likely to be due to the fact that these observations were all taken at different times of year and at different locations on the planet.

Major processes contributing to diurnal changes in water vapour column abundance are believed to be regolith adsorption/desorption (Houben, 1999; Titov, 2002), water ice cloud formation (Whiteway et al., 2009; Tamppari et al., 2010), and fog/surface frost (Smith et al., 2009b; Tamppari et al., 2010).

More recent results paint a less consistent and contradictory picture. With one exception, SPICAM and OMEGA have failed to observe significant diurnal variation in the water vapour column (Maltagliati et al., 2011b; Trokhimovskiy et al., 2015). However, it should be noted that because of Mars Express' orbit its instruments are generally restricted to investigating diurnal changes in polar areas (they cannot perform retrievals when passing over the nightside as they rely on reflected sunlight). Maltagliati et al. (2011b) compared their 08h–18h results with those of TES (14h) and found no prominent diurnal variations (within 4–5 pr. µm). Similarly for SPICAM no significant diurnal changes within its sensitivity (∼4 pr. µm) were found. The one exception to this are in the results of Melchiorri et al. (2009). Daily variability of water vapour column abundance was measured over the south polar region by OMEGA during the southern spring/summer period (L_s=250–270°) outside the CO_2 ice cap. An increase of a few precipitable

microns was seen during the day, peaking in the early to mid-afternoon in line with Titov (2002).

Additional recent observations have been based around the in situ craft: Phoenix and Curiosity. Using results from Phoenix (L_s=76.5–148°) Smith et al. (2009b) and Whiteway et al. (2009) saw water vapour partial pressure drop rapidly at 18h from daytime values of 2 Pa to less than 0.01 Pa at 01.5h. Combining Phoenix and CRISM data Tamppari et al. (2010) calculated a diurnal column abundance change of 15 pr. µm during L_s=108.3–109.1°. Additionally, Pankine & Tamppari (2015) used TES data from over the Phoenix site (from before it had landed) for northern spring/summer and saw 10–20 pr. µm changes. In contrast, at the Curiosity site (Gale crater) though extensive diurnal change was observed in water vapour mixing ratios (10–30 ppmm at night-time to 50–80 ppmm after sunrise), no significant change was seen in the water vapour column abundance (Savijärvi et al., 2016; McConnochie et al., 2018).

1.4 Thesis Outline

The aim of this thesis is to assess the ability of Mars Climate Sounder (MCS) to retrieve water vapour. In Chapter 2 the instrument and its host spacecraft Mars Reconnaissance Orbiter (MRO) are described including the observation process and the problems that were found with the B2 and B3 water vapour channels during pre-flight tests. The methods and theory behind the retrievals data analysis used are detailed in Chapters 3 & 4. Chapters 5 & 6 discusses the series of sensitivity studies and their results that were performed in order to gauge the water retrieval performance with MCS data. Laboratory measurements of the MCS B3 filter material spectral passband, investigating the passband broadening, are described along with their findings in Chapter 7. Vertical profile water vapour retrievals are performed and their results presented and compared with datasets from other instruments in Chapter 8. Finally, Chapter 9 summarises the main conclusions and gives suggestions for future work.

2

Mars Climate Sounder and Mars Reconnaissance Orbiter

In this section a brief overview is given of the Mars Climate Sounder (MCS) instrument and Mars Reconnaissance Orbiter (MRO) spacecraft, MCS data and calibration along with current problems with the investigation. This chapter draws heavily on certain sources and to prevent needless repetition of citations these sources will now be listed. For §2.1: Zurek & Smrekar (2007), for §2.2: McCleese et al. (2007), for §2.3.1: McCleese et al. (2007) and Adlen (2004), and for §2.3.3: Kleinböhl et al. (2009). Other sources are cited normally.

2.1 Description of MRO Spacecraft

Mars Reconnaissance Orbiter (MRO) is a NASA spacecraft that was launched on 12 August 2005, entering orbit on the 10 March 2006. Six months later it finished aerobraking on 30 August 2006 and is presently in a near-polar, near circular, low altitude (∼300 km), 03h/15h sun-synchronous orbit*. One of the primary objectives of MRO is to track and enhance our understanding of the Martian water cycle. Since arriving at Mars it has been returning a deluge of data on the Martian atmosphere, surface and sub-surface whilst also functioning as a relay station for missions on the surface of Mars (e.g. the Mars rovers and Phoenix lander). There

*The spacecraft passes over any given point of the planet's surface at the same local mean solar time on the dayside and has a local mean solar time 12 hours later when passing over the nightside, except for near the poles.

Table 2.1 | MRO Science Capabilities.

Credit: Reproduced from Zurek & Smrekar (2007), 'An overview of the Mars Reconnaissance Orbiter (MRO) science mission'. Journal of Geophysical Research (Planets), 107, 25–1. Copyright 2007 by the American Geophysical Union (0148-0227/07/2006JE002701).

Instrument Capabilities (Ref. to 300 km)		
CRISM	Multi-spectral Survey ∼70 channels ∼200 m/pixel bin	Hyperspectral Imaging 18 m/pixel 10.8 km swath 6.5 nm spectral resoln 0.4–3.92 µm
CTX	High Resolution Imaging Panchromatic (minus blue) Stereo by Revisit	6 m/pixel 30 km swath SNR > 20
HiRISE	Very High Resoln Imaging 1.2 km swath (NIR & BG) Stereo by Revisit	0.3 m/pixel 6 km swath (red) SNR > 150
MARCI	Daily Global Monitoring 180° FOV	7 Bands 0.28–0.8 µm 5 VIS: 1–7 km/bin 2 UV: 10–30 km/bin
MCS	Daily Global Profiling Broadband solar 8 thermal IR arrays	Limb Sounding 0–80 km. ∼5 km vertical resoln
SHARAD	Radar Profiler 1 × 6 km footprint Profile to ∼70.5 km depth	15–25 MHz band SAR processing down-track ∼10 m vertical resoln

has been so much data, in fact, that it has been granted extensions since the end of the initial two-year Primary Science Phase (PSP). Results of note include: measuring the amount of water ice in the northern ice cap (Putzig et al., 2009), finding ground water ice exposed in new craters (Byrne et al., 2009), finding water ice in lobate debris aprons (Plaut et al., 2009), measurement of aqueous minerals (Murchie et al., 2009) and even capturing photographs of avalanches in progress (Russell et al., 2008).

The orbiter carries a payload of six scientific instruments for remote sensing, covering the spectrum from the visible to the far infrared with spatial resolutions ranging from 1 km to 30 cm. A brief summary of the capabilities of each instrument is given in Tbl. 2.1. Fig. 2.1 shows how the instruments work together over their respective spectral ranges to track the progress of the Martian water cycle and Fig. 2.2 shows the location of each instrument on the payload deck. The spacecraft also performs the critical function of telecommunications relay for missions on the surface of Mars. This has included the Martian rovers: Curiosity, Spirit and Opportunity; and the Phoenix lander.

To cope with the large amount of data returned, MRO is equipped with a 3-metre high-gain antenna (HGA) coupled with two powerful 100 W X-band travelling-wave tube amplifiers. On-board systems are powered by two 50 Ah battery systems, which are charged by two solar array

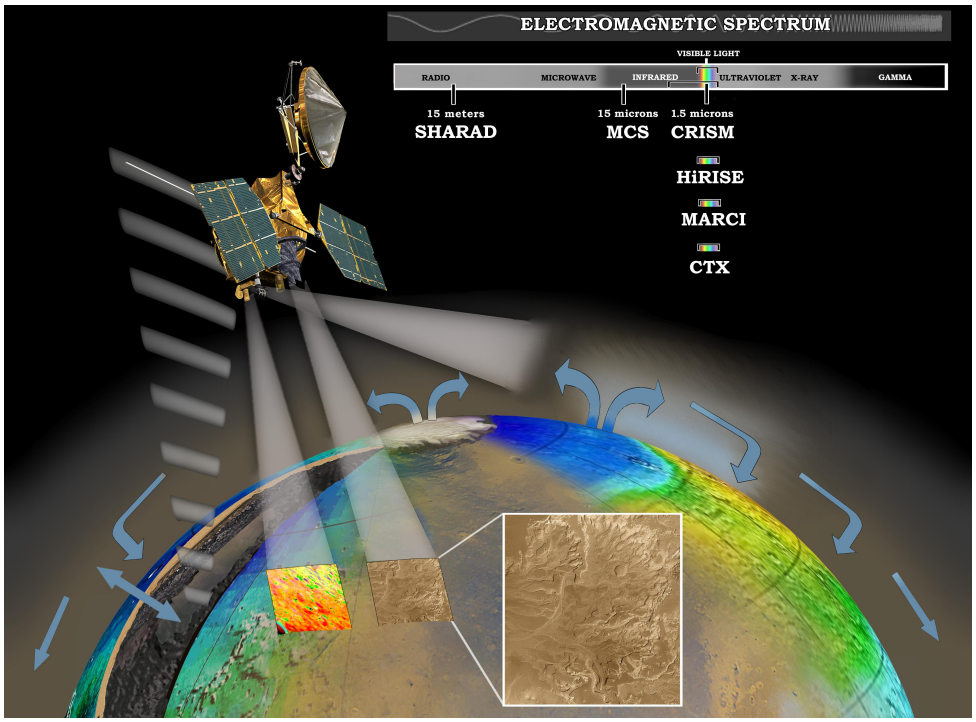
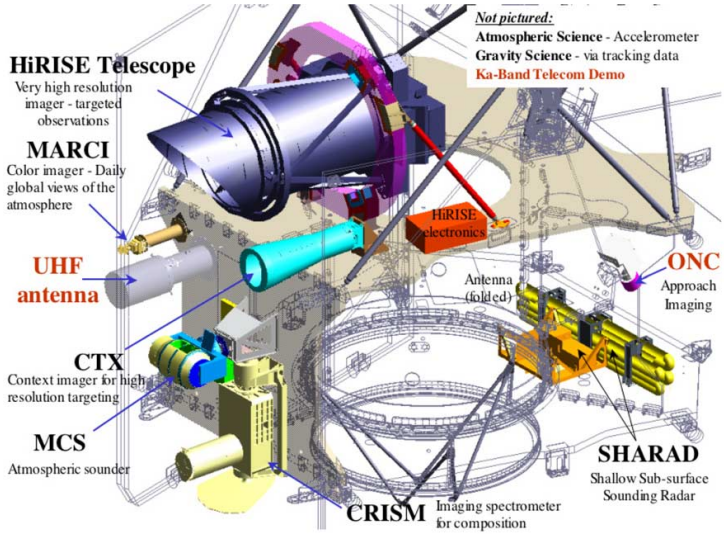


Figure 2.1 | An artist's impression of how MRO and its complement of instruments track, measure and explore the Martian water cycle. Courtesy of NASA/JPL.

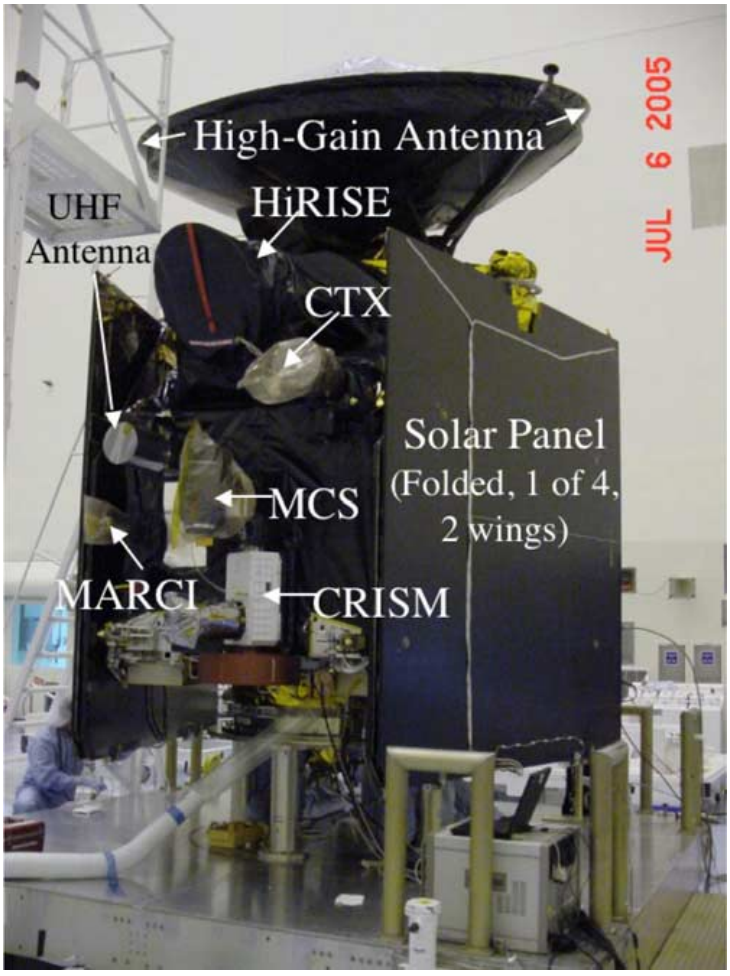
wings with an area of 20 square metres, generating 600 W even at Mars aphelion. The spacecraft is significantly larger than Mars Global Surveyor and Mars Odyssey, with a height of ∼7 m when the HGA is stowed and a width of ∼14 m when the solar arrays are fully extended. It weighed 2180 kg at launch including 1199 kg of fuel for its 20 thrusters (including six main thrusters). This thesis concerns only one instrument aboard MRO, Mars Climate Sounder (MCS), which will be described in the rest of this chapter.

2.2 MCS: Instrument Overview

Mars Climate Sounder (MCS) is NASAs third attempt to monitor the current climatology of Mars after the unfortunate losses of the Pressure Modulator Infrared Radiometer (PMIRR) (Irwin, 1991) on both the Mars Observer and Mars Climate Orbiter spacecraft (McCleese et al., 2007). It continues building on the Martian climatology record started by Mars Global Surveyor (MGS) in 1997, complemented by Mars Odyssey, meaning there has now been continual coverage for over 10 Martian years. Its purpose is to observe the 4-dimensional (3 spatial dimensions and 1 temporal) variation of the atmosphere with regard to the vertical and horizontal distributions of temperature, pressure, dust and water vapour. See Tbl. 2.2 for a summary of the science



(a) MRO science instruments



(b) MRO

Figure 2.2 | **(a)** A schematic diagram indicating the location of the MRO science instruments (black captions) and engineering components (red captions) as deployed on the spacecraft nadir panel and middle deck. The SHARAD radar is mounted on the aft deck of the orbiter, near the main engine cluster. (Note: MARCI was relocated along the deck edge below the UHF antenna). **(b)** MRO at Kennedy Space Centre prior to integration with launch vehicle. The solar arrays are folded up and the instrument deck is visible with each instrument being labelled (they are covered with protective covers and purge bags).

Credit: Reproduced from Zurek & Smrekar (2007), 'An overview of the Mars Reconnaissance Orbiter (MRO) science mission'. Journal of Geophysical Research (Planets), 107, 25–1. Copyright 2007 by the American Geophysical Union (0148-0227/07/2006JE002701).

Table 2.2 | MCS Observation Modes and Science Objectives.

Credit: Reproduced from McCleese et al. (2007), 'Mars Climate Sounder: An investigation of thermal and water vapor structure, dust and condensate distributions in the atmosphere, and energy balance of the polar regions'. Journal of Geophysical Research (Planets), 112, E05S06. Copyright 2007 by the American Geophysical Union (0148-0227/07/2006JE002790$09.00).

Observation Mode	Measurement Objective	Science Objective	High-Level Science Goal
In Track Limb	Staring Vertical profiles of temperature, pressure, aerosols, and water vapour	Global monitoring of atmospheric properties	Atmospheric circulation, interannual climate variations, annual water, and dust cycles
Nadir Sounding	Surface infrared radiance and broadband solar reflectance	Characterization of surface and sub-surface thermal state and thermal properties	Climate, distribution, and state of surface and subsurface water
Polar Buckshot Scanning	Net polar radiative balance	Annual carbon dioxide frost budget	Interannual and secular climate variations, and global change

objectives of the mission.

MCS is an infrared radiometer with nine spectral channels ranging from 0.3–50 µm that observes in both limb and nadir viewing geometries. It consists of a capsule containing the optics bench, two telescopes and analogue and digital electronics boards, suspended from a yoke. The yoke supports the instrument, contains the instrument calibration targets, power conditioning and drive electronics and provides the mechanical/electrical interface to the spacecraft. Movement of the instrument is facilitated by two actuators on the yoke, one between the capsule and a yoke 'prong' for elevation and one on the bottom of the yoke for azimuthal motion. This allows for a range of motion of 270° in both axes providing a view of the full hemisphere below the nadir-pointed payload deck. The whole instrument weighs only 9 kg consuming 11 W of power, compared with 44 kg and 40 W for PMIRR. See Fig. 2.3 for a detailed view of the external configuration of MCS.

The instrument's nine spectral channels are split into two groups with corresponding focal planes and telescopes. The first group are six 'A' channels, where channels A1–A5 use mid-infrared optical interference filters (400–870 cm^{-1}) with A6 being a broadband channel in the visible. The second group are the three 'B' channels, using far infrared mesh filters (220–340 cm^{-1}). See Fig. 2.4 for a plot of the channel filter profiles (as measured during pre-flight testing). Each channel consists of a 21-element linear thermopile detector array, with each detector mapping a 5 km × 8.5 km field of view (FOV) when used in the limb viewing geometry (covering a range of 105 km) and a 1 km × 1.7 km FOV for a nadir geometry. The vertical resolution of 5 km corresponds to approximately half an atmospheric scale height. The spectral characteristics of each channel and its use are given in Table. 2.3. A diagram of how the arrays



Figure 2.3 | The MCS flight instrument photographed during calibration at JPL. Major elements of the instrument are identified.

Credit: Reproduced from McCleese et al. (2007), 'Mars Climate Sounder: An investigation of thermal and water vapor structure, dust and condensate distributions in the atmosphere, and energy balance of the polar regions'. Journal of Geophysical Research (Planets), 112, E05S06. Copyright 2007 by the American Geophysical Union (0148-0227/07/2006JE002790$09.00).

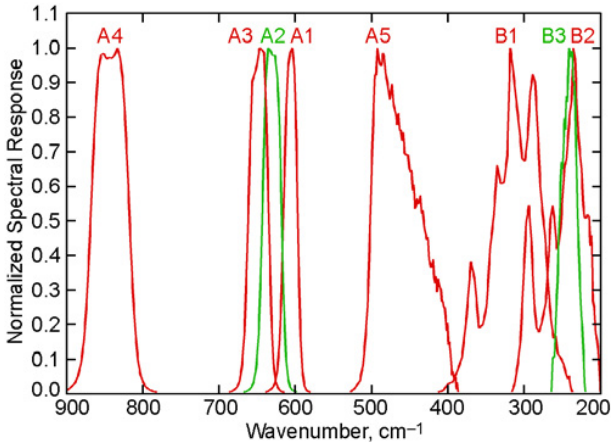


Figure 2.4 | Normalized measured response of MCS thermal spectral channels. Channels A2 and B3 are in green to make the curves easily visible.

Credit: Reproduced from McCleese et al. (2007), 'Mars Climate Sounder: An investigation of thermal and water vapor structure, dust and condensate distributions in the atmosphere, and energy balance of the polar regions'. Journal of Geophysical Research (Planets), 112, E05S06. Copyright 2007 by the American Geophysical Union (0148-0227/07/2006JE002790$09.00).

Table 2.3 | MCS Spectral Channel Band Passes, Noise Equivalent Radiance for a two second integration and Measurement Functions†. Noise values for A6 were not stated in these publications and A6 is not used for work in this thesis.

Credit: Reproduced from McCleese et al. (2007), 'Mars Climate Sounder: An investigation of thermal and water vapor structure, dust and condensate distributions in the atmosphere, and energy balance of the polar regions'. Journal of Geophysical Research (Planets), 112, E05S06. Copyright 2007 by the American Geophysical Union (0148-0227/07/2006JE002790$09.00). NER data from Kleinböhl et al. (2009), 'Mars Climate Sounder limb profile retrieval of atmospheric temperature, pressure, and dust and water ice opacity'. Journal of Geophysical Research (Planets), 114, E10006. Copyright 2009 by the American Geophysical Union (0148-0227/09/2009JE003358$09.00).

Telescope/ Channel Number	Band Pass, cm^{-1}	Band Centre, µm	NER (mWm^{-2} sr^{-1}/cm^{-1})	Measurement Function
A1	595–615	16.5	0.0557	temperature 20 to 40 km
A2	615–645	15.9	0.0399	temperature 40 to 80 km and pressure
A3	635–665	15.4	0.0419	temperature 40 to 80 km and pressure
A4	820–870	11.8	0.0287	dust and condensate (D&C) extinction 0 to 80 km
A5	400–500	22.2	0.0278	temperature 0 to 20 km, D&C extinction 0 to 80 km
A6	3300–33000	1.65	-	polar radiative balance
B1	290–340	31.7	0.0453	temperature 0 to 20 km and D&C extinction 0 to 80 km
B2	220–260	41.7	0.0568	water vapour 0 to 40 km and D&C extinction 0 to 80 km
B3	230–245	42.1	0.174	water vapour 0 to 40 km and D&C extinction 0 to 80 km

†D is dust; C is condensates of H_2O and CO_2.

project onto the limb is given in Fig. 2.5, which can be directly compared with Fig. 2.6 which shows the projection of the A-channel detector array onto the limb or the ground. MCS started taking data on the 24 September 2006 (L_s=110°).

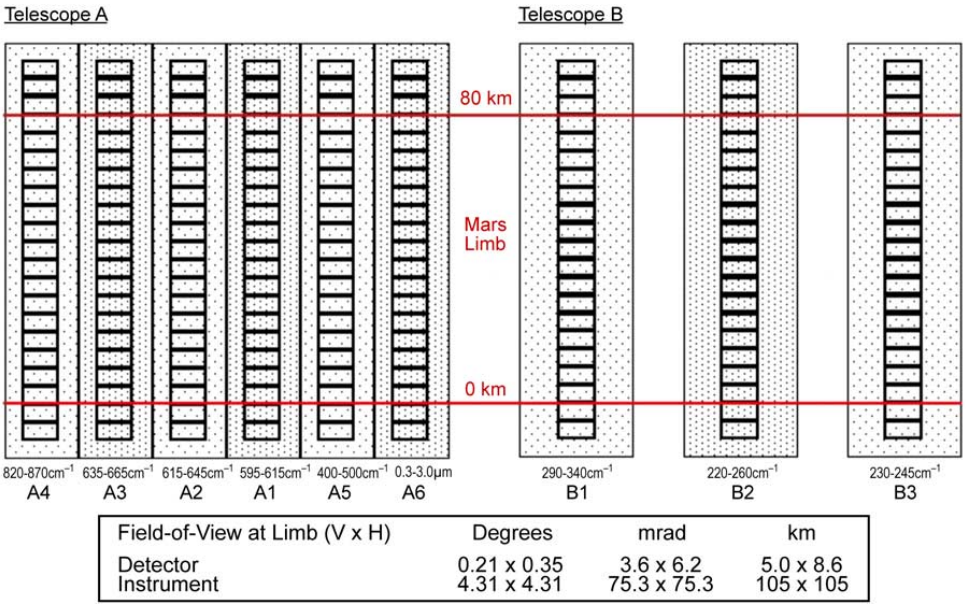
2.2.1 Optics and Mechanisms

The two identical reflecting telescopes of MCS (with 3 mirrors each) are off-axis, all-reflective, telecentric with 4 cm apertures and FOVs of 4.3°. The telescopes are mounted as 'mirror-images' of each other with parallel optical axes. The tertiary mirror focuses a f/1.7 beam through the bandpass filters and on to the focal plane detectors. The baffles, mounted close to the back surfaces of the filters, act as light pipes and define the FOV response for each detector element.

Limb-sounding measurements are strongly influenced by vertical FOV response, so it is important to make sure FOV wings are reduced as much as possible. Focal plane baffles reduce wing response produced by scattering within the filters and by thermal radiation re-emitted from the detectors. Other measures used to reduce FOV wing response due to scattering and diffraction include apodizing mirror edges with gold black†, post-polishing of the mirrors (with silicon dioxide-protected aluminium coating) and Martin Black treatment‡ on exposed surfaces. To reduce stray light after one reflection external baffles are used. A cross-section of the MCS telescopes is presented in Fig. 2.7.

†An optical coating enhancing infrared absorption (Harris et al., 1948; Pompea & Breault, 1995).

‡An anodization treatment for aluminium substrates to create optically black surfaces (Pompea & Breault, 1995).



Field-of-View at Limb (V x H)	Degrees	mrad	km
Detector	0.21 x 0.35	3.6 x 6.2	5.0 x 8.6
Instrument	4.31 x 4.31	75.3 x 75.3	105 x 105

Figure 2.5 | MCS fields of view projected at the limb of Mars. The telescope A and B FOV responses are aligned to be superimposed within one-half FOV in the horizontal direction and one-tenth FOV in the vertical (shown separated for clarity).

Credit: Reproduced from McCleese et al. (2007), 'Mars Climate Sounder: An investigation of thermal and water vapor structure, dust and condensate distributions in the atmosphere, and energy balance of the polar regions'. Journal of Geophysical Research (Planets), 112, E05S06. Copyright 2007 by the American Geophysical Union (0148-0227/07/2006JE002790$09.00).

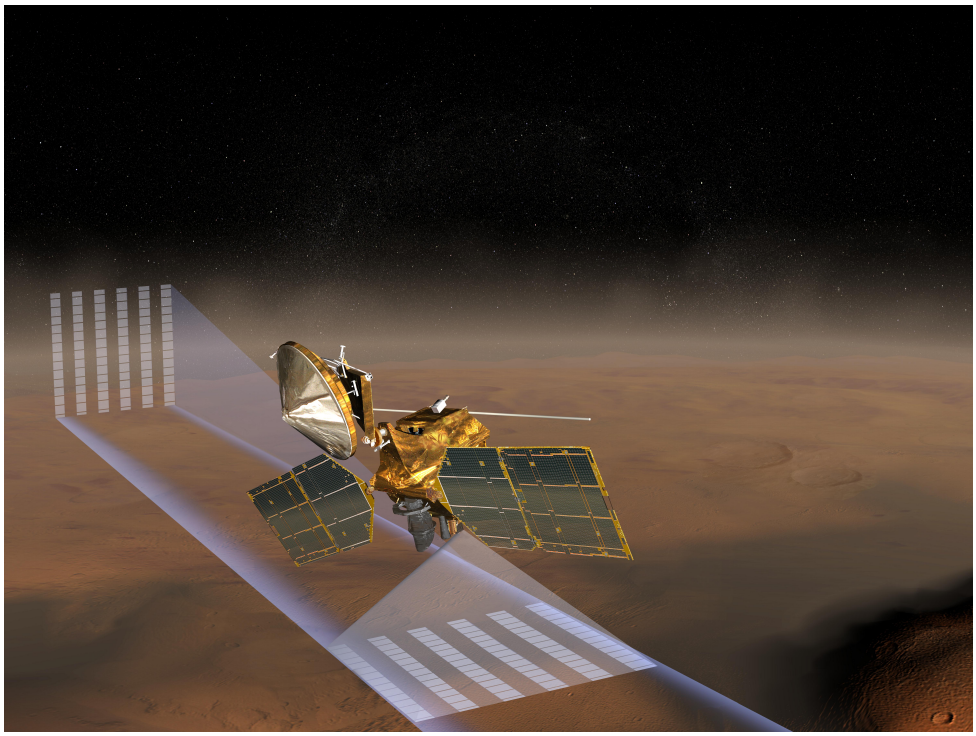


Figure 2.6 | An artist's impression of MCS performing limb and nadir observations at Mars, note the arrays of squares which show the projection of the detector arrays on the limb and ground respectively. The spacecraft is travelling in the direction of the limb projection. Courtesy NASA/JPL-Caltech.

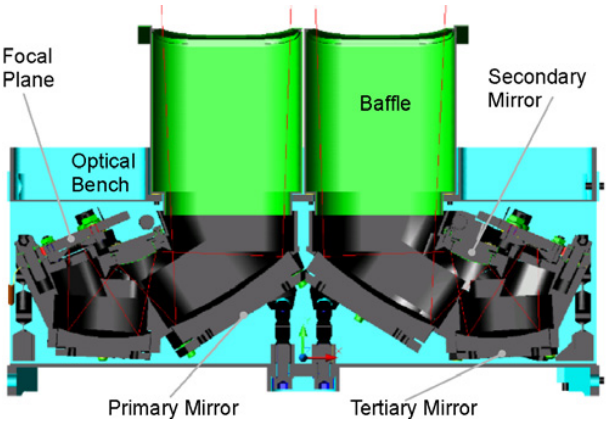


Figure 2.7 | Mechanical cross-section of MCS telescopes and optical bench (reference rays are faint red lines).

Credit: Reproduced from McCleese et al. (2007), 'Mars Climate Sounder: An investigation of thermal and water vapor structure, dust and condensate distributions in the atmosphere, and energy balance of the polar regions'. Journal of Geophysical Research (Planets), 112, E05S06. Copyright 2007 by the American Geophysical Union (0148-0227/07/2006JE002790$09.00).

It is also important to control for the effect of thermal drift with MCS, as it is an unchopped radiometer. The main source of variable energy likely to cause thermal instability of the instrument is the day-to-night contrast in solar illumination and Martian surface temperature, experienced once per orbit at the terminator. This effect is reduced by maximising the thermal mass of the telescope, maximising the thermal conductivity between component parts and conductively isolating the telescopes via fibreglass washers from the surrounding optical bench which sees most of the variable environmental heat load (from the instrument thermal blankets and external baffles). Temperature control is applied to the optical bench, which acts as a stable radiative 'oven' for the telescopes and focal planes.

Brushless stepper motor actuators for elevation and azimuth allow the instrument FOV to be aimed over the full hemisphere below the spacecraft; the motors have a range of 270° in both axes. Each motor is contained in a twist-capsule assembly along with gearing, position sensing diodes and flexible leads (to supply data, signal and power). Step-size for the motors is 30° and after gearing down (ratio of 297:1) the resulting step-size becomes 0.1°. This corresponds to half of the vertical instrument FOV for limb observations, i.e. 2.5 km or one-quarter of the Martian atmospheric scale height (∼10 km).

2.2.2 Focal Plane Assembly and Detectors

The spectral passbands of the channels on MCS are defined using filters mounted in metal frames, incorporating detector baffles, directly in front of the detector arrays as part of the focal plane assembly (see Fig. 2.8). The filters fill almost the whole 2π FOV above the detector.

The aluminium alloy baffles are positioned directly between the filters and detectors with the purpose of reducing transmission of off-axis rays produced by reflections within the assemblies and by reflection and emission from the detector surfaces. They have an anodized coating with a low large angle reflectivity preferentially reducing off-axis reflections. Around the detector arrays the baffles split into cells, forming walls around individual detectors.



Figure 2.8 | MCS filter assemblies.

Credit: Reproduced from McCleese et al. (2007), 'Mars Climate Sounder: An investigation of thermal and water vapor structure, dust and condensate distributions in the atmosphere, and energy balance of the polar regions'. Journal of Geophysical Research (Planets), 112, E05S06. Copyright 2007 by the American Geophysical Union (0148-0227/07/2006JE002790$09.00).

For the A telescope, channels A1–A5 (400–870 cm^{-1}) use multilayer interference filters manufactured by the University of Reading, UK. They have a germanium substrate, chosen because of the material's mechanical robustness and high optical transmission over the full spectral range (there is a germanium absorption band at 500 cm^{-1} but its effects are negligible given the thinness of the substrates). The remaining channel, A6, is the broadband visible channel (3300–33000 cm^{-1}). The filter is made of UV22 glass, chosen for its blocking from 2000–3300 cm^{-1}. On the B telescope are the three far infrared channels B1–B3 (220–340 cm^{-1}). Each filter comprises of a stack of copper meshes mounted on a polypropylene substrate. They were manufactured by Cardiff University.

Thermal stability of the filters is crucial to obtain accurate and trustworthy results. This is because the filters function as sources of black body radiation at wavelengths away from their narrow spectral windows, so small differences in the temperature of the filter will lead to measurable signals at wavelengths where the detector absorbs. The temperature difference due to changing scene, e.g. between a nadir (surface) observation and a limb (atmosphere) observation is potentially large enough to cause a measurable, but spurious effect. A temperature change of 5 mK gives a signal equivalent to 1% true signal change in A3. To counteract this the filters are mounted in good thermal contact with a large thermal mass.

Each channel consists of an array of 21 thermopile detectors (or pixels). Each detector consists of a silicon-nitride membrane with twelve Bi-Sb-Te/Bi-Te thermocouples connected in series. These thermocouples measure the temperature difference between the thermally isolated absorber and substrate. The detectors are coated in gold black to provide high absorptivity and have a flat spectral response between 222 and 3.33×10^4 cm^{-1} (0.3–45 µm).

Two sources of noise are associated with the thermopile detectors. One is flicker noise ($1/f$ noise) and the other is Johnson-Nyquist (thermal noise). The MCS observation cycle consists of two-second signal integration intervals, interspersed every 34 seconds with instrument views of space. This corresponds to a frequency range of 0.03–0.25 Hz. Thus, given the low frequencies it can be seen how flicker noise becomes significant in the detector signal readout and subsequent amplification. Fortunately thermopile detectors have intrinsically low flicker noise when read out with high-input-impedance voltage amplifiers as there is negligible current flow. For the amplification, drastic reduction of flicker noise is achieved by taking the roughly DC signal coming from the detectors and modulating it at 64 kHz (remembering that it is proportional to $1/f$) using an electronic chopping circuit.

The thermal noise for the 100 kΩ MCS detectors is 40 $nV/Hz^{1/2}$. With a 100 kΩ source the input-referred noise for the readout chip is 70 $nV/Hz^{1/2}$ for 0.03 to 0.25 Hz. Hence the readout chip is the dominant focal plane noise source. Despite this readout noise, the MCS focal planes exhibit a specific detectivity of $D^*=8 \cdot 10^8$ $cmHz^{1/2}/W$ for 0.03 to 0.25 Hz. Specific detectivity is a measure of photodetector performance, defined as $D^* = \frac{\sqrt{A \cdot \Delta f}}{\mathrm{NEP}}$, where A is the area of the detector, Δf is the bandwidth and NEP is the noise equivalent power. Noise Equivalent Radiance values for MCS channels are given in Tbl. 2.3.

2.2.3 Observation Strategy, Cycle and Viewing Modes

The aim of the MCS observational strategy is a continuous record of Martian climatology over the mission lifetime. This is accomplished by uninterrupted (with some exceptions, see §2.2.4) repetitive measurements over the mission lifetime. Using on-board software MCS performs repetitive measurements autonomously. The controlling software is table-driven and is loosely keyed to the spacecraft's latitude. The aspheric shape of Mars is sufficient to require latitude-dependent (though not longitudinal) adjustments to MCS pointing for limb-staring observations.

The observation cycle consists of shifting between viewing modes (using two-second measurement integration intervals). The normal cycle is Nadir-Limb-Space: First the nadir for four

seconds (or two measurement integration intervals), second the forward limb for 16 seconds (eight measurement integration intervals) and third a view of space above the limb for four seconds. Including the motion of MCS between viewing modes one normal cycle has a duration of 34 seconds, so that atmospheric profiles are acquired every 110 km or 1.86° in latitude. Interspersed among these cycles are occasional views of the calibration target (see below). Calibration is achieved using a combination of the space views and views of the calibration target. Each of the viewing modes is briefly described below:

Nadir/Off-nadir In the nadir, MCS views straight down. Since 9 October 2007 off-nadir observations with surface incidence angles of 60–70° have been used instead because of the elevator slewing problems (see §2.3.3).

Limb Forward in-track limb measurements are made in the direction of the spacecraft velocity vector (see Fig. 2.6). This was chosen as it allows combination with corresponding nadir measurements of the same scene, made earlier in the orbit and also gives line-of-sight overlap for successive vertical profiles. It also lowers the risk of viewing the sun directly by accident. Though not the default, cross-track limb observations are also occasionally made in order to obtain coverage of local time of day variability in the atmosphere. The cross-track limb is approximately 1.5 hours ahead/behind the local time of the in-track limb at the equator. Time of day coverage increases poleward and is complete at ±67° latitude.

Polar Buckshot These are off-nadir observations for use when MRO is above the poles. They are used to measure the angular dependence of emitted and reflected light at the top of the atmosphere in order to characterize the Martian polar radiative balance. This is made possible because of instrument's full range of articulation in elevation/azimuth. Buckshot observations are arranged in concentric circles around the pole to sample emission angles while providing geographical coverage. The pattern is repeated until the polar cap has been covered.

Calibration target A calibration black body of known temperature is used as reference point for MCS and is viewed approximately 10 times an orbit. There is also a solar calibration target for use with the A6 channel, viewed two times an orbit. For more details see §2.2.5.

Space view Also used for calibration this gives a reference zero radiance value for MCS to use.

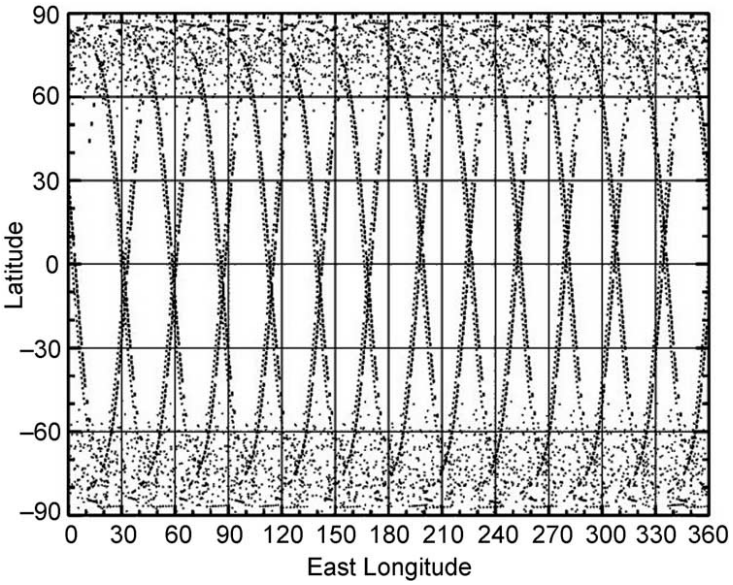


Figure 2.9 | Equirectangular projection of 24 hours of MCS observational coverage. Each observation is plotted as a point, either on the surface for surface views or at the location of the tangent point of the array for limb observations. The ascending (day) tracks slant from lower right to upper left, while the descending (night) tracks slant in the opposite direction.

Credit: Reproduced from McCleese et al. (2007), 'Mars Climate Sounder: An investigation of thermal and water vapor structure, dust and condensate distributions in the atmosphere, and energy balance of the polar regions'. Journal of Geophysical Research (Planets), 112, E05S06. Copyright 2007 by the American Geophysical Union (0148-0227/07/2006JE002790$09.00).

2.2.4 Observational Coverage

MRO is currently in a near-circular polar orbit that has nominal equator crossing times of 03h and 15h, with an orbital period of 112 min 12 s. It has a periapsis altitude of 255 km at the south pole and an apoapsis altitude of 350 km at the north pole. An inclination of 92.6° was chosen to give full latitudinal coverage and assure the fixed equator crossing time mentioned above; using this means the orbit precession rate is matched to the mean velocity of Mars about the Sun.

Coverage for 24 hours of observations is given in Fig. 2.9. The gaps in the observation tracks are due to calibration measurements. The limb observations have a spacing of 110 km (1.86°) in latitude and an orbit-to-orbit longitudinal spacing of 27°, determined by the rotation of Mars. At high latitudes limb observations are made less frequently to accommodate buckshot observations, though this is compensated for by the convergence of orbital tracks near the pole.

Though coverage is generally continuous, proceeding via the observational cycles just discussed, there are breaks whenever the MRO spacecraft rolls by more than 9° from the on-nadir position. This occurs because other instruments on MRO occasionally require a roll with values of up to 30°. This is highly unsatisfactory as it breaks the continuous coverage. When MRO rolls the line of detectors for each channel is no longer at right angles to the horizon, but at an angle. Consequently when MRO rolls by greater than 9° the detector arrays no longer cover the full vertical range (0–80 km).

Roll angles of less than 9° can be accommodated by the two detector margin at the top and bottom of the arrays (see Fig. 2.5). This problem has been mitigated somewhat by the MRO

Project Science Group's request to limit large rolls of greater than 9°, as this is entirely possible for most observations with good forward planning (most surface targets can then be seen within 30 days).

For cases where a roll of greater than 9° is unavoidable, MCS can be commanded to change from its normal cycle to an alternating slew mode. In this case MCS slews back and forth to provide two overlapping FOVs that together provide coverage of the full 0–80 km range; such data are then flagged. Such large rolls are necessary for the High Resolution Imaging Science Experiment (HiRISE) camera when taking a stereo image pair, one large roll per stereo pair. These observations disrupt continuity of MCS measurements for 15 minutes, or 48° in latitude.

Additionally HiRISE needs a still platform from which to take its highest resolution images. It was found during ground testing that the jitter from the MCS motor while moving exceeded the allowance for a still platform. As a result of this MCS is commanded to 'Freeze' when HiRISE is performing such observations. This requires it to view the limb and remain stationary for the duration of the high-resolution imaging. It is commanded to return to its normal routine after waiting for 60–90 seconds. These results are also flagged.

2.2.5 In-Flight Calibration

Using views of space and views of the calibration targets MCS performs a two-point in-flight radiometric calibration on its signals to correct for the effects of thermal drifts. The space views are achieved by slewing MCS so that it is pointing above the limb (see §2.2.3). This provides a zero radiance reference for all MCS channels. Space views are obtained at 34-second intervals during normal cycle operations.

There are two calibration targets on MCS: for the infrared there is a black body mounted in the yoke directly underneath the main MCS capsule, for the broadband visible channel A6 there is a solar calibration target that forms a 'tongue' on the yoke. See Fig. 2.3 for the location of both targets.

The black body target is used approximately 10 times an orbit. For an infrared calibration view MCS slews in elevation until the target completely fills the FOV of both telescopes. To meet the MCS radiometric calibration requirement of better than ±0.5% at 300 K, the target must be thermally uniform with its temperature known to an accuracy of better than ±0.25 K and an emissivity accuracy of better than ±0.0035. These requirements are fulfilled by using a grooved aluminium plate blackened with the Martin Black anodization process. Target temperature is

monitored by two platinum resistance thermometers (embedded in the centre of the viewed area for each telescope). One of the sensors coupled with a distributed heating element (located on the rear surface of the target) is used to control the target temperature. MCS is designed such that the distance between the target and telescope apertures is deliberately very small. The target has non-zero reflectivity though this is compensated for by keeping the target temperature to within a few degrees of the telescope temperature.

The solar calibration target (used to provide a second calibration point for A6) is used twice an orbit as the sun rises or sets over the limb of Mars, at which point MCS slews so that the target fills the FOV of the A telescope. The target works by diffusively scattering solar radiation into the telescope. For these measurements the sun is at an angle of roughly 15° below the local horizontal. To meet the target absolute radiometric calibration requirement of ±3%, reflectivity needs to be almost Lambertian; the target was tested before launch over the expected range of viewing and illumination angles. It is also very important that the reflectivity does not change significantly over the course of the mission. The target is a textured aluminium plate that is suspended and thermally isolated from a supporting base structure. Together the target and base structure form a calorimeter which can be used as a means of self-calibration. By monitoring the temperatures of the target and base structure, changes in the target's reflectivity can be discerned and corrected for in the relevant measurements. During the cruise to Mars the MRO spacecraft was configured to enable two tests to be performed on the solar target. These tests were to ascertain the effect (probably darkening) on the target of prolonged exposure to solar UV radiation. A two-point comparison established that after 40–50 hours of exposure any change in target reflectivity that had occurred was less than 0.1%.

2.3 Detection of Water Vapour and Problems

2.3.1 The Water Vapour Channels B3 and B2

The MCS design includes two spectrally co-located channels for the detection of water vapour: the narrow B3 (230–245 cm^{-1}) and the wider B2 (220–260 cm^{-1}). The narrow B3 channel was to be located between two strong water absorption features, while the broader B2 channels includes both of these features. As the channels are centred at similar wavelengths they should have had similar sensitivity to dust but markedly different sensitivities to water vapour. This should have allowed the retrieval of the water mixing ratio and dust extinction simultaneously

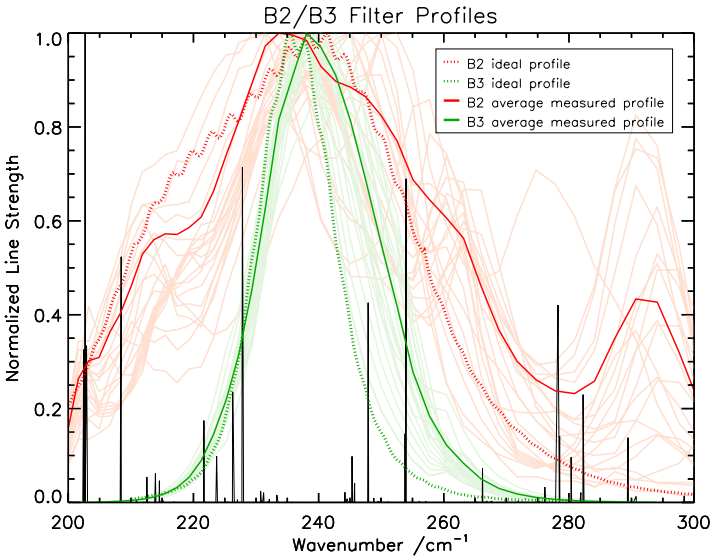


Figure 2.10 | Normalized profiles of the B3 and B2 filters for an ideal case (the filters as they would be if operating perfectly) and average measured case (the filter profiles for each channel averaged over all 21 detectors). Individual detector profiles are given in the background as light red/green lines. Also shown on the plot are the normalized line strengths for water vapour. Not shown is the dust extinction though this is approximately constant in the spectral interval over which the filters operate. The main broadening effect of B3 can be seen, though additional broadening and an extra peak can be seen in B2.

given separate information on the temperature profile. Unfortunately it has turned out that the B-channel mesh filters failed to meet their specifications, despite testing done at the time of manufacture. Pre-flight testing revealed that the spectral profiles of these filters were not as they should be and have instead resulted in a much wider than expected B3 response (see Fig. 2.10 and Fig. 2.4) and a similar, though smaller, effect in B2. There is a large variability range in individual detector response, as shown in Fig. 2.10. This broadening effect has compromised the proposed B3/B2 ratio detection method and the cause is explored as a topic of this thesis.

2.3.2 Extended FOV Wings

Despite all the efforts taken to ensure FOV functions with low wings, the instrument as flown has been observed with FOV functions that have large wings. This effect was observed when the top pixels looking at space during limb observations were not registering zero radiance. These large wings mean that during a limb observation even the top pixels can 'see' lower parts of the atmosphere and possibly even the ground. Work has been done on this anomaly by Dr G. Lawson, Dr N. Teanby and Prof. P. G. J. Irwin. A FOV-averaging method has been incorporated into the retrieval process. This method also takes into account rotation of the FOV (i.e. when the detector array was rotated from its normal position) for limb observations. This is discussed in §2.4.1.

2.3.3 Elevation Slew-Impairment

After starting observations during northern summer/southern winter at Mars on 24 September 2006 (L_s=110°) MCS performed nominal limb/nadir scanning of the atmosphere until 18 January 2007 (L_s=169°) when the elevation slewing process for MCS registered problems. The problem was manifesting itself in the form of position errors—a difference between the measured and target elevation of MCS (i.e. where it should be pointing). It was found that MCS was consistently stopping short of its target elevation. The problem continued to worsen until the decision was taken by the instrument team to leave MCS 'staring' at the limb (similar to the freezing procedure mentioned earlier) by not using the elevation actuator. This action was taken as there were worries that MCS may jam, and that this would likely be in a position where it could not obtain any useful observations. Limb-staring was used from 9 February 2007 until 14 June 2007 through northern autumn/southern spring. On 14 June 2007 MCS resumed slewing between the limb and space with occasional slews to the black body calibration target, though the nadir views have been modified to off-nadir views with incidence angles of between 60° and 70°. This was because in tests performed during the limb-staring period it was found that if smaller slewing angles were used the problem vanished. This was a great improvement and should give adequate measurements to perform retrievals.

One of the consequences of limb-staring was the systematic variation in the altitudes covered by the MCS detector arrays, due to the non-circular nature of the MRO orbit (see §2.2.4) and Mars. For example, at southern latitudes coverage extends upward to only 55 km while at high northern latitudes the lowest element of the detector array lifted 15 km off the planet. Another consequence is that the data has limited calibration. This is a twofold problem: firstly, because space views (i.e. zero radiance reference) were only being returned a few times a day, when the spacecraft rolled and pointed MCS towards space instead of every 34 s as is normally the case. Secondly, it was impossible for MCS to view the black body calibration target. The calibration target was instead being modelled using the previous three months worth of data. As a result of these problems, data from this period is of a heavily degraded quality.

2.4 Data Pipeline

Data from MCS are relayed via the MRO high-gain antenna back to Earth where they are received by the radio telescopes of the Deep Space Network. From here the data goes to the

Jet Propulsion Laboratory (JPL) in California. These data, Level 0 unpacked data products, are processed by the JPL pipeline to produce Level 1 data i.e. calibrated radiances with some viewing geometry information. The data are subsequently downloaded over the Internet to Oxford to be further processed by the Oxford pipeline (written by Dr N. Teanby) to make it suitable for use in NEMESIS.

The geometry information provided by the JPL data are limited and is based on the detector array as a whole rather than individual detectors. It also uses the Mars Reference Ellipsoid as its basis. The Oxford pipeline extrapolates from this information in order to calculate the geometry for individual detectors and transforms to a Martian topography basis[§]. It also takes into account FOV rotation and averaging (see next section). In order to increase the signal-to-noise ratio, an average is taken of neighbouring limb observations. In a nominal cycle a sequence of eight two-second limb observations (Kleinböhl et al., 2009; McCleese et al., 2007) are acquired bracketed by on-planet or space observations (see §2.2.3). The first three of these limb measurements contain thermal transients from the preceding, warmer, on-planet observations. Consequently the last five measurements in the sequence of eight are used for the average. Finally the limb observations are paired with the nearest nadir observation within 1° of latitude/longitude, normally the bracketing on-planet observation.

2.4.1 FOV Rotation and Averaging

To correct for the problems of inaccurate FOVs a procedure was developed by Dr G. Lawson and then integrated into the NEMESIS retrieval model (see Chapter 4) by Dr N. Teanby and Prof. P. G. J. Irwin. Firstly, the FOV response of the detectors is corrected for rotation about the boresight (in the azimuth/elevation plane). Secondly, the corrected FOV response is convoluted with the radiation from the scene and then integrated over all possible viewing angles to give the final FOV-averaged radiance.

Accurate curves of FOV response in both the horizontal and vertical directions were obtained from laboratory measurements[¶] made of detectors during testing prior to launch.

Rotation of the detector position about the boresight is achieved with the use of a rotation

[§]This is done using data taken with Mars Laser Orbiter Altimeter (MOLA) on Mars Global Surveyor (MGS). The data were taken from NASA's Planetary Data Store (PDS).

[¶]The FOVs for all of the detectors were measured using a target projector in a thermal vacuum test chamber (McCleese et al., 2007).

matrix, $\mathbf{R}$:

$$\mathbf{R} = \begin{bmatrix} \cos\theta & -\sin\theta \\ \sin\theta & \cos\theta \end{bmatrix}, \tag{2.1}$$

where θ is the angle of rotation about the boresight. Taking the Cartesian coordinates of the detector and multiplying by $\mathbf{R}$ gives the rotated coordinates as

$$\begin{bmatrix} x' \\ y' \end{bmatrix} = \begin{bmatrix} \cos\theta & -\sin\theta \\ \sin\theta & \cos\theta \end{bmatrix} \begin{bmatrix} x \\ y \end{bmatrix}, \tag{2.2}$$

where x and y are the original coordinates of the detector and the x' and y' are the rotated coordinates. For NEMESIS only the vertical component is needed:

$$y' = x\sin\theta + y\cos\theta. \tag{2.3}$$

Now let $\mathbf{h}_{\mathrm{FOV}}$ be a column vector containing the detector horizontal FOV response with the corresponding angular axis in the column vector $\mathbf{x}_{\mathrm{FOV}}$. Similarly set $\mathbf{v}_{\mathrm{FOV}}$ as the detector vertical FOV response with $\mathbf{y}_{\mathrm{FOV}}$ as the axis. The transformed (i.e. rotated) FOV axis for the vertical component, $\mathbf{x}_{\mathrm{VRFOV}}$, is then

$$\mathbf{x}_{\mathrm{VRFOV}} = \cos\theta \cdot \left(\mathbf{y}_{\mathrm{FOV}} - \begin{bmatrix} y \\ \vdots \\ y \end{bmatrix} \right) + \begin{bmatrix} y' \\ \vdots \\ y' \end{bmatrix}. \tag{2.4}$$

Likewise for the horizontal component, $\mathbf{x}_{\mathrm{HRFOV}}$:

$$\mathbf{x}_{\mathrm{HRFOV}} = \sin\theta \cdot \left(\mathbf{x}_{\mathrm{FOV}} - \begin{bmatrix} x \\ \vdots \\ x \end{bmatrix} \right) + \begin{bmatrix} y' \\ \vdots \\ y' \end{bmatrix}. \tag{2.5}$$

Taking $\mathbf{x}_{\mathrm{VRFOV}}$ and $\mathbf{v}_{\mathrm{FOV}}$ together they can then be thought of as the function, $v_{\mathrm{RFOV}}(x)$, to represent the rotated detector vertical component FOV response. Similarly $\mathbf{x}_{\mathrm{HRFOV}}$ and $\mathbf{h}_{\mathrm{FOV}}$ create the horizontal component function $h_{\mathrm{RFOV}}(x)$.

The final detector vertical FOV response, $f_{\mathrm{RFOV}}(x)$, is the convolution of the vertical and

horizontal component functions:

$$f_{\mathrm{RFOV}}(x) = (v_{\mathrm{RFOV}} * h_{\mathrm{RFOV}})(x) = \int_{-\infty}^{+\infty} v_{\mathrm{RFOV}}(p) h_{\mathrm{RFOV}}(x-p)dp, \tag{2.6}$$

where p is a dummy variable.

Taking radiance as a function of viewing angle, $S_\nu(\theta_{\mathrm{view}})$[‖], and convolving it with the FOV function $f_{\mathrm{RFOV}}(\theta)$ (where x has been exchanged with θ, the angle away from the boresight for the FOV), gives the FOV-averaged radiance 'seen' by the detector, M_ν:

$$M_\nu = (S_\nu * f_{\mathrm{RFOV}})(\theta) = \int_{-\infty}^{+\infty} S_\nu(\phi) f_{\mathrm{RFOV}}(\theta-\phi)d\phi, \tag{2.7}$$

where ϕ is a dummy variable. It should be noted that though it is generally mathematically accurate to perform a convolution integration between $-\infty$ and $+\infty$, it is not required for Eqs 2.6 and 2.7, it is only really necessary to compute the integration between $-\frac{\pi}{2}$ and $+\frac{\pi}{2}$ as this covers the complete range of viewing angles that are actually physically possible for the detector.

[‖]The quantity θ_{view} refers to the angle from the detector boresight of the radiance arriving at the detector. For the limb viewing case, $S_\nu(\theta_{\mathrm{view}})$ describes the radiation coming from different heights in the atmosphere whereas for the nadir case it describes the radiation coming from different emission angles.

3

Radiative Transfer Modelling

The theory of radiative transfer underpins all forms of remote sensing as it describes the link between the state of the atmosphere (e.g. temperature, pressure and composition) and the electromagnetic radiation measured at different wavenumbers—the atmospheric spectrum. This is possible because of the fact that the constituent molecules and aerosols of an atmosphere interact with the radiation field through the microscopic processes of absorption, emission and scattering, leaving unique signatures of their presence. These signatures take the form of a combination of continuum radiation and spectral lines defined by their position, shape and strength. These spectra can then be compared with the laboratory measurements in order to determine the conditions (temperature, pressure, composition &c.) under which they were formed. Using the theory of radiative transfer to simulate the radiation leaving an atmosphere as a function of the atmospheric state is known as *forward modelling*. Examples of this for the Martian atmosphere are given in Figs 3.1 and 3.7.

3.1 Molecular Spectroscopy

A molecule's energy state has several degrees of freedom corresponding to the physical processes by which photons may interact with it. These are electronic (movement of electrons between atomic energy levels), vibrational (bending and stretching of molecular bonds), rotational (spinning of a molecule depending on its moments of inertia) and translational (movement of the

molecule). Planetary atmosphere spectra tend to peak in the infrared corresponding to their temperatures and at these wavelengths photons lack enough energy for electronic transitions to be possible. Instead infrared photons promote rotational and vibrational transitions which are then responsible for the copious number of lines seen in these spectra (Irwin, 2008).

Examples of simulated Martian spectra can be seen in Fig. 3.1. These were created using data from the Mars Climate Database (MCD; see §3.4) MY24 scenario using the NEMESIS software suite (see §3.3, Chapter 4). As can be seen from the figure, the Martian atmosphere is mostly optically thin in in the infrared, except for the several strong carbon dioxide bands, some water vapour bands and aerosol features due to suspended dust and water ice clouds (see §3.3.1). Upwards of about 500 cm^{-1} the spectrum is mainly composed of CO_2 bands due to rotational and vibrational transitions, with the band at 667 cm^{-1} being particularly prominent. The central wavenumbers of the bands are set by the vibrational lines. Each of the vibration lines is then surrounded by a cluster of rotational lines giving the bands their fine structure (as changes in the rotational energy levels are generally much smaller than the vibrational ones). Below 500 cm^{-1} the spectrum is mainly composed of weaker (though still significant) bands due to rotational transitions in water vapour (as in the far infrared photons are so low in energy that they cannot cause vibrational transitions). The effect of water vapour on the spectrum can be clearly seen in Fig. 3.1 where several spectra corresponding to increasing amounts of water vapour have been plotted.

Spectral lines can appear in emission or in absorption, depending on a combination of the environmental conditions of the line-forming region and viewing geometry. Both processes occur simultaneously, resulting in both gains and losses of spectral radiance, L_ν, at a particular wavenumber. All of these physical processes are incorporated into the radiative transfer equation, that allows the calculation of the net change of radiance and accordingly the emitted radiation at the top of the atmosphere that might be measured by an orbiting spacecraft.

3.2 The Radiative Transfer Equation

Consider a beam of radiation of wavenumber ν and of unit cross-sectional area travelling through a plane-parallel atmosphere. Radiation $L_{\nu 0}$ enters the atmosphere at z_0 and leaves at z_1 (see Fig. 3.2). The beam is at an angle θ to the vertical. If the atmosphere is radiatively active then the beam will be affected by scattering and absorption, which will reduce the spectral radiance $L_{\nu 0}$.

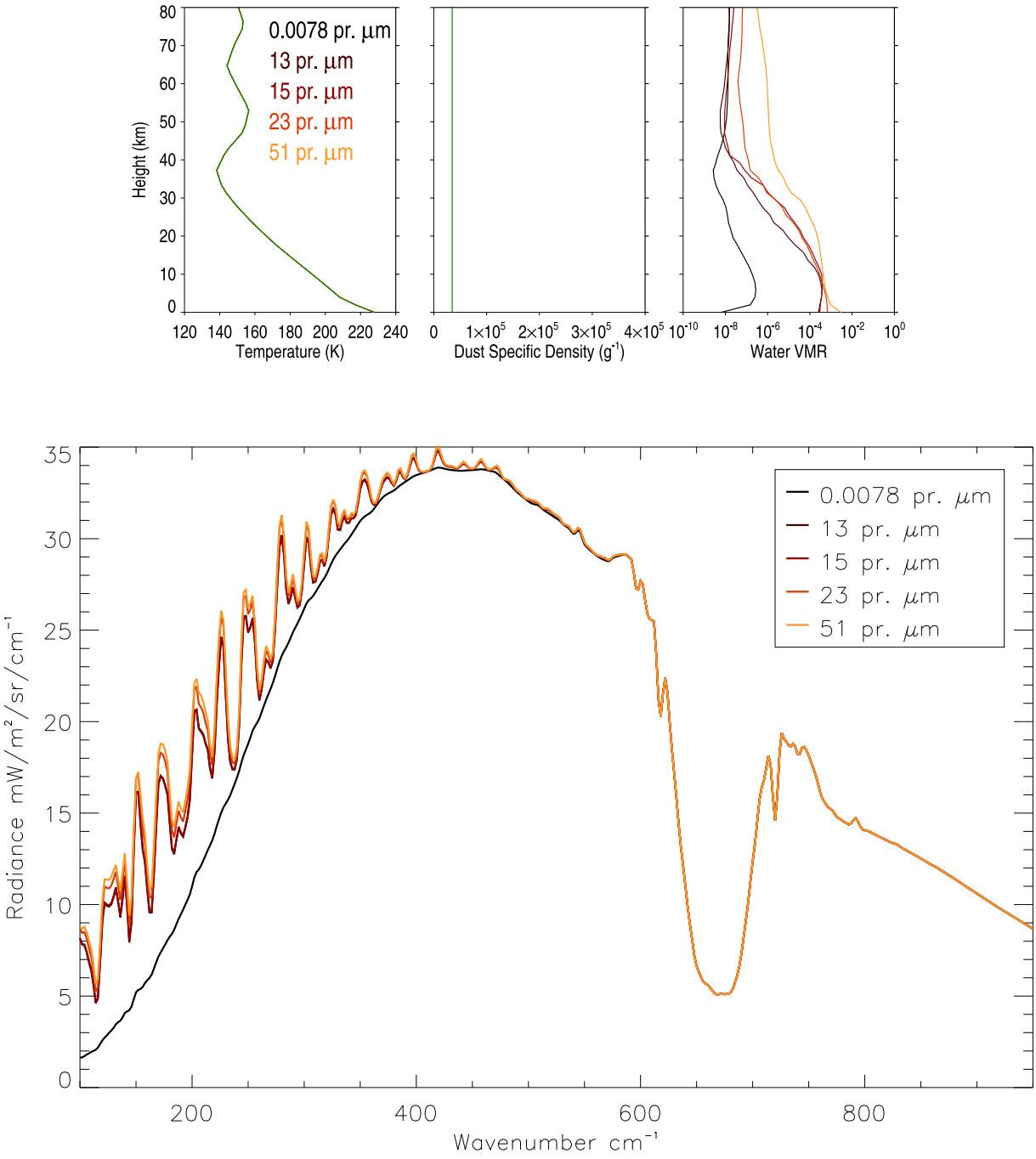


Figure 3.1 | (**Top**) Temperature, dust and water profiles used to simulate spectra below (same temperature and dust profile with all water profiles). Temperature and water profiles taken from the MCD (L_s=114°, 15h LST). Dust profile has constant specific density (particles per gram of atmosphere) with height with column optical depth of 0.1 at 1075 cm^{-1} (r_{eff}=1.6 µm, v_{eff}=0.3, gamma distribution). An equatorial temperature profile was used (0°N, 60°W) in conjunction with water profiles of varying abundances from different latitude bands: *0.0078 pr. µm:* (80°S, 60°W), *13 pr. µm:* (0°N, 60°W), *15 pr. µm:* (30°N, 60°W), *23 pr. µm:* (60°N, 60°W) and *51 pr. µm:* (80°N, 60°W). (**Bottom**) Plot of simulated Martian equatorial limb pencil-beam FOV spectrum (2 cm^{-1} resolution) at a height of 4 km for a range of different water vapour abundances. Ranging from 'dry' with a column abundance of <1 pr. µm up to a 'wet' case of 51 pr. µm. Units of radiance are mW m^{-2} sr^{-1} (cm^{-1})$^{-1}$. The legend indicates the associated column abundance for a given spectrum.

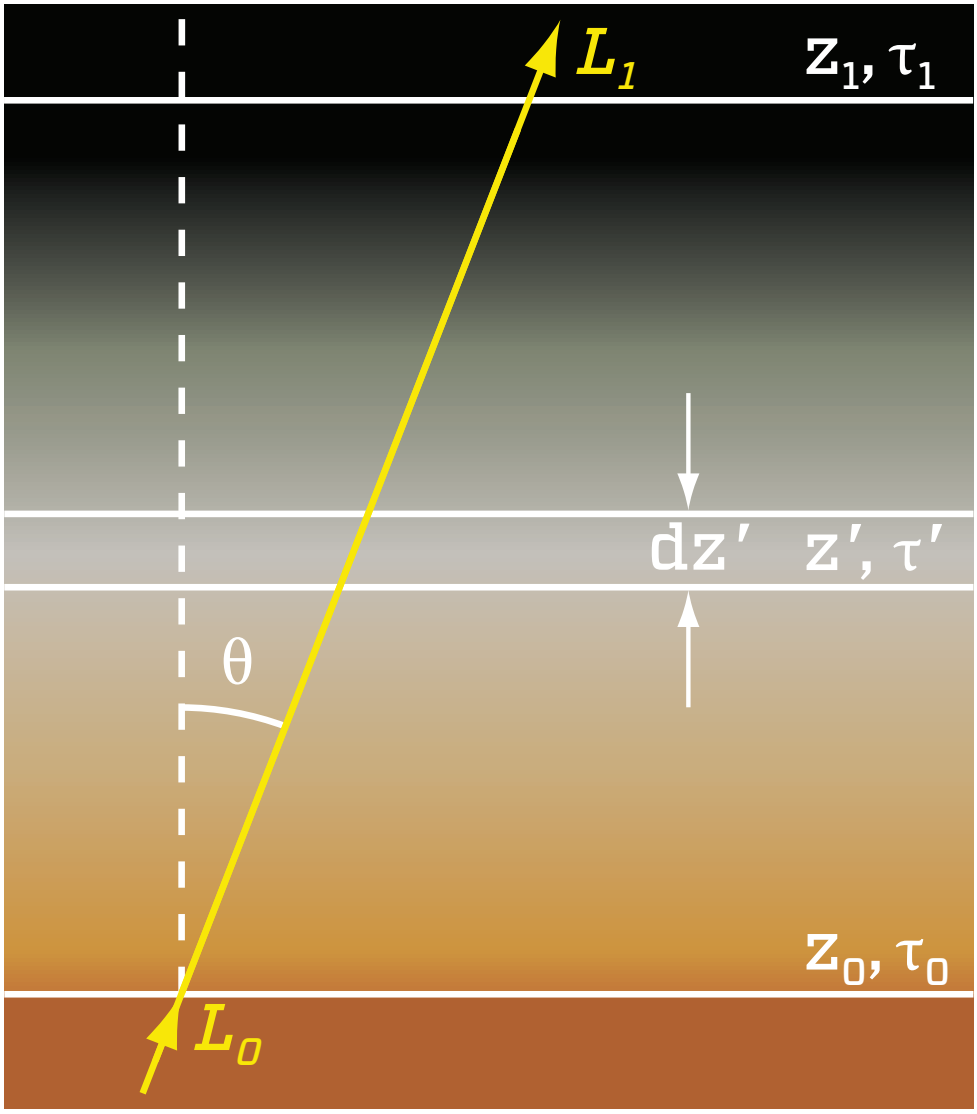


Figure 3.2 | Radiative transfer through in a plane-parallel atmosphere.

Lambert's Law states that the the fractional decrease of spectral radiance is proportional to the mass of absorbing or scattering material encountered by the beam in the distance dz. So

$$dL_\nu^{ext} = -k_\nu(z)\rho_a(z)L_\nu(z)\frac{dz}{\mu}, \tag{3.1}$$

with

$$k_\nu = a_\nu + s_\nu, \tag{3.2}$$

$$\mu = \cos\theta, \tag{3.3}$$

where $\rho_a \frac{dz}{\mu}$ is the mass encountered (since the beam has unit cross-sectional area) with ρ_a as the density of radiatively active gas and k_ν is called the *extinction coefficient*—the sum of the absorption coefficient a_ν and the scattering coefficient s_ν.

If the gas is also emitting radiation an extra term must be added to the right-hand side of Eq. 3.1 to represent the additional spectral radiance being added to the beam. This term will also be proportional to $\rho_a \frac{dz}{\mu}$ (mass encountered). Thus we get

$$dL_\nu^{em} = -k_\nu(z)\rho_a(z)J_\nu(z)\frac{dz}{\mu}, \tag{3.4}$$

where J_ν is called the the *source function* and represents the sum of the thermally emitted and scattered radiation.

Combining Eqs 3.1 and 3.4 the radiative transfer equation (also called *Schwarzchild's Equation*) is obtained:

$$dL_\nu = dL_\nu^{ext} + dL_\nu^{em}, \tag{3.5}$$

$$\mu\frac{dL_\nu}{dz} = -k_\nu(z)\rho_a(z)[L_\nu(z) - J_\nu(z)]. \tag{3.6}$$

To solve Eq. 3.6 start by introducing the optical thickness τ_ν defined as

$$\tau_\nu(z) = \int_{z_0}^{z} k_\nu(z')\rho_a(z')dz' \tag{3.7}$$

The equation of radiative transfer (Eq. 3.6) can now be rewritten

$$\mu \frac{dL_\nu}{d\tau_\nu} + L_\nu = J_\nu. \tag{3.8}$$

Using the integrating factor $\exp(\frac{\tau_\nu}{\mu})$ Eq. 3.8 can be re-expressed as

$$L_\nu e^{\frac{\tau_\nu}{\mu}} = \int J_\nu e^{\frac{\tau'_\nu}{\mu}} \frac{d\tau'_\nu}{\mu} + C, \tag{3.9}$$

where C is a constant of integration. Remembering that the spectral radiance at the base of the atmospheric model, z_0, is $L_{\nu 0}$ Eq. 3.9 then becomes

$$L_\nu(z) = \int_0^{\tau_\nu(z)} J_\nu(\tau'_\nu) e^{-\frac{(\tau_\nu(z)-\tau'_\nu)}{\mu}} \frac{d\tau'_\nu}{\mu} + L_{\nu 0} e^{-\frac{\tau_\nu(z)}{\mu}}. \tag{3.10}$$

The spectral radiance emerging from the top of the atmosphere is then

$$L_{\nu 1} = L_\nu(z_1) = \int_0^{\tau_\nu(z_1)} J_\nu(\tau'_\nu) e^{-\frac{(\tau_\nu(z_1)-\tau'_\nu)}{\mu}} \frac{d\tau'_\nu}{\mu} + L_{\nu 0} e^{-\frac{\tau_\nu(z_1)}{\mu}}. \tag{3.11}$$

The spectral radiance $L_{\nu 1}$ can now be understood in terms of Fig. 3.2. The second term on the right hand side of the equation represents the radiance from the base of the atmosphere, z_0 attenuated by an exponential factor due to extinction experienced travelling through the rest of the atmosphere to z_1. The first term represents the sum of the contributions emitted from elements of optical path $d\tau'_\nu$, at different distances z' along the path each attenuated by the factor $\exp\left(-\frac{(\tau_\nu(z_1)-\tau'_\nu)}{\mu}\right)$ due to extinction over the remaining optical path $\tau_\nu(z_1) - \tau'_\nu$ (corresponding to the distance $z_1 - z'$).

Now introduce the transmittance $\mathcal{T}_\nu(z_1, z_2)$ which defines the fraction of spectral radiance leaving z_1 that reaches z_2:

$$\mathcal{T}_\nu(z_1, z_2) = \exp\left(-\left|\int_{z_1}^{z_2} k_\nu(z)\rho_a(z)\frac{dz}{\mu}\right|\right) = \exp\left(-\left|\frac{\tau_\nu(z_2) - \tau_\nu(z_1)}{\mu}\right|\right). \tag{3.12}$$

In the case of no scattering and assuming local thermodynamic equilibrium $J_\nu = B_\nu$, the Planck function

$$B(\nu, T) = \frac{2hc^2\nu^3}{\exp\left(\frac{hc\nu}{k_B T}\right) - 1}, \tag{3.13}$$

where ν is the wavenumber, T is the kinetic temperature, h is the Planck constant, c is the speed

of light and k_B is the Boltzmann constant.

Using the transmittance (Eq. 3.12) the spectral radiance $L_{\nu 1}$ (Eq. 3.11) can be rewritten as

$$\begin{aligned} L_{\nu 1} &= L_\nu(z_1) \\ &= \int_{z_0}^{z_1} B_\nu(z) \frac{\partial \mathcal{T}}{\partial z} dz + L_{\nu 0} \mathcal{T}(z_0, z_1) \\ &= \int_{z_0}^{z_1} B_\nu(z) \mathcal{K}_\nu(z) dz + L_{\nu 0} \mathcal{T}(z_0, z_1) \\ &= \int_{z_0}^{z_1} \mathcal{C}_\nu(z) dz + L_{\nu 0} \mathcal{T}(z_0, z_1), \end{aligned} \tag{3.14}$$

where $\mathcal{K}_\nu(z) = \frac{\partial \mathcal{T}}{\partial z}$ is known as the *transmission weighting function*, which peaks roughly where the optical depth is unity (Irwin, 2009). The product $\mathcal{C}_\nu(z) = B_\nu(z)\mathcal{K}_\nu(z)$ is commonly known as the *contribution function*; the peak of this function shows the atmospheric level that most of the radiation is coming from. The total radiance can be viewed as a weighted average of the black body radiance from each atmospheric level (Houghton et al., 1984). These equations require substantial modification if scattering aerosols are not negligible.

3.2.1 Limb Viewing

The advantage of a nadir viewing geometry is that of high horizontal spatial resolution. This comes at the cost of low vertical resolution due to broad weighting functions (Irwin, 2009). In addition to nadir viewing the MCS instrument is also capable of limb viewing. Contrasted with nadir viewing limb viewing has the advantage of having high vertical spatial resolution (thinner weighting functions in the vertical) but a low horizontal spatial resolution due to long paths through atmosphere. This high vertical resolution is useful for gas abundances which vary rapidly with altitude, e.g. water vapour in the Martian atmosphere. The longer path lengths give increased sensitivity to trace constituents (Irwin, 2009).

For limb viewing (see Fig. 3.3) the radiative transfer equation looks very similar to Eq. 3.14 but instead of integrating vertically, integration is performed along the path l (Irwin, 2009):

$$L_{\nu 1}^{limb} = \int_{l_0}^{l_1} B_\nu(l) \frac{\partial \mathcal{T}}{\partial l} dl = \int_{z_0}^{z_1} B_\nu(z) \mathcal{K}'_\nu dz \tag{3.15}$$

where

$$\mathcal{K}'_\nu = \frac{\partial \mathcal{T}}{\partial l} \frac{dl}{dz}. \tag{3.16}$$

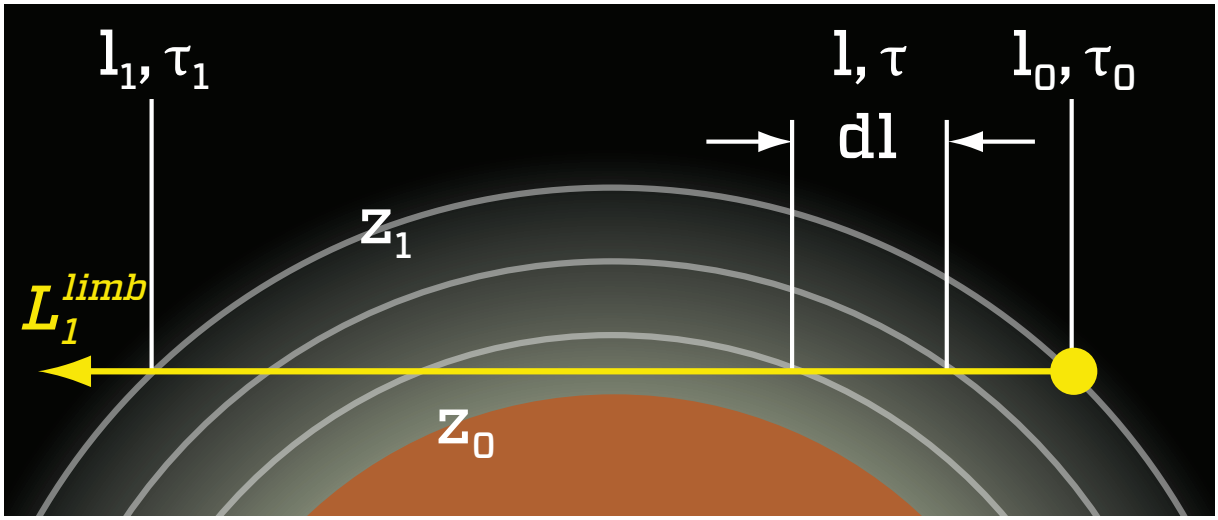


Figure 3.3 | Radiative transfer in an atmosphere with a limb viewing geometry. Note that the atmosphere has been split into layers (assumed homogeneous) and that the top and bottom of the atmospheric model are labelled by z_1 and z_0 respectively.

Observations performed by MCS make the best use of both geometries as they combine limb and nadir views of the same location (see Chapter 2 for details).

3.3 Calculating Transmission

The transmission of an atmospheric path at wavenumber, ν, is a function of pressure, temperature, mole fraction of gases, aerosol extinction and the sum of the contribution of all the spectral absorption lines present at that particular wavenumber. Transmission can then be calculated numerically by splitting the model atmosphere into N layers that are equally spaced in log p. The choice of using log p as opposed to equal spacing in either p or z is justified by its resulting computational expediency. This is because it provides higher resolution (i.e. more closely spaced layers) in the lower atmosphere where variables such as temperature, pressure, composition &c. may change rapidly with height whereas in the upper atmosphere it provides lower resolution (i.e. more widely spaced layers) where atmospheric variables change more smoothly. This results in fewer wasted calculations and so makes the overall calculation more computationally efficient. For nadir viewing (under the assumption of a plane-parallel atmosphere) the discretized form Eq. 3.14 is

$$L_{\nu 1}^{nadir} = \sum_{n=1}^{N} B_n \Delta \mathcal{T}_n + L_{\nu 0} \mathcal{T}_N, \tag{3.17}$$

where $\Delta\mathcal{T}_n = \mathcal{T}_N - \mathcal{T}_n$, is the difference in transmission from the base of the atmosphere to the top of the nth layer.

An equivalent discretized form of Eq. 3.15 can be formed for limb viewing by splitting the limb path into M subpaths:

$$L_{\nu 1}^{limb} = \sum_{m=1}^{M} B_m \Delta\mathcal{T}_m, \tag{3.18}$$

where $\Delta\mathcal{T}_m = \mathcal{T}_M - \mathcal{T}_m$, is the difference in transmission from the beginning of the limb path to end of the mth subpath.

For nadir viewing the transmission over n layers in a plane-parallel atmosphere, $\mathcal{T}_n$, depends on the optical depth, taking into account the sum of all the opacity sources in each of the n atmospheric layers:

$$\mathcal{T}_n = \exp\left(-\sum_{i=1}^{n} \frac{\Delta\tau_n}{\mu}\right), \tag{3.19}$$

where $\Delta\tau_n$ is the vertical optical depth of the nth layer and μ is as defined in §3.2 and Eqs. 3.20. The equivalent for the limb path transmission over m subpaths, $\mathcal{T}_m$, summing the opacity sources in each of the m atmospheric subpaths is:

$$\mathcal{T}_m = \exp\left(-\sum_{j=1}^{m} \Delta\tau_m\right), \tag{3.20}$$

where $\Delta\tau_m$ is the optical depth of the mth subpath. Upon transformation to the numerical form of the integration there is a worrying possibility of systematic offsets being introduced. This is reduced to a manageable amount by ensuring there are enough layers to accurately track the changes in an inhomogeneous atmosphere.

In the NEMESIS retrieval software used for this thesis, the forward model splits the atmosphere into a number of equivalent homogeneous layers sufficient to resolve transmission weighting functions for the spectral range used. This is done in log pressure as discussed above. Path lengths through the layers are then calculated to allow determination of mean properties for each layer. This process is demonstrated in Fig. 3.4 and uses the cosine rule to calculate length of a path, s_0, as follows from Irwin (2004):

$$s_0 = \sqrt{(z_1^2 - z_0^2 \sin^2\theta)} - z_0 \cos\theta, \tag{3.21}$$

where z lengths are as shown in the figure and θ is the viewing angle. For nadir and near-

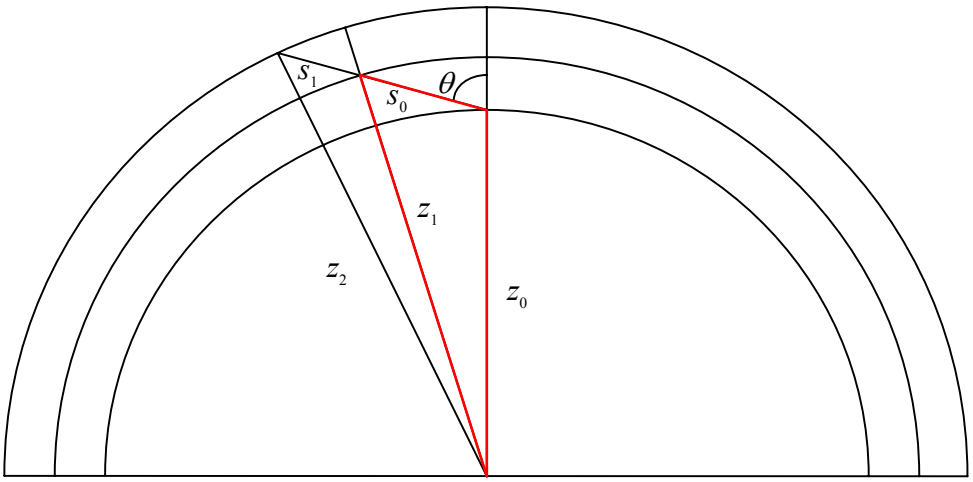


Figure 3.4 | Schematic showing how NEMESIS calculates path lengths through layers. Reproduced/adapted from Irwin (2004) with kind permission of the author.

nadir simulations without scattering, NEMESIS does not use the plane-parallel approximation. Instead, it assumes a spherical atmosphere for both limb and nadir calculations. Mean temperature and pressure are calculated as absorber weighted means along the viewing angle and the integration is performed using Simpson's rule. Similar integrations are used for absorber/aerosol amounts along the line-of-sight.

3.3.1 Sources of Opacity

Spectral Lines

Molecules with permanent or transient dipoles* can transition between quantized energy states by the absorption or emission of photons at specific wavelengths. In planetary atmospheres this process takes place via one of the processes described in §3.1 (vibration, rotation &c.). These transitions leave the signature of spectral lines. Ideally a single line centred at wavenumber ν_0 would be described by the following

$$k(\nu) = S\delta(\nu - \nu_0), \tag{3.22}$$

where $k(\nu)$ is the absorption/emission coefficient at wavenumber ν, S is the line strength and $\delta(\nu - \nu_0)$ is the Dirac-delta function centred at ν_0. In reality spectral lines are not infinitely thin

*Electric dipoles are necessary for a molecules to interact with the radiation field. Molecules with no permanent dipole will show no spectral features unless temporary dipoles are induced by bending and stretching modes (e.g. CO_2) or collisions allowing so-called 'forbidden transitions'. Alternatively higher-order electric multipoles may be strong enough to produce spectral features.

as various physical effects cause broadening of these sharp peaks. To incorporate these effects Eq. 3.22 is replaced by

$$k(\nu) = Sf(\nu - \nu_0), \tag{3.23}$$

where is $f(\nu - \nu_0)$ is the lineshape function, normalised such that

$$\int_0^{+\infty} f(\nu - \nu_0)d\nu = 1, \tag{3.24}$$

and S is now the integrated line strength

$$S = \int_0^{\infty} k(\nu)d\nu. \tag{3.25}$$

The first type of broadening (setting the ultimate limit of narrowness of a spectral line) is known as *natural broadening*. It results from the fact that the photons are emitted and absorbed in a finite period of time Δt and because of Heisenberg's Uncertainty Principle this gives a spread in energy levels leading to a spread in frequency. The broadening is then described as

$$\Delta\nu \approx \frac{1}{c\Delta t}. \tag{3.26}$$

A related form of broadening is *collisional broadening* (also known as *pressure broadening* as it becomes dominant at high pressures). This occurs when the molecule absorbing or emitting a photon undergoes a collision, interrupting the process and so shortening Δt resulting in broadening similar to, but wider than that of natural broadening. In a planetary atmosphere the time between collisions tends to be much shorter than the natural lifetime of excited states and so collisional broadening dominates, leading to much wider lines than would be given by natural broadening alone. The lineshape for collisional broadening is

$$f_L(\nu - \nu_0) = \left(\frac{\gamma_L}{\pi}\right) \frac{1}{(\nu - \nu_0)^2 + \gamma_L^2}, \tag{3.27}$$

where the half-width at half maximum is

$$\gamma_L = \frac{1}{2\pi t_c} = \gamma_{L0} \frac{p}{p_0} \left(\frac{T_0}{T}\right)^{n_L}. \tag{3.28}$$

The parameter t_c is the mean time between collisions that depends on density and thus for

atmosphere mostly on pressure (Irwin, 2009). Hence it is possible to rewrite γ_L in the alternative form given on the right hand side of the equation where γ_{L0} is the linewidth at the reference temperature and pressure, T_0 and p_0 respectively. The temperature coefficient n_L is by simple theory equal to 0.5, although in reality it varies from molecule to molecule (Irwin, 2009).

Another form of broadening results from the Doppler shifting of spectral lines due to line-of-sight motion (with a Maxwell-Boltzmann distribution of speeds) of the absorbing/emitting molecules. In absorption molecules approaching the observer absorb at slightly higher frequencies than those receding and in emission photons are blue- and red-shifted respectively. The lineshape due to *Doppler broadening* is a convolution of the Dirac-delta function and the Maxwell-Boltzmann distributions and is thus

$$f_D(\nu - \nu_0) = \frac{1}{\gamma_D \sqrt{\pi}} \exp\left(-\frac{(\nu - \nu_0)^2}{\gamma_D^2}\right), \tag{3.29}$$

where

$$\gamma_D = \frac{\nu_0}{c}\left(\frac{2k_B T}{m}\right)^{\frac{1}{2}} = \gamma_{D0}\left(\frac{T}{T_0}\right)^{\frac{1}{2}}. \tag{3.30}$$

Here k_B is the Boltzmann constant and m is the mass of a single molecule. An alternative form is given on the right hand side where γ_{D0} is the value of γ_D at the reference temperature T_0. The half-width at half maximum is $\gamma_D(\ln 2)^{\frac{1}{2}}$.

In planetary atmospheres natural broadening is normally negligible and the other two mechanisms dominate. At high pressures the broadening is dominated by collisional broadening, while at low pressures Doppler broadening dominates. This is because collisional broadening is directly proportional to pressure, which falls exponentially with height, while Doppler broadening is proportional to $T^{\frac{1}{2}}$ which decreases much less rapidly (Irwin, 2009). Between these two extremes both processes have a significant impact on the broadening and so a combination of the Lorentzian (shape due to natural and collisional broadening) and Doppler lineshapes is needed. This is achieved by a convolution of the two and results in the Voigt profile:

$$f_V(\nu - \nu_0) = \frac{B}{\gamma_D \pi^{\frac{3}{2}}} \int_{-\infty}^{+\infty} \frac{\exp(-A^2)}{(A - x^2) + B^2} dx \tag{3.31}$$

where

$$A = \frac{\nu - \nu_0}{\gamma_D} \tag{3.32}$$

$$B = \frac{\gamma_L}{\gamma_D} \tag{3.33}$$

The Voigt profile has no analytical solution and so must be integrated numerically. Examples of all three types of profile are given in Fig. 3.5. Note the extended wings of the Lorentzian (and Voigt) profile that mean that collisional broadening has an effect on the lineshape far from the line centre.

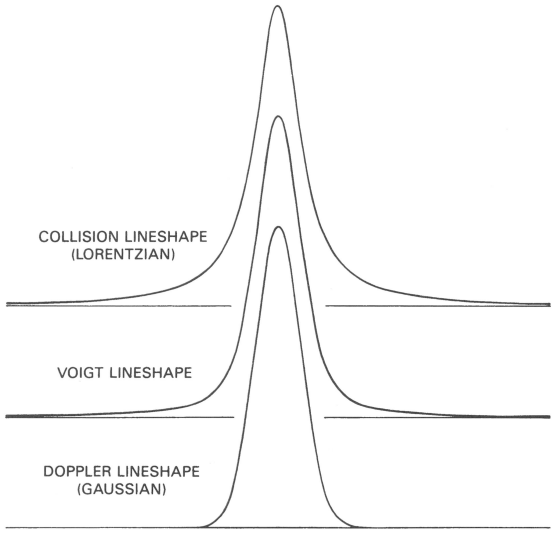


Figure 3.5 | Lorentzian (collision), Voigt and Doppler lineshapes. All three are shown with the same maximum amplitude and with the same full-width at half-maximum amplitude. The Voigt lineshape is one of a continuum of profiles between Gaussian and Lorentzian, depending on the degree of collision broadening.

Credit: Reproduced from Hanel et al. (2003)., 'Exploration of the Solar System by Infrared Remote Sensing: Second Edition', © Cambridge University Press 2003. Reproduced with permission of The Licensor through PLSclear.

The vast amount of molecular spectral line data required for complex radiative transfer calculations in planetary atmospheres is stored in large databases. This thesis uses line data from the HITRAN 2004 molecular spectroscopic database (Rothman et al., 2005) for gaseous CO_2 and H_2O though adjustments are required for their broadening parameters in the Martian atmosphere as compared with Earth's atmosphere.

For CO_2, temperature dependencies for collisional broadening are only given for broadening in air and not in CO_2. To estimate a self-broadened half-width requires the use of results from Yamamoto et al. (1969). They provide calculated collisionally-broadened half-widths for broadening by both N_2 and CO_2 at three different temperatures ranging from 180 to 300 K, as a function of the rotational quantum number of the initial state of the transition. The temperature dependence of line broadening is represented by fitting these calculations to the expression (Kleinböhl et al., 2009)

$$\gamma(T) = \gamma_0 \cdot \left(\frac{T_0}{T}\right)^n \tag{3.34}$$

for broadening by both CO_2 and N_2, where γ_0 is defined at the reference temperature T_0 and n is the temperature coefficient. For CO_2 the temperature coefficient is scaled from the HITRAN

air broadening as

$$n_{CO_2} = n_{air,HITRAN} \cdot \frac{n_{CO_2,Yamamoto}}{n_{N_2,Yamamoto}} \tag{3.35}$$

according to the rotational quantum number of the initial state for each line. As mentioned above lineshapes are modelled using the Voigt function, but for self-broadened CO_2 lines a few wavenumbers away from the centre the behaviour is strongly sub-Lorentzian (Burch et al., 1969). This is due to an effect known as *collisional line mixing* (Lévy et al., 1992). In Lorentzian lineshape theory colliding molecules are modelled as hard elastic spheres whereas in reality what takes place are rotational inelastic collisions between molecules causing a transfer of energy between rotational bands. This results in line intensities of neighbouring lines being transferred into each other and the lines are coupled. The lineshape for such a function can be described by the following

$$f_{SL}(\nu - \nu_0) = f_L(\nu - \nu_0) \cdot \chi(\nu - \nu_0) \tag{3.36}$$

where the Lorentz lineshape has been multiplied by the correction factor χ, whose value depends on the distance from the line centre. Close to the line centre $\chi = 1$ where the behaviour is Lorentzian. The values of χ used in this thesis were obtained by Prof. P. G. J. Irwin. The data for self-broadened CO_2 presented in Fig. 14 from Burch et al. (1969) was fitted between 6 and 300 cm^{-1}. These data were measured in the 2400 cm^{-1} region which is the lowest frequency where data are available. Using a polynomial to ensure a smooth transition between 3 and 6 cm^{-1} the following values were obtained (see Fig. 3.6)

$$\chi = \begin{cases} 1; & |\nu - \nu_0| \leq 3 \text{ cm}^{-1} \\ -1.40253 & \\ +1.92162|\nu - \nu_0| & \\ -4.79585 \cdot 10^{-1}|\nu - \nu_0|^2 & \\ +3.53706 \cdot 10^{-2}|\nu - \nu_0|^3; & 3 \text{ cm}^{-1} < |\nu - \nu_0| \leq 6 \text{ cm}^{-1} \\ 10^{-0.233 - 1.087 \cdot 10^{-2}|\nu - \nu_0|}; & 6 \text{ cm}^{-1} < |\nu - \nu_0| \leq 46 \text{ cm}^{-1} \\ 10^{-0.133 - 1.3 \cdot 10^{-2}|\nu - \nu_0|}; & 46 \text{ cm}^{-1} < |\nu - \nu_0| \leq 136 \text{ cm}^{-1} \\ 10^{-0.7 - 8.8 \cdot 10^{-3}|\nu - \nu_0|}; & |\nu - \nu_0| > 136 \text{ cm}^{-1} \end{cases} \tag{3.37}$$

For H_2O, HITRAN provides line data for broadening in air and in water vapour itself, but not in CO_2. Data for water vapour line broadening in CO_2 is found in Brown et al. (2007). They provide modelled CO_2-broadened half-widths and temperature dependencies for the pure rotational

band between 200 and 900 cm^{-1} (covering the entire spectral range of MCS). Validation of their modelling comes from the comparison of measurements with theoretical calculations of CO_2-broadened water vapour line half-widths for the ν_2 fundamental band; good agreement was found.

This thesis uses the isotopic fractionation of standard mean ocean water with heavy oxygen isotopes; for HDO an enhanced D/H ratio of 5.5 is assumed in accordance with results from Krasnopolsky et al. (1997).

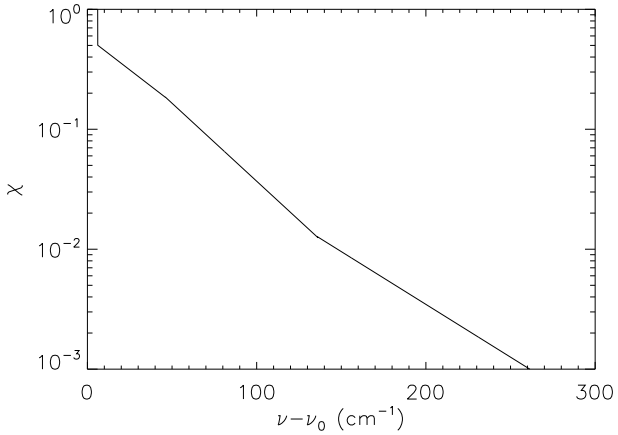


Figure 3.6 | A plot of the CO_2 lineshape correction factor, χ. For $|\nu - \nu_0| \leq 3$ cm^{-1}, χ=1.

Aerosols

One of the biggest sources of spectroscopically active agents in the Martian atmosphere are aerosols, primarily dust and water ice. Governed by their microphysical properties these act through the processes of absorption and scattering. These properties can be parametrized by the use of the extinction cross-section, σ_ν^{ext} (cm^{-2}):

$$\sigma_\nu^{ext} = \sigma_\nu^{abs} + \sigma_\nu^{sca}. \tag{3.38}$$

For this thesis unless stated otherwise (for some of the tests in Chapter 5) it is assumed that $\sigma_\nu^{ext} = \sigma_\nu^{abs}$ (i.e. single-scattering albedo of zero) as the effects of scattering in the thermal infrared are small due to the low optical depths at these wavelengths (Kleinböhl et al., 2009; see §3.3.4 for a comparison between scattering and non-scattering radiative models). The opacity due to aerosols in each atmospheric layer is then

$$d\tau_{aer}(z,\nu) = \rho(z)N(z)\sigma_\nu^{abs}dz \tag{3.39}$$

where $\rho(z)$ is the atmospheric density, $N(z)$ is the number density (number of particles per gram of atmosphere) at height z and where σ_ν^{abs} is pre-calculated using the OZONETABLE code, part of the NEMESIS/RADTRANS suite (Irwin et al., 2008). This algorithm uses Mie theory to calculate the single-scattering phase functions and extinction cross-sections for spherical particles based on the specific optical properties and aerosol sizes for each aerosol mode (Hansen and

Table 3.1 | Parameters, radii (in μm) and variances for dust and water ice

Aerosol type	a	b	c	r_{eff}	v_{eff}
Dust	2.24	8.04	0.647	1.06	0.3
Water ice	12.6	31.4	0.436	1.41	0.15

Travis, 1974). The output is the spectral dependence of both the absorption cross-section and the single-scattering albedo. For this thesis we have followed the procedure of Kleinböhl et al. (2009, 2011) for aerosol refractive indices and size distributions. We use refractive index data from Wolff et al. (2006) for dust and Warren (1984) for water ice. In addition we have also used more recent water ice data from Warren and Brandt (2008).

Unless otherwise stated the size distributions for our radiative transfer calculations use the modified-gamma distribution from Kleinböhl et al. (2009):

$$n(r) \sim r^a e^{-br^c} \tag{3.40}$$

where n is the number of particles with radius r, and a, b and c are distribution parameters. With, G, the geometric cross-sectional area of particles per unit volume (Kleinböhl et al., 2009; Hansen and Travis, 1974)

$$G = \int \pi r^2 n(r) dr \tag{3.41}$$

the effective radius of the particle distribution is

$$r_{eff} = \frac{1}{G} \int r \pi r^2 n(r) dr \tag{3.42}$$

and the effective variance

$$v_{eff} = \frac{1}{G r_{eff}^2} \int (r - r_{eff}) \pi r^2 n(r) dr \tag{3.43}$$

The parameters used for this thesis and their respective radii and variances are given in Tbl. 3.1.

To aid understanding of the spectral behaviours of dust and water ice two examples have been given in Figs 3.7 and 3.8. Simulated results for increasing dust abundances are given in Fig. 3.7. The effect of dust can be clearly seen; note that dust has been treated as purely absorbing (single-scattering albedo of zero). As the amount of dust is increased the overall

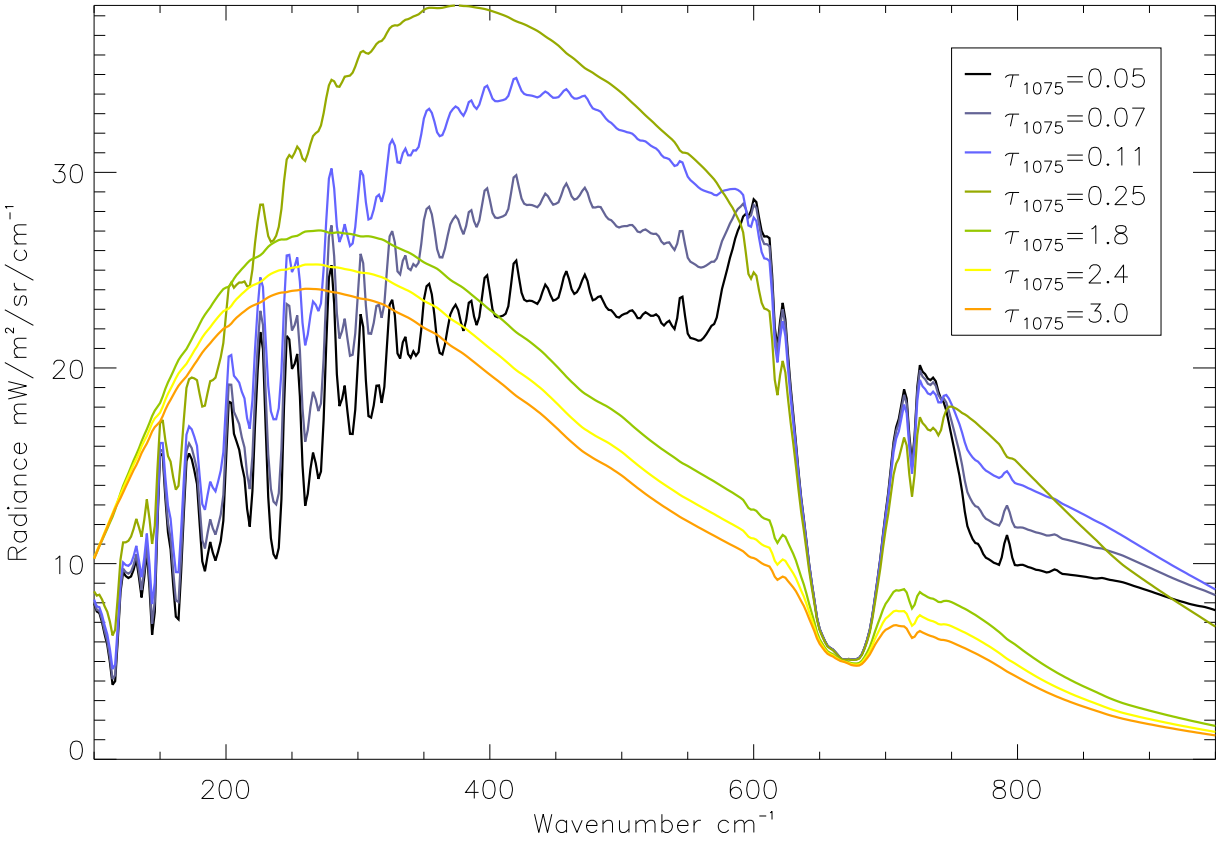


Figure 3.7 | Plot of simulated Martian equatorial limb spectra (2 cm^{-1} resolution, pencil-beam FOV) at a height of 1 km for a range of different dust abundances (constant specific density with height) with column optical depths calculated at 1075 cm^{-1}, using same temperature profile as Fig.3.1. A gamma distribution with r_{eff}=1.6 and v_{eff}=0.4 was used. Ranging from a relatively 'clear' atmosphere with a column opacity τ_{1075}=0.05 to a very opaque τ_{1075}=3.0 for dust storm conditions. All spectra correspond to a water vapour column abundance of 13 pr. μm (same water profile from Fig.3.1) and dust has been treated as purely absorbing (single-scattering albedo of zero). Units of radiance are mW m^{-2} sr^{-1} $(cm^{-1})^{-1}$. The legend indicates the associated optical depth for each spectrum.

radiance increases as the extra dust contributes extra emission while at the same time 'washing out' the other spectral lines. This effect continues until τ_{1075}=1.8 at which point the overall radiance drops with increasing amounts of dust. At this point the optical depth along the limb path is >1 i.e. the atmosphere becomes optically thick. This is because absorption and emission take place simultaneously, but as the amount of dust is increased absorption becomes dominant. In other words not all the emission taking place along the path contributes to the final radiance as one cannot 'see' anything along the path past the point where it becomes optically thick. This means for a limb path that only altitudes higher than the tangent altitude contribute radiance. As temperature decreases with height this leads to lower observed total radiance.

The 'washing out' effect is caused by the fact that the dust is optically thick and so the absorption between the spectral lines is stronger, reducing the relative depth between the con-

tinuum and bottom of the gas absorption lines. The effect is observed in the 667 cm^{-1} CO_2 band.

The effect of water ice clouds is shown in Fig. 3.8. In the top panel are two infrared spectra from Mariner 9 observations. The one taken over the Tharsis Ridge contained several water ice clouds in the field of view (confirmed by on-board cameras) whilst the one taken over Arcadia was nearly cloud free (Hanel et al., 2003; Curran et al., 1974). Given in the lower panel is a model spectrum for small ice crystals which matches well with the Tharsis Ridge spectrum especially with the strong feature at 229 cm^{-1}.

3.3.2 Line-by-Line Models

To calculate the monochromatic radiance L_ν travelling along an atmospheric path requires the knowledge of all the absorption coefficients from the various sources of opacity contained therein (gases, aerosols &c.) contributing at wavenumber ν. In radiative transfer modelling the path is split into small subpaths and for each of the subpaths the absorption coefficients and hence the transmission are calculated (see §3.2). The final transmission over the whole path is the product of all the subpath transmissions.

Over the course of the atmospheric path the temperature and pressure are likely to vary (so temperature and pressure will be different in different subpaths). As most of the sources of opacity will be dependent on temperature and pressure this will require calculation of all the absorption coefficients for all the subpaths along the main path. This involves the calculation of the absorption coefficient for every line of every gas from the line strengths and lineshapes, both of which are functions of temperature and pressure. This *line-by-line* method is the most accurate but as many thousands of lines may contribute to the absorption at a particular wavenumber[†] ν it is easy to see how this becomes very computationally expensive and slow.

For most situations spectral calculations are done for comparison with real measured spectra which have a finite spectral resolution. As a result the transmission used in radiative transfer function need to be integrated over the instrument function (Irwin, 2009). A faster alternative model for calculating finite-resolution spectra is the correlated-k method which is discussed below. This model sacrifices some accuracy in favour of computational expediency but given that line parameters used to generate line-by-line spectra are sometimes accurate to only 10% it is perfectly reasonable to use it (Irwin, 2009).

[†]For instance wing contributions from neighbouring strong lines.

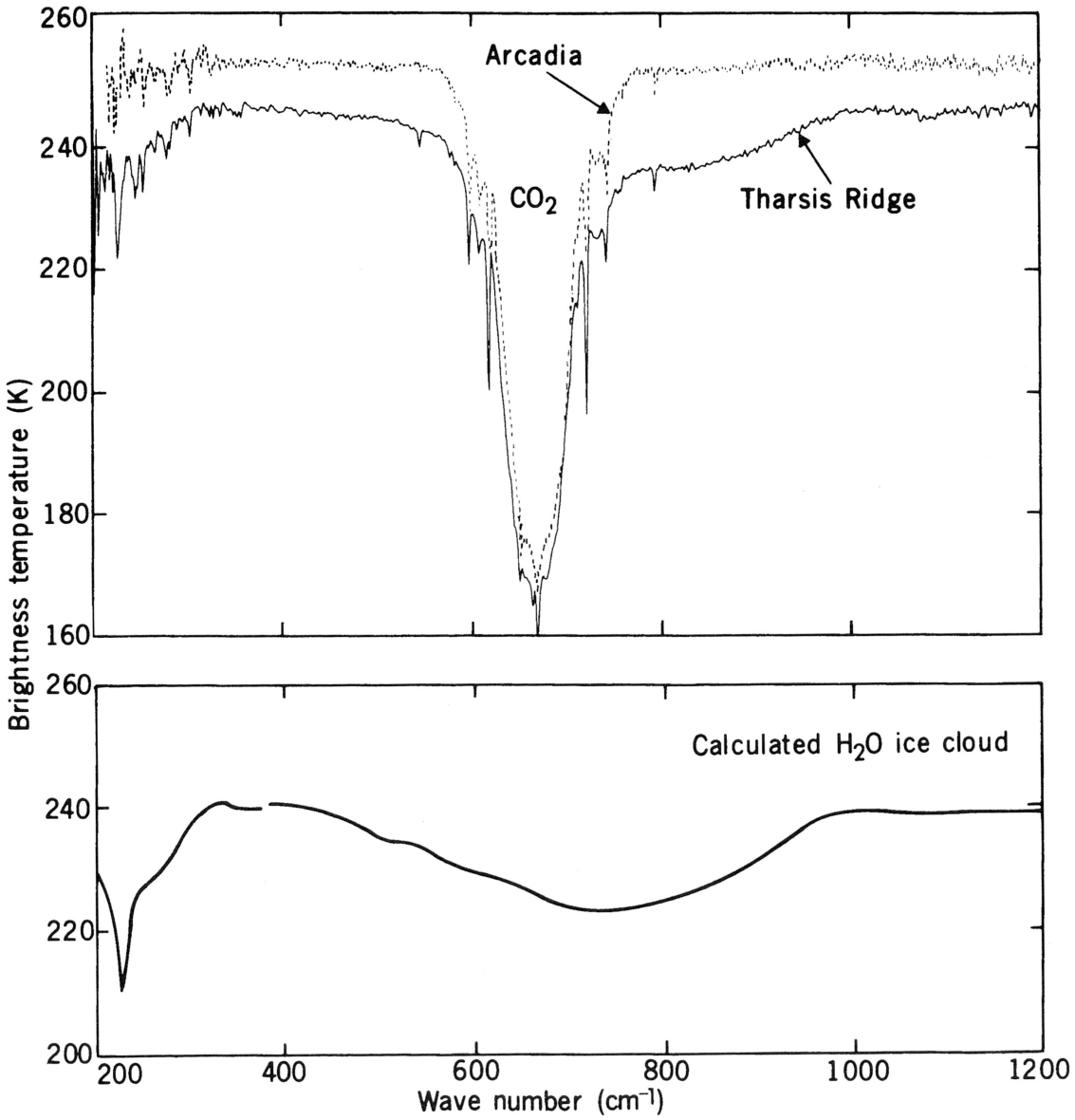


Figure 3.8 | Martian spectra over the Tharsis Ridge and Arcadia. The Tharsis Ridge area contained water ice clouds. The lower spectrum was calculated with such clouds.*Please note that the image was directly copied from the source and the break in the spectrum at 400 cm^{-1} is present in the original.*

Credit: Curran et al. (1973), 'Mars: Mariner 9 Spectroscopic Evidence for H_2O Ice Clouds', 182, 381–383. Reprinted with permission from AAAS.

3.3.3 Correlated-*k* Models

An alternative to the computationally expensive line-by-line approach is to replace the rapidly varying absorption coefficient $k(\nu)$ with a smoother function of absorption coefficients that requires fewer quadrature points—the k-distribution function. In a homogeneous atmosphere with uniform pressure and temperature the mean transmission for a path of absorber amount m is given by

$$\overline{\mathcal{T}}(m) = \frac{1}{\Delta\nu}\int_{\nu}^{\nu+\Delta\nu} \exp\left(-k(\nu)m\right) d\nu, \tag{3.44}$$

where the absorption coefficient $k(\nu)$ is the summation of all line contributions at wavenumber ν. When evaluating Eq. 3.44 numerically a very fine wavenumber step $d\nu$ must be chosen as $k(\nu)$ is a rapidly varying function of wavenumber. From Eq. 3.44 it should be apparent that when calculating the mean transmission within a given spectral interval the ordering of the absorption coefficient is immaterial. All that is required is knowledge of what fraction of the frequency domain $f(k)dk$ is occupied by absorption coefficients between k and $k + dk$ (Irwin, 2009; Irwin et al., 2008). Thus the integral over wavenumber space may be replaced by one over k space leading to

$$\overline{\mathcal{T}}(m) = \int_{0}^{\infty} \exp\left(-km\right) f(k)dk. \tag{3.45}$$

Introducing a cumulative frequency distribution defined as

$$g(k) = \int_{0}^{\infty} f(k)dk, \tag{3.46}$$

where $g(k)$ is a smooth, single-valued, monotonically increasing function with the unique, smoothly varying inverse, $k(g) = g^{-1}(k)$ (Irwin et al., 2008), Eq. 3.45 may then be rewritten as

$$\overline{\mathcal{T}}(m) = \int_{0}^{1} \exp\left(-k(g)m\right) dg \backsimeq \sum_{i=1}^{N} \exp\left(-k_i m\right) \Delta g_i. \tag{3.47}$$

where the inverse $k(g)$ is the k-distribution. Upon discretization the mean transmission is suitably approximated by the right hand side of Eq. 3.47, where k_i is the k-distribution calculated at each of the N quadrature points and where Δg_i are the quadrature weights.

The benefit of this method now becomes apparent. As $k(g)$ is a much smoother function than the rapidly varying $k(\nu)$ far fewer quadrature points are needed and so far fewer calculations are required for the mean transmission integration. In other words the integration has become

much more computationally efficient. The k-distributions may be pre-calculated for each gas for a range of temperatures and pressures found in real atmospheres and then stored in look-up tables for rapid interpolation and calculation of the mean transmission (Irwin, 2009). There will often be cases where lines from multiple gases overlap. In these cases the lines are assumed to be uncorrelated to each other and the k-distributions of the different gases are combined following the method of Lacis & Oinas (1991). An example for rotational lines of H_2O with the associated functions $f(k)$, $g(k)$ and $k(g)$ is given in Fig. 3.9. Note the smoothness of the cumulative frequency distribution $g(k)$ (see [c] and [d]) compared with $k(\nu)$ (see [a]).

A problem arises when one wishes to look at real atmospheres, as these are inhomogeneous and so temperature and pressure vary rapidly with height. This is a problem as the above method assumes that the absorption coefficient is constant but in reality it is dependent on temperature and pressure (affecting parameters such as half-width and line strength). In the monochromatic case the solution is to split the path through the atmosphere into subpaths whose transmissions are then multiplied together to calculate the total transmission. For the same solution to work in the mean transmission case the absorption coefficient in the different layers of the atmosphere would need to be spectrally correlated, that is to say the strongest absorption within a given spectral bin always needs to be at the same wavenumber for different atmospheric layers, as does the the second-strongest and so on until the weakest. Fortunately, it has been found that this assumption is valid (Lacis & Oinas, 1991). This assumed correlation is what then lends the theory its name—the correlated-k approximation. Thus k-distributions may effectively be multiplied together as though they were monochromatic; the mean transmission of the inhomogeneous path is then

$$\overline{\mathcal{T}} \backsimeq \sum_{i=1}^{N} \exp\left(-\sum_{j=1}^{M} k_{ij} m_j\right) \Delta g_i \tag{3.48}$$

where the path has been split into M subpaths.

For this thesis k-distribution tables were produced for use with the NEMESIS retrieval software (Irwin et al., 2008) which applies the correlated-k method to calculating atmospheric radiances. Channel-integrated tables (because MCS is a radiometer) were produced for carbon dioxide and water vapour between 185 and 913 cm^{-1}. Absorption coefficients were gridded onto twenty equally spaced (linear) temperatures (70–300 K) and twenty equally spaced (natural log) pressures (1.13×10^{-7} to 0.0183 bar) for rapid interpolation with 10 Gaussian quadrature points.

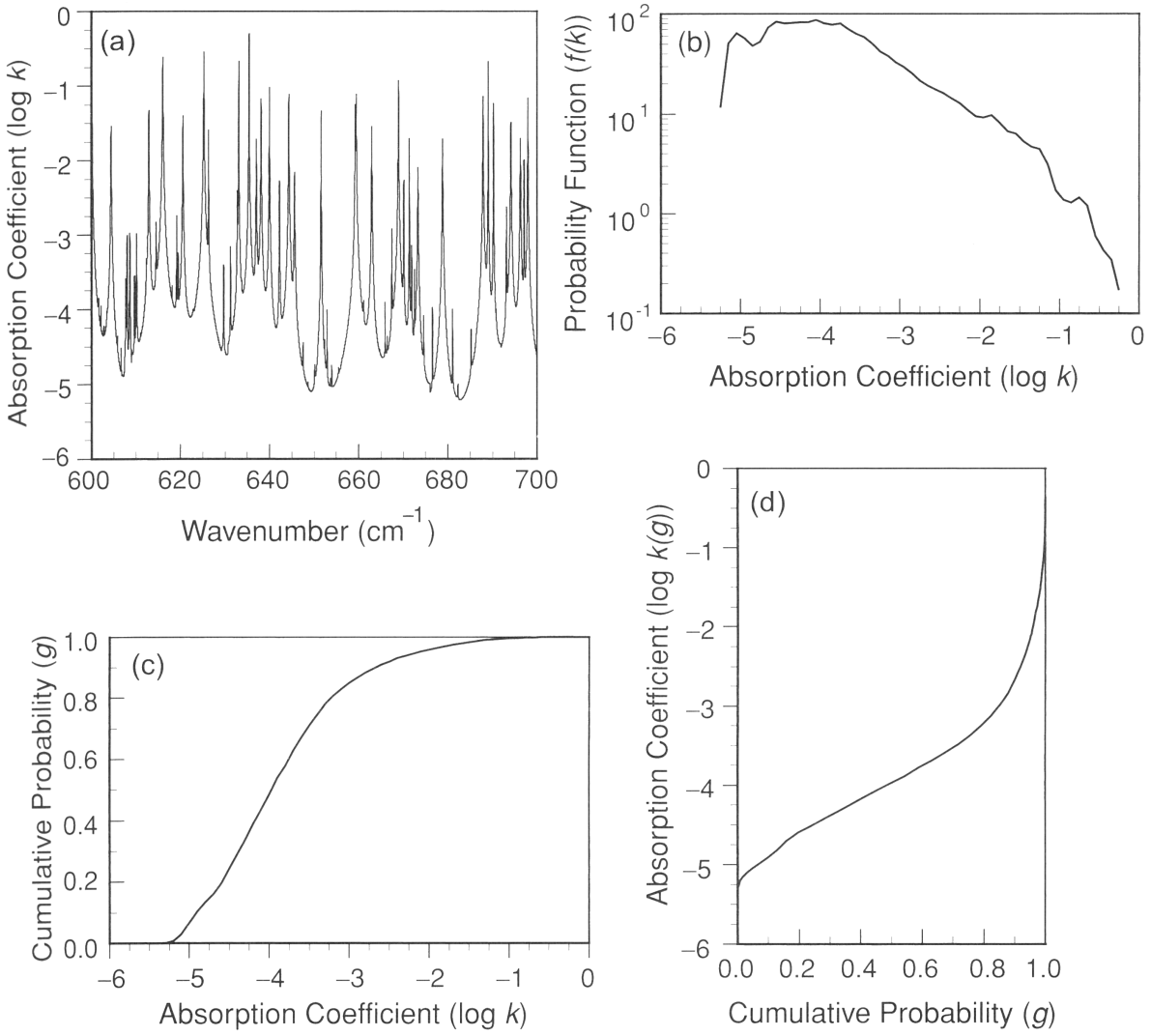


Figure 3.9 | **(a)** Absorption coefficients for rotational lines of H_2O with a resolution of 0.01 cm^{-1} for $p = 600$ mb and $T = 260$ K. **(b)** The probability function (or frequency distribution) $f(k)$ of the absorption coefficient. **(c)** The cumulative probability function (or cumulative frequency distribution) $g(k)$ for $f(k)$ shown in (b). **(d)** The inverse of $g(k)$, which is identical to (c) but with the axes interchanged.

Credit: Reprinted from 'An Introduction to Atmospheric Radiation', Liou (2002), 'Chapter 4: Thermal Infrared Radiation Transfer in the Atmosphere', 129, Copyright (2002), with permission from Elsevier.

The calculated radiance depends upon the temperature, pressure and abundances of gases and aerosols within the model atmosphere.

To test the accuracy of the correlated-k approximation a radiance comparison with the line-by-line method was performed for two model atmospheres; a northern hemisphere midlatitude summer profile and a southern midlatitude winter one. Limb radiances at different tangent altitudes and nadir radiances were generated using both methods for each atmospheric model with the MCS detector fields-of-view. Dust and water ice parameters are as given in Tbl. 3.1. The results are given in Figs 3.10 and 3.11. Atmospheric profiles were taken from the MCD MY24 scenario (see §3.4; details specified in figure captions).

For the northern midlatitude summer atmosphere in Fig. 3.10 we see the temperature, aerosol (almost zero water ice) and water profiles at the top followed by the generated limb and nadir radiances and finally the corresponding percentage differences with error due to the noise equivalent radiance. For the A1–A3 channels, those with significant CO_2 absorption, we can see the error is below 1% where the noise levels are not significant and within the error curves at higher altitudes. For A4 the percentage difference is a little larger than the NESR curves below 15 km, but given that the radiance in this channel is low compared with the others, it is much less significant when looking at the absolute radiance difference. For the A5 channel there is a peak error of 3% outside the NESR curve. For B1 we see an error outside the NESR curve that peaks at about 4% at 15 km and similarly for B2.

The results for the southern midlatitude atmosphere are given in Fig. 3.11. In this atmosphere we see there is practically zero dust and water vapour, but significant water ice opacity. This is a more challenging atmosphere due to the lower radiances in all channels and leads to higher percentage errors than the previous case. For A1 the difference is only slightly worse than the NESR curve, a similar but slightly better result is seen for the A3 channel. For A2, A4 and B1 channels the results are better, staying within the NESR curve. The largest percentage errors are seen in the A5 and B1 curves. Although this case looks significantly worse than the previous atmosphere it is important to note that absolute radiance difference error is still low which can be seen from the channel radiance plots. Looking at both sets of simulation results it can be seen that the correlated-k approximation is of sufficient accuracy for use in MCS retrievals.

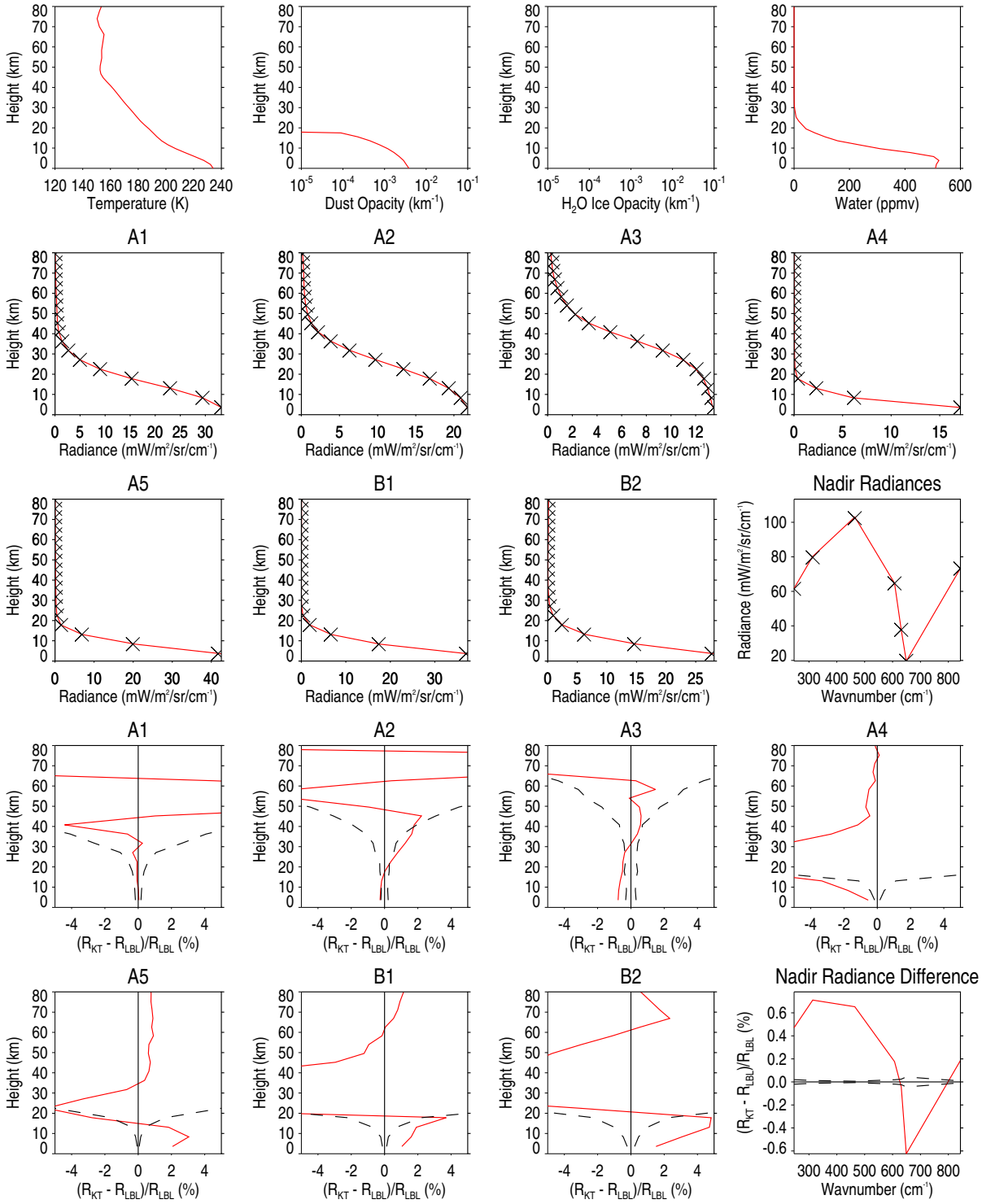


Figure 3.10 | **(Row 1)** Northern midlatitude summer temperature profile with corresponding aerosol and water profiles (From MCD: L_s=114°, 15h (LST), [51.1°N, 85.4°E]). **(Rows 2, 3)** Calculated limb and nadir radiances for MCS channels: Line-by-line model (red line) and correlated-k (crosses). **(Rows 4, 5)** Percentage differences between radiances calculated using the correlated-k approximation (R_{KT}) and a line-by-line calculation (R_{LBL}) for the MCS channels (red lines). The black dashed lines gives the noise levels for the limb and nadir for an average of five measurements.

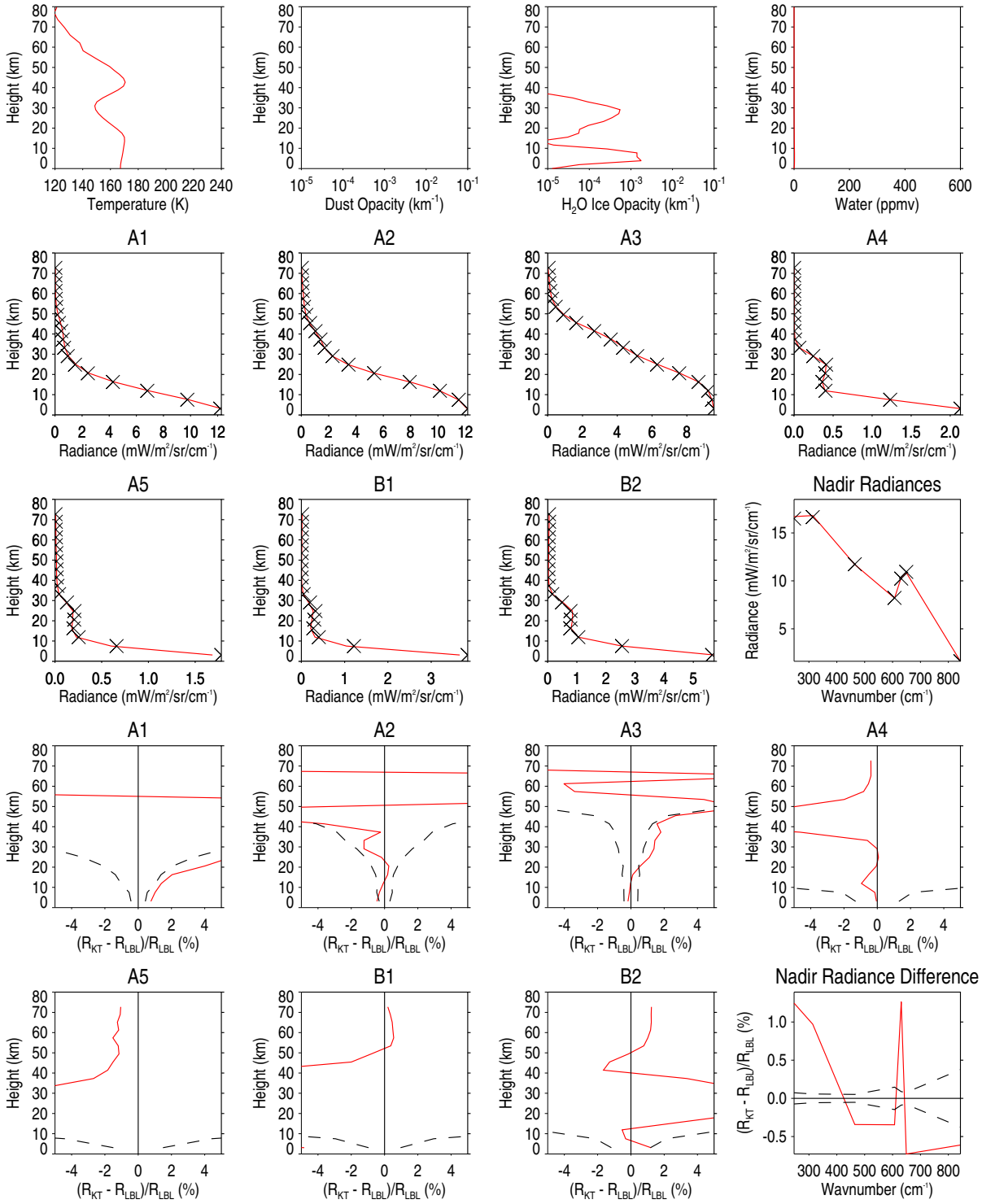


Figure 3.11 | As in Fig. 3.10 but for southern polar midlatitude profile (From MCD: L_s=114°, 03h (LST), [50.8°S, 108.6°W]).

3.3.4 Scattering Tests

Scattering and NEMESIS

When including scattering in radiative transfer modelling it is no longer sufficient to use the Planck function, $B_\nu(T)$, as the source function. Instead, it must be modified to include a scattering component. The new source function, S_ν, is then

$$S_\nu = B_\nu(T)(1-\omega_\nu) + \omega_\nu \oint L_\nu P(\alpha) d\Omega, \tag{3.49}$$

where $B_\nu(T)$ is the Planck function at wavenumber ν and temperature T, ω_ν is the single-scattering albedo ($\sigma_\nu^{sca}/\sigma_\nu^{ext}$), L_ν is the spectral radiance and $P(\alpha)$ is the scattering phase function with scattering angle α. On the RHS, the first term gives the emission contribution and the second term gives the radiation scattered into the beam.

In the NEMESIS the phase function is approximated using a variant of the Henyey-Greenstein function (Henyey & Greenstein, 1941; Irwin, 2004) for simplicity and computational efficiency

$$P(\alpha) = \frac{1}{4\pi}\left[f\frac{1-g_1^2}{\left(1+g_1^2-2g_1\cos\alpha\right)^{3/2}}\right] + (1-f)\left[f\frac{1-g_2^2}{\left(1+g_2^2-2g_2\cos\alpha\right)^{3/2}}\right], \tag{3.50}$$

where f is a fraction between 0 and 1 and g_1 and g_2 are asymmetry parameters, measures of the anisotropy of the scattering. The two terms on the RHS represent the forward- and backward-scattering peaks respectively. This variant makes it more flexible than the original single-peaked function (i.e. strong forward or backwards peak) proposed in Henyey & Greenstein (1941). The NEMESIS/RADTRANS multiple scattering calculations are performed in a plane-parallel geometry to evaluate S_ν and $P(\alpha)$. Using the calculated source function, the forward model integrates the radiative transfer equation along the limb/nadir path in a curved atmosphere (see 3.3). For more information see Irwin et al., (2008).

Test Method

To test the accuracy of our absorption-only approximation (see §3.3.1) we have performed comparisons between scattering and non-scattering radiative transfer calculations for a series of representative Martian conditions following a similar approach to the Kleinböhl et al. (2011, 2009) papers. This was done using the forward model of the NEMESIS/RADTRANS suite. Fig. 3.12 and Tbl. 3.2 give an overview of the different atmospheric conditions used in the simulations.

Scenarios are split into two base categories. Firstly, midlatitude northern summer hemisphere (NH)—the T_1 cases. Secondly, southern winter hemisphere (SH)—the T_2 cases. The T_1 and T_2 scenarios correspond to temperature profiles with their corresponding water vapour profiles, with peak abundances of 500 ppmv for T_1 and 2 ppmv for T_2 (both peaks below 10 km). These have been extracted from the Mars Climate Database MY24 scenario (see §3.4).

Dust is assumed to be homogeneously mixed for different dust loadings, while water ice is modelled as a layer, or as a constant extinction from 20 km to the ground. All simulations use the aerosol extinction and single-scattering albedoes as described in §3.3.1. Limb and nadir radiances were simulated and include the effects of the MCS channel fields-of-view. For the limb views the full array of 21 detectors was modelled with boresight heights ranging from below the horizon (i.e. pointing at surface) for the bottom detector to above 70 km for the top.

Test Results and Discussion

The results from the simulations are given in Figs 3.13–3.17. The models are specified using the text in the square brackets, these show the combination of temperature, water and aerosol profiles used for the model atmosphere e.g. T_1 + D_1 means an atmosphere that uses the T_1 (temperature and water) and D_1 (dust) profiles. For the limb plots positive differences correspond to an overestimate by the absorption-only model while negative differences are underestimates.

The agreement between the absorption-only and scattering radiative transfer calculations is good or reasonable for all the scenarios tested with a maximum absolute radiance difference of about 2 $mW/m^2/sr/cm^{-1}$ being seen (in A5), but mostly being much smaller. Percentage differences for the SH winter T_2 scenarios are generally higher than NH summer T_1 cases because the lower temperatures lead to lower radiances with comparable absolute radiance differences. Near the surface the absorption-only model tends to overestimate radiances while in the 10–30 km region it tends to underestimate, this is likely caused by the extended MCS field-of-views.

Differences in the primary water ice channel, A4, below 10 km vary over 5–30%, being generally higher for ice-only scenarios and lower when dust is present. In the 10–30 km region when ice is present percentage differences vary over 10–20%. For the dust-only cases the difference can get up to nearly 40% (T_1 + D_2). This is not concerning as the absolute differences are small and A4 is the primary ice retrieval channel and the equivalent differences in the dust channel, A5, are much smaller. Above 30 km the differences get quite high, but this is due to the lower contribution from limb emission radiances versus scattering at these altitudes.

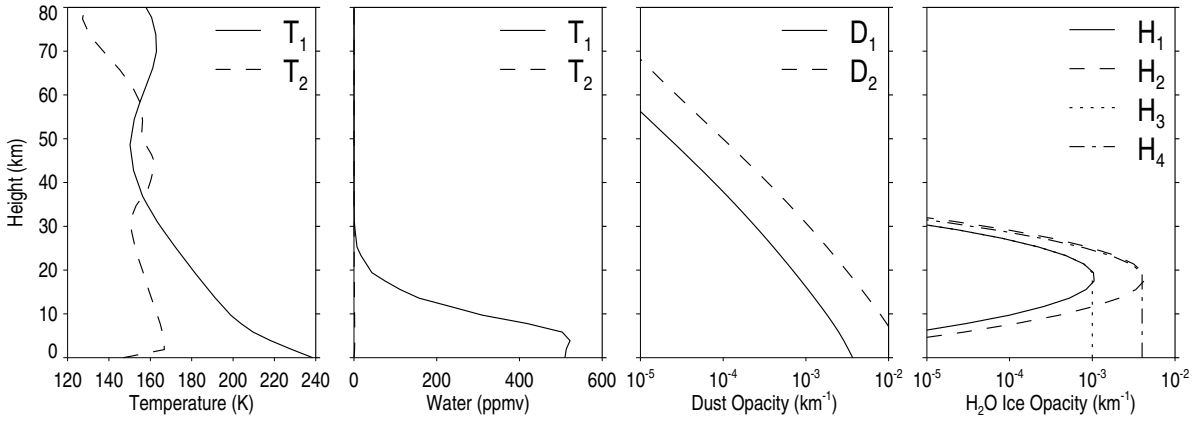


Figure 3.12 | Model profiles of temperature **(left)** with corresponding water vapour profiles **(centre left)**, dust extinction **(centre right)** and water ice ice extinction **(right)** used in the different radiative transfer calculations. The T_2 water vapour profile (dashed line) appears to be absent in the plot above, but because of its low value it is running along the y-axis.

Table 3.2 | Description of model parameters for model profiles seen in Fig. 3.12.

Model	Profile Type/s	Description
T_1	Temperature & Water	NH midlatitude summer temperature profile with T_{surf}=271 K, and water profile with maximum VMR of ∼500 ppmv. From MCD: L_s=114°, 15h (LST), [51.1°N, 85.4°E].
T_2	Temperature & Water	SH midlatitude winter temperature profile with T_{surf}=146 K, and water profile with maximum VMR of ∼2 ppmv. (From MCD: L_s=114°, 03h (LST), [50.8°S, 108.6°W])
D_1	Aerosol-Dust	Dust aerosol profile with nadir optical depth at A5 of about 0.045 (0.13 at 1075 cm^{-1}), high normal opacity.
D_2	Aerosol-Dust	Dust aerosol profile with nadir optical depth at A5 of about 0.2 (0.6 at 1075 cm^{-1}), dust storm level.
H_1	Aerosol-Water Ice	Water ice aerosol profile with layer at 20 km with a peak extinction of 10^{-3} at A4.
H_2	Aerosol-Water Ice	Water ice aerosol profile with layer at 20 km with a peak extinction of $4 \cdot 10^{-3}$ at A4.
H_3	Aerosol-Water Ice	Same as H_1 but layer extended down to ground.
H_4	Aerosol-Water Ice	Same as H_2 but layer extended down to ground.

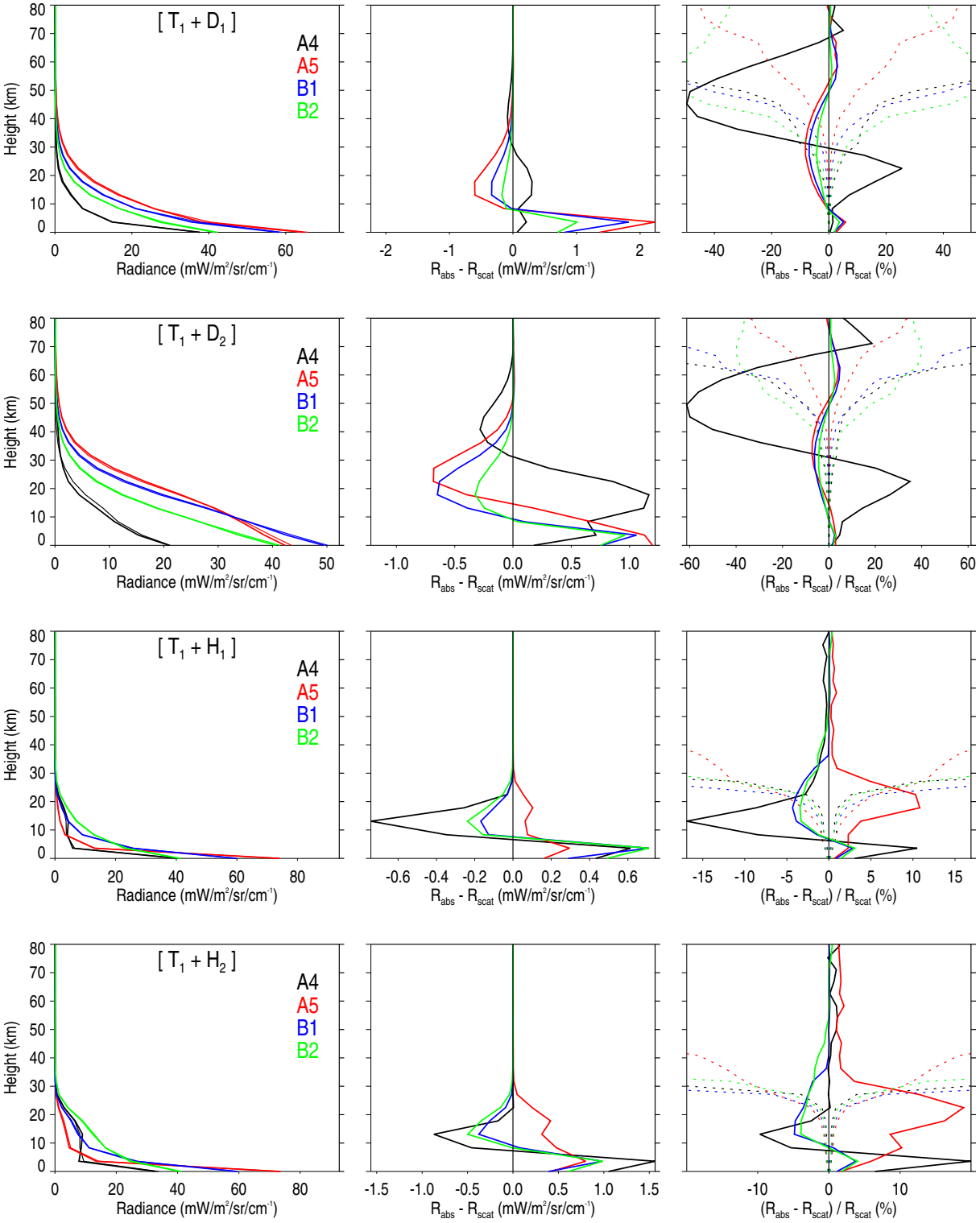


Figure 3.13 | Comparison of calculated limb radiances for various models (one model per row). The model atmosphere is specified by the black text in square brackets in the left panel e.g. $T_1 + D_1$ means an atmosphere that uses the T_1 (temperature and water) and D_1 (dust) profiles. **(Left Column)** Limb radiance profiles for MCS channels calculated for absorption-only (thin line) and scattering (thick line) radiative transfer. The MCS channel is indicated by the line colour according to the legend in top right. **(Middle Column)** Radiance difference between the absorption-only and scattering calculations for the profiles in the left panel using the same line colours. **(Right Column)** Percentage difference between the absorption-only and scattering calculations for the profiles in the left panel using the same colours. The dashed lines indicate the MCS channel noise levels for an average of five measurements, using the same channel colours.

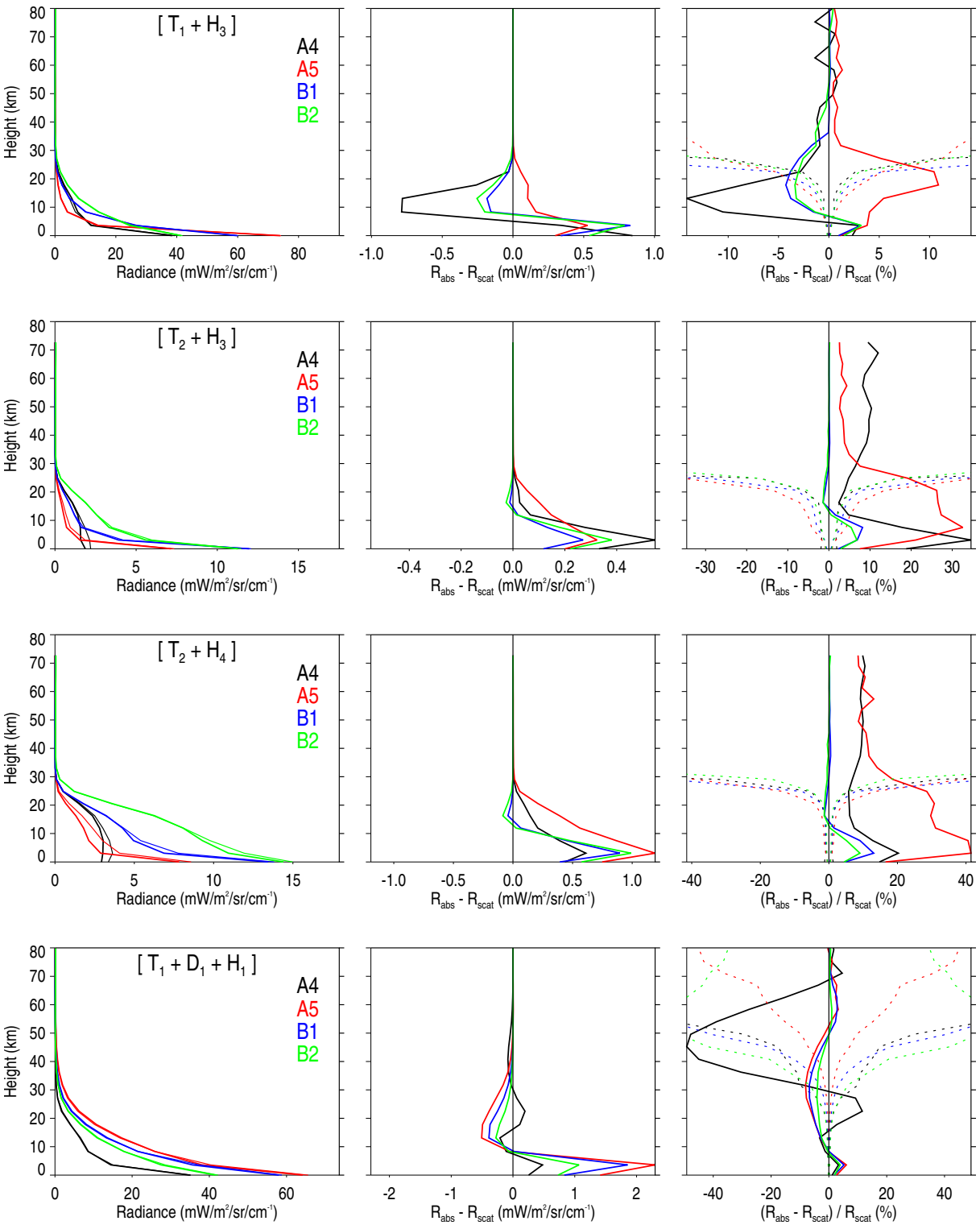


Figure 3.14 | Continued from Fig. 3.13.

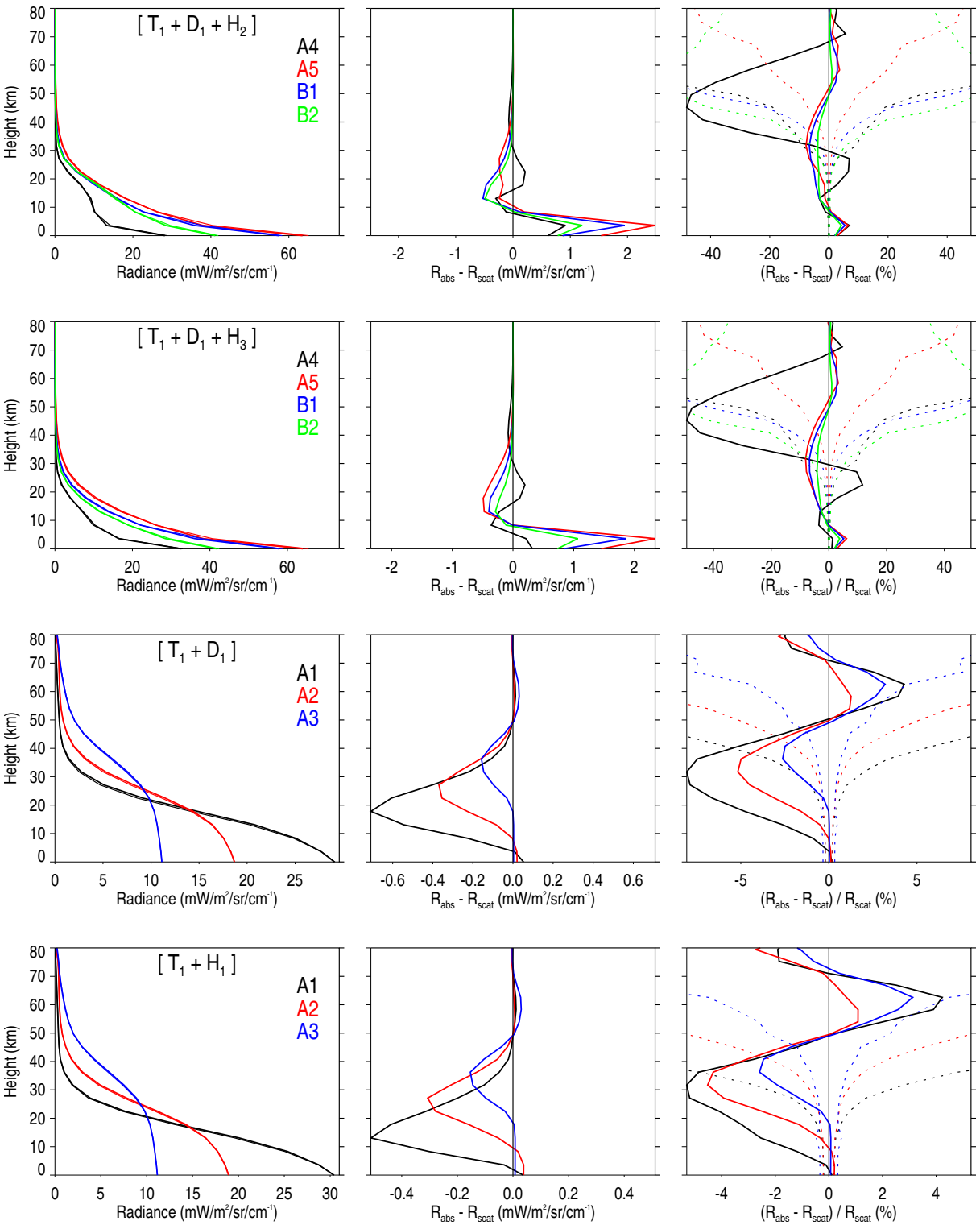


Figure 3.15 | Continued from Fig. 3.14.

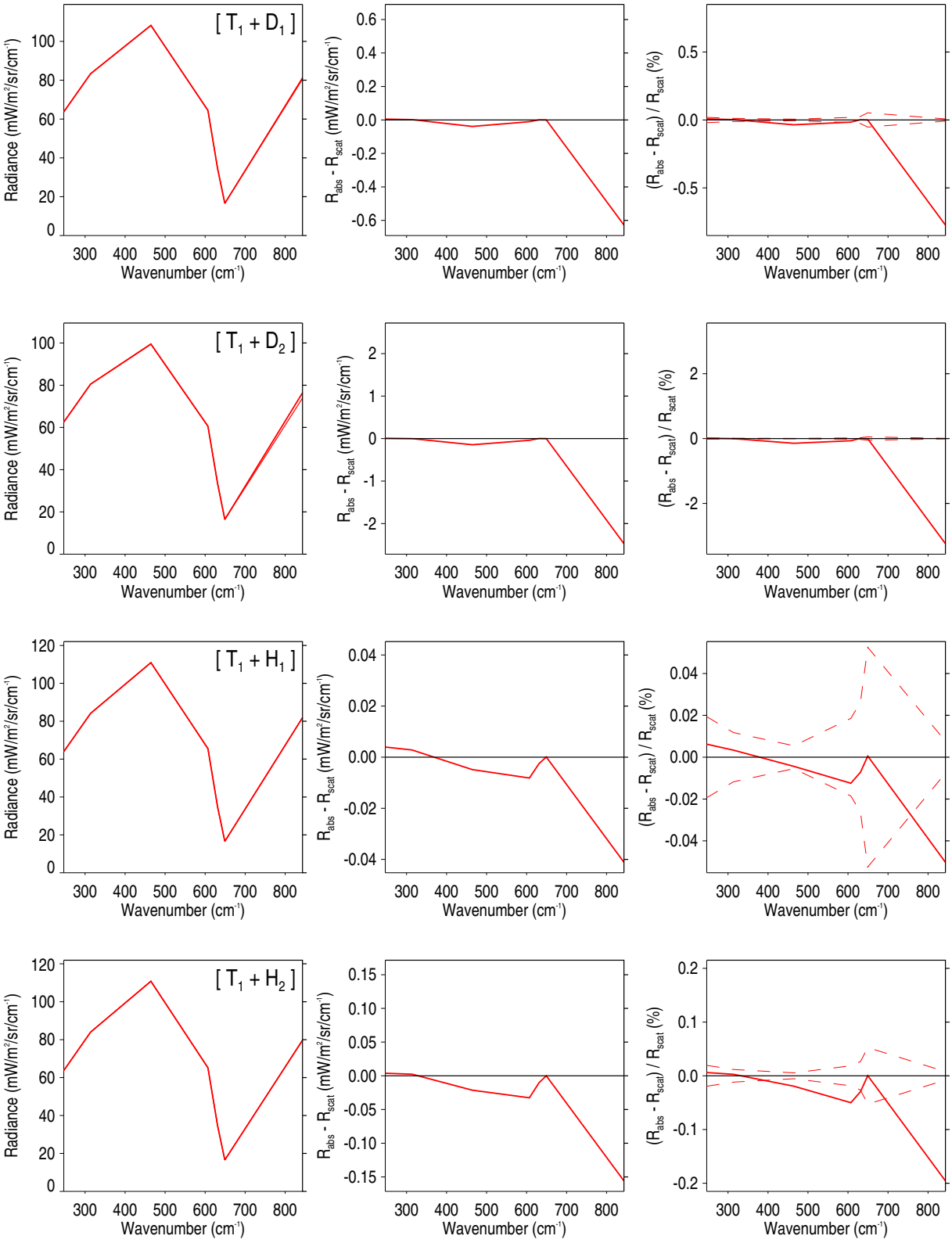


Figure 3.16 | Comparison of calculated nadir radiances for various models (one model per row). The model atmosphere is specified by the black text in square brackets in the left panel e.g. $T_1 + D_1$ means an atmosphere that uses the T_1 (temperature and water) and D_1 (dust) profiles. **(Left Column)** Nadir radiance profiles for MCS channels calculated for absorption-only (thin line) and scattering (thick line) radiative transfer. **(Middle Column)** Radiance difference between the absorption-only and scattering calculations for the profiles in the left panel. **(Right Column)** Percentage difference between the absorption-only and scattering calculations for the profiles in the left panel. The dashed lines indicate the MCS channel noise levels for an average of five measurements.

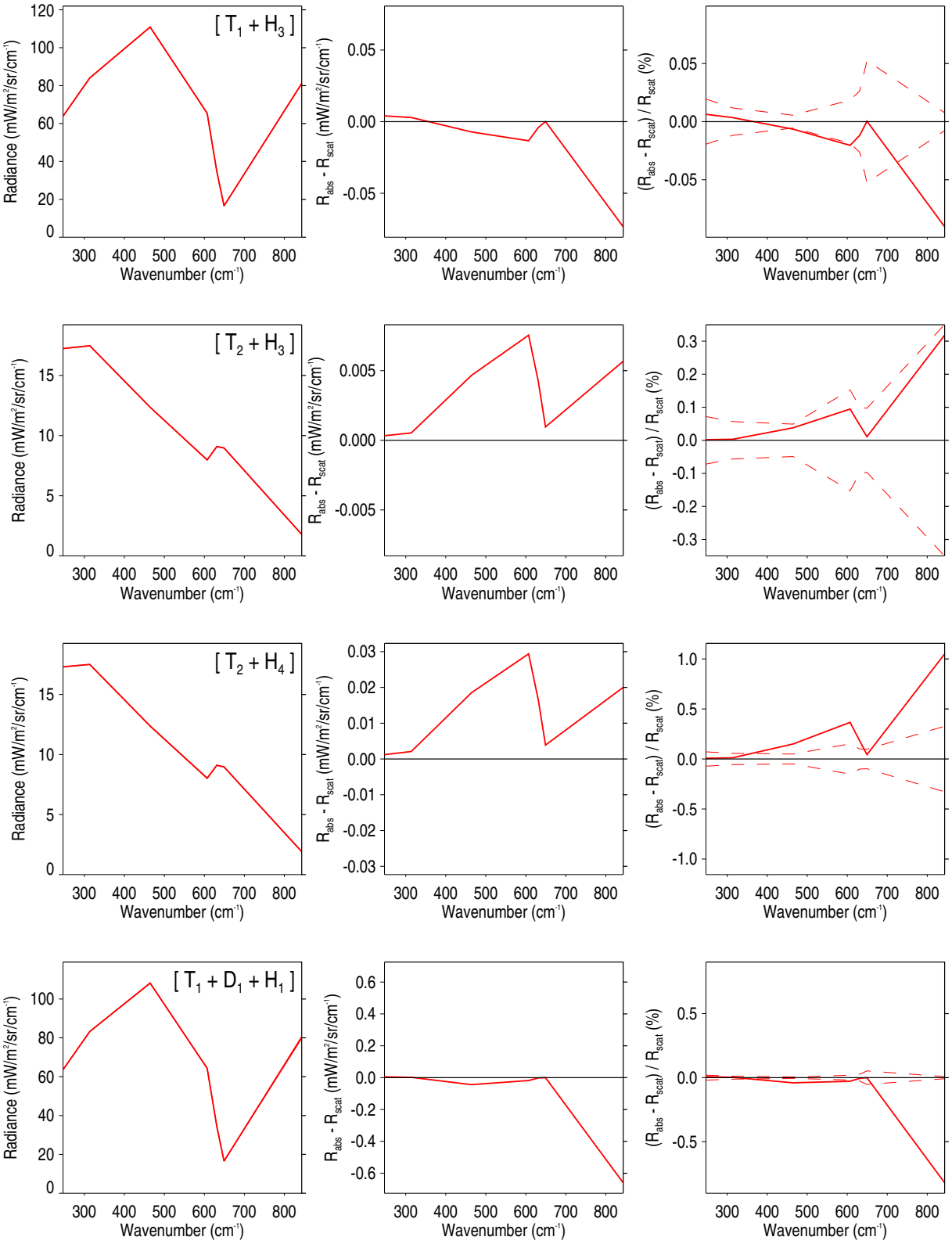


Figure 3.17 | Continued from Fig. 3.16.

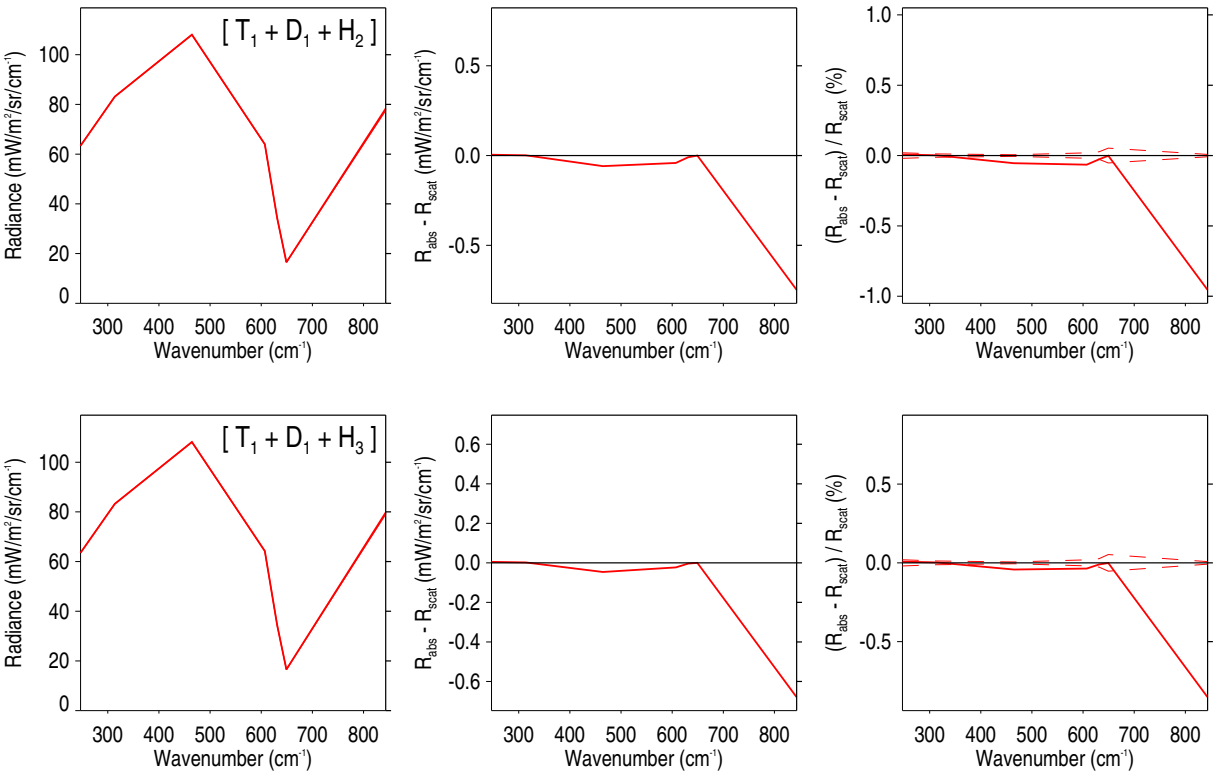


Figure 3.18 | Continued from Fig. 3.17.

For the primary dust channel, A5, below 10 km differences are below 5% except for the T_2 scenarios, where no dust is present. For the T_2 scenarios the percentage differences are much higher at about 40%. As A5 is mainly sensitive to dust rather than ice, the lack of dust means low radiances in the channel whilst having comparable absolute radiance differences to other scenarios. This leads to the high percentage differences seen. Above 10 km the difference remains below 10% when dust is present, but increases to 10–30% for ice-only cases (for the reasons just discussed). As for the A4 case above, this is less concerning given that it is primarily a dust channel and the absolute differences are still low.

At all altitudes the differences in B1 follow A5 closely when dust is present and B2 when ice is the only aerosol. Differences in B2 peak below 10 km and are mostly below 5% increasing up to 10% only for the T_2 scenarios where radiances are low due to very low water abundance and low radiance.

Absolute differences for A1–A3 (see Fig. 3.15) are lower than the other channels due to being in the CO_2 absorption band. This is because being in the presence of an absorber reduces the single-scattering albedo of the medium as whole (Kleinböhl et al., 2011). Percentage differences peak at 30 km with maximum values of 5–8% in A1. As the A1 channel is furthest from the

centre of the CO_2 band, it is the least affected by gaseous absorption and hence affected the greatest by scattering. Nadir differences in all channels are low, peaking at 3% in A4.

Though the radiance differences are good or reasonable they are often larger than the noise. This means they will need to be treated as systematic errors in the retrieval. For the aerosols the relative radiance difference (10–30%) is expected to be comparable to the error in the retrieved extinction in optically thin cases. These differences are very similar in scale to those found in (Kleinböhl et al., 2009) for scattering versus absorption-only radiative transfer. It is also important to note that the dust models D_1 and D_2 represent worst-case scenarios. For D_1, the dust optical depth modelled here is at higher end of what would be expected for this season (Montabone et al., 2015). More typical values would be about half this value with correspondingly lower radiance differences. For D_2, the opacity is at dust-storm level (Montabone et al., 2015), being optically thick in the lowest few kilometres. Consequently, most retrievals including dust performed for this thesis should result in higher accuracy, suffering less from errors due to an absorption-only model.

For water, calculating the errors is more complex. An estimate of the error was gained by fitting a power law, for radiance at a given height/detector versus water VMR, for scaled T_1 and T_2 water profile model runs with scattering. These were scaled to column abundances in the range 1–100 pr. µm. For both models at a height of 16 km (corresponding to 50% peak VMR), this gives the relation $x \approx (R/A)^{0.44}$, where x is the water VMR (ppmv), R is the B2 radiance ($\mathrm{nW/cm^2/sr/cm^{-1}}$) and A is a constant. For a 5% excess radiance error this corresponds to a 10% excess water abundance error and for a 10% radiance error a 24% abundance error. The excess radiation in B2 in the lower atmosphere is generally less than 5% and the error in B2 due to scattering is comparable to the ∼10% error due to the line data (see §3.3.2) and so our water retrievals should not be overly affected.

3.3.5 Assumption of Local Thermodynamic Equilibrium

For this work we assume the Martian atmosphere is in Local Thermodynamic Equilibrium (LTE). The strongest CO_2 vibrational bands are in LTE in the lower and middle atmosphere up to ≈80 km (Kleinböhl et al., 2009); above this the assumption starts to break down. As the focus of this thesis is the retrieval of water vapour which is confined well below 80 km this assumption is deemed reasonable. Even so the actual error in temperature at these high altitudes is small, of the order of 2–4 K (Kleinböhl et al., 2009).

3.4 Martian Reference Atmosphere

A reference atmosphere is used to provide an *A Priori* (i.e. first-guess) atmosphere for use in the retrieval of atmospheric parameters (for more on this see Chapter 4). This reference atmosphere coupled with the Radiative Transfer Theory described above allows for the simulation of Martian spectra. The primary sources of data used to build a reference atmosphere in this thesis are the the Mars Climate Database (MCD) Version 4.1 (Forget et al., 2006) and the MCS Level 2 (L2) Retrievals performed by Kleinböhl et al. (2009).

The MCD is a database of statistics describing the climate and environment of the Martian atmosphere. It has been assembled on the basis of output from multi-annual integrations of the the Global Climate Model (GCM) jointly developed by Laboratoire de Météorologie Dynamique du CNRS, France; University of Oxford, UK; Instituto de Astrofísica de Andalucía, Spain, with support from the European Space Agency (ESA), and Centre National d'Études Spatiales (CNES).

The MCD covers altitudes up to ≈250 km using a full thermosphere model (though for this thesis it is only used up to maximum of ≈100 km). It provides data for huge amount of atmospheric variables: temperature, surface pressure, winds (horizontal and vertical), atmospheric density, atmosphere turbulent energy, CO_2 ice cover, thermal and solar radiative fluxes, dust column opacity, water vapour and ice (column and mixing ratio), O_3, CO, O, O_2, N_2 and CO_2 volume mixing ratios. It also provides a full water cycle model (including dust coupling effects). Year-to-year variability and dust content variations are accounted for with simulation of 'years' with differing dust content: (1) baseline 'MY24' (Martian Year 24) scenario based on assimilation of TES observations in 1999–2001 (the scenario used for this thesis); (2–3) 'clear' (cold) and 'dusty' (warm) scenarios to bracket the reality and (4) a global dust storm scenario. The seasonal cycle is captured with the storage of 12 'typical' days (averaged over 30° of L_s) around the year (which are interpolated with good accuracy when needing a time in-between). The diurnal cycle is captured with the storage of environmental data 12 times per day (with accurate interpolation when required; Forget et al., 2006).

The MCS L2 dataset comprises of the profiles retrieved from 4 h blocks of MCS observations and is split into two structures. The first gives auxiliary information such as date, local time, solar zenith angle, location, surface and areoid radii. It also contains quality flags and identifies which detectors were used in the retrieval of a given profile. The second structure contains the

retrieved profiles themselves mapped onto a pressure grid of 105 levels from $1.8789{\cdot}10^{3}$ Pa to $4.2470{\cdot}10^{-3}$ Pa covering the whole MCS height range set by

$$p_i = p_{\text{ref}} \cdot e^{-\frac{i-10}{8}}, \tag{3.51}$$

where i is the level and p_{ref} is 610 Pa. The second structure contains retrieved profiles for temperature, dust opacity at A5 in km^{-1}, ice opacity at A4 in km^{-1} along with their respective errors. It also contains retrieved pressure and surface temperature. The retrieved quantities are only reported for levels where sufficient information could be extracted from the radiances; other levels are marked as 'missing'.

It makes practical sense to use the (MCD) for this purpose due to the highly variable nature of the Martian climate, both spatially and temporally. The Mars GCMs have also been extensively validated using observational data (Forget et al., 2006). The advantage of the L2 dataset is that it gives an obvious starting place for our retrievals given that that they are based on the same observations for the same instrument. This simplifies the creation of the *a priori* (APR) and gives a likely accurate place to start from.

The model atmosphere is constructed with 39 altitude levels and covers a height range of 0–100 km; the MCD or L2 profiles are interpolated onto this grid. It is constructed using the following variables:

Temperature/Pressure Surface values and vertical profiles above the surface.

Gases: CO_2, N_2 and Water Vapour Vertical profiles of volume mixing ratio. For CO_2 and N_2 these are uniformly mixed to the top of the atmosphere with values of 0.9532 and 0.027 respectively. For radiative transfer modelling N_2 is treated as being spectroscopically inert and is included for composition/pressure purposes only. Water vapour varies massively spatially and temporally.

Aerosols: Dust and Water Ice Clouds Profiles of specific concentration are constructed in units of number of aerosol particles per gram of atmosphere (g^{-1}).

For temperature, pressure, dust, ice and surface temperature L2 data are used where available with MCD values being used directly or in extrapolation of missing values. This is because L2 retrieval products do not always contain full profiles as described above. In these cases extrapolations have to be made in order to have have full APR profiles for conducting retrievals

which are explained next. Extrapolated values at heights between the ground and the bottom of the L2 profile are referred to as lower values and those above the L2 profile (up to 100 km) are upper values.

For pressure profiles, the missing values, p_{extrap}, at height z, are extrapolated

$$p_{\text{extrap}}(z) = p_0 e^{-\frac{z-z_0}{H}} \tag{3.52}$$

where p_0 is the reference pressure at z_0, the top/bottom of the L2 profile and H is the Martian scale height of 10.8 km. For temperature profiles, lower values are replaced with MCD data that have been shifted and scaled down to the ground. The shift is calculated

$$\Delta T = T_{\text{L2}}(z_0) - T_{\text{MCD}}(z_0) \tag{3.53}$$

where ΔT is the L2-MCD temperature shift at height z_0, the bottom value of the L2 profile and T_{L2} and T_{MCD} are the corresponding temperatures for the L2 and MCD temperature profiles respectively. This shift is added to all the MCD values below z_0 to the surface

$$T_{\text{shift}}(z < z_0) = T_{\text{MCD}}(z < z_0) + \Delta T \tag{3.54}$$

where $T_{\text{shift}}(z < z_0)$ are the shifted values. Then the scaling is done such that the the temperature at ground level of the extrapolated profile matches the MCD value (for the equivalent time and location) and the top value matches the bottom of the L2 data. The extrapolated profile, $T_{\text{extrap-lo}}(z < z_0)$, is then

$$T_{\text{extrap-lo}}(z < z_0) = S[T_{\text{shift}}(z < z_0) - T_{\text{L2}}(z_0)] + T_{\text{L2}}(z_0) \tag{3.55}$$

where the scaling factor, S, is

$$S = \frac{T_{\text{MCD}}(z = 0) - T_{\text{L2}}(z_0)}{T_{\text{shift}}(z = 0) - T_{\text{L2}}(z_0)} \tag{3.56}$$

A central moving average with a width of 20 km is then applied to smooth the join between the L2 and extrapolated values starting at 20 km above the join.

For upper values a constant temperature shift of the MCD profile at the extrapolated heights to match the top of the L2 profile is used, mirroring Eqs 3.53 and 3.54. An example of fully

extrapolated profile with smoothing is given in Fig. 3.19. If a temperature inversion layer is present in the lower extrapolated values from the MCD, $T_{\mathrm{extrap-lo}}(z < z_0)$, the scaling and smoothing are only applied up to the peak of the inversion layer, rather than to the surface, to preserve the layer peak and MCD profile below at their original values.

For aerosols the opacity profiles from the L2 data need to be converted into units of specific particle density, g^{-1} (particles per gram of atmosphere) for use in retrievals. This is done with the equation:

$$N(z) = \frac{\tau_{\mathrm{L2}}(z,\nu)}{\rho(T(z),p(z)) \cdot \sigma_{\nu}^{ext} \cdot s} \tag{3.57}$$

where $N(z)$ is the aerosol specific concentration at height z, $\tau_{\mathrm{L2}}(z,\nu)$ is the limb extinction (km^{-1}) at wavenumber ν, $\rho(T(z),p(z))$ is the atmospheric density at z as a function of temperature, T and pressure, p, σ_{ν}^{ext} is the extinction cross-section at ν and $s = 1$ km. The value of ν for dust profiles is 463.510 cm^{-1} (centre of A5 channel) and 843.394 cm^{-1} for ice (centre of A4 channel) with the extinction cross-sections calculated according to the method in §3.3.1.

For the dust profile, missing lower values are replaced with a profile constant with height equal to the specific concentration value at the bottom of the L2 profile. This process is mirrored for missing upper values in dust and ice, but at a minimum value of 1 g^{-1}, a zero equivalent abundance[‡]. See Fig. 3.19 for an example dust profile extrapolation. For the ice profile, lower values are extrapolated via an exponential decay of the form:

$$N_{\mathrm{extrap-lo}}(z < z_0) = N_{\mathrm{L2}}(z_0) e^{\frac{z-z_0}{H_{ice}}} \tag{3.58}$$

where $N_{\mathrm{L2}}(z_0)$ is the ice concentration at the bottom of the L2 profile at the height z_0 and $H_{ice} = 1.25$ km. This scale height was chosen to match observed profile decay observed in more complete L2 profiles.

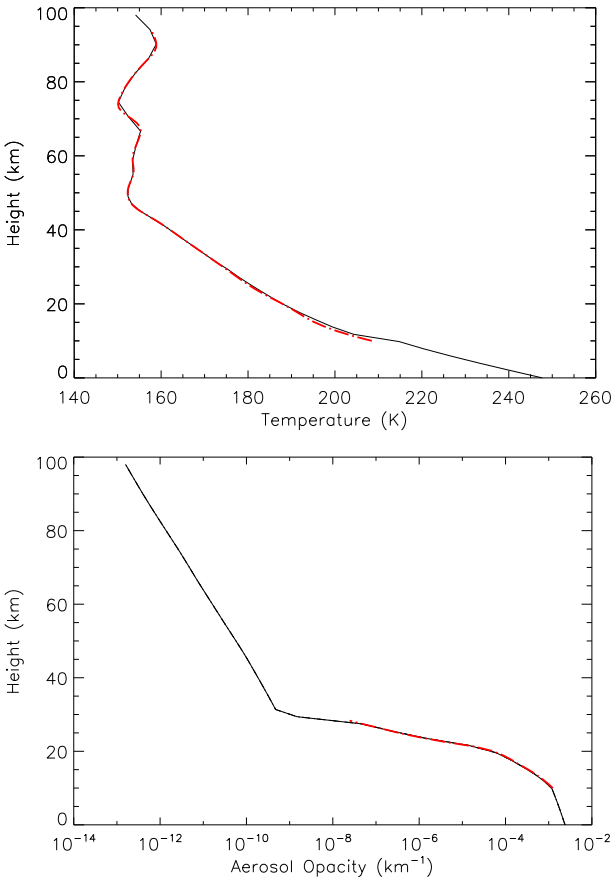


Figure 3.19 | (**Top**) NH midlatitude summer temperature profile after extrapolation from L2 using MCD. L2 profile shown by red line. Extrapolated profile shown by black line. (**Bottom**) Extrapolated dust profile. Colours as for temperature.

[‡]A negligible amount in NEMESIS, as it cannot handle zero due to calculating using logarithms of abundances.

For surface temperature and pressure retrievals
L2 data was used where available otherwise the MCD data served as fallback. For retrievals with no nadir radiances surface temperature was not retrieved. Water vapour VMR profiles are taken directly from the MCD.

Mostly these L2 based profiles are used in this thesis, but occasionally more MCD data are used to generate the model atmosphere instead. If the MCD data are used for dust the visible column optical depth is extracted and then converted to that at 1075 cm^{-1} by dividing the MCD value by 1.36 (Forget et al., 2005); this is because the dust values have been derived from the TES retrieved dust opacity by Smith (2004). This is then used to scale a dust profile generated using the OZONETABLE code mentioned earlier with either a Conrath profile shape with an inflection coefficient of 0.007 (Conrath, 1975) or with a uniform profile. Alternatively a fixed optical depth profile may be set instead. For water ice, a mass mixing ratio vertical profile is extracted from the MCD and is then converted to specific concentration using the parameters of the selected ice distribution (effective radius, r_{eff} and width v_{eff} of the distribution). This may be used directly or scaled to a predefined optical depth. Alternatively a uniform profile may be used.

4

Retrieval Theory

In this section retrieval theory and its implementation in Oxford's planetary retrieval software NEMESIS (Non-linear optimal Estimator for Multivariate spectral analysis) are outlined. Work and results for this section are based on Rodgers (2000), Houghton et al. (1984), Irwin et al. (2004, 2008), Irwin (2009), de Kok (2007) and Fletcher (2007). 0

4.1 What is Retrieval Theory?

Retrieval theory deals with solving the inverse problem. But what is the inverse problem? Both of these questions are most easily answered in terms of an example from remote sounding. Imagine a planetary atmosphere with known relationships for quantities such as temperature, pressure and composition. Using radiative transfer theory (as discussed in Chapter 3) it is possible to model its spectrum—this is the direct problem. When the reverse is done, that is, to measure the radiances from the spectrum at a finite set of frequencies and then to try and extract quantities such as temperature, pressure and composition profiles it is known as the inverse problem. Retrieval theory can be used to solve many other inverse problems, but given the subject of this thesis it seems best to continue and explain in this context.

Initially, this may seem like a simple problem as all that needs to be done to get a solution is to tweak the parameters (temperature, composition &c.) of the model until the measured and calculated radiances match. For example consider a region of the thermal infrared where

all atmospheric absorption is due to a well-mixed gas, like the 600 cm^{-1} region of the Martian atmospheric spectrum that is due to CO_2. Suppose the simulated spectrum was too bright at this wavelength then it would be correct to deduce that the model temperature profile was too warm at roughly the altitude where the weighting function (see §3.2) peaked. Hence, the model temperature profile would need to be 'cooled' at this altitude to achieve a better fit to the measured radiance (Irwin, 2009). Unfortunately the problem is not that simple.

Firstly, due to the transmission weighting function the radiance at any given wavelength is the weighted average of thermal emission over a continuous range of altitudes (see §3.2). This results in significant smoothing of vertical temperature structure (and hence a loss of information); to appreciate this consider nadir-viewing where the transmission weighing functions have widths of approximately one scale height (Irwin, 2009). Consequently, there are an infinite number of model temperature profiles that would result in the same radiance as the measured one. The effects of this problem can be mitigated by including spectral data from a range of wavelengths and/or using a range of emission angles in order that the resulting weighting functions cover a range of altitudes (Irwin, 2009).

Secondly, the model seeks to extract continuous profiles (i.e. profiles with an infinite number of points) from a finite set of measurements (i.e. the radiances). This makes the inverse problem *ill-posed*.

Thirdly, without due care experimental noise in the measured spectrum can greatly be amplified by the fitting process. This is because noise is confused with genuine radiance, which the model then attempts to fit. This can lead to fictitious oscillations in the resulting profile. This makes the inverse problem *ill-conditioned*.

Initially, the prospects of a solution look rather bleak, as all of these difficulties mean that there are an infinite number of model profiles whose simulated spectra will fit the measured spectrum to within the measurement error. Thankfully, in real life profiles of atmospheric variables (temperature, composition &c.) are generally *smoothly varying* functions. Consequently with sufficient vertical smoothing the discernment of a realistic solution is possible (Irwin, 2009).

At this point it is important to note that the choice of temperature, pressure and composition are arbitrary and that any other physical property could be modelled additionally to or instead of those used in this example e.g. surface temperature. Also parameters do not need to be specified for every level in the atmosphere. This means it is possible to choose to parametrise a vertical profile simply with just a fractional scale height and a deep volume mixing ratio.

4.2 The Forward Model

Bearing in mind the above, the spectrum from a planetary atmosphere can be modelled as follows:

$$\mathbf{y} = \mathbf{F}(\mathbf{x}) + \epsilon, \tag{4.1}$$

where $\mathbf{y}$ is the rank m measurement vector (containing the measured radiances, i.e. the spectrum), $\mathbf{x}$ is the rank n atmospheric state vector (containing the values of parameters such as temperature, pressure, composition &c.) and where $\mathbf{F}(\mathbf{x})$ is the forward model, i.e. the physics of the system. It contains the relationships between the atmospheric state and radiance (including the effects of instrument optics, viewing geometry, instrument resolution &c.) The vector ϵ contains estimates of the measurement radiance noise. This is used to construct the measurement error covariance matrix (where brackets indicate the expected value):

$$\mathbf{S}_\epsilon = < \epsilon \epsilon^{\mathrm{T}} > . \tag{4.2}$$

Using the Taylor expansion Eq. 4.1 can be linearised about a reference state $\mathbf{x_0}$:

$$\mathbf{y} - \mathbf{F}(\mathbf{x_0}) = \frac{\partial \mathbf{F}(\mathbf{x_0})}{\partial \mathbf{x}}(\mathbf{x} - \mathbf{x_0}) + \epsilon = \mathbf{K}(\mathbf{x} - \mathbf{x_0}) + \epsilon, \tag{4.3}$$

with

$$\mathbf{K} = \frac{\partial \mathbf{F}(\mathbf{x_0})}{\partial \mathbf{x}} \qquad K_{ij} = \frac{\partial F_i(x_{0,i})}{\partial x_j}, \tag{4.4}$$

where $\mathbf{x_0}$ represents some typical state known to be close to the solution $\mathbf{x}$ and $\mathbf{K}$ is the $(m \times n)$ matrix of functional derivatives known as the 'Jacobian'. It describes how each element of the modelled radiances vector $\mathbf{F}(\mathbf{x_0})$ should change with alterations to the state vector $\mathbf{x}$. The form on the right of Eq. 4.4 shows the value of each element.

4.3 Exact Solutions

Taking Eq. 4.3 and setting $\mathbf{x_0} = 0$ gives

$$\mathbf{y} = \mathbf{K}\mathbf{x} + \epsilon, \tag{4.5}$$

where the Jacobian becomes

$$\mathbf{K} = \frac{\partial \mathbf{y}}{\partial \mathbf{x}}. \tag{4.6}$$

An exact solution for $\mathbf{x}$ can be obtained by expressing it as a linear function of m variables for which there are m equations defining the coefficients. The exact linear solution is

$$\hat{\mathbf{x}} = \mathbf{G}\mathbf{y}, \tag{4.7}$$

where $\mathbf{G}$ is known as the 'Gain Matrix' (the generalized inverse of $\mathbf{K}$). It is the derivative of the estimated state with respect to the measurement and gives the contribution of each measurement in $\mathbf{y}$ (i.e. measured radiance and error) to the estimated state vector. Therefore it can also be written as

$$\mathbf{G} = \frac{\partial \widehat{\mathbf{x}}}{\partial \mathbf{y}}. \tag{4.8}$$

Upon expansion with Eq. 4.5, Eq. 4.7 becomes

$$\hat{\mathbf{x}} = \mathbf{G}\mathbf{y} = \mathbf{G}(\mathbf{K}\mathbf{x} + \epsilon) = \mathbf{A}\mathbf{x} + \mathbf{G}\epsilon, \tag{4.9}$$

where the term $\mathbf{A}$, known as the 'Averaging Kernel' is

$$\mathbf{A} = \mathbf{G}\mathbf{K}. \tag{4.10}$$

and where $\mathbf{G}\epsilon$ is the contribution function error term.

The Averaging Kernel serves a similar purpose to the Gain Matrix, but this time for a change in state instead of a change in radiance. Therefore it can be rewritten as

$$\mathbf{A} = \frac{\partial \widehat{\mathbf{x}}}{\partial \mathbf{x}}. \tag{4.11}$$

It is a measure of the sensitivity of the retrieved state to the true atmospheric state. It shows the response to a δ-function perturbation of the state for each member of the state. For the case of a continuous profile the width of the averaging kernel provides the resolution of the retrieval. In other words it indicates how the true profile is smoothed by the retrieval.

Exact solutions are well-posed so that $m = n$ and so the averaging kernel becomes a unit matrix. This means $\mathbf{G} = \mathbf{K}^{-1}$ so that $\hat{\mathbf{x}} = \mathbf{x} + \mathbf{K}^{-1}\epsilon$. Exact solutions are generally ill-conditioned so that if the Gain Matrix becomes large then the experimental error ϵ will be greatly amplified

to errors $\mathbf{G}\epsilon$ in the estimate of the state. Taking more measurements may make the problem worse (Houghton et al., 1984). Consequently, this method is not normally employed in remote sensing.

4.4 Least Squares

A simple and standard solution for any case where there are more measurements than unknowns ($m > n$) is the 'least squares fit'. It aims to find the the set of elements $\widehat{\mathbf{x}}$ that minimise the sum-square difference (known as the 'cost function') between the the actual (noisy) measurements $\mathbf{y}$ and the predicted measurements $\mathbf{F}(\widehat{\mathbf{x}})$

$$\chi^2 = (\mathbf{y} - \mathbf{F}(\widehat{\mathbf{x}}))^{\mathrm{T}} \mathbf{S}_\epsilon^{-1} (\mathbf{y} - \mathbf{F}(\widehat{\mathbf{x}})). \tag{4.12}$$

The solution for the state vector, $\hat{\mathbf{x}}$, and the corresponding covariance matrix, $\hat{\mathbf{S}}$, are then

$$\hat{\mathbf{x}} = (\mathbf{K}^{\mathrm{T}} \mathbf{S}_\epsilon^{-1} \mathbf{K})^{-1} \mathbf{K}^{\mathrm{T}} \mathbf{S}_\epsilon^{-1} \mathbf{y} \tag{4.13}$$

$$\hat{\mathbf{S}} = (\mathbf{K}^{\mathrm{T}} \mathbf{S}_\epsilon^{-1} \mathbf{K})^{-1}, \tag{4.14}$$

where $\hat{\mathbf{S}}$ gives the contribution of the measurement error covariance matrix, $\mathbf{S}_\epsilon$, to the final error in $\hat{\mathbf{x}}$. Unfortunately, for the reasons discussed in §4.1 this method often leads to solutions that are ill-posed (it is often the case for planetary spectra that $m < n$) and ill-conditioned. One remedy to this is to sacrifice vertical resolution by parameterising profiles with fewer parameters e.g. representing a composition profile as a mean mole fraction.

This is obviously an oversimplification and so if increased vertical resolution is desired additional constraints (in the form of *a priori* assumptions) are required to prevent meaningless solutions. A number of approaches to this problem have been discussed in the literature (Hanel et al., 2003; Houghton et al., 1984; Rodgers, 2000 and Irwin, 2009). They all give the same conclusion that the precision of the retrieved profile depends on the vertical averaging applied or assumed. As a result remotely sensed spectra may be inverted to yield very accurate, but smoothed profiles, becoming increasingly inaccurate as less vertical smoothing is applied (Irwin, 2009). Ultimately then, there is a trade-off between error and vertical resolution. One method for addressing all of these issues is the 'optimal estimation' method described in the following section.

4.5 Linear Optimal Estimation

Optimal estimation improves upon the 'exact solutions' and 'least squares' method by the addition of *a priori* estimates $\mathbf{x_a}$, with *a priori* error covariances $\mathbf{S_a}$. This gives more constraint on the problem and so aids in selecting the physically realistic solution from the range of possible answers. These *a priori* estimates are virtual measurements. They are obtained from prior knowledge or modelling and provide information about the profile in the same way as real measurements.

Starting again with Eqs 4.5 and 4.6 the best solution is the one where the probability function of the state given the measurements, $P(\mathbf{x}|\mathbf{y})$, is maximised i.e. where

$$\frac{\partial P(\mathbf{x}|\mathbf{y})}{\partial \mathbf{x}} = 0. \tag{4.15}$$

Using Bayes' theorem this probability can be written as

$$P(\mathbf{x}|\mathbf{y}) = \frac{P(\mathbf{y}|\mathbf{x})P(\mathbf{x})}{P(\mathbf{y})}. \tag{4.16}$$

The Gaussian probability distribution around zero for the parameter $\mathbf{z}$ is given as

$$P(\mathbf{z}) = \frac{1}{(2\pi)^{\frac{n}{2}}|\mathbf{S_z}|^{\frac{1}{2}}} \exp\left(-\frac{\mathbf{z}^{\mathrm{T}}{\mathbf{S_z}}^{-1}\mathbf{z}}{2}\right), \tag{4.17}$$

where $\mathbf{S_z}$ is the corresponding covariance matrix.

The term $P(\mathbf{y}|\mathbf{x})$ denotes the probability of the measurements given the state; this is the same as the probability distribution of the error vector ϵ and so

$$P(\mathbf{y}|\mathbf{x}) = P(\epsilon). \tag{4.18}$$

If it is assumed that $P(\epsilon)$ is a Gaussian distribution around zero, then taking Eq. 4.17 and setting $\mathbf{z} = \mathbf{y} - \mathbf{K}\mathbf{x}$ with $\mathbf{S_z} = \mathbf{S}_\epsilon$ gives

$$P(\epsilon) = \frac{1}{(2\pi)^{\frac{n}{2}}|\mathbf{S}_\epsilon|^{\frac{1}{2}}} \exp\left(-\frac{(\mathbf{y}-\mathbf{K}\mathbf{x})^{\mathrm{T}}{\mathbf{S}_\epsilon}^{-1}(\mathbf{y}-\mathbf{K}\mathbf{x})}{2}\right). \tag{4.19}$$

Likewise the error in the state can be found by setting $\mathbf{z} = \mathbf{x} - \mathbf{x_a}$ with $\mathbf{S_z} = \mathbf{S_a}$ and so

$$P(\mathbf{x}) = \frac{1}{(2\pi)^{\frac{n}{2}} |\mathbf{S_a}|^{\frac{1}{2}}} \exp\left(-\frac{(\mathbf{x} - \mathbf{x_a})^{\mathrm{T}} \mathbf{S_a}^{-1} (\mathbf{x} - \mathbf{x_a})}{2} \right). \tag{4.20}$$

Finally, $P(\mathbf{y})$ will be some function of $\mathbf{y}$. Substituting the above terms into Eq. 4.16 and taking the natural logarithm gives (Rodgers, 2000)

$$-2 \ln P(\mathbf{x}|\mathbf{y}) = (\mathbf{y} - \mathbf{K}\mathbf{x})^{\mathrm{T}} \mathbf{S}_\epsilon{}^{-1} (\mathbf{y} - \mathbf{K}\mathbf{x}) + (\mathbf{x} - \mathbf{x_a})^{\mathrm{T}} \mathbf{S_a}^{-1} (\mathbf{x} - \mathbf{x_a}) + f(\mathbf{y}), \tag{4.21}$$

where $f(\mathbf{y})$ is a function of $\mathbf{y}$ that also contains all of the multiplicative constants of the form $\frac{1}{(2\pi)^{\frac{n}{2}} |\mathbf{S_z}|^{\frac{1}{2}}}$.

Maximising $P(\mathbf{x}|\mathbf{y})$ means minimising Eq. 4.21. Therefore Eq. 4.21 is a sort of cost function similar to Eq. 4.12. Unlike Eq. 4.12 this function not only aims to minimise the difference between the measured spectrum, $\mathbf{y}$, and the modelled spectrum, $\mathbf{K}\mathbf{x}$, but also to minimise the deviation of the assumed state vector, $\mathbf{x}$, from the *a priori* state, $\mathbf{x_a}$ (this is the additional constraint that what was mentioned at the beginning of this section). Thus the optimal solution to the state vector is the one that fulfills both of these conditions. To find the minimum of the Eq. 4.21, it must be differentiated with respect to $\mathbf{x}$,

$$\frac{\partial(-2 \ln P(\mathbf{x}|\mathbf{y}))}{\partial \mathbf{x}} = \left(\mathbf{K}^{\mathrm{T}} \mathbf{S}_\epsilon^{-1} \mathbf{K} + \mathbf{S_a^{-1}} \right) \mathbf{x} - \left(\mathbf{K}^{\mathrm{T}} \mathbf{S}_\epsilon^{-1} \mathbf{y} + \mathbf{S_a^{-1}} \mathbf{x_a} \right), \tag{4.22}$$

and the optimal solution found for when $\frac{\partial(-2 \ln P(\mathbf{x}|\mathbf{y}))}{\partial \mathbf{x}} = 0$. This is given as

$$\begin{aligned} \widehat{\mathbf{x}} &= \left(\mathbf{K}^{\mathrm{T}} \mathbf{S}_\epsilon^{-1} \mathbf{K} + \mathbf{S_a^{-1}} \right)^{-1} \left(\mathbf{K}^{\mathrm{T}} \mathbf{S}_\epsilon^{-1} \mathbf{y} + \mathbf{S_a^{-1}} \mathbf{x_a} \right) \\ &= \mathbf{x_a} + \left(\mathbf{K}^{\mathrm{T}} \mathbf{S}_\epsilon^{-1} \mathbf{K} + \mathbf{S_a^{-1}} \right)^{-1} \mathbf{K}^{\mathrm{T}} \mathbf{S}_\epsilon^{-1} \left(\mathbf{y} - \mathbf{K}\mathbf{x_a} \right) \\ &= \mathbf{x_a} + \mathbf{S_a} \mathbf{K}^{\mathrm{T}} \left(\mathbf{K} \mathbf{S_a} \mathbf{K}^{\mathrm{T}} + \mathbf{S}_\epsilon \right)^{-1} \left(\mathbf{y} - \mathbf{K}\mathbf{x_a} \right), \end{aligned} \tag{4.23}$$

with the total covariance matrix

$$\begin{aligned} \widehat{\mathbf{S}} &= \left(\mathbf{K}^{\mathrm{T}} \mathbf{S}_\epsilon^{-1} \mathbf{K} + \mathbf{S_a^{-1}} \right)^{-1} \\ &= \mathbf{S_a} - \mathbf{S_a} \mathbf{K}^{\mathrm{T}} \left(\mathbf{K} \mathbf{S_a} \mathbf{K}^{\mathrm{T}} + \mathbf{S}_\epsilon \right)^{-1} \mathbf{K} \mathbf{S_a}. \end{aligned} \tag{4.24}$$

Eq. 4.23 can be rewritten as

$$\widehat{\mathbf{x}} = \mathbf{x_a} + \mathbf{G}(\mathbf{y} - \mathbf{K}\mathbf{x_a}), \tag{4.25}$$

where the Gain Matrix, $\mathbf{G}$, becomes

$$\begin{aligned} \mathbf{G} &= \left(\mathbf{K}^{\mathrm{T}}\mathbf{S}_{\epsilon}^{-1}\mathbf{K} + \mathbf{S}_{\mathbf{a}}^{-1}\right)^{-1}\mathbf{K}^{\mathrm{T}}\mathbf{S}_{\epsilon}^{-1} \\ &= \mathbf{S_a}\mathbf{K}^{\mathrm{T}}\left(\mathbf{K}\mathbf{S_a}\mathbf{K}^{\mathrm{T}} + \mathbf{S}_{\epsilon}\right)^{-1}. \end{aligned} \tag{4.26}$$

4.6 Non-Linear Optimal Estimation and NEMESIS

So far only linear solutions have been discussed, but unfortunately the physics of real atmospheres is much more complicated and for that reason a non-linear approach becomes necessary. The non-linear scheme described in this section is the one that is actually implemented in NEMESIS.

Sources of non-linearity include (Houghton et al., 1984):

a) Temperature dependence of the atmospheric transmittance,

b) Wavenumber dependence of the Planck function between spectral bands,

c) The dependence of transmittance on absorber concentration when sounding for composition,

d) Non-linear constraints.

Items *a)* and *b)* lead to relatively small non-linearities while the rest can be much larger (Houghton et al., 1984). If the problem is not too non-linear it is possible to find solutions iteratively (Rodgers, 2000).

As the case for temperature, *a)*, is nearly linear the elements of the Jacobian (the rate of change of spectral radiance with temperature), $\mathbf{K}$, are not strongly dependent on the temperature profile. After the Jacobian is calculated this allows the best-fit temperature profile to be found in a single step (Irwin, 2009).

When retrieving composition, aerosol or clouds the non-linearities tend to be much larger. This is because small changes in their quantities strongly affect the atmospheric transmission and hence the Jacobian. This becomes even more complicated if scattering is being taken into account. Consequently, when solving iteratively their retrieval is computationally expensive with the Jacobian having to be recalculated for every step in the worst cases (Irwin, 2009).

Starting with Eq. 4.1 and following the Bayesian formalism of §4.5, where the forward model is now a general function of the state, the measurement error is Gaussian and there is a prior estimate with a Gaussian error; the following modified cost function is arrived at:

$$-2\ln P(\mathbf{x}|\mathbf{y}) = (\mathbf{y}-\mathbf{F}(\mathbf{x}))^{\mathrm{T}}{\mathbf{S}_\epsilon}^{-1}(\mathbf{y}-\mathbf{F}(\mathbf{x})) + (\mathbf{x}-\mathbf{x_a})^{\mathrm{T}}{\mathbf{S_a}}^{-1}(\mathbf{x}-\mathbf{x_a}) + f(\mathbf{y}). \tag{4.27}$$

As for the linear case the optimal solution, $\widehat{\mathbf{x}}$, is found when $P(\mathbf{x}|\mathbf{y})$ is maximised, i.e. when the derivative of Eq. 4.27 is set to zero,

$$\frac{\partial(-2\ln P(\mathbf{x}|\mathbf{y}))}{\partial \mathbf{x}} = -\left(\frac{\partial \mathbf{F}(\mathbf{x})}{\partial \mathbf{x}}\right)^{\mathrm{T}} \mathbf{S}_\epsilon^{-\mathbf{1}}(\mathbf{y}-\mathbf{F}(\mathbf{x})) + \mathbf{S_a^{-1}}(\mathbf{x}-\mathbf{x_a}) = 0. \tag{4.28}$$

This can then be rewritten as

$$-\widehat{\mathbf{K}}^{\mathrm{T}}(\widehat{\mathbf{x}})\mathbf{S}_\epsilon^{-\mathbf{1}}(\mathbf{y}-\mathbf{F}(\widehat{\mathbf{x}})) + \mathbf{S_a^{-1}}(\widehat{\mathbf{x}}-\mathbf{x_a}) = 0, \tag{4.29}$$

where

$$\frac{\partial \mathbf{F}(\mathbf{x})}{\partial \mathbf{x}} = \mathbf{K}(\mathbf{x}). \tag{4.30}$$

This equation must be solved numerically, the difficulty involved depending on the non-linearity of the forward model (Rodgers, 2000). As mentioned earlier, if the problem is not too non-linear it can be solved iteratively via Newtonian Iteration. For the general vector equation $\mathbf{g}(\mathbf{x}) = \mathbf{0}$, the iteration of Newton's Method has the same form as the scalar version (Rodgers, 2000),

$$\mathbf{x_{n+1}} = \mathbf{x_n} + \left(\frac{\partial(\mathbf{g}(\mathbf{x_n}))}{\partial \mathbf{x}}\right)^{-1} \mathbf{g}(\mathbf{x_n}), \tag{4.31}$$

where the inverse is a matrix inverse. Taking the LHS of Eq. 4.29 as $\mathbf{g}$, the matrix becomes

$$\frac{\partial(\mathbf{g}(\mathbf{x_n}))}{\partial \mathbf{x}} = \mathbf{S_a^{-1}} + \mathbf{K}^{\mathrm{T}}\mathbf{S}_\epsilon^{-\mathbf{1}}\mathbf{K} - \frac{\partial \mathbf{K}^{\mathrm{T}}}{\partial \mathbf{x}}\mathbf{S}_\epsilon^{-\mathbf{1}}(\mathbf{y}-\mathbf{F}(\mathbf{x})). \tag{4.32}$$

where $\mathbf{g}$ is the derivative of the cost function. The second-order derivative of the cost function is then $\frac{\partial(\mathbf{g}(\mathbf{x_n}))}{\partial \mathbf{x}}$, it is called the 'Hessian'. It contains both the first-derivative of the forward model, the Jacobian, $\mathbf{K}$, and the second-derivative, $\frac{\partial \mathbf{K}^{\mathrm{T}}}{\partial \mathbf{x}}$, which is a complicated object. This is because it is a vector where its elements are matrices, which are then postmultiplied by the vector, $\mathbf{S}_\epsilon^{-\mathbf{1}}(\mathbf{y}-\mathbf{F}(\mathbf{x}))$ before the resulting vector of vectors is assembled into a matrix (Rodgers, 2000).

Thankfully, for the moderately non-linear case this term is negligible. Substituting Eqs 4.29 and 4.32 into Eq. 4.31, while omitting this term gives the Gauss-Newton Method resulting in the solution

$$\begin{aligned}
\mathbf{x_{n+1}} &= \mathbf{x_n} + \left(\mathbf{S_a^{-1}} + \mathbf{K_n^T S_\epsilon^{-1} K_n}\right)^{-1} \left[\mathbf{K_n^T S_\epsilon^{-1}}(\mathbf{y} - \mathbf{F}(\mathbf{x_n})) - \mathbf{S_a^{-1}}(\mathbf{x_n} - \mathbf{x_a})\right] \\
&= \mathbf{x_a} + \left(\mathbf{S_a^{-1}} + \mathbf{K_n^T S_\epsilon^{-1} K_n}\right)^{-1} \mathbf{K_n^T S_\epsilon^{-1}}[(\mathbf{y} - \mathbf{F}(\mathbf{x_n})) - \mathbf{K_n}(\mathbf{x_a} - \mathbf{x_n})] \\
&= \mathbf{x_a} + \mathbf{S_a K_n^T}\left(\mathbf{K_n S_a K_n^T} + \mathbf{S}_\epsilon\right)^{-1} [(\mathbf{y} - \mathbf{F}(\mathbf{x_n})) - \mathbf{K_n}(\mathbf{x_a} - \mathbf{x_n})] \\
&= \mathbf{G}\left(\mathbf{y} - \mathbf{F}(\mathbf{x_n})\right) - \mathbf{A}\left(\mathbf{x_a} - \mathbf{x_n}\right), \qquad (4.33)
\end{aligned}$$

where $\mathbf{K_n} = \mathbf{K}(\mathbf{x_n})$ and the total covariance, $\widehat{\mathbf{S}}$, is the same as given in Eq. 4.24. *A priori* constraint is enforced at every iteration of the retrieval, as can be seen by the presence of $\mathbf{x_a}$ in the equation above (Irwin, 2009). Unfortunately, this iterative scheme can become unstable, as the Jacobian (rate of change of radiance with state vector elements for all wavelengths in the spectrum) for the $\mathbf{n}$th iteration, $\mathbf{K_n}$, can change drastically between successive iterations (as mentioned earlier). To prevent the retrieval algorithm from becoming unstable (i.e. to limit the deviation from the previous best fit), a Levenberg-Marquardt type braking parameter is applied in NEMESIS (Irwin et al. 2004; 2008; Irwin, 2009). This uses the state vectors, $\mathbf{x_{n+1}}$ and $\mathbf{x_n}$, in conjunction with the cost function, ϕ, to calculate a modified state vector, $\mathbf{x'_{n+1}}$, to be used in the next iteration, and is given by

$$\mathbf{x'_{n+1}} = \mathbf{x_n} + \frac{\mathbf{x_{n+1}} - \mathbf{x_n}}{1 + \lambda}, \qquad (4.34)$$

with (c.f. Eq. 4.27)

$$\phi = \left(\mathbf{y} - \mathbf{F}(\mathbf{x_n})\right)^{\mathrm{T}} \mathbf{S}_\epsilon{}^{-1} \left(\mathbf{y} - \mathbf{F}(\mathbf{x_n})\right) + \left(\mathbf{x_n} - \mathbf{x_a}\right)^{\mathrm{T}} \mathbf{S_a}{}^{-1} \left(\mathbf{x_n} - \mathbf{x_a}\right), \qquad (4.35)$$

where λ is initially set to 1.0 and changed according to the change in the cost function, ϕ, at each stage of the iteration. If ϕ decreases then $\mathbf{x_n}$ is updated to $\mathbf{x'_{n+1}}$ and λ is multiplied by 0.3. If ϕ increases then $\mathbf{x_n}$ is left unchanged and λ is multiplied by a factor of 10. The decision to use 0.3 and 10 as the multipliers is subjective to an extent, but they must be not reciprocals of each other. This is to prevent the iterations oscillating back and forth, stuck in an endless loop. Additionally, it is also important that the smaller number (0.3) be greater than the reciprocal of the bigger number (10). This gives smooth smooth convergence by preventing λ from reducing

too quickly (Irwin, 2009).

The estimate, $\mathbf{x_n}$ (where the initial guess $\mathbf{x_0} = \mathbf{x_a}$), is used in the forward model to generate a new synthetic spectrum and Jacobian, $\mathbf{K_n}$. At each stage $\mathbf{G_n}$ and $\mathbf{A_n}$ are calculated and ϕ evaluated. The retrieval is deemed to have converged when the change in ϕ between successive iterations, $\Delta\phi$, is less than a user-chosen limit (default value of 0.1%). As the retrieval moves towards convergence $\lambda \to 0$ and the estimate becomes optimal (Irwin et al., 2008).

It should be noted that although for temperature, the elements of $\mathbf{x_n}$ are set to the actual temperature values in NEMESIS, for all other variables, such as composition, the elements of $\mathbf{x_n}$ are set to logarithmic values. This ensures that the modelled atmospheric profiles never become negative (Irwin et al., 2008).

4.6.1 Errors

There are many sources of error that need to to be taken into account to provide a complete error analysis for the final state state vector, $\hat{\mathbf{x}}$. These are as follows:

a) **Random measurement noise, ϵ:** This is the Noise Equivalent Spectral Radiance (NESR) of the MCS detectors and is a source of measurement error. It is assumed to be uncorrelated between measurements and is reduced by averaging of measurements (see Chapter 2).

b) **Incomplete physical description in radiative transfer calculations:** The absence of scattering and the assumption that the atmosphere is in local thermodynamic equilibrium (LTE), as non-LTE modelling is beyond the scope of this thesis. The assumption of non-scattering was tested in Chapter 3 where the assumption of non-LTE was also discussed.

c) **Inaccurate linedata:** Poor reproduction of spectral lineshapes due to omission of weak spectral lines from laboratory measurements, inaccurate intensities &c. Additionally, for this work, the use of the sub-Lorentzian CO_2 broadening approximations and the Voigt lineshape to describe broadening of spectral features. Linedata were discussed in Chapter 3.

d) **Correlated-*k*:** Accuracy of this approximation depends on how well the chosen number of Gaussian quadrature points sample the distribution of absorption coefficients. This requires a balance, too few and the k-distribution is not accurately represented, too many and

the approximation becomes computationally expensive. Consequently, this approximation has difficulties representing very small features and in this case line-by-line approaches should be employed instead to achieve high precision. This assumption was tested in Chapter 3.

e) **Instrument calibration:** Radiometric calibration, channel filter shapes, FOV effects (including those due to the extended FOV wings of the MCS detectors) all need to be taken into account. Details of this were given in Chapter 2.

f) **Instrument pointing errors:** Correct orbital geometry for an observation is crucial for accurate results. Incorrect latitudes, longitudes and viewing geometries will lead to the wrong radiances being simulated to fit the measurements. This becomes more problematic at high orbital inclinations when the focal plane footprints move quickly over the planet's surface. For MCS, limb pointing is accurate to within ±1 km (Kleinböhl et al., 2009).

g) **Line-of-sight effects:** For viewing geometries where the path has a significant vertical slant and particularly for limb observations, the path through the atmosphere is long (with a significant horizontal component) and so may sample regions with different temperature, composition &c., leading to horizontal averaging of results when a single atmospheric column is considered. For MCS limb views, the horizontal resolution can be defined as the width of the area of the horizontal weighting function corresponding to 50% emissivity (Kleinböhl et al., 2009). This is ∼150 km in the lower atmosphere (0–40 km) and ∼300 km in the upper atmosphere (>40 km).

h) **Cumulative errors:** When performing a two-stage retrieval (see §4.6.3), any errors in the first stage will be inherited by the second stage. Therefore the temperatures and aerosol opacities of the line-forming regions must be accurately modelled in the first stage to prevent the spurious modelling of gaseous absorption/emission features in the second stage.

Error *a)* is taken to be Gaussian distributed random noise while errors *b)–h)* are systematic. They are both represented in the measurement covariance matrix, $\mathbf{S}_\epsilon$ as

$$\mathbf{S}_\epsilon(i,i) = \epsilon_m(i)^2 + \epsilon_f(i)^2, \tag{4.36}$$

where the NESR component, *a)*, is represented by ϵ_m and the systematic errors, *b)–h)* are

represented by a forward modelling error, ϵ_f. Off-diagonal elements of the matrix are assumed to be zero as the errors are taken to be independent.

It is an unusual procedure in optimal estimation to add the systematic forward modelling errors to $\mathbf{S}_\epsilon$. This is because the method is developed based on the assumption that the measurement covariance matrix is just Gaussian distributed random noise (i.e. ϵ_m). Nevertheless, this addition of the forward modelling errors allows for the first order inclusion of their gross effect into the retrieval results (Irwin et al., 2008).

The assumed errors for the *a priori* state, $\mathbf{x_a}$, are given in the *a priori* covariance matrix. For temperature, the diagonal elements are set to the square of the assumed error, $\epsilon_\mathbf{a}$, whereas for all other variables the error is fractional as the values of elements of $\mathbf{x_a}$ are logarithmic (as discussed earlier) and given as

$$\mathbf{S_a}(i,i) = \left(\frac{\epsilon_\mathbf{a}(i)}{\mathbf{x_a}(i)}\right)^2. \tag{4.37}$$

When retrieving vertical continuous profiles, off-diagonal elements (representing cross-correlation) decrease away from the diagonal according to the 'correlation length', l_c, the length scale in units of $\ln p$ over which the inter-level correlation drops off by $\frac{1}{e}$. They are given by Rodgers (2000) as

$$\mathbf{S_a}(i,j) = (\mathbf{S_a}(i,i)\mathbf{S_a}(j,j))^{\frac{1}{2}} \exp\left(-\frac{\left|\ln\left(\frac{p(i)}{p(j)}\right)\right|}{l_c}\right), \tag{4.38}$$

where $p(i)$ and $p(j)$ are the pressures at the i-th and j-th atmospheric levels. For this thesis values in the range of 1.0–2.0 have been used (more details in the relevant chapters). It is set to match the vertical resolution of an MCS observation.

The contribution of the measurement error covariance matrix to the final error in the retrieved state vector, $\widehat{\mathbf{x}}$, is given as

$$\mathbf{S_m} = \mathbf{G}\mathbf{S}_\epsilon\mathbf{G}^\mathrm{T}. \tag{4.39}$$

Similarly, vertical smoothing could introduce bias towards the *a priori* models causing unnecessary removal of real vertical structures, so the smoothing error is given as

$$\mathbf{S_n} = (\mathbf{A} - \mathbf{I})\,\mathbf{S_a}\,(\mathbf{A} - \mathbf{I})^\mathrm{T} \tag{4.40}$$

where $\mathbf{I}$ is the identity matrix. The total error is then given as formal retrieval error covariance matrix:

$$\mathbf{S_t} = \mathbf{S_m} + \mathbf{S_n} = \widehat{\mathbf{S}} = \left(\mathbf{K}^\mathrm{T}\mathbf{S}_\epsilon^{-\mathbf{1}}\mathbf{K} + \mathbf{S_a^{-1}}\right)^{-1}. \tag{4.41}$$

Unless otherwise stated, the retrieval errors quoted in this thesis are derived directly from the diagonal elements of this matrix. These errors represent the range of values in the final state vector for which the forward modelled spectrum will fit the measured spectrum within the error.

4.6.2 Tuning

Optimal estimation retrievals must be tuned to provide a suitable solution. Weighting too strongly towards the measurements (by having small measurement errors and a low constraint to the *a priori*, $\mathbf{K_n S_a K_n^T} > \mathbf{S}_\epsilon$) lets the solution tend to be exact. Although this gives apparently small retrieval errors (Eq. 4.41), the resulting unrealistic profile will have high frequency perturbations (i.e. a 'wiggly' line). Conversely, weighting too strongly to the *a priori* constraint gives a retrieval that has no information from the measurements themselves ($\mathbf{K_n S_a K_n^T} < \mathbf{S}_\epsilon$). This means that retrieved profile ends up the same as the *a priori* profile. Therefore retrievals are tuned, with appropriate smoothing, to provide the most reasonable estimates by looking at the ratio of the two weightings, $\mathbf{K_n S_a K_n^T}/\mathbf{S}_\epsilon$. Therefore there is a trade-off between unrealistic high frequency perturbations and vertical smoothing to get a suitable inversion (Rodgers, 2000; Irwin et al., 2008).

4.6.3 Functional Derivatives, Vertical Sensitivity and Multi-Stage Retrievals

The Jacobian, $\mathbf{K}$, introduced previously is the matrix of functional derivatives. Each element gives a partial derivative of the modelled radiance with respect to an element of the state vector. A functional derivative can be more generally described as $\frac{\partial L_\nu}{\partial x_i}$ where L_ν is the radiance at wavenumber ν and x_i denotes some model parameter. For the case of a continuous profile x_i can be taken to be some atmospheric variable (i.e. temperature, composition &c.) defined at a particular altitude, h_i, and thus the functional derivative gives the sensitivity of the radiance, L_ν, to the variable, x_i, at altitude h_i. In other words the Jacobian gives an idea of the information content of the measured spectrum*.

It is also normally the case for a given path through the atmosphere (limb or nadir) that corresponding functional derivatives will not be δ-function shaped and thus will have some finite width (indicating the cross-correlation defined in Eq. 4.38). This means that radiance, L_ν, is also sensitive to the same atmospheric variable at a neighbouring altitudes.

*It is important to note that except for the 'Exact Solution' case, the Jacobian is defined as the derivative of the forward model, $\mathbf{F}(\mathbf{x_n})$, not the measured spectrum, $\mathbf{y}$, thus it actually gives the sensitivity of the forward model to the assumed state vector, $\mathbf{x_n}$. However, when the observed spectra and fitted spectra match it can be assumed that the Jacobian is representative of the sensitivity to $\mathbf{y}$.

Table 4.1 | MCS Spectral Channel Band Passes and Measurement Functions⁂.

Credit: Reproduced from McCleese et al. (2007), 'Mars Climate Sounder: An investigation of thermal and water vapor structure, dust and condensate distributions in the atmosphere, and energy balance of the polar regions'. Journal of Geophysical Research (Planets), 112, E05S06. Copyright 2007 by the American Geophysical Union (0148-0227/07/2006JE002790$09.00).

Telescope/ Channel Number	Band Pass, cm^{-1}	Band Centre, µm	Measurement Function
A1	595–615	16.5	temperature 20 to 40 km
A2	615–645	15.9	temperature 40 to 80 km and pressure
A3	635–665	15.4	temperature 40 to 80 km and pressure
A4	820–870	11.8	dust and condensate (D&C) extinction 0 to 80 km
A5	400–500	22.2	temperature 0 to 20 km, D&C extinction 0 to 80 km
A6	3300–33000	1.65	polar radiative balance
B1	290–340	31.7	temperature 0 to 20 km and D&C extinction 0 to 80 km
B2	220–260	41.7	water vapour 0 to 40 km and D&C extinction 0 to 80 km
B3	230–245	42.1	water vapour 0 to 40 km and D&C extinction 0 to 80 km

⁂D is dust; C is condensates of H_2O and CO_2.

Additional complications can arise from the fact that L_ν can also depend on a multiple atmospheric variables. For instance, imagine modelling the atmospheric radiance L_ν to match observations from space, for a spectral region that is sensitive to both an absorbing aerosol and temperature. If the modelled radiance is too low this could be because the simulated amount of aerosol is too high (leading to the functional derivatives moving higher up in the atmosphere) or because the simulated temperature profile is too low at the altitude where the functional derivative peaks.

Without due care, all of these complications can lead to degeneracy (i.e. multiple state vectors giving the same model spectrum that fits the observation). To resolve the first problem the observation must be tailored such that the functional derivatives are not too wide with distinct peaks and decent separation in order to cover the whole of the desired altitude range. To solve the second problem requires the selection of spectral regions that are uniquely sensitive to the variable being investigated.

For MCS retrievals a combination of limb and nadir geometries is used (see Chapter 2). Plots of the functional derivatives of MCS channels (for the vertical continuous profile variables considered in this thesis) are given in Figs 4.1 & 4.2 alongside a table of altitude sensitivities in Tbl. 4.1). The plotted functional derivatives are for a retrieval from simulated radiance data calculated using the Mars Climate Database climatology (see figure captions for details).

The main channels for temperature on MCS are A1, A2 and A3. Examination of Fig. 4.1 and Tbl. 4.1 shows how between them their functional derivatives cover the lower, middle and

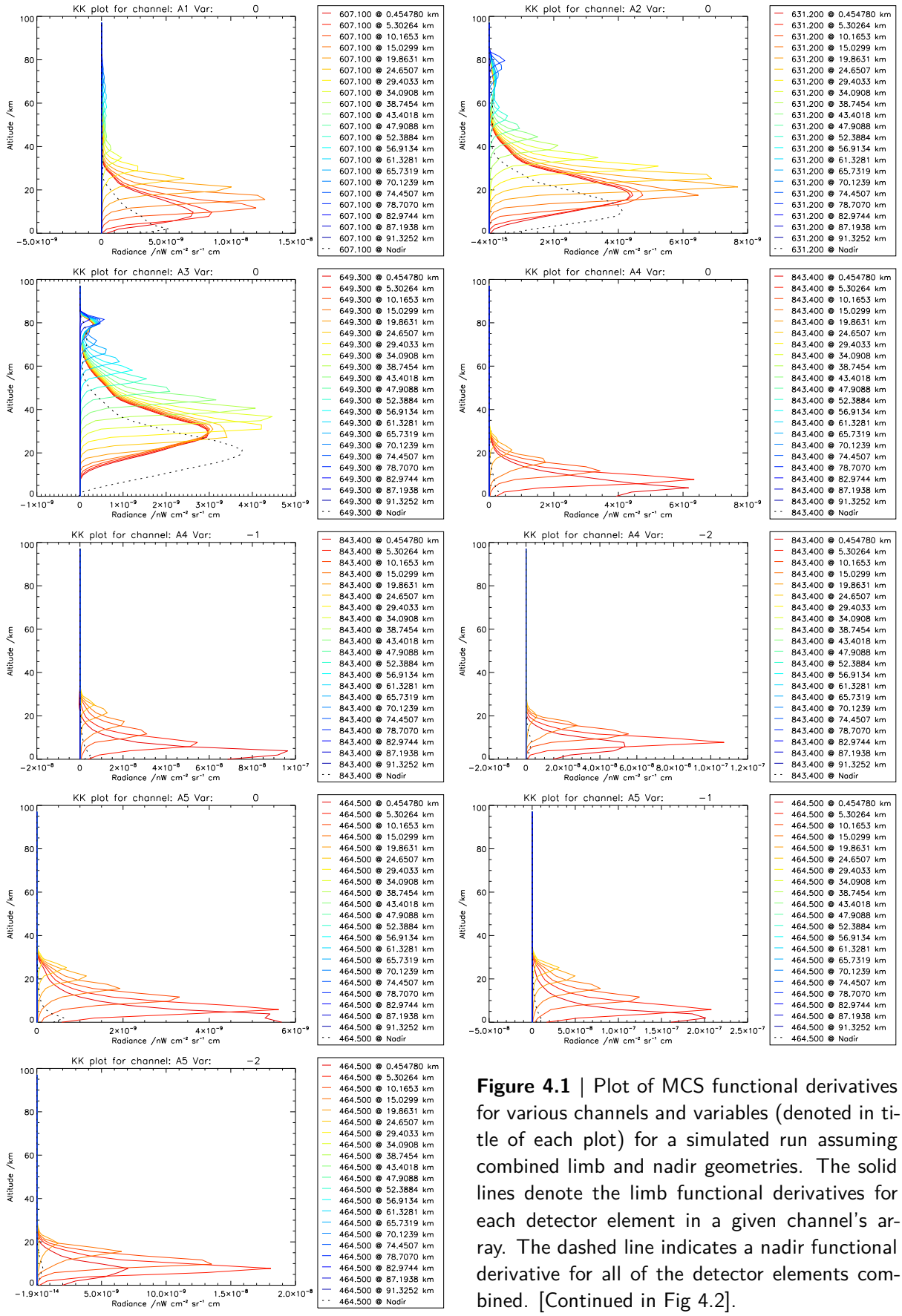


Figure 4.1 | Plot of MCS functional derivatives for various channels and variables (denoted in title of each plot) for a simulated run assuming combined limb and nadir geometries. The solid lines denote the limb functional derivatives for each detector element in a given channel's array. The dashed line indicates a nadir functional derivative for all of the detector elements combined. [Continued in Fig 4.2].

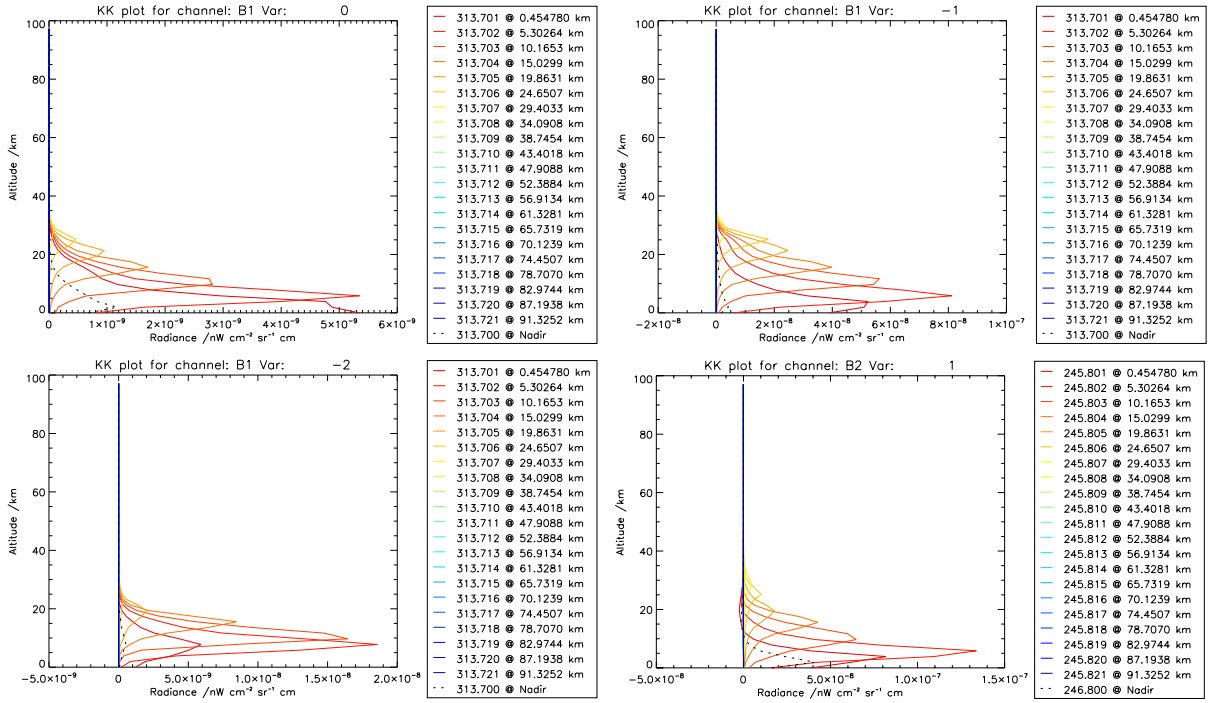


Figure 4.2 | [Continued from Fig. 4.1]. Dust distribution is roughly constant to a height of about 30 km with a column dust opacity at A5 of $\tau_{dust} = 0.01$. For water ice there are two layers centred at around 10 km and 30 km with a column opacity at A4 of $\tau_{ice} = 0.01$. (From MCD MY24 scenario:L_s=114.25°, Lat=69.953°N, Lon=79.952°E). Aerosols are treated as absorption-only with no scattering (see §3.3.1). Key for variables: (0) Temperature, (-1) Dust, (-2) Water Ice, (1) Water Vapour.

upper atmosphere respectively. These channels are clustered around one side of the large CO_2 band at 667 cm^{-1} in the Martian atmospheric spectrum (see Fig. 3.1), with A1 being near the edge of the band (where the atmosphere is fairly clear) and A3 being at the centre (where the atmosphere is optically thick and so 'seeing' much higher in the atmosphere). The CO_2 is well mixed up to to the top of the atmosphere and other variables have little effect in this spectral region making these channels the ideal choice for a temperature/pressure profile retrieval.

There is additional sensitivity to temperature near the surface in A4, A5 and B1, though their sensitivities are dominated by aerosols (dust and water ice) which have functional derivatives that are at least an order of magnitude larger. This large difference means there is less sensitivity to temperature below about 10 km and so at these very low altitudes the retrieval relaxes back to *a priori* profile.

For the aerosols the main channels used are A4 and A5 for water ice and dust respectively. The functional derivatives indicate that aerosol can be retrieved with confidence in the 10–30 km altitude range, as this is where there is vertical overlap with the temperature information from A1–A3. Unfortunately, for this retrieval the modelled water ice cloud at 30 km remained

undetected as it lies above the sensitivity range.

For the variables discussed thus far (temperature and aerosols) there is enough 'unique' (i.e. not degenerate) sensitivity for simultaneous retrieval. For water vapour there are complications as B2 has significant sensitivity to dust and water ice as well as water vapour (see Tbl. 4.1 and Chapter 2) and so the implementation of a multi-stage retrieval becomes necessary to prevent spurious results. This is the methodology that is implemented in this thesis with the use of NEMESIS.

In the first stage, profiles for temperature and aerosol are retrieved. In the second stage, a profile for water vapour is retrieved. The NEMESIS software loads the retrieval products for the first stage (for temperature and aerosol) and uses them to set up the model atmosphere for the second stage (i.e. they are fixed and can no longer vary). The effects of the retrieval errors of the first stage on the retrieval of the water vapour are calculated as an extra effective forward modelling error, which is added to $\mathbf{S}_\epsilon$ (Irwin et al., 2008). More details on the implementation are given in Chapters 5 and 8.

4.7 L2 Retrievals

In this section we briefly outline the retrieval procedure used by Kleinböhl et al. (2009) to obtain the MCS Level 2 (L2) Retrievals dataset and then compare it to the optimal estimation method used for our retrievals. Kleinböhl et al. (2009) used a modified version of the Chahine retrieval algorithm (Chahine, 1970; 1972). It is an iterative general relaxation method to invert the radiative transfer equation to retrieve the atmospheric state, $\mathbf{x}$.

4.7.1 L2 Modified Chahine Method

Remembering the basic forward model equation, Eq. 4.1, an initial run of the forward model with a first guess of the state vector, $\mathbf{x}_0$, is used to generate a set calculated radiances $\mathbf{F}(\mathbf{x}_0)$, where the zero subscript indicates the initial iteration. These calculated radiances are compared to the measured radiances, $\mathbf{y}$, to generate the scale factor vector, $\mathbf{s}_0$ and calculate the radiance residuals, $\Delta\mathbf{y}_0 = \mathbf{y} - \mathbf{F}(\mathbf{x}_0)$. Multiplying the state vector by the scale factor, gives a new perturbed state vector, $\mathbf{x}_1$ ready for the next iteration. The perturbed state vector is then used to calculate a new set of radiances, $\mathbf{F}(\mathbf{x}_1)$ which should be closer to the measurements than the initial run (i.e. smaller residuals, $\Delta\mathbf{y}_1 < \Delta\mathbf{y}_0$). These new radiances are then used to generate

a new scale factor vector for perturbing the state, ready for the next run through. This process repeats iteratively according to

$$\mathbf{x}_{n+1} = \mathbf{s}_n \mathbf{x}_n \tag{4.42}$$

$$\Delta \mathbf{y}_n = \mathbf{y} - \mathbf{F}(\mathbf{x}_n), \tag{4.43}$$

where n is the iteration number, attempting to minimise the residuals, $\Delta \mathbf{y}_n$, with successive iterations. A simple example of the scale factor vector would be

$$\mathbf{s}_n = \frac{\mathbf{y}_{\text{meas}}}{\mathbf{y}_{\text{calc}}} = \frac{\mathbf{y}}{\mathbf{F}(\mathbf{x}_n)}. \tag{4.44}$$

This gives the solution for an absorber in an optically thin isothermal atmosphere where radiance is approximately proportional to absorber amount (Kleinböhl et al., 2009). More complex definitions are often needed, depending on the parameter being retrieved. These are beyond the scope of this brief method description and are detailed in Kleinböhl et al. (2009).

In the original Chahine method, the length of $\mathbf{y}$ (measurements) and $\mathbf{x}$ (state) are chosen to be equal, with i elements each. The altitudes of individual elements of the state vector, x_i are chosen to be at or near the peaks of the weighting functions, i.e. level of maximum response to radiance element, y_i. For the modified L2 method, it was deemed desirable to have a fixed altitude grid instead, giving a common basis for elements of $\mathbf{x}$. Assuming $\mathbf{x}$ has j elements, the information in the i measurements, $\mathbf{y}$, has to be distributed over the j elements. This can be done with the weighting functions, $K_{j,i}$, which describe the sensitivity of a measurement, y_i to the the individual x_j. These can then be use to generate the scale factor vector, $\mathbf{s}'$, with j elements (each containing a weighted average)

$$s'_j = \left(\sum_i s_i \cdot K_{j,i} \right) \Bigg/ \sum_i K_{j,i} \tag{4.45}$$

The elements of $\mathbf{s}'$ can then be used to update the j elements of the state vector for the iterative procedure (c.f. Eq. 4.42)

$$x_j^{(n+1)} = s_j'^{(n)} x_j^{(n)}. \tag{4.46}$$

The iteration proceeds until either satisfying convergence criteria or reaching a maximum num-

ber of iterations. The L2 method retrieves several different quantities (temperature, pressure, aerosol) which are likely to interact. Consequently, they used a nested loop procedure where they iterated by one step in temperature/pressure, followed by an inner loop iterating substeps in aerosol, before making the next iteration step in temperature/pressure.

4.7.2 Comparison of L2 Method with Optimal Estimation

The NEMESIS optimal estimation and L2 retrieval methodologies have a number of significant differences. Optimal estimation can be described as a constrained matrix method, while the L2/Chahine method is an unconstrained general relaxation method (Puliafito et al., 1995). The constraint in optimal estimation comes from the use of the *a priori* which provides additional information to the retrieval, not available to the the L2/Chahine method (see §4.5). The *a priori* also provides smoothing which helps remove unrealistic oscillations introduced by over-fitting to the noise. The L2/Chahine method does not have this and instead has to manually apply smoothing to get rid of ripples caused by the weighting functions and remove oscillations.

In addition, through the use of the covariance matrices (see §4.5 & 4.6.1), optimal estimation provides an intrinsic error analysis that takes account of errors from various sources: *a priori* profile errors, forward modelling errors, smoothing errors and measurement errors (noise). Including these contributions it is able to provide a quantitative total retrieval error. The L2/Chahine method cannot do this and has to resort to either: a) manually perturbing atmospheric quantities level by level in the state vector and running a radiative transfer calculation for each to see the impact, which increases computational expense or b) making approximations of this perturbation process to save time at the expense of error accuracy.

As a result of all the above, optimal estimation is likely to offer a distinct advantage in regions of the atmosphere with low information content. In these regions the L2/Chahine method is prone to over-fit to the measurements, due to the lack of additional constraint and smoothing. In contrast, the optimal estimation retrieved profile will be smoother and gradually relax back towards the *a priori*, resulting in a lower total retrieval error and potentially extending the 'useful' altitude range of the retrieved profile. Evidence of this can be seen in the results of Puliafito et al. (1995) who compared five retrieval algorithms including optimal estimation and the Chahine method using measurements and simulations of the Millimetre-Wave Atmospheric Sounder (MAS) flown on spacelab shuttle missions. Their study also indicated that both methods gave similar answers in regions of the atmosphere with high information content.

5

Sensitivity Studies I: Radiance Effects

Measurements of the spectral response of the B2 and B3 filters discussed in Chapter 2 have shown that they are wider than expected and this is likely to have an impact on their ability to retrieve water vapour. This chapter presents results of sensitivity studies undertaken to assess the impact of this spectral broadening on B2 and B3 radiances. The first part of the chapter presents results from simulation testing of the sensitivity of the B3-B2 radiance ratio to water vapour, starting with detector radiance ratio simulations in §5.1, scatter plots of observed B3 vs B2 radiances in §5.2 and B3-B2 scatter plots with simulated radiances testing the effects of atmospheric parameters on the ratio performance in §5.3. The second part of the chapter investigates the sensitivity to water vapour when only using B2 radiances, starting with radiance residuals due to water vapour from observations in §5.4 and concluding with simulating the effect on B2 radiances of varying aerosol size distributions in §5.5.

5.1 Ratio Sensitivity Simulations in Limb Viewing

A key quantity that can be used to assess MCS's ability to detect water is the B3/B2 radiance ratio. If MCS were behaving ideally the B3/B2 ratio should only change when water vapour is present, as any other effect, especially dust ought to be divided out when calculating the ratio. MCS should have a similar sensitivity to dust in these channels, but different sensitivities to water vapour (see §2.3.1 for more details). However, if the channels have no differential

sensitivity to water, then the ratio should just remain a constant, assuming that the channels have a similar sensitivity to other atmospheric parameters such as dust and temperature.

In order to test the sensitivity of the MCS B3/B2 ratio a number of radiative transfer simulations of the B3 and B2 channels for limb viewing were performed using NEMESIS with a model atmosphere from the MCD (northern hemisphere summer observation at 51°N). In these simulations the water vapour column abundance of the atmosphere was varied over the range 1–100 pr. µm, while all other parameters where held fixed. This allows the isolation of the effect of water vapour on B3/B2 radiance ratio.

Simulations were performed for two cases: an ideal case where the filter spectral response of the channels is as originally specified (i.e. without broadening) and a case where the spectral response is as measured by McCleese et al. (2007). A comparison of the filter spectral response for both cases can be seen in Fig. 2.10.

5.1.1 Simulation and Data Processing

For this simulation the model atmosphere was constructed using data from the MCD (MY24 scenario) for temperature, pressure, CO_2 and N_2 and water vapour. The dust profile was assumed to be uniformly mixed to the top of the atmosphere with a column optical depth of $\tau = 0.045$ at A5 (0.134 at 1075 cm^{-1}, typical NH Summer Value; Montabone et al. 2015). The dust distribution parameters are as defined in Tbl. 3.1, with dust assumed to have non-scattering (absorption-only) behaviour. These assumptions were made to optimize the speed of simulation and simplify the problem. The model atmosphere used is the T_1 + D_1 model, one of those used in the scattering tests in §3.3.4 as shown in Fig. 3.12), where T_1 denotes the NH summer mid-latitude temperature profile and D_1 the summer dust profile used.

The base water vapour profile from the MCD has a 29 pr. µm column abundance. It is uniform up to the condensation height and then drops off (see water vapour panel in Fig. 3.12). For the simulation, NEMESIS was run for a number of times with the initial water vapour profile being scaled to different column abundances given in Tbl. 5.1. The water vapour column abundance of the atmosphere was varied in the range of 1–100 pr. µm for a representative range of values/conditions on Mars. By holding all other variables constant and only varying the atmospheric water vapour content, it was possible to isolate of the effect of water on B3 and B2 detector radiances without any other processes competing, which may mask water features or produce other features that could have confused analysis.

Table 5.1 | Water Vapour Abundances used with NEMESIS

Water Column Abundance (pr. µm)	Water VMR at 8 km (ppmv)
1	14
5	68
10	135
20	270
25	338
29	392
40	540
60	811
80	1080
100	1351

The simulation was performed for two cases, all at a limb-viewing boresight height of 8 km above the surface (near the peak of the water vapour profile) with water vapour abundances being varied as described above:

- *Ideal Case* – NEMESIS was used to generate synthetic radiances for the ideal filter profiles. The ideal filter profiles were constructed by using measurement test data provided by Cardiff University (the manufacturer of the meshes). This data included spectral bandpass data for the individual mesh layers of the B-filters. Individual mesh layers all met specification (i.e. with no broadening observed). These were combined to produce the ideal filter response profile, which is narrower than that observed in MCS (see §2.3.1). It is important to note that these filter (spectral response) profiles are for a detector-averaged ideal case and do not take into account the spectral responses for individual detectors. These simulations also did not include MCS FOV response and are for a pencil-beam FOV. Synthetic radiances were generated for the water vapour abundances in Tbl. 5.1. The output synthetic radiances for the B3 and B2 channels were ratioed and a plot of the results generated. This plot can then be used as a reference benchmark and demonstrates how the ratio would be seen to change if MCS worked ideally.

- *Individual Detectors Case* – NEMESIS was used to generate synthetic radiances for the measured filter profiles for each individual detector (including the MCS detector FOV response). These are the filter profiles as measured by McCleese et al. (2007). The simulated radiances were then used to calculate B3/B2 ratio for individual detector pairings. Simulating the full detector arrays for B2 and B3 with their individual filter spectral responses

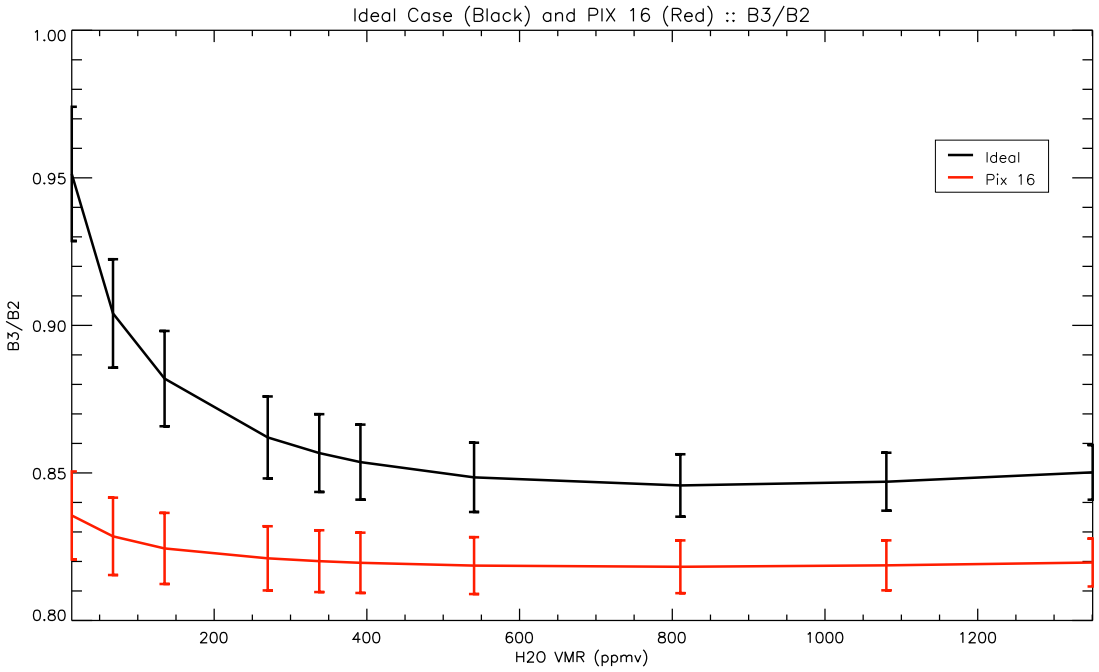


Figure 5.1 | Plot of B3/B2 ratio versus water VMR at 8 km for the *Ideal* case (black line) and Pix 16 (red line) from the *Individual Detectors* case (that is the sixteenth detector of the MCS array). Error bars indicate the error in the ratio due to detector noise.

enabled us to see whether all the detectors were equally affected by the broadening process. This would allow us to identify if there any individual detectors that are not too badly affected, which could then be used for real analysis of the Martian atmospheric water abundance. All detectors were set to limb-viewing at a boresight height of 8 km. This was done to simplify analysis and maximize the chance of finding a B3/B2 detector pair sensitive to water (as there is more water in the lower atmosphere, see Chapter 1). If it was found that any single detector pair worked it could be slewed manually through all tangent heights in the atmosphere.

5.1.2 Results and Discussion

The results of the simulations are shown in Fig. 5.1. For the *Ideal* case it can be seen that a large change in the B3/B2 ratio is readily apparent over the range of water abundances tested. The change of ∼9% is significantly larger than the detector ratio noise error bars, which vary from ∼2% at low abundances down to ∼1%. These results show how, when operating ideally MCS is able to use the ratio to discern the water vapour amount and can be used as a benchmark against which to test the real performance of the instrument.

For the *Individual Detectors* case we can see a ratio curve for sixteenth detector of MCS,

this curve is representative of the results for the remaining detectors as they are all very similar. The curve is much flatter indicating reduced performance against the *Ideal* case, a total drop of only ∼1.5%. This is much smaller than the ratio noise error which varies from ∼1.5–1% showing that the ratio change would be unable to detect the water signal above the noise. This supports what was stated by McCleese et al. (2007), that the broadening of the B3 filter is a problem that seriously impairs MCS's ability to detect water.

Many of the assumptions that were made for this simulation are likely to have improved, rather than worsened the result for the *Individual Detectors* case. As dust would normally be confined to a layer/s in the lower atmosphere rather than uniformly mixed, the concentration of dust seen by the limb-path of the simulation would have been higher in order to maintain the same column optical depth. The lack of scattering would also have helped as it meant there is lower radiance contribution from dust.

5.2 B3/B2 Scatter Plots of Observed & Simulated Radiances

Following on from the ratio tests above we continue to investigate the relationship between the B3 and B2 radiances with scatter plots of observed and simulated radiances. In this test the limb radiances of each channel for a given detector (i.e. boresight altitude) are plotted against each other. In the ideal scenario, for a given pair of B3-B2 radiances at a particular boresight we would expect to see more radiance in the B2 channel (wider FWHM see §2.3.1) than B3 when water is present. Consequently, when plotting all limb radiances on a B3 vs B2 scatter plot one would expect to get a straight line through the origin when there is no water present, i.e. $\mathrm{RAD}_{\mathrm{B3}}[d] = \mathrm{RAD}_{\mathrm{B2}}[d]$ (where d corresponds to given detector/height), giving a gradient of unity. When water is present there would be additional radiance in B2 due to emission, i.e. $\mathrm{RAD}_{\mathrm{B3}}[d] < \mathrm{RAD}_{\mathrm{B2}}[d]$, resulting in 'branches' (or scatter) of varying gradients less than one between the line and the B2 axis. If the B3-B2 channel pairing has reduced water sensitivity we would expect less scatter towards the B2 axis with radiances clustering towards the 1:1 ($\mathrm{RAD}_{\mathrm{B3}}[d] = \mathrm{RAD}_{\mathrm{B2}}[d]$) line. In order to compare an ideal scenario with the actual state of MCS, the simulation was performed using B3/B2 filter profiles as they should have been (i.e. without broadening) had they met their intended specification.

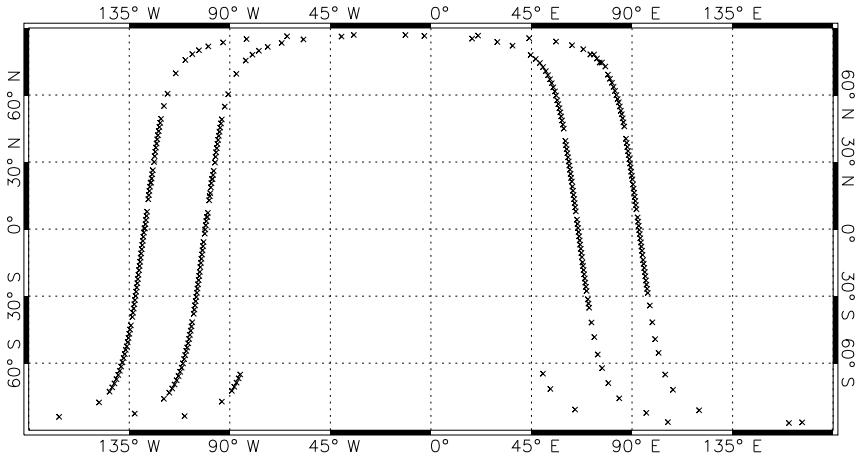


Figure 5.2 | Plot of B3/B2 observation/simulation locations (04–08h UT 1 October 2006, L_s=115°).

5.2.1 Data, Processing and Simulation

MCS limb observations used came from a 4 h (04–08h UT) observation block, taken on the 1 October 2006, during northern hemisphere summer (L_s=115°) at local surface times of 03h and 15h. This data was taken before MCS suffered its elevation slew impairment (see §2.3.3). A map showing the observation locations is given in Fig. 5.2. For the simulated B3-B2 detector radiances, the NEMESIS software was used for radiative transfer modelling with aerosol scattering. This was done with the same observation geometries/times as for the MCS observations, in conjunction with model atmospheres generated using L2 data and water profiles from the MCD as outlined in §3.4. Aerosol parameters for dust and ice are as given in §3.3.1 and scattering is as described in §3.3.4. The L2 data used contains retrievals performed by Kleinböhl et al. (2009) for the observed radiances used in this test. Limb radiances were generated for all 21 detectors of the B2 and B3 channels (with MCS detector FOVs). The simulation was done using idealised versions of the B3/B2 filter spectral response (those used for the previous test, the dotted profiles from Fig. 2.10) to provide a benchmark to assess MCS water vapour sensitivity.

5.2.2 Results and Discussion

Scatter plots of B3 radiances versus B2 radiance for the MCS limb observations and simulation are given in Fig. 5.3. The top plot (a) is for the observed radiances and the bottom plot (b) is for the simulated radiances with ideal filter profiles. Each point is colour coded according to which detector it corresponds to. This is indicated by the legend where 'PIX01' is the lowest detector in the array with limb boresight altitudes in the range of -10–0 km and 'PIX21' is the

highest corresponding to 80–90 km. The black diagonal line running through the origin is the 1:1 reference line indicating where $\mathrm{RAD}_{\mathrm{B3}}[d] = \mathrm{RAD}_{\mathrm{B2}}[d]$.

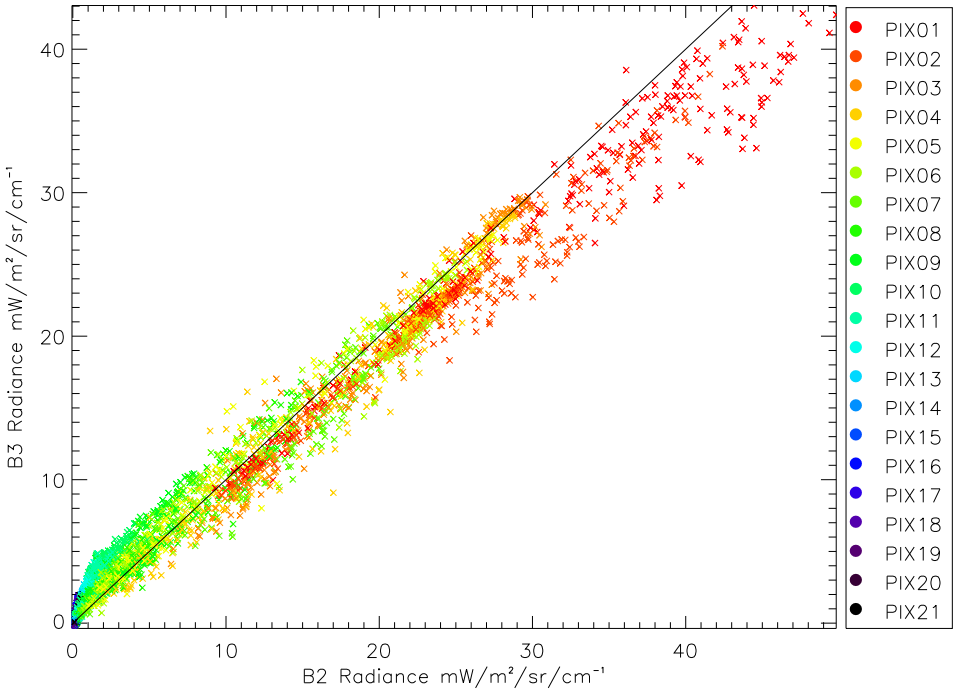
In both plots we see that the highest radiances correspond to the lowest detectors, i.e. lower heights in the atmosphere where more radiance is present. In addition, this area is where the scatter towards the B2 axis is broadest, corresponding to the greater amounts of water vapour in the lower atmosphere. Looking at the lower radiances, less scatter is seen with points closer to the 1:1 reference line corresponding to smaller radiance difference between the channels. The lower radiances correspond to the higher detectors.

There are also two significant differences between the plots. Firstly, the amount of scatter towards the B2 axis is consistently broader in the simulated results, showing reduced sensitivity to water vapour for the B3:B2 radiance ratio in the observed radiances case. This is especially evident in the top right of the plots for the highest radiances where we see a ≈25% reduction in the width of the scatter (i.e. distance of points from 1:1 line). Secondly, in the observed radiances case there are a large number of radiances above the 1:1 reference line. This is unexpected as it means $\mathrm{RAD}_{\mathrm{B3}}[d] > \mathrm{RAD}_{\mathrm{B2}}[d]$. From the colour coding we can see that the effect is biggest in PIX05 (20–30 km) upwards to PIX12 (40–50 km) for radiances below 10 $\mathrm{mW/m^2/sr/cm^{-1}}$. The affect is likely due a combination of the greater B3 detector NESR (∼2 $\mathrm{mW/m^2/sr/cm^{-1}}$ for B3 compared to ∼0.05 $\mathrm{mW/m^2/sr/cm^{-1}}$ for B2) and the extended FOV wing response discussed in §2.3.2 indicating that the B3 channel is 'seeing' radiances from lower levels of the atmosphere. If the B3 FOV extends further than the B2 one for the same detector/height this could give a B3 radiance greater than B2.

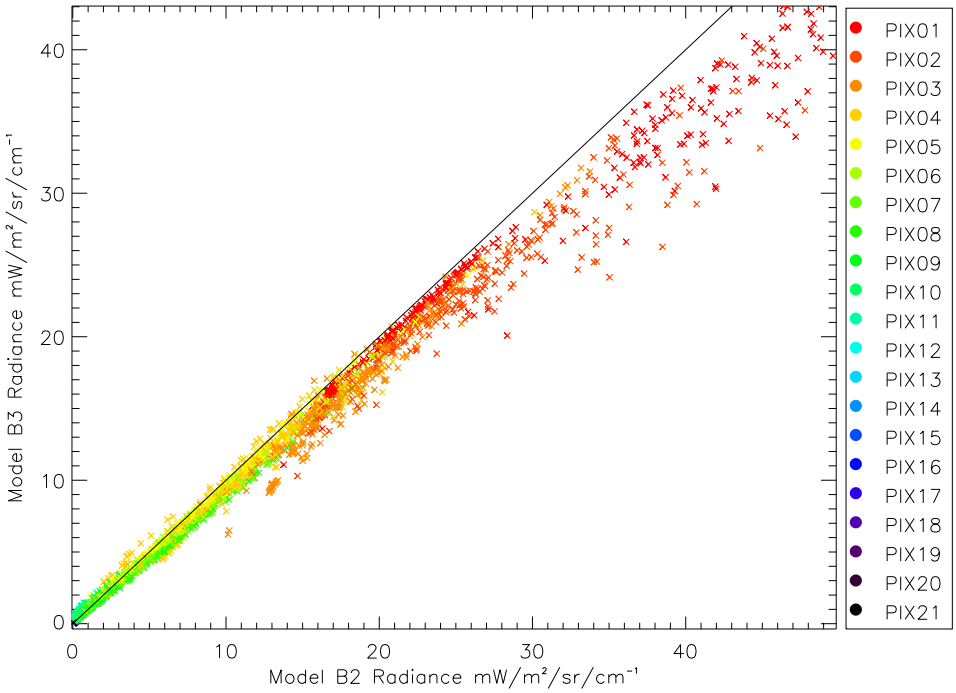
Even though a reduced branching effect is seen in the observed radiances plot with scatter towards the B2 axis, this is not a guarantee of water vapour sensitivity, especially in light of the results from detector ratio testing in §5.1. It could be the case that another atmospheric phenomenon could be responsible, such as temperature or aerosol.

5.3 B3/B2 Scatter Sensitivity Simulations

So far in this chapter the focus of investigating the B3/B2 ratio has been with regards to water vapour alone. To further understand the impact of the filter spectral broadening, the effect of other atmospheric parameters, dust and temperature, on the ratio needs to be studied. If B2 and B3 have significant sensitivity to either or both of these parameters, additional work will



(a) B3/B2 Scatter Plot for Limb Radiances



(b) B3/B2 Scatter Plot for Simulated Limb Radiances

Figure 5.3 | **(a)** Scatter plot of limb B3/B2 radiances from one 4 h MCS observation data block (L_s=115°). Points are coloured by pixel (see legend) where 'PIX01' corresponds to boresight altitudes of -10–0 km and 'PIX21' to about 80–90 km. The black line is the 1:1 reference line where $\mathrm{RAD}_{\mathrm{B3}}[d] = \mathrm{RAD}_{\mathrm{B2}}[d]$. **(b)** Simulated B3/B2 radiances with ideal filter profiles using the corresponding MCS-L2 retrievals (for the above observations) for model atmosphere.

need to be done in the retrievals to disentangle their effects on the measured radiances from those of water vapour.

NEMESIS was used to perform radiative transfer simulations of the B3 and B2 radiances for limb-viewing, using the measured spectral responses of the channels. This was done for a sequence of three series where water vapour, temperature and dust were independently varied. For the water and dust simulation series, a northern hemisphere summer (L_s=114°) equatorial model atmosphere was used from the MCD. For the temperature series, MCD profiles were used from five different latitudes covering the range, 80°S–80°N. The results of each series were then used to produce B3-B2 scatter plots in the same way as §5.2. Searching the resulting B3/B2 scatter plots for 'branches' towards the B2 axis would show the impact of each of the parameters on the ratio and whether it is uniquely changed by water vapour abundance or not.

5.3.1 Simulation Procedure

The model atmospheres were constructed using data from the MCD (MY24 scenario) for temperature, pressure, CO_2, N_2 and water vapour. The base model water, temperature and dust profiles are shown in Fig. 5.4 indicated by the blue lines. The base water vapour profile from the MCD has an 11 pr. µm column abundance. For the water series this profile is scaled, the scale factors with the resulting column abundance and maximum volume mixing ratios (VMR) are given in Tbl. 5.4 (base profile has scale factor 1.0). The other profiles used for the temperature series are also shown in the figure, indicated by the other coloured lines with an identifier in the legend. The identifier is used in Tbl. 5.3 and shows the respective locations and surface temperatures (base profile is T_2). The base dust profile was assumed to be uniformly mixed to the top of the atmosphere with a column optical depth of τ_{1075}=0.1 at 1075 cm^{-1} (τ_{A5}=0.034 at A5), a typical NH summer value (Montabone et al. 2015). For the dust series this profile is scaled, for a representative range of conditions, the resulting column optical depths with descriptions are given in Tbl. 5.3 (base profile is case 2). The dust distribution parameters are as defined in Tbl. 3.1 and the simulations include Mie multiple scattering with NEMESIS (see §3.3.4).

For each series the titular parameter was varied while holding other parameters fixed, using the parameters as given in the tables. For the water series, the base temperature and dust profile were held constant while scaling the water vapour profile for each run. For the temperature series, the base dust and water vapour profiles were used while changing the temperature profiles. For the dust series the base water and temperature profiles are used while scaling the dust profile.

Table 5.2 | Water abundances used for simulations where water content was varied. The base model for the temperature and dust series is emphasised in italics.

Scale Factor	Column Abundance (pr. µm)	Maximum Water VMR (ppmv)
0.1	1	29
0.5	5	144
1.0	*11*	*288*
2.0	22	576

Table 5.3 | Locations of temperature profiles and corresponding surface temperatures used from MCD (MY24 scenario, L_s=114°). The base model for the water and dust series is emphasised in italics.

Model	Latitude	Longitude	Surface Temperature (K)
T_1	81.1S	120.1W	145
T_2	*0.7S*	*93.2W*	*251*
T_3	29.9N	89.1W	265
T_4	51.1N	85.4W	271
T_5	80.5N	68.2W	222

Table 5.4 | Dust abundances used for simulations where dust content was varied. The base model for the water and temperature series is emphasised in italics.

Model	Optical Depth at 1075 cm^{-1} (τ_{1075})	Optical Depth at 463 cm^{-1} (τ_{A5})	Description
0	0.05	0.017	Clear
1	0.07	0.023	" "
2	*0.10*	*0.034*	*Normal*
3	0.25	0.084	" "
4	1.8	0.60	High Dust (Dust Storm)
5	2.4	0.80	" "
6	3.0	1.0	Very Dusty (Major Dust Storm)

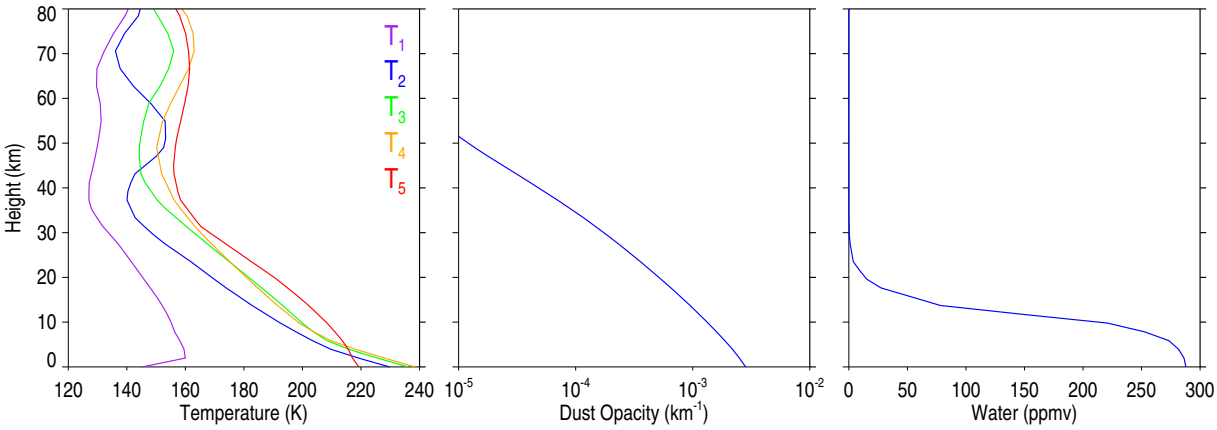


Figure 5.4 | Model profiles of temperature (left) with base dust profile extinction with column optical depth τ_{1075}=0.1 (centre) and 11 pr. µm column abundance base water vapour profile (right) used in the different radiative transfer calculations.

Isolating each parameter like this allows a systematic investigation of the effect of each on the B3/B2 radiance ratio. The profiles were used to run radiative transfer simulations for limb-viewing (including MCS detector FOVs) with the B2 and B3 detector arrays where each detector corresponds to a different boresight altitude. The mapping of detectors to boresight height are given in Tbl. 5.5. After the simulations have been run the resulting radiances are plotted onto B3-B2 scatter plots pairing equivalent detectors together (e.g. fifth detector of B3 with fifth detector of B2).

5.3.2 Results and Discussion

Results for each series are given below followed by discussion. For the B3-B2 scatter plots each point is colour coded according to which detector-pair it corresponds to. This is indicated by the legend where 'PIX01' is the lowest detector in the array with limb boresight altitude of -3 km (i.e. pointing at surface) and 'PIX21' is the highest corresponding to 80 km. The black diagonal line running through the origin is the 1:1 reference line indicating where $\mathrm{RAD}_{\mathrm{B3}}[d] = \mathrm{RAD}_{\mathrm{B2}}[d]$ where d refers to the detector number.

Water Series Results

Results from the water series simulations are given in Fig. 5.5. At first glance the results seem to be as expected, with varying degrees of 'branching' towards the B2 axis for differing atmospheric water vapour content. Closer examination reveals that counter-intuitively, as the water vapour contents increases in the atmosphere and the radiance changes the branches move upwards and

Table 5.5 | Detector Boresight Height mapping used for NEMESIS simulations with MCD profiles

Detector №	Height (km)
PIX01	-3.4
PIX02	1.0
PIX03	5.5
PIX04	10.0
PIX05	14.4
PIX06	18.8
PIX07	23.1
PIX08	27.5
PIX09	31.7
PIX10	36.0
PIX11	40.1
PIX12	44.2
PIX13	48.4
PIX14	52.4
PIX15	56.4
PIX16	60.4
PIX17	64.4
PIX18	68.2
PIX19	72.1
PIX20	75.9
PIX21	79.7

leftwards, i.e. towards the 1:1 reference line. This is most easily seen by looking at the pattern of changes for a single detector pairing. For PIX02 (orange) points the distances from the 1:1 line are shown in grey on the figure, marked d_S where S is the scale factor from Tbl. 5.4. The lower left point (circle, $d_{0.1}$) corresponds to the minimum 1 pr. µm case and the upper right (diamond, $d_{2.0}$) to the maximum 22 pr. µm. This pattern is repeated over all detector-pairings except PIX01, but is most pronounced for the lower atmosphere where the radiances and water VMRs are higher. If one draws a line through all the detectors for each case in the series it becomes apparent that the lines moves closer to the 1:1 line as the water vapour abundance is increased. In other words as the water vapour abundance is increased, the radiance increases in both channels and the B3/B2 ratio moves towards unity. This is most likely due to the broadened FWHMs of the B3 channel in particular.

For PIX01 (points in dotted ellipse) the limb path intercepts the surface, so it is seen in absorption rather than emission. As a result of this the B3 radiance (vertical) order is reversed from that of the other results, with the 1 pr. µm (diamond) case at the bottom instead of the top. However, the pattern of decreasing distance from the 1:1 line with increasing water vapour is maintained i.e. increased absorption with more water.

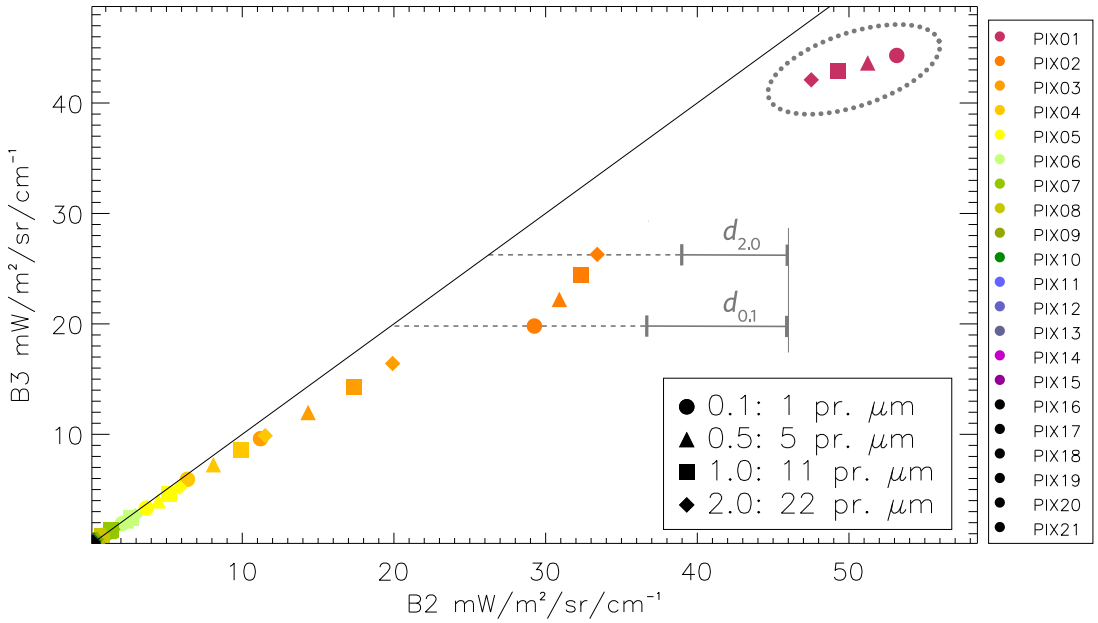


Figure 5.5 | Simulated scatter plot where water has been varied in the range of 1–22 pr. µm, with τ_{1075}=0.1 for dust, for equatorial temperature profile during northern hemisphere summer. Colour identifies detector and plot symbol which water profile was used (legend gives scale factor and column abundance). As the amount of water vapour is increased radiance increases in both channels causing points to move up and right. Counter-intuitively, as the water abundance is increased the radiance in B3 increases more quickly than that in B2 causing points to move closer to the 1:1 line. This can be seen in the representative PIX02 (orange) cases. The grey lines compare the distances d_S from the 1:1 line, where S is the scale factor. The dotted ellipse surrounds the PIX01 results which intercepts the surface.

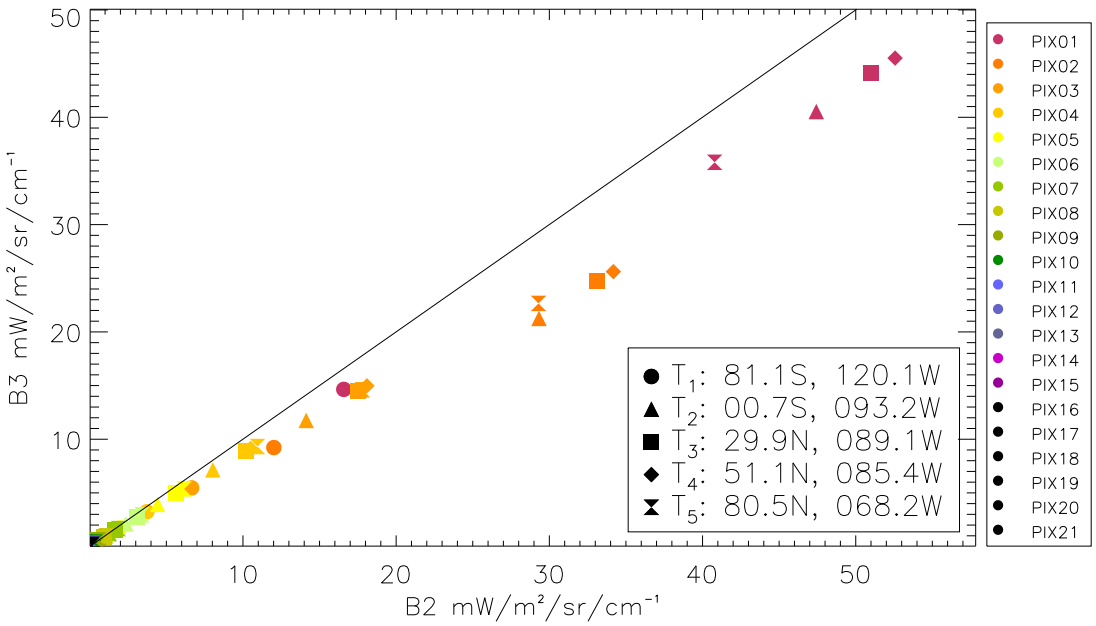


Figure 5.6 | Simulated scatter plots with varying temperature profiles (indicated by plot symbol) with fixed dust optical depth, τ_{1075}=0.1, and water content, 11 pr. µm. As the temperature profile is varied no further deflection from 1:1 reference line occurs. Warmer temperature profiles have an equal increase of radiance in both channels (points move up and right). Existing deflection from the 1:1 reference line caused is caused by water vapour present. However for cooler temperature profiles a decrease in deflection is observed due to the drop in radiance in both channels (points move down and left).

Temperature Series Results

Results from the temperature series simulations are given in Fig. 5.6. Despite all of these profiles using the same base water vapour profile and dust opacity, some branching is observed, showing that temperature variation can affect the B3/B2 ratio. For the warmer temperature profiles, at equatorial (T_2) and mid-latitude (T_3 and T_4) locations, the points all cluster at the maximum deflection towards the B2 axis. The only significant variation being up along an imaginary line drawn at this maximum deflection branch, as the radiances increase in both channels. This means the B3/B2 ratio remains almost constant for these cases. For the cooler temperature profiles, the polar models T_1 and T_5, reduced branching (deflection) towards the B2 axis is observed as the radiances in both channels decrease. This leads to a B3/B2 ratio closer to unity as radiances move closer to the 1:1 reference line.

Dust Series Results

Results from the dust series simulations are given in Figs 5.7–5.9. Despite all of these profiles using the same base water vapour profile and temperature profile, significant branching is ob-

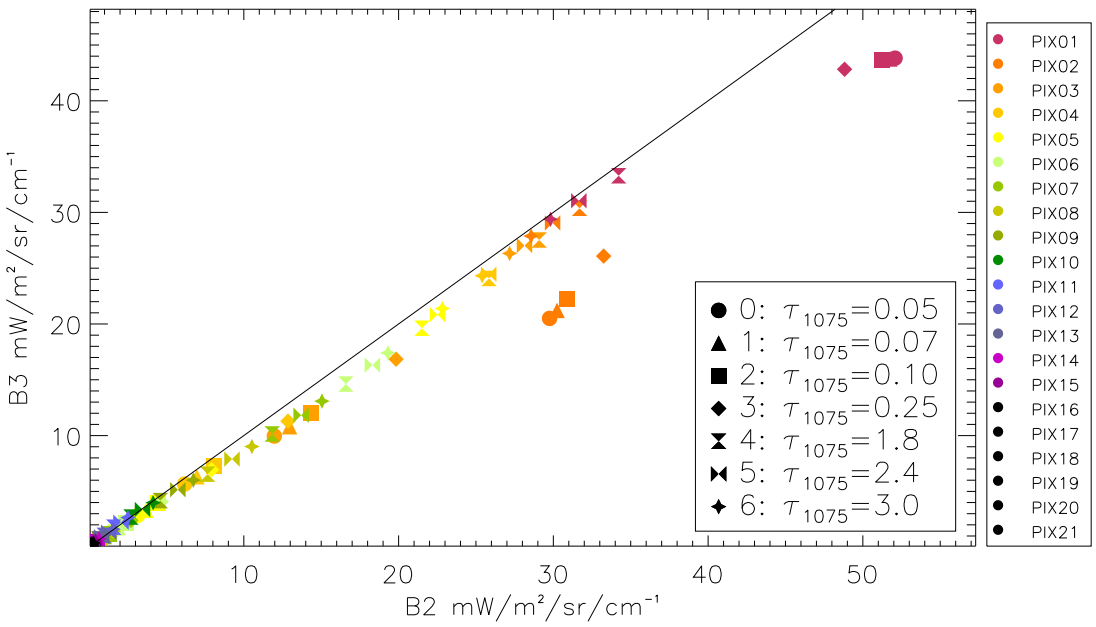


Figure 5.7 | Simulated scatter plots with varying dust profiles (equatorial temperature profile during northern hemisphere summer with water content, 11 pr. μm) with the model indicated by the symbol in the legend. The dust optical depth, τ_{1075}, varies over the range 0.05–3.0. Initially, increasing the amount of dust makes the points move up and right and towards the 1:1 reference line diagonally (increased radiance in B3 and B2). This has the effect of 'masking' the water signal. The points nearest the B2 axis have the lowest amount of dust. As the dust is increased further the atmosphere becomes optically thick and at τ_{1075} ≥1.8 the dust saturates the channels and points lie along the 1:1 reference line. Increasing the opacity further then only has the same effect as decreasing the temperature i.e. points move further down the reference line due to decreased radiance in both channels which are optically thick.

served, showing that dust opacity variation can affect the B3/B2 ratio. The main trend across the results is that as the dust opacity is increased the branching towards the B2 axis decreases and moves towards the 1:1 reference line. In other words the water signal is reduced and increasingly 'masked' by dust, even for typical summer low opacity values of τ_{1075}=0.1. Eventually increasing opacity reaches the point where the points are almost indistinguishable from the 1:1 reference line and hence undetectable. This can be seen by comparing the very clear atmosphere (τ_{1075}=0.05) in Fig. 5.8 with the dusty case (τ_{1075}=1.80) in Fig. 5.9. Increased dust opacity leads to reduced water vapour sensitivity in the B3/B2 ratio. A second pattern is how the radiances change as dust opacity is increased. For results where τ_{1075}=1.80 the radiance increases in both channels as the opacity increases. However, as dust opacity increases from τ_{1075}=1.80 radiances are seen to decrease as the limb paths become optically thick.

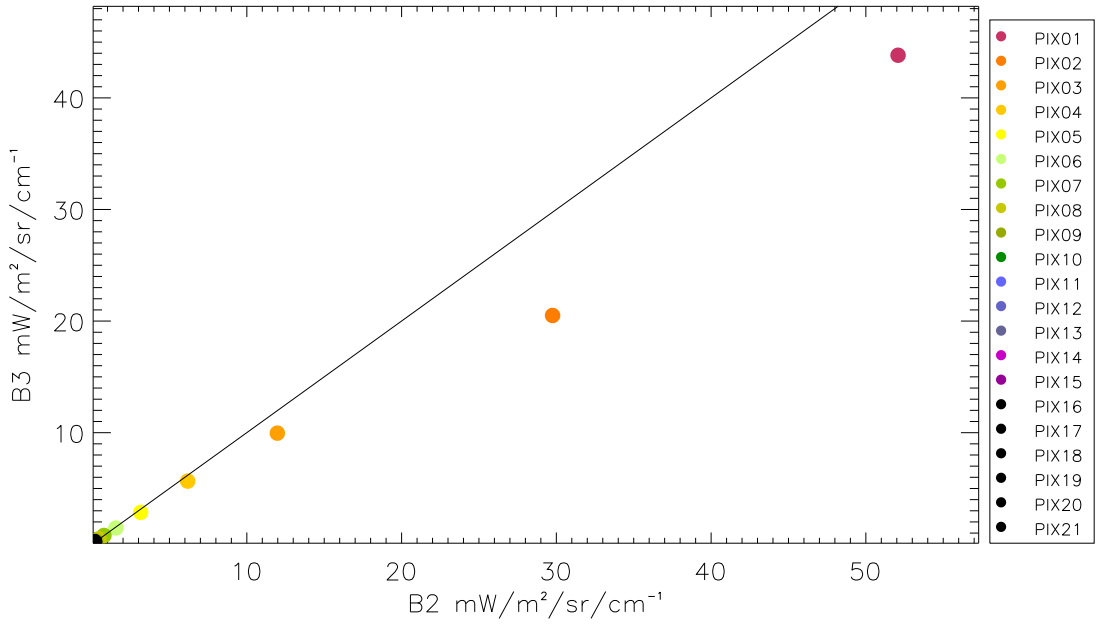


Figure 5.8 | Clear dust case τ_{1075}=0.05 for equatorial temperature profile during northern hemisphere summer with water content, 11 pr. µm. The deflection from the 1:1 reference line due to the water can be clearly seen.

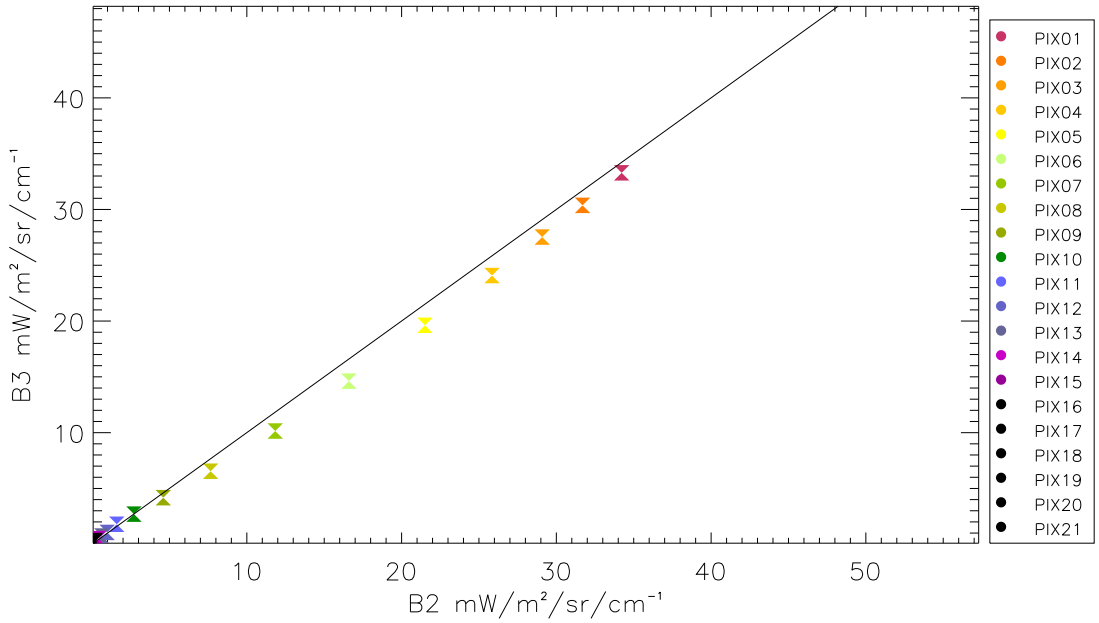


Figure 5.9 | High dust case τ_{1075}=1.80, for equatorial temperature profile during northern hemisphere summer with water content, 11 pr. µm. The deflection due to water as seen in the previous figure is much smaller as the B3:B2 radiance ratio lies close to unity. The presence of increased dust has 'masked' the water signal. The overall radiance levels have dropped as the profile becomes increasingly optically thick.

Discussion and Conclusions

From this series of tests it can be seen that the B3/B2 ratio is sensitive to changes in water vapour, temperature and dust opacity. Increases in water vapour for a given temperature and dust profile are observed to have the counter-intuitive behaviour of moving the ratio towards the 1:1 case, i.e. no sensitivity to water vapour. This is most likely due to the significant broadening of the B3 channel FWHM. Decreases in temperature, while holding the dust and water vapour profiles constant, lead to the ratio moving towards the 1:1 line due to lower water vapour emission. Most importantly, increases in dust opacity are observed to move the ratio towards 1:1, masking the water signal, leading to reduced sensitivity to water vapour. Unless the dust emission is accurately modelled, allowing accurate assessment of the contributions to the radiance of dust and water, the amount of water vapour retrieved would have significant error.

This suggests that the original retrieval method using the pair of B3-B2 channels to retrieve water vapour independent of aerosol is highly compromised. As a result of this retrievals will have to be done in two stages. In the first stage temperature, pressure, surface temperature and aerosol are retrieved using a a combination of channels from A1–A5 and B1. These retrieved values are then fixed for the second stage where water is retrieved using B2 alone.

5.4 B2 Radiance Residuals for Water Vapour

In this section we detail work done on calculating radiance residuals due to water vapour in the B2 channel. As has been described earlier the direct retrieval of water vapour using the B3-B2 ratio from MCS observations is virtually impossible. Instead the retrieval needs to be broken down into a two-stage process, whereby all parameters bar water vapour are retrieved first, followed by the water vapour retrieval itself. Initial attempts at retrieval proved extremely challenging. In response to this the following investigation into water vapour radiance residuals was carried out to enhance understanding of the dataset and improve the retrieval methodology. By using a method of looking at radiances directly, tentative conclusions can be drawn about water vapour distribution in the Martian atmosphere in the hope of identifying regions and times where water vapour can be successfully retrieved.

In this study NEMESIS was used for a two-stage analysis on daytime measurements from a 4 h block of MCS observations. In the first stage retrievals were performed, using A1–A3 and

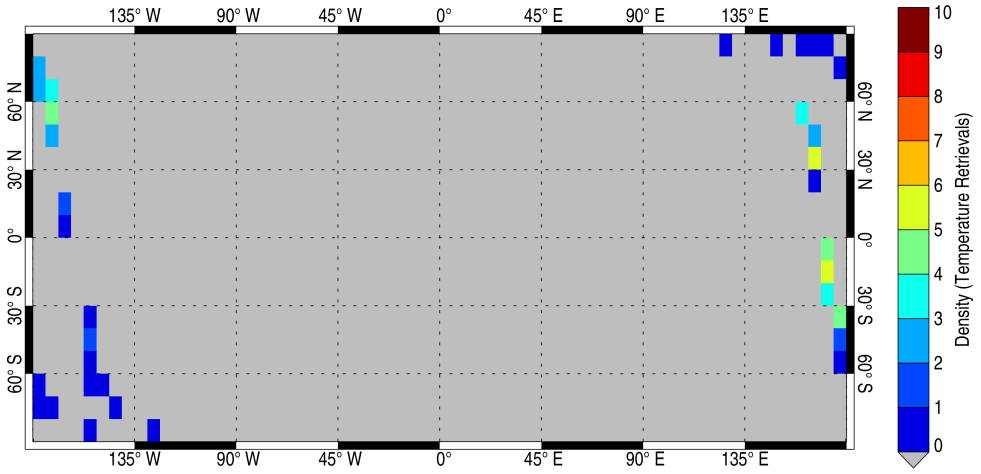


Figure 5.10 | Density histogram map of the daytime MCS observation locations on Mars used for the retrievals/residuals at L_s=111°.

A5, for temperature, dust, pressure and surface temperature while setting the water abundance to zero. In the second stage the retrieved parameters and 'zero water' abundance were used to model the radiance seen in B2. This ought to model the atmosphere as seen by MCS with no water present. The simulated 'zero water' radiances in B2 can then be subtracted from the real MCS measurements to generate radiance residuals. These radiance residuals act as first-order proxy to water vapour location. Inaccuracies in the dust modelling (e.g. wrong particle size giving different opacities at longer wavelengths) or the neglect of water ice may lead to errors in the residuals. This could lead to false positives e.g. aerosol aliasing as water vapour signal.

5.4.1 Observations

Daytime MCS observations came from a 4 h (16h–00h UT) observation block, taken on 24 September 2006 (L_s=111°) during northern summer for local surface times between 06h and 18h but mostly at 15h (due to MRO's orbit, see Chapter 2 for details). This data was taken before MCS suffered its elevation slew impairment (see Chapter 2) and hence includes fully calibrated nadir and limb data. A plot of observation locations is given in Fig. 5.10. When possible limb radiance observations were combined with local nadir observations <1° away in latitude and longitude.

5.4.2 Retrieval and Residual Method

A Priori Models

The *a priori* atmosphere models were constructed using data from the MCD (MY24 scenario), as described at the end of §3.4 (MCD-only case). Profiles for temperature/pressure, CO_2 and N_2, with a value for surface temperature are extracted corresponding to the time and location of the MCS observation being used. The water vapour profile is set to have a VMR of 10^{-11} constant with height, an effectively zero water abundance (NEMESIS cannot handle zero values).

The MCD value of dust column optical depth at 1075 cm^{-1} was used to scale a dust profile that is uniform with height (constant specific density, particles per gram of atmosphere). The dust was modelled using the gamma size distribution and complex refractive index data from §3.3.1. The gamma distribution is characterised via the first two moments of the distribution; $a = r_{eff}$, the effective radius of the dust particle (i.e. mean geometric dust grain radius) and $b = v_{eff}$ the effective width of the distribution (Hansen & Travis, 1974):

$$n(r) = \text{constant } r^{(1-3b)/b} e^{-r/ab}. \tag{5.1}$$

with r_{eff}=1.4 μm and v_{eff}=0.3 for this residuals study. For the sake of computational expediency the dust was modelled as non-scattering (absorption-only). A retrieval run without scattering takes ∼1 min whereas when scattering is included the computational time increases to >10 h. Therefore the current investigation would have taken far too long to have been practical. The results of §3.3.4 show that this is an acceptable approximation.

Retrieval/Residuals Method

The retrievals are performed and the B2 radiances calculated using the following procedure for each MCS observation:

Stage One: Using *a priori* information in combination with the zero-abundance water vapour profile, retrievals of temperature, pressure, dust and other parameters were performed using channels A1–A3, A5 and B1 as a dummy channel (the dummy channel radiance was not used in the retrieval but simply for NEMESIS to be able to map detectors to the correct heights). The choice of not using the B1 channel was due to its high sensitivity to water ice as well as dust. As water ice was not included in this simplified early retrieval/residuals procedure it could not

be used to retrieve dust. If nadir radiances were included in the MCS observation then surface temperature was also retrieved. For the pressure retrieval the *a priori* was set using the MCD pressure value at 28 km.

Stage Two: The retrieved values from the first stage with the zero-abundance water vapour profile are used as input for a radiative transfer simulation run of the NEMESIS. This modelled the radiances as seen in B2 if no water were present for the MCS observation. These zero-abundance water radiances for B2 can be subtracted from the measured B2 radiances to give the radiance residuals, R_{resid},

$$R_{\text{resid}}(d) = R_{\text{meas}}(d) - R_{\text{sim}}(d), \tag{5.2}$$

where R_{meas} is the MCS observed B2 radiance for the detector, d, and $R_{\text{sim}}(d)$ is the simulated zero-water B2 radiance. This calculation is applied to both limb radiances and nadir radiances. Assuming all of the parameters other than water have been accounted for (except for the inherent uncertainty associated with the dust), the radiance residuals ought to be mostly due to water vapour. This means they should be useful as a qualitative indicator of where water vapour is present in the atmosphere.

Stage Three: Finally, the temperature retrievals, dust retrievals, measured B2 radiance and B2 radiance residuals are binned in 10° latitude bins and used to produce zonally averaged latitude-altitude maps of the respective parameters. The radiance residuals can then be compared to expectations of where water vapour ought to be (i.e. from models and previous observations) to ascertain the sensitivity of B2 and the retrieval process to water vapour and gain a sense of the vertical structure of water vapour in the Martian atmosphere.

Detector Selection

Not all limb detectors are used in the first stage of the retrieval. Limb detectors with boresight altitudes below 1 km are removed from the retrieval. This is done to limit the effect of the extended FOV-wings discussed in §2.3.2, as surface emission from the surface is likely to 'pollute' detector radiances from this close to the ground.

The temperature channels A1, A2 and A3 are located in the CO_2 absorption band, with A3 nearest the band centre and A1 furthest out. These three channels are sensitive to different altitude ranges due to the different levels of CO_2 absorption in each channel (see §4.6.3). Below

Table 5.6 | MCS channels used in the radiance/residuals study with limb detector boresight height criteria. *Height Selection* shows the selection rule used for a given channel's detectors. *Stage* indicates which stage of the radiance/residuals process the detectors are used.

Channel	Height Selection (km)	Stage
A1	>5	Stage One
A2	>15	Stage One
A3	>25	Stage One
A5	>1	Stage One
B1	>1	Stage One (Dummy)
B2	>1	Stage Two

these altitudes the channel becomes opaque with a wide contribution function, i.e. the channel contains little to no useful information. The A3 channel with highest absorption corresponds to the highest altitudes and A1 with the lowest absorption to the lowest altitudes. To improve retrieval accuracy detectors with no useful information are removed as in Kleinböhl et al. (2009). In their paper A-channel detector selection is based on a CO_2 line-of-sight channel optical depth threshold of 2.0. For this study a simplified detector selection scheme is used based on typical height ranges generally consistent with these thresholds. Detector selection rules are given in Tbl. 5.6.

5.4.3 Results

The results of the retrievals, measured B2 radiances and B2 radiance residuals are presented in Figs 5.11–5.14 and are discussed below. As water vapour is the main focus of the study, retrievals of temperature and dust are only discussed briefly.

Temperature Retrieval

A map of zonally averaged temperature and surface temperature is given in Fig. 5.11 alongside corresponding MCS L2 data for comparison (binned at the same resolution). Results seem realistic with the northern hemisphere (experiencing summer) being warmer than the southern hemisphere (experiencing winter) and maximum temperatures occurring in the equatorial region. Also visible is 'polar-warming' in the middle atmosphere over the the colder southern polar vortex (McCleese et al., 2010). The northern polar vortex is also visible as a weak temperature minimum at 40 km, with an overlying north polar warming (though less intense than its southern counterpart).

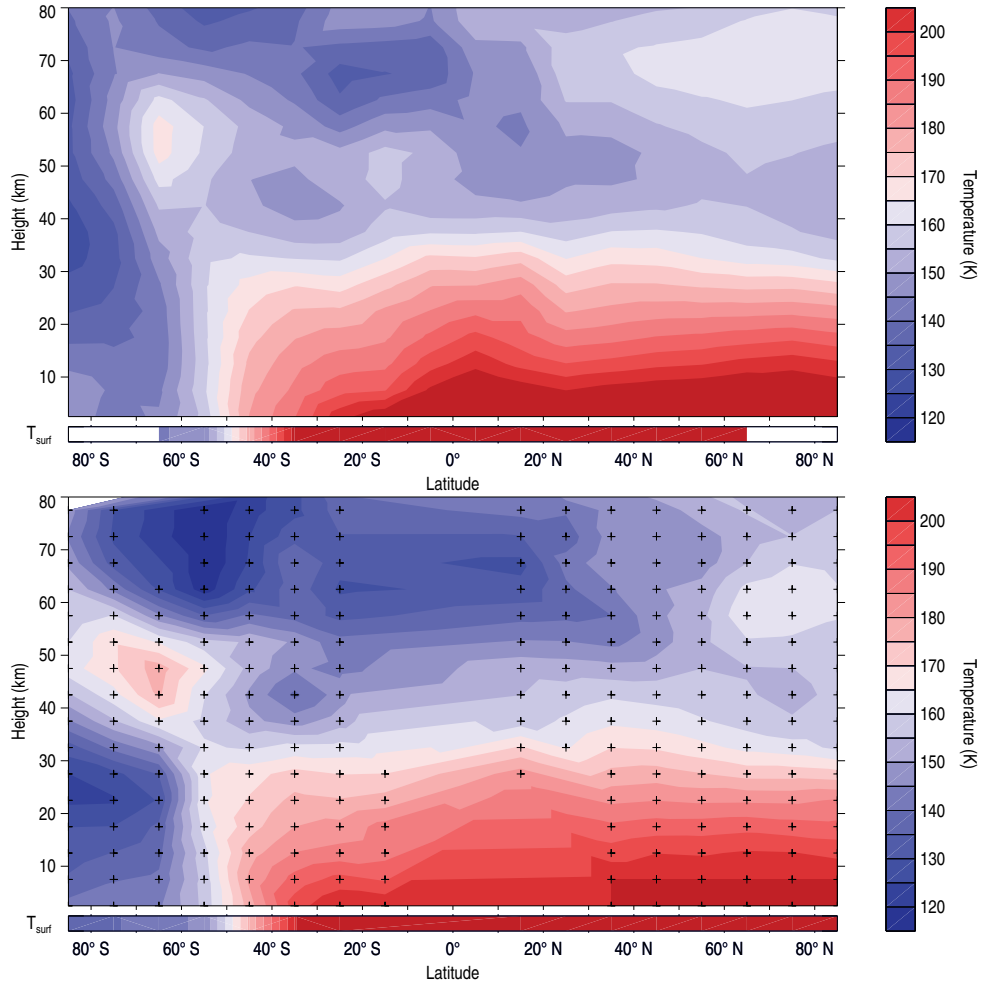


Figure 5.11 | **(Top)** Zonally averaged (10° latitude bins) temperature plot for Mars at L_s=111° (Northern Summer). As expected the Northern Hemisphere is warmer than the Southern Hemisphere. The bar beneath contains surface temperatures retrieved where nadir observations were available. White regions correspond to regions with no nadir observations. **(Bottom)** MCS L2 results for comparison where crosses mark bin locations (due to applied thresholds not all regions contain data).

Retrieved temperatures compare well with L2 data. The main differences are seen in the polar warming maxima. In the L2 results the southern maximum is about 10 km higher and 10 K warmer and also extends to higher latitudes. In our results the north polar warming maximum is about 10 km higher at 70 km and twice as wide in latitude. Differences are most likely due to difference in retrieval and analysis methodologies. The L2 retrievals were performed with the inclusion of water ice and with more complex detector selection rules based on limb path opacity (see §8.2.3). Additionally, applied quality control measures to L2 data removed results deemed to be erroneous (see §3.4).

Dust Retrieval

A map of zonally averaged dust with height is given in Fig. 5.12 alongside corresponding MCS L2 data for comparison. Dust is measured in units of optical depth per kilometre at A5. The general trend of more dust in the northern hemisphere than the southern, with a maximum at the equator is physical and corresponds to the higher temperatures in the northern and equatorial regions. Higher temperatures aid dust loading in the atmosphere (Read & Lewis, 2004). Coverage in L2 results is quite sparse, due to the opacity thresholds and detector selection rules (see above). This is most prominent in the equatorial band which has very few results in the L2 data, except for some values above 25 km. This region experiences higher dust opacities (Kleinböhl et al., 2009; Montabone et al., 2015).

Where the datasets coincide the results are reasonably similar, though L2 aerosol results are lower in opacity and vertical extent. For the main dust channel, A5, the detector selection cut-off of 1 km may be too low with the extended FOV wings. The extended wings could allow higher detectors to 'see' lower dust layers or the surface, causing an alias dust signal higher up and giving a false greater vertical extent. Other factors causing disagreement between the datasets are the difference in methodology and analysis (see above) including not retrieving water ice. It is likely that a combination of theses effects is responsible for the observed results.

The most unreliable region in our results is likely to be the equatorial region, where the dust opacity is very high and limb paths may well be optically thick to above 20 km. This region also contains the aphelion cloud belt (see §1.3.3), so there may also be a contribution from water ice which we do not retrieve.

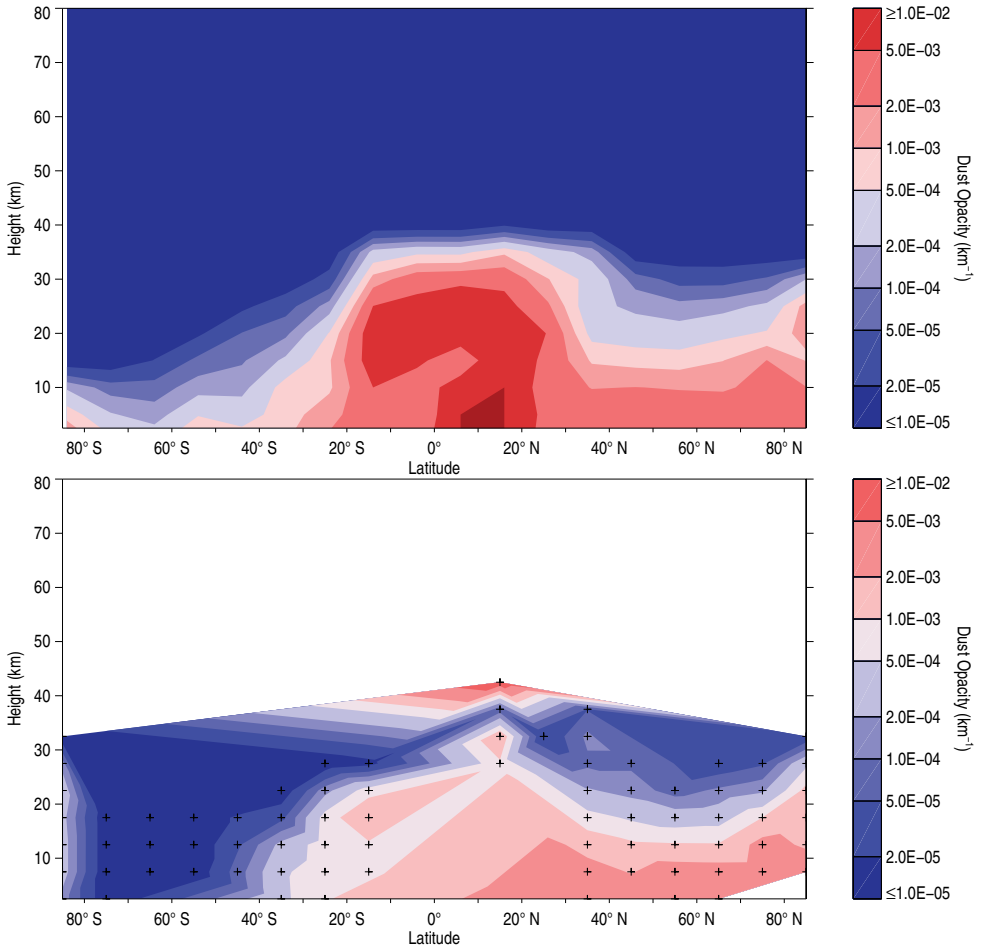


Figure 5.12 | **(Top)** Zonally averaged (10° latitude bins) dust plot at L_s=111°. **(Bottom)** MCS L2 results for comparison where crosses mark bin locations and white regions mark missing data. Due to applied thresholds not all regions contain data.

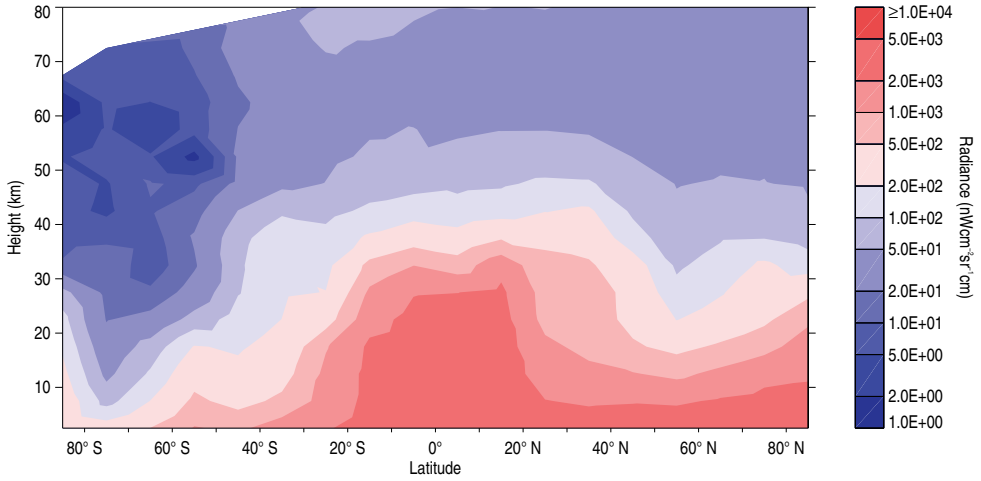


Figure 5.13 | Zonally averaged (10° latitude bins) measured radiances in B2 at L_s=111°. The radiance observed should be due to water and dust with possible contributions from water ice. The white region in the top left corner is missing data, due to MRO's orbit when near the south pole. In this region the tangent altitude corresponding to the highest MCS detector limb paths is below 80 km.

Measured B2 Radiances and B2 Radiance Residuals

A map of the observed radiances for B2 is given in Fig. 5.13. Higher B2 radiances are seen at the equator and in northern hemisphere. Southwards of the equator the B2 radiance very quickly falls to low levels. North of the equator the radiance forms a layer from the surface to about 20 km. There is a large 'plume' of radiance extended in height at the equator, reaching up to nearly 40 km. It would be expected that for regions of similar temperature and aerosol opacity (when optically thin) that higher radiances correspond to greater amounts of water vapour. Cooler regions would give lower radiances than hotter ones for the same amount of water vapour.

The radiances seen in the northern hemisphere and equator below 20 km match what would be the expected distribution of water vapour for northern summer, i.e. higher abundances of water vapour at northern latitudes. The unusual component is the large plume of radiance at the equator. This is because even with the warmer equatorial temperatures large amounts of water vapour are very unlikely to be this high in the atmosphere, as it is above the expected condensation level. Also, the highest water abundances at this time of year would be further north. It is highly likely that most of this radiance is due to dust and possibly water ice. The case for dust is supported by the large dust plume that is also observed at the equator in Fig. 5.12. The case for water ice by the fact that the aphelion cloud belt forms at these latitudes and heights at this time of year.

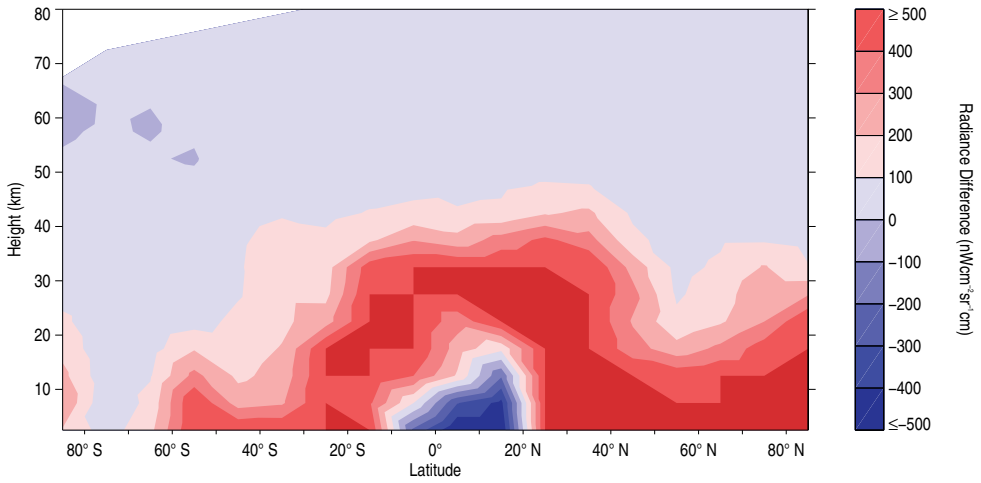


Figure 5.14 | Zonally averaged (10° latitude bins) radiance residuals for B2 at L_s=111°. By taking residuals ([*observed radiances with water*] − [*synthetic radiance with no water*]) it is hoped that the locations of water vapour can be observed disentangled from radiance due to dust. The white region in the top left corner is missing data as explained in Fig. 5.13.

The radiance residuals for B2 are presented in Fig. 5.14. These have been calculated by subtracting the synthetic no-water radiances (the radiative transfer simulated radiances using the retrieved profiles with no water) from the MCS B2 measurements. Theoretically, assuming high accuracy in the retrieval and radiative transfer modelling with no water, the residuals should map very closely to the water vapour distribution. This is because in the residuals the radiances due to factors other than water, particularly aerosol, should be subtracted out. This would then give positive residuals where water is located and zero residuals where it is not. Residuals are expected to scale with water vapour amount and temperature in similar manner as the raw radiances case discussed earlier.

The radiance residuals as actually calculated do not perfectly match the theoretical description given above. The most obvious signifier of this being the negative residuals present at the equator. Negative residuals (or lower than expected residuals) mean that synthetic no-water radiances have overestimated the B2 non-water radiance component. This could be due to either insufficient absorption or too much emission. Either case indicates that the model has failed to accurately reproduce non-water atmospheric conditions, the instruments viewing conditions or both. In relation to atmospheric conditions the most likely factor is inaccurate modelling of aerosol. This could be due to incorrect dust extinction cross-sections, incorrect dust abundances or the neglect of water ice. In regards to the instrument this could be caused by the detector extended FOV wings. For near-surface observations the FOVs for the lowest detectors will ‘see’ the ground through the atmosphere. This provides a warm background for the atmosphere

meaning spectral lines are seen in absorption rather than emission, resulting in the negative or lower than expected radiance residuals. The reason the effect is not observed at latitudes outside this region is due to the colder surface temperatures at the poles and southern hemisphere (in winter)—so the ground is not warmer than the atmosphere above it. Extended FOVs can also cause radiance aliasing, i.e. radiances from lower altitudes are falsely attributed to higher altitudes (for detectors with higher boresight altitudes). It is probable that the actual explanation for the model deficiencies is a combination of some or all of the above.

Given the problems described above it is unlikely that the residual radiances observed are entirely disentangled from effects other than water. Despite this the positive residuals roughly match the expected water vapour distribution, with higher residuals at northern latitudes. An unexpected 'arch' is observed at 20°S–40°N reaching up to nearly 40 km. As for the case of the equatorial plume seen in the B2 radiances plot, water vapour is not expected this high up. Here the problem is the opposite of that for the negative radiances, i.e. the synthetic radiances are too low, due to too much absorption or insufficient emission. Inaccurate aerosol modelling and FOV aliasing are potential culprits.

5.4.4 Conclusions

The results from this residuals study have provided qualitative mapping of atmospheric water vapour. They have also highlighted a number of deficiencies in the radiative transfer modelling and retrieval process mainly in terms of aerosol modelling. It is likely that water ice will need to be included in future water vapour retrievals. It will also be important to test the effect of the choice of aerosol size distribution on B2 radiances and water vapour retrievals, especially when it is incorrect. This is the topic of the following section and Chapter 6.

5.5 Effect of Dust/Ice Particle Size on B2 radiances

Previous simulations have shown that dust opacity acts to mask the water vapour signal in the B3-B2 radiance ratio. Additionally, results from the radiance residuals retrievals in the previous section highlight the importance of including water ice in the retrieval process. This means a split retrieval process has to be undertaken as it seems that water cannot be retrieved independently of aerosol as originally conceived, i.e. a two-stage retrieval is needed (see previous section). As water vapour cannot be retrieved independently it is important that the correct aerosol opacity

at B2 is obtained in the first stage, as otherwise the aerosol contribution to radiance in B2 will be incorrect leading to the wrong amount of water vapour being retrieved. This depends on accurately modelling the extinction cross-section which depends on the chosen particle size distribution model. Therefore it is important to assess the sensitivity of the radiance in B2 to the choice of aerosol particle size distribution.

To test for this sensitivity two series of limb-viewing radiative transfer simulations were conducted with NEMESIS, one for dust and one for water ice size distributions. This was done using the measured B2 filter profiles. In the first series differing dust size distributions are tested and in the second this process is repeated for differing ice size distributions. For each series the extinction cross-section and single-scattering albedo (SSA) profiles are normalized to the value from a chosen particle size distribution at their respective primary retrieval channel wavenumber, A5 (464 cm^{-1}) for dust and A4 (843 cm^{-1}) for water ice. This allows simulation using the same aerosol specific particle density (particles per gram) vertical profile, while holding the optical depth constant at the normalized wavenumber (see Eqn 3.39). Gauging the extent of the impact of aerosol size distribution on B2 (245 cm^{-1}) radiance will allow for determination of its impact on water vapour retrievals.

5.5.1 Simulation Procedure

For this simulation the model atmosphere was constructed using data from the MCD (MY24 scenario) for temperature, pressure, CO_2, N_2 and water vapour. For the dust series the dust profile was assumed to be uniformly mixed to the top of the atmosphere with a column optical depth of $\tau_{A5} = 0.045$ at the normalization channel A5. The model atmosphere used is the T_1 + D_1 model used in the scattering tests in §3.3.4 (see Fig. 3.12). For the water ice series the same temperature profile is used but the dust is replaced with water ice. This is the T_1 + H_1 model from the scattering tests. The aerosol vertical profile consists of a water ice layer at 20 km with a peak extinction of 10^{-3} at A4.

Two different water vapour profiles are used for the tests. The first is the profile corresponding to T_1 from the MCD, with a 29 pr. µm column abundance and maximum VMR of 500 ppmv, this is the *water* profile. It is uniform up to the condensation height and then drops off (see water vapour panel in Fig. 3.12). The second is the *no water* profile and has a VMR of 10^{-11} constant with height, effectively zero water abundance (NEMESIS cannot handle zero values).

Aerosol size distributions are modelled using either the gamma or modified gamma distri-

Table 5.7 | Dust size distributions used for simulation.

r_{eff} (μm)	v_{eff}	Type
1.06	0.3	Modified Gamma (a=2.24, b=8.04, c=0.647)
1.5	0.4	Modified Gamma (a=2, b=8.15, c=0.52)
1.6	0.3	Gamma
1.8	0.25	Gamma
2.4	0.2	Gamma
3.0	0.15	Gamma

Table 5.8 | Ice size distributions used for simulation.

r_{eff} (μm)	v_{eff}	Type
1.41	0.15	Modified Gamma (a=12.6, b=31.4, c=0.436)
2.0	0.1	Gamma
3.0	0.1	Gamma
4.0	0.1	Gamma
6.0	0.1	Gamma

butions. Complex refractive indices are as described in §3.3.1. The gamma distribution is characterised via the first two moments of the distribution; $a = r_{eff}$, the effective radius of the aerosol particle (i.e. mean geometric grain radius) and $b = v_{eff}$ the effective width of the distribution (Hansen & Travis, 1974) as defined by Eq. 5.1. The modified gamma distribution is characterised by the three parameters a, b and c as defined in §3.3.1, but also supplies values for r_{eff} and v_{eff}.

Sets of dust/ice particle size distributions were chosen to reflect a range of conditions on Mars based on the work of Wolff & Clancy (2003), Wolff et al. (2006) and Kleinböhl et al. (2009, 2011). Details of these are given in Tables 5.7 and 5.8. Extinction cross-sections and single-scattering albedoes were generated for these using the complex refractive index data described above over the range 100–1200 cm^{-1}. The extinction and SSA profiles were then normalized: for dust to the A5 values of the r_{eff}=1.06 μm profiles and for water ice to the A4 values of the r_{eff}=1.41 μm profiles. These are all shown in Figs 5.15–5.20.

The important region in the normalized extinction/SSA plots is that of the B2 channel (220–260 cm^{-1}). In Figs 5.17 & 5.20 'zoomed' versions of Figs 5.16 & 5.19 are presented concentrating on the B2 spectral region. A spread of extinction/SSA values is seen this region for each of the different sizes. Increasing r_{eff} leads to increased extinction/SSA over the whole B2 spectral range.

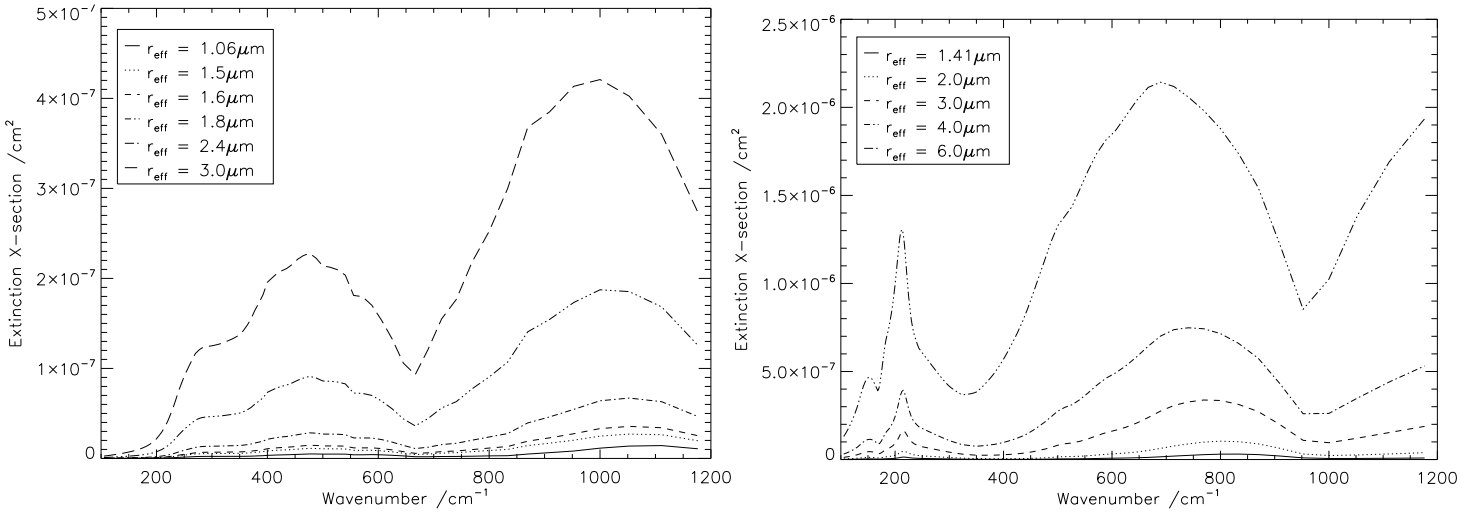


Figure 5.15 | Extinction Cross-Sections for Particle Size Distributions: **(Left)** Dust. **(Right)** Water ice.

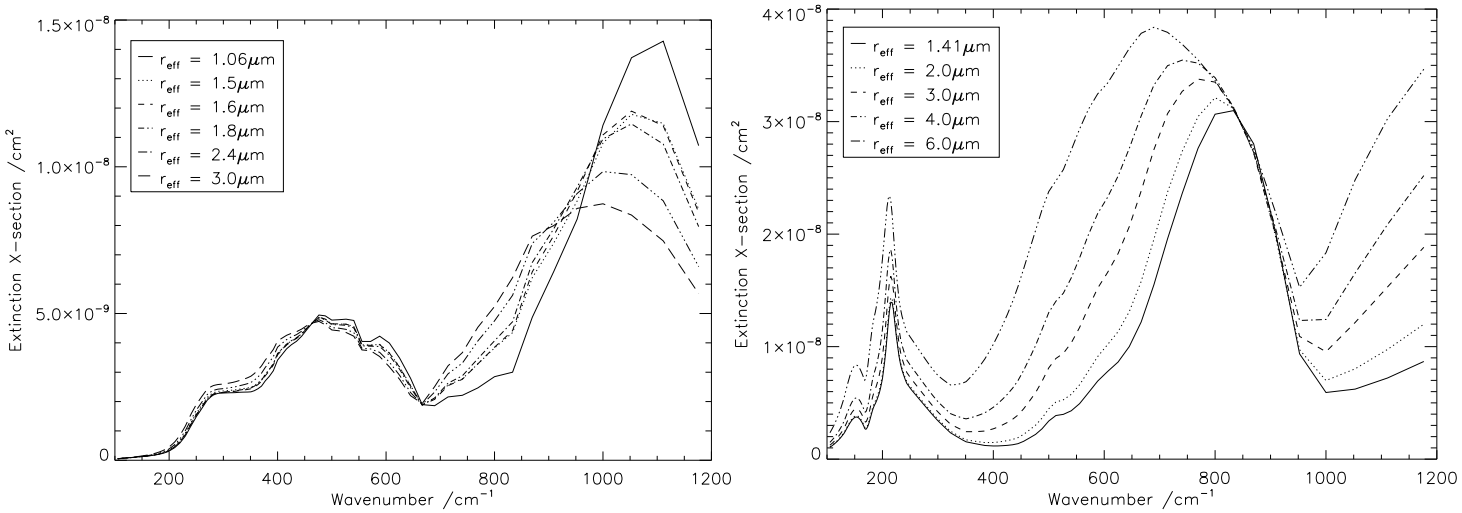


Figure 5.16 | Normalized Extinction Cross-Sections for Particle Size Distributions: **(Left)** Dust normalized to the A5 (464 cm^{-1}) value of the r_{eff}=1.06 μm profile. **(Right)** Water ice normalized to the A4 (843 cm^{-1}) value of the r_{eff}=1.41 μm profile.

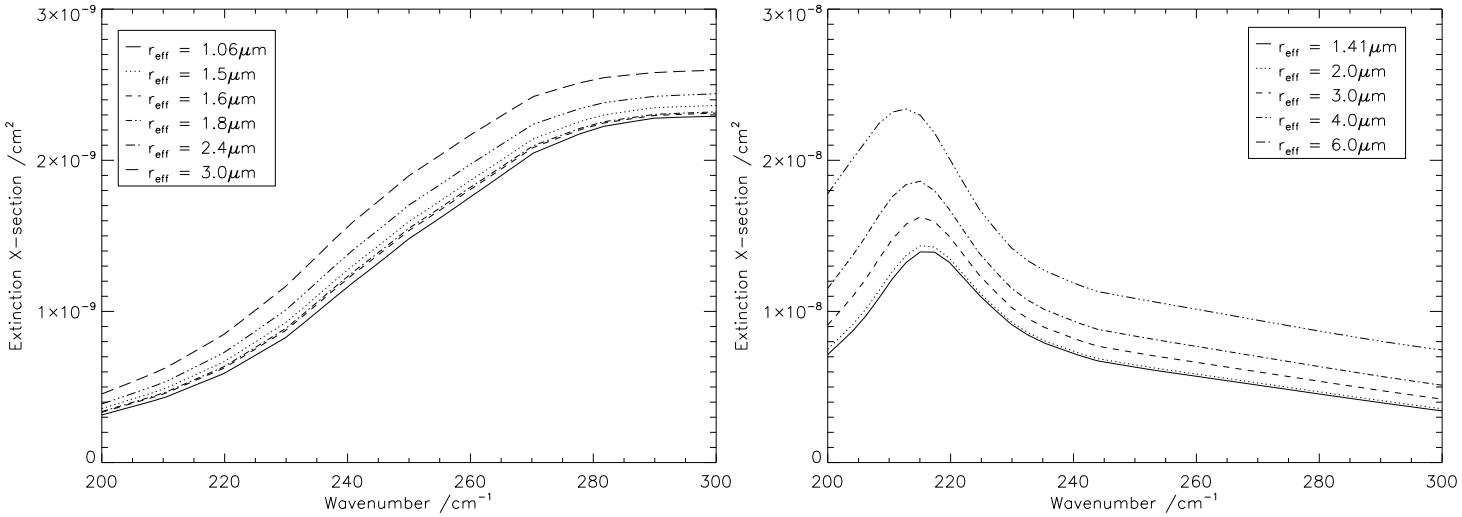


Figure 5.17 | Same as Fig. 5.16 but zoomed into wavenumber range corresponding to B2.

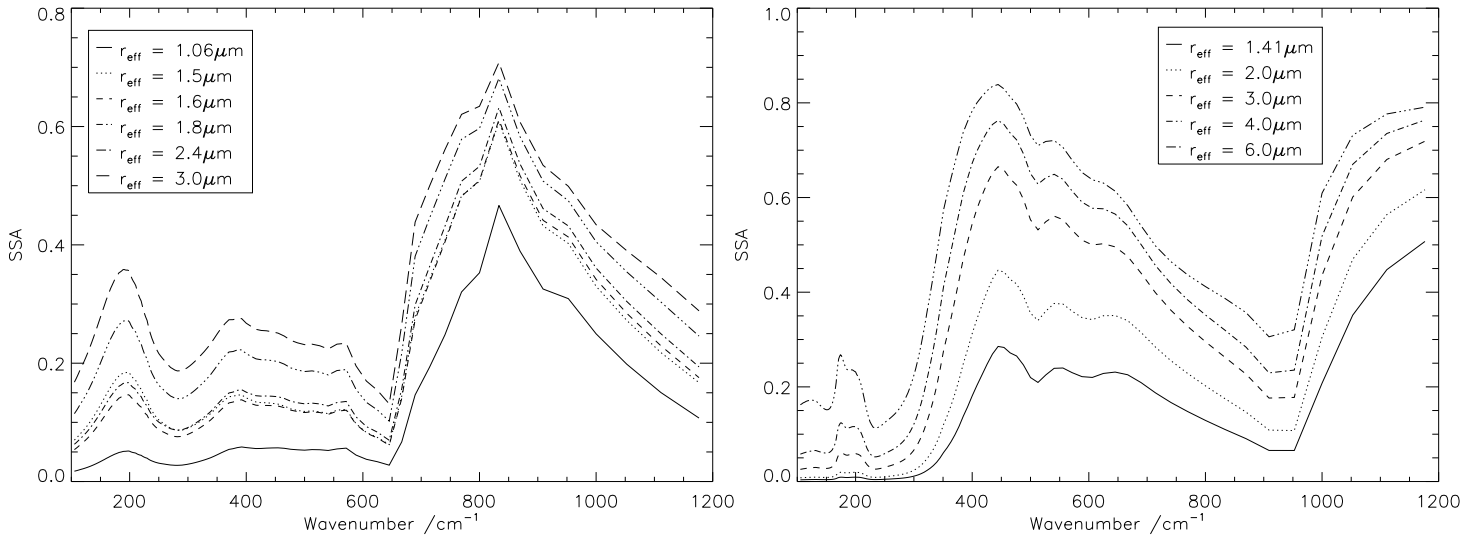


Figure 5.18 | SSA for Particle Size Distributions: **(Left)** Dust. **(Right)** Water ice.

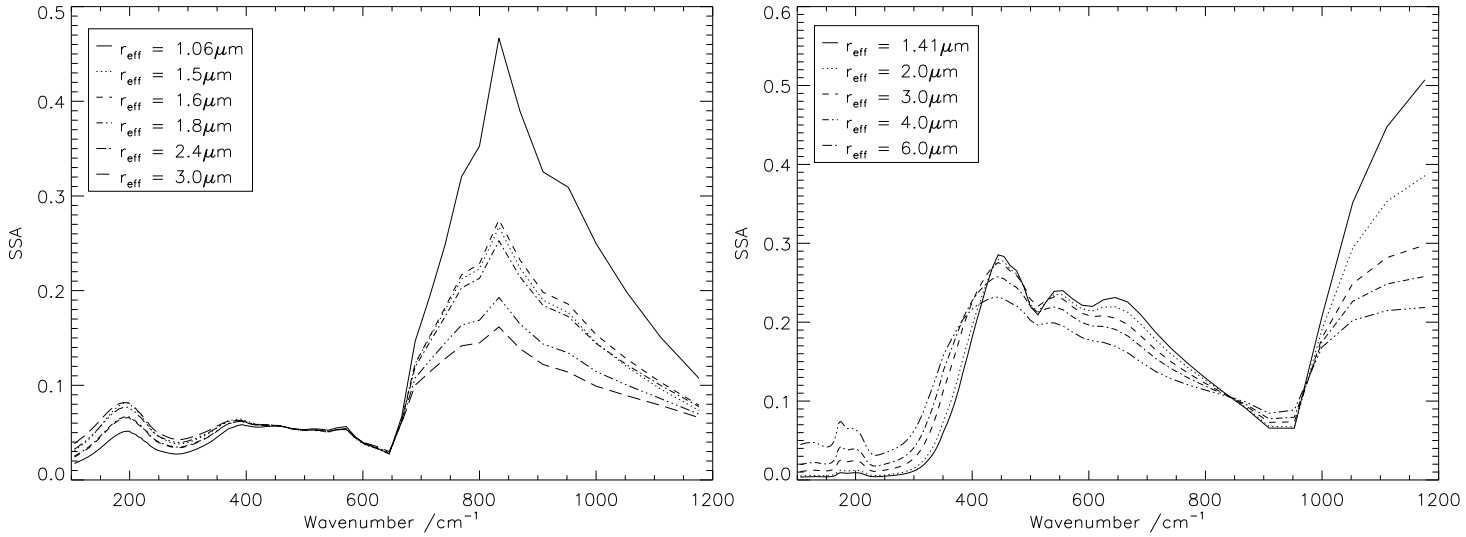


Figure 5.19 | Normalized Extinction SSA for Particle Size Distributions: **(Left)** Dust normalized to the A5 (464 cm^{-1}) value of the r_{eff}=1.06 μm profile. **(Right)** Water ice normalized to the A4 (843 cm^{-1}) value of the r_{eff}=1.41 μm profile.

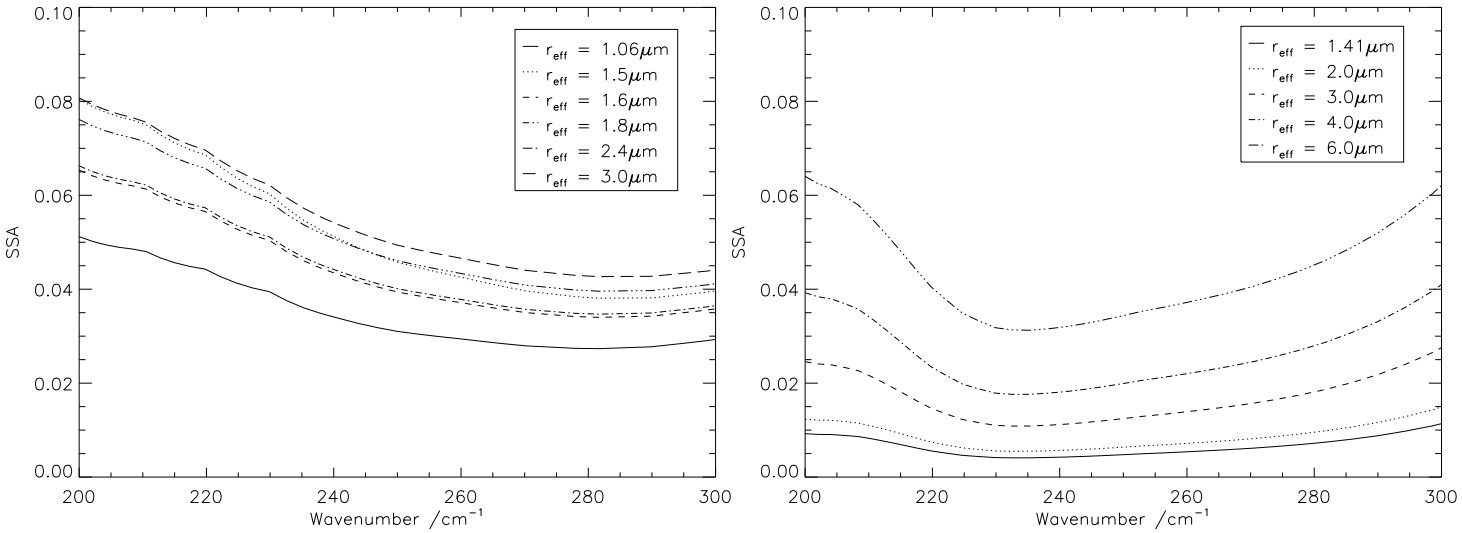


Figure 5.20 | Same as Fig. 5.19 but zoomed into wavenumber range corresponding to B2.

For each series simulation NEMESIS was run twice with each normalized aerosol size distribution for limb viewing (including the MCS detector FOVs and using the measured B2 filter profiles). Firstly with the *water* profile and secondly with the *no water* profile. The detector boresight heights are given in Tbl. 5.9. The results were then used to create vertical B2 radiance and difference profiles. To calculate the radiance difference profiles for each series a reference profile was needed as a 'zero' baseline. All other radiance profiles in a series would be subtracted from this special case. This would be the *no water* case for the normalization particle size distribution, $r_{eff} = r_{\mathrm{norm}}$. For the dust series this is the [$r_{eff} = r_{\mathrm{norm}}$=1.06 μm : *no water*] case and for the water ice series [$r_{eff} = r_{\mathrm{norm}}$=1.41 μm : *no water*] case. The difference profile, $R_{\mathrm{diff}}(r_{eff}, h)$, was then calculated,

$$R_{\mathrm{diff}}(r_{eff}, h) = R_{\mathrm{B2}}(r_{eff}, h) - R_{\mathrm{B2}}(r_{\mathrm{norm}}, h), \tag{5.3}$$

where r_{eff} is particle size distribution and h is detector boresight height. $R_{\mathrm{B2}}(r_{eff}, h)$ is the radiance profile and $R_{\mathrm{B2}}(r_{\mathrm{norm}}, h)$ is the baseline radiance profile (*no water*) at the normalization distribution described above.

5.5.2 Results and Discussion

Plots of vertical radiance profiles are given in Figs 5.21a & 5.22a for the dust and ice series results respectively. The corresponding radiance difference profiles are given in Figs 5.21b & 5.22b. For results in both series it is seen that for the same value of r_{eff} the *water* case is substantially

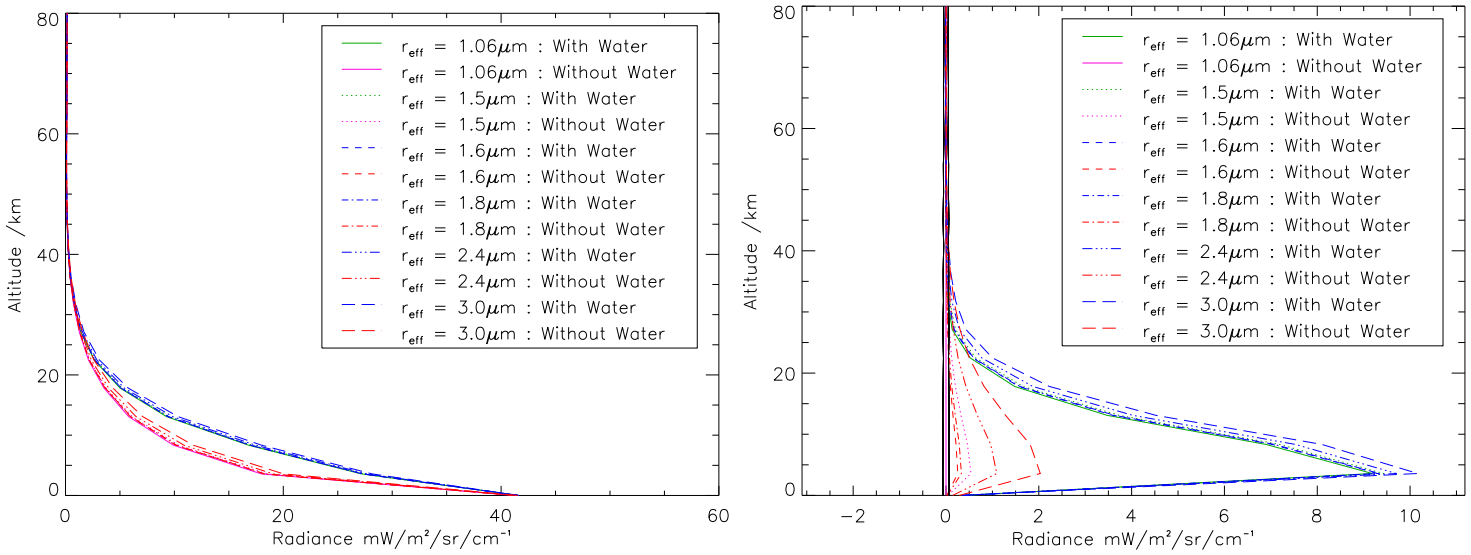
Table 5.9 | Detector Boresight Heights used for NEMESIS aerosol particle size simulations.

Detector №	Height (km)
PIX01	-1.2
PIX02	3.6
PIX03	8.3
PIX04	13.1
PIX05	17.8
PIX06	22.5
PIX07	27.1
PIX08	31.7
PIX09	36.2
PIX10	40.8
PIX11	45.2
PIX12	49.6
PIX13	54.0
PIX14	58.3
PIX15	62.6
PIX16	66.9
PIX17	71.1
PIX18	75.2
PIX19	79.4
PIX20	83.5
PIX21	87.5

different from the corresponding *no water* case, and that changes in r_{eff} lead to changes in radiance as well.

Looking at the vertical radiance profiles for both series it can be seen that the radiances for the dust series are greater than the those of the water ice series, for both *water* and *no water* cases. This is particularly noticeable at about 10 km. When comparing the *no water* and equivalent *water* cases for a given series and aerosol size distribution it becomes easy to disentangle the radiance contribution of the water from that of the aerosol. In the *no water* case the radiance in B2 is due to all atmospheric parameters other than water vapour, with the aerosol contribution being the dominant one. For the *water* case we can then see the additional radiance added by the presence of water vapour.

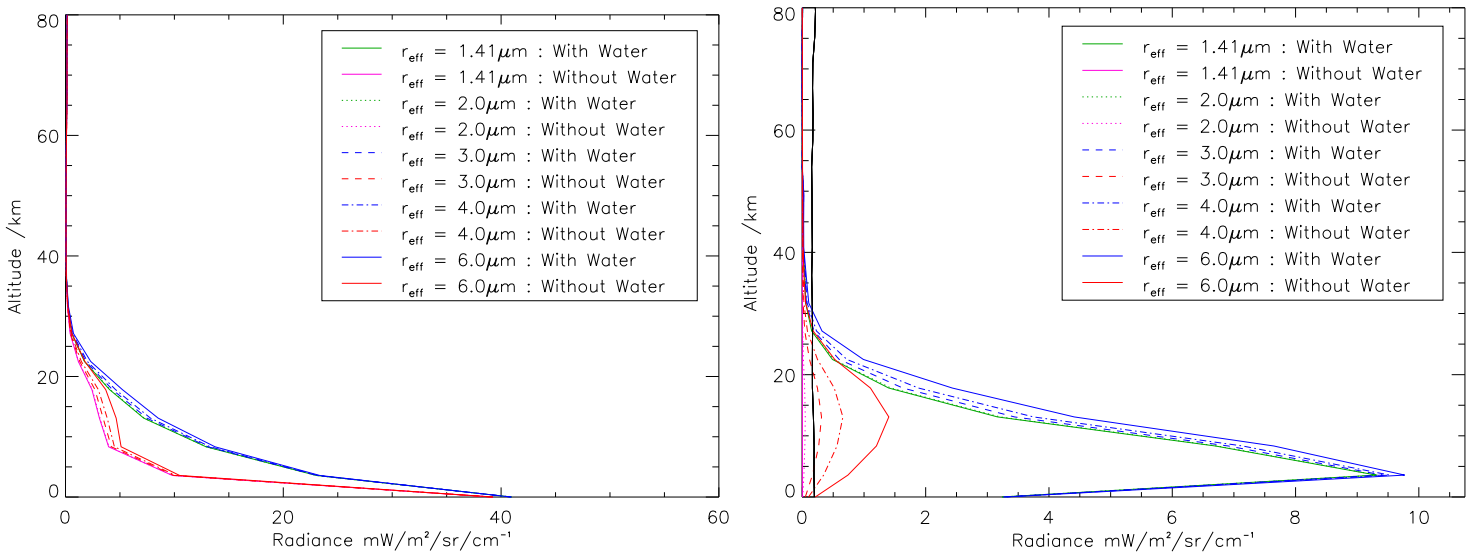
It can be seen that for both series all of the *water* cases (i.e. different size distributions) are clustered together as are all of the equivalent *no water* cases. This pattern is repeated in the radiance difference profiles. In Fig. 5.21b at 5 km (near the 500 ppmv peak of the water vapour profile, see water profile in Fig. 3.12) we see a spread in *no water* cases of 2 $\mathrm{mW/m^2/sr/cm^{-1}}$ and 1 $\mathrm{mW/m^2/sr/cm^{-1}}$ for the equivalent *water* cases. The *water*/*no water* difference at 5 km ranges from a maximum of 9 $\mathrm{mW/m^2/sr/cm^{-1}}$ for r_{eff}=1.06 μm to a minimum of 8 $\mathrm{mW/m^2/sr/cm^{-1}}$ for



(a) Radiance Profiles in B2 with A5 Normalized Dust

(b) Radiance Differences in B2 with A5 Normalized Dust

Figure 5.21 | **(a)** Synthetic radiance profiles in B2 using A5 normalized dust size distributions. A large difference is seen between the *water* and *no water* cases. Small changes are seen between different dust distributions. **(b)** Synthetic radiance differences in B2 using A5 normalized dust size distributions. The [r_{eff}=1.06 μm: *no water*] case is used as the 'zero' reference line. The black lines are MCS detector noise values. A large difference is seen between the *water* and *no water* cases. Small changes are seen between different dust distributions.



(a) Radiance Profiles in B2 with A4 Normalized Ice

(b) Radiance Differences in B2 with A4 Normalized Ice

Figure 5.22 | **(a)** Synthetic radiance profiles in B2 using A4 normalized water ice size distributions. A large difference is seen between the *water* and *no water* cases. Small changes are seen between different ice distributions. **(b)** Synthetic radiance differences in B2 using A4 normalized ice size distributions. The [r_{eff}=1.41 μm: *no water*] case is used as the 'zero' reference line. The black lines are MCS detector noise values. A large difference is seen between the *water* and *no water* cases. Small changes are seen between different ice distributions.

r_{eff}=3.0μm. For the water ice series the spread at 5 km in *no water* cases is 1 mW/m^2/sr/cm^{-1} and 0.5 mW/m^2/sr/cm^{-1} for the equivalent *water* cases. The *water*/*no water* difference at 5 km ranges from a maximum of 9.5 mW/m^2/sr/cm^{-1} for r_{eff}=1.41 μm to a minimum of 9.0 mW/m^2/sr/cm^{-1} for r_{eff}=6.0 μm.

In other words the radiance spread between profiles due to particle size distribution is smaller than the difference caused by the addition of water. This is a positive sign as it shows that, at the opacities and VMRs simulated, the change in B2 radiance using the measured filter profiles is mainly controlled by the presence or absence of water vapour rather than the change in aerosol size distribution.

For the *water* profiles the fractional contribution to the B2 radiance from aerosol (i.e. *no water* profile) is generally much bigger in the dust series than in the ice series for heights below about 15 km. This is likely due to the difference in aerosol distribution. The dust profile has a constant specific density with height (particles per gram of atmosphere) while the water ice distribution is confined to layer centred at 20 km (see H_1 in Fig. 3.12). The water ice layer lies above the water vapour (i.e. ice forms above the condensation height) reflecting the situation that would be found in reality. Though dust is not likely to have a uniform distribution with height, it does not have the same height range restriction and is often likely to be co-located with water vapour.

From these tests it can be seen that it is important to include dust and water ice aerosols in the retrieval process, as they make significant contributions to radiance in the B2 channel. The cases tested here reflect the radiative effects of aerosol in the optically thin domain; not including them would lead to the false attribution of radiance to water vapour leading to an overestimate of water vapour. In the optically thick domain it is likely the opposite would occur as limb paths will not fully probe the atmosphere. For the simulated opacities it is seen that including aerosols is important to the radiative transfer, but the choice of particle size distribution is less so as the water vapour signal is dominant. However, the correct choice of particle size distribution becomes more important as optical depths increase. Further testing is needed to gauge the impact on retrieval accuracy, this is done in the next section.

5.6 Summary

The tests and simulations in this chapter have shown that the intended procedure for retrievals of water vapour with MCS, using the B3/B2 detector radiance ratio, is not possible. As designed, the channels would have had similar sensitivities to aerosol and different sensitivities to water vapour. Using the B3/B2 ratio would then allow simultaneous retrieval of water vapour and aerosol. Unfortunately, because the B2 and B3 spectral bandpasses are wider than originally specified, both channels have similar sensitivities to dust and water and thus the B3/B2 ratio is useless.

As a consequence of the above the B2 channel must be used on its own in a two-stage water vapour retrieval. This is challenging as B2 is sensitive to both aerosol and water vapour. This fact was suggested by B2 radiance residual tests which sought to gauge the sensitivity of the channel to water vapour (§5.4). Subsequent simulations of the affect of dust and ice on B2 radiance confirmed that the channel has significant radiance contributions from aerosol when present.

6

Sensitivity Studies II: Effect of Aerosol Size on Retrievals

It was established in the previous chapter that the choice of aerosol size distribution has an impact on the B2 radiances. It is now important to gauge what effect using the wrong aerosol model would have on two-stage water retrieval accuracy. An analysis was performed that would simulate this. Firstly, radiative transfer simulations were performed with NEMESIS using normalized aerosol extinction cross-sections in a similar fashion to the previous section. The extinction cross-section profiles were normalized to the value of a chosen particle size distribution at their respective primary retrieval channel wavenumber, A5 (464 cm^{-1}) for dust and A4 (843 cm^{-1}) for water ice. This allows simulation using the same aerosol specific particle density (particles per gram of atmosphere) vertical profile, while holding the optical depth constant at the normalized wavenumber (see Eqn 3.39). These simulations were used to produce synthetic MCS measurements of model atmospheres that could be used for retrieval testing. Two series of simulated synthetic measurements were produced, one for testing dust and one for water ice.

Dust synthetic measurements were produced for model atmospheres using dust distributions from r_{eff}=1.06 to 2.4 μm with column optical depths, τ_{A5}, ranging from 0.01 to 0.1. Dust particle size distributions were normalized to the A5 value of the r_{eff}=1.06 μm distribution. Water ice synthetic measurements were produced for model atmospheres using ice distributions from r_{eff}=1.0 to 4.0 μm with column optical depths, τ_{A4}, ranging from 0.01 to 0.1. Ice particle

Table 6.1 | Locations of profiles from MCD (MY24 scenario, L_s=114°) with corresponding surface temperatures and water column abundances.

Model	Latitude	Longitude	Surface Temperature (K)	Water Column Abundance (pr. μm)
41	20.4N	90.5W	260	26
56	51.1N	85.4W	270	29
66	70.0N	79.3W	245	46

size distributions were normalized to the A4 value of the r_{eff}=1.41 μm distribution.

Secondly, two-stage water retrievals are performed on these synthetic measurements. For the dust series all retrievals are performed using the r_{eff}=1.06 μm normalization distribution and for the water ice series with r_{eff}=1.41 μm distribution. This is done regardless of the distribution that synthetic measurements being retrieved from were created with. The aim of this procedure is to test the retrieval accuracy of water vapour when the wrong aerosol distribution is used over a range of optical depths. Additionally, some tests were performed using covariance matrices and one-stage retrievals to assess if the impact of wrong retrieval aerosol distribution can be detected using this way.

6.1 Method

6.1.1 Synthetic Measurement Creation

Three northern hemisphere model atmospheres in summer (L_s=114°) were constructed using data from the MCD (MY24 scenario) for temperature, pressure, CO_2, N_2 and water vapour. Details of these are given in Tbl. 6.1. Dust profiles were constructed using a Conrath profile shape with an inflection coefficient of 0.007 (Conrath, 1975) then scaled to the required column optical depth. For water ice, a profile was extracted from the MCD which was then scaled to the required optical depth.

Aerosol size distributions are modelled using either the gamma or modified gamma distributions. Complex refractive indices are as described in §3.3.1. The gamma distribution is characterised via the first two moments of the distribution; $a = r_{eff}$, the effective radius of the dust particle (i.e. mean geometric dust grain radius) and $b = v_{eff}$ the effective width of the distribution (Hansen & Travis, 1974) as defined by Eq. 5.1. The modified gamma distribution is characterised by the three parameters a, b and c as defined in §3.3.1, but also supplies values

Table 6.2 | Dust size distributions used to generate synthetic measurements. Normalization distribution is marked with an asterisk.

r_{eff} (μm)	v_{eff}	Type
1.06*	0.3	Modified Gamma (a=2.24, b=8.04, c=0.647)
1.4	0.3	Gamma
1.8	0.3	Gamma
2.4	0.3	Gamma

Table 6.3 | Ice size distributions used to generate synthetic measurements. Normalization distribution is marked with an asterisk.

r_{eff} (μm)	v_{eff}	Type
1.0	0.1	Gamma
1.41*	0.15	Modified Gamma (a=12.6, b=31.4, c=0.436)
2.0	0.1	Gamma
4.0	0.1	Gamma

for r_{eff} and v_{eff}.

Sets of dust/ice particle size distributions were chosen to reflect a range of conditions on Mars based on the work of Wolff & Clancy (2003), Wolff et al. (2006) and Kleinböhl et al. (2009, 2011). Details of these are given in Tables 6.2 and 6.3. Extinction cross-sections were generated for these using the complex refractive index data described above over the range 100–1200 cm^{-1}. The extinction profiles were then normalized: for dust to the A5 values of the r_{eff}=1.06 μm profiles and for water ice to the A4 values of the r_{eff}=1.41 μm profiles. The normalization procedure was the same as that used in §5.5.

For each series GenerateMCSSPX (part of the NEMESIS suite) was used with model atmospheres to generate the synthetic MCS observations for use in the retrievals. This included limb and nadir viewing radiances/detectors together with the effect of MCS detector FOVs. For the dust series synthetic observations were produced for model atmospheres at each normalized size distribution, with five different column optical depths, τ_{A5}: 0.01, 0.025, 0.05, 0.075 and 0.1. For the water ice series this process was repeated for water ice column optical depths, τ_{A4}: 0.01, 0.025, 0.05, 0.075, 0.1. In addition, the water ice model atmospheres included a dust profile with τ_{A5}=0.025 using the dust normalization distribution, r_{eff}=1.06 μm. The optical depths and profiles were chosen as representative of the conditions found on Mars during northern hemisphere summer. Dust and ice were modelled with no scattering (absorption-only, see §3.3.4).

As part of the modelling process by GenerateMCSSPX random perturbations are introduced into each of the profiles and surface temperature. Perturbations are added to the atmospheric variable, x, as

$$x_p(i) = x(i) + dx(i), \tag{6.1}$$

where x_p gives the randomly perturbed value and dx is the random perturbation. The variable x can either be a vector (e.g. temperature profile) or a scalar (e.g. surface temperature), where i denotes the element of x. For vector cases, such as a temperature/composition profile each element, i corresponds to the profile value at a given height. When x is a vector dx is calculated as

$$dx(i) = A_x \cdot \sin\left(\frac{2\pi \cdot i}{l_x} + \phi_x\right) \cdot \epsilon(i), \tag{6.2}$$

with

$$A_x = \text{RAND}([0,1]) \tag{6.3}$$

$$l_x = l_c \cdot (0.5 + 19.5 \cdot \text{RAND}([0,1])) \tag{6.4}$$

$$\phi_x = 2\pi \cdot \text{RAND}([0,1]), \tag{6.5}$$

where l_c is the correlation length (see Chapter 4), RAND([0, 1]) is a pseudo-random number generated between 0 and 1 and $\epsilon(i)$ is a vector that scales the perturbation: for temperature, 2 K, for dust and ice, $x(i)/2$ (specific particle density) and for water vapour $x(i)/2$ (VMR). To vary surface temperature the perturbation is calculated as

$$dx = 2\,(\text{RAND}([0,1]) - 0.5) \cdot \epsilon, \tag{6.6}$$

where ϵ=2 K. Examples of the models used before perturbation/scaling are given in Fig. 6.1.

6.1.2 Retrieval of Synthetics

Retrievals of the synthetic MCS observations were performed with NEMESIS in two stages, with temperature, aerosol and surface temperature being retrieved in the first stage. For the second stage, the water retrieval, a bracketed approach was used. Three different *a priori* were used, all using VMRs constant with height, 10^{-7}, 10^{-5} and 10^{-3} with a 50% *a priori* error. These are hereafter referred to as the 'left', 'centre' and 'right' brackets. Three water retrievals were then

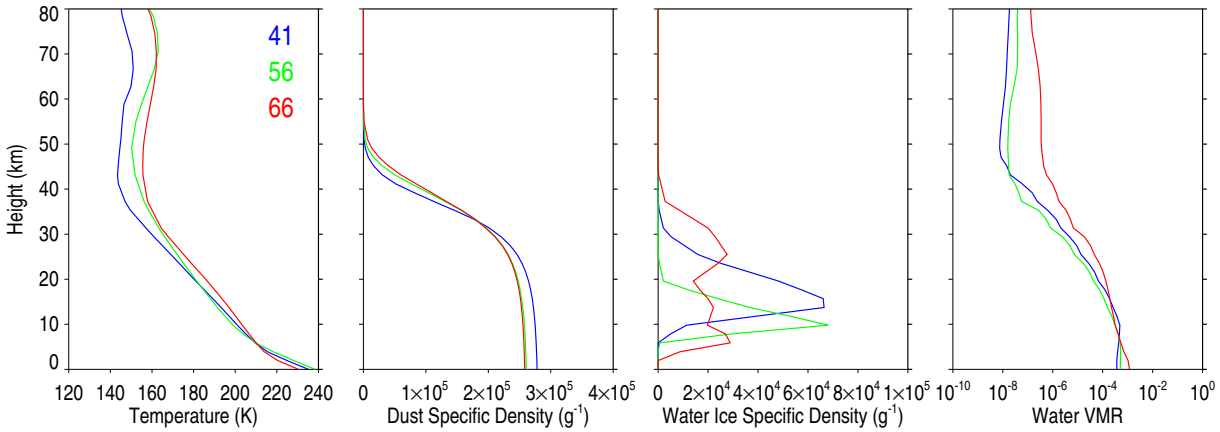


Figure 6.1 | Model profiles for temperature, aerosol and water vapour used before perturbation. They have been colour coded by model (see legend). Dust uses Conrath-type profiles, with τ_{A5}=0.025. While for ice a layer, with τ_{A4}=0.01 is used. For other aerosol column optical depths modelled the same profile shapes are used but scaled.

performed with the results of the first stage, one with each bracket. This allows for sensitivity testing of the water retrieval. Where there is information in the retrieval the three retrieved profiles will converge, while elsewhere they will relax towards their initial *a priori* values.

For the first stage the *a priori* profiles for temperature/pressure, CO_2 and N_2, with a value for surface temperature, were extracted from the MCD (MY24 scenario) corresponding to the time and location of the synthetic MCS observation being used (local surface time 15h). The dust profile is uniform with height with $\tau_{A5}=10^{-3}$ (50% *a priori* error). When water ice is used the profile is uniform with height with $\tau_{A4}=10^{-4}$ (200% *a priori* error). Dust and ice were retrieved assuming no scattering (absorption-only, see §3.3.4).

The retrieval/analysis procedure is as follows for each model atmosphere with its corresponding synthetic MCS observation:

Stage One: Using all of *a priori* information, retrievals of surface temperature, temperature, dust and water ice (for the ice series) were performed using channels A1–A5 and B1. For dust the cross-sections from r_{eff}=1.06 μm normalization distribution were used. For ice, when retrieved the cross-sections from r_{eff}=1.41 μm normalization distribution.

Stage Two: The retrieved values from the first stage are used to set the atmospheric state for the water retrieval. Using each of the water bracket *a priori* profiles the water retrieval is performed three times with the B2 channel.

Stage Three: Analysis is performed to examine the difference between the model atmosphere and the retrieved profiles. This is in two stages. Firstly, a visual inspection of the

difference is carried out of the modelled and retrieved profiles. Secondly, a numerical approach is performed using a difference metric described in the next section.

6.2 Results

6.2.1 Dust Series: First Stage

For this series the model dust cross-sections at A5 for r_{eff} modes 1.06–2.4 μm were normalized to the value from the r_{eff}=1.06 μm. This normalization distribution was then used for the retrievals of all modes and all opacities, with τ_{A5} ranging from 0.01 to 0.1.

In the first stage retrievals the *a priori* (APR) temperature is very close to the to the retrieved profiles, essentially modelling it as known. It allows the isolation of the effects of wrong retrieval mode (i.e. dust size distribution) on dust and water, and is an approximation of using the L2 retrievals of Kleinböhl et al. (2009) as the APR. These are similarly likely to lie very close to the true profile. Retrieval of temperature and dust is similar in all cases and is a close fit to the modelled profile used to generate the synthetic measurements. This holds even for the worst-case scenario, where the measurements were modelled with r_{eff}=2.4 μm—the dust mode furthest from the retrieval mode, r_{eff}=1.06 μm. This is shown in Fig. 6.2, which is representative of all cases, as the results are almost identical. The figure gives the results of the temperature retrieval, improvement factor of the temperature profile and the dust retrieval.

The improvement factor, $\mathbf{x_i}$, is defined as:

$$\mathbf{x_i} = 1 - \left(\frac{\mathbf{S_n}/\mathbf{x_n}}{\mathbf{S_a}/\mathbf{x_a}} \right) \tag{6.7}$$

where $\mathbf{x_a}$ and $\mathbf{x_n}$ are the APR and retrieved values of water respectively; and $\mathbf{S_a}$ and $\mathbf{S_n}$ are the corresponding errors (as defined in Chapter 4). As $\mathbf{S_n}$ decreases, $\mathbf{x_i}$ approaches one. The improvement factor is an indicator of where information is found in a retrieval, with values closer to one indicating more information. In the middle panel of the figure it can be seen that most information is in the 5–60 km range. This can be verified by looking at the top panel and seeing that the retrieved profile (black line) follows the model profile (red line) most closely in that height range and relaxes back to the APR elsewhere. For dust, the retrieval fits the model up to 50 km and even captures a lot of the perturbation 'wiggles' before relaxing back to the APR.

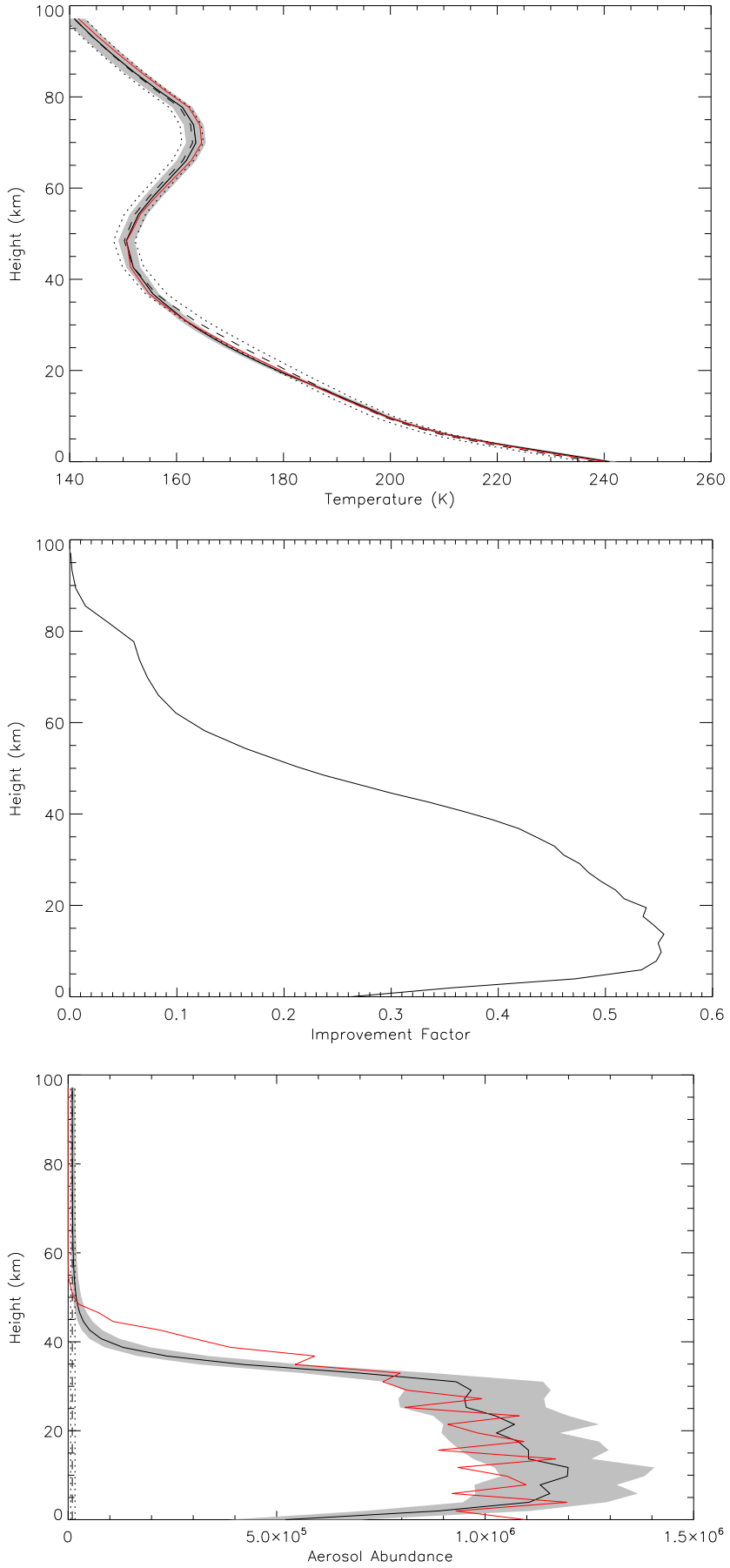


Figure 6.2 | Retrieved profiles for [r_{eff}=2.4 μm, τ_{A5}=0.1, Model 56] case: (**Top**) Temperature, (**Middle**) Temperature Improvement Factor, (**Bottom**) Dust (particles g^{-1}). It was retrieved assuming r_{eff}=1.06 μm. Key: *A priori* (dashed line), *A priori error* (dotted lines), retrieved profile (black line), retrieval error (grey shading), synthetic measurement profile (red line).

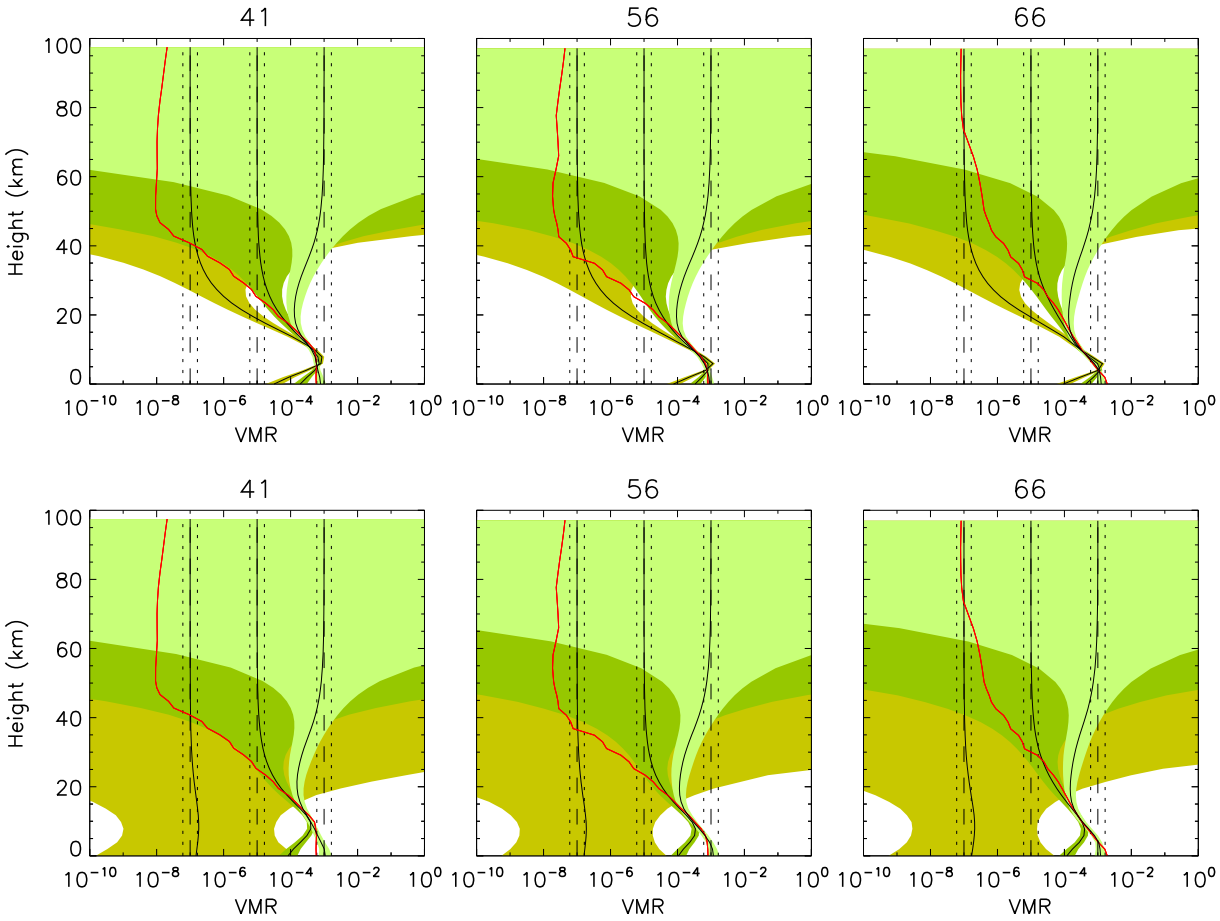


Figure 6.3 | Bracket water retrievals for r_{eff}=1.06 µm cases: (**Top**) τ_{A5}=0.01 (**Bottom**) τ_{A5}=0.1. All retrieved assuming r_{eff}=1.06 µm. Key: *A priori* (dashed line), *A priori error* (dotted lines), retrieved profile (black line), retrieval error (green shading), synthetic measurement profile (red line).

6.2.2 Dust Series: Second Stage (Water)

A general idea of the performance trend in the dust series retrievals can be demonstrated by visual examination of the water retrieval profiles. This is done by plotting the model profile and superimposing all of the bracket retrieval profiles. Areas where the bracket and model profile converge are those where the retrieval has information and is successful. Showing the results of all the retrievals in this way here is impractical. Therefore we limit results shown here to the extreme cases of dust model mode and opacity, as these are sufficient to show the trend. After the visual inspection results the numerical analysis is discussed. This gives a fuller picture of the behaviour as the model dust mode and opacity are varied.

Fig. 6.3 shows the retrievals for the model mode, r_{eff}=1.06 µm. This is the same as the retrieval mode. This is a best-case scenario as it shows what happens when the dust mode is known. Results are shown for the lowest optical depth case, τ_{A5}=0.01 and the highest, τ_{A5}=0.1.

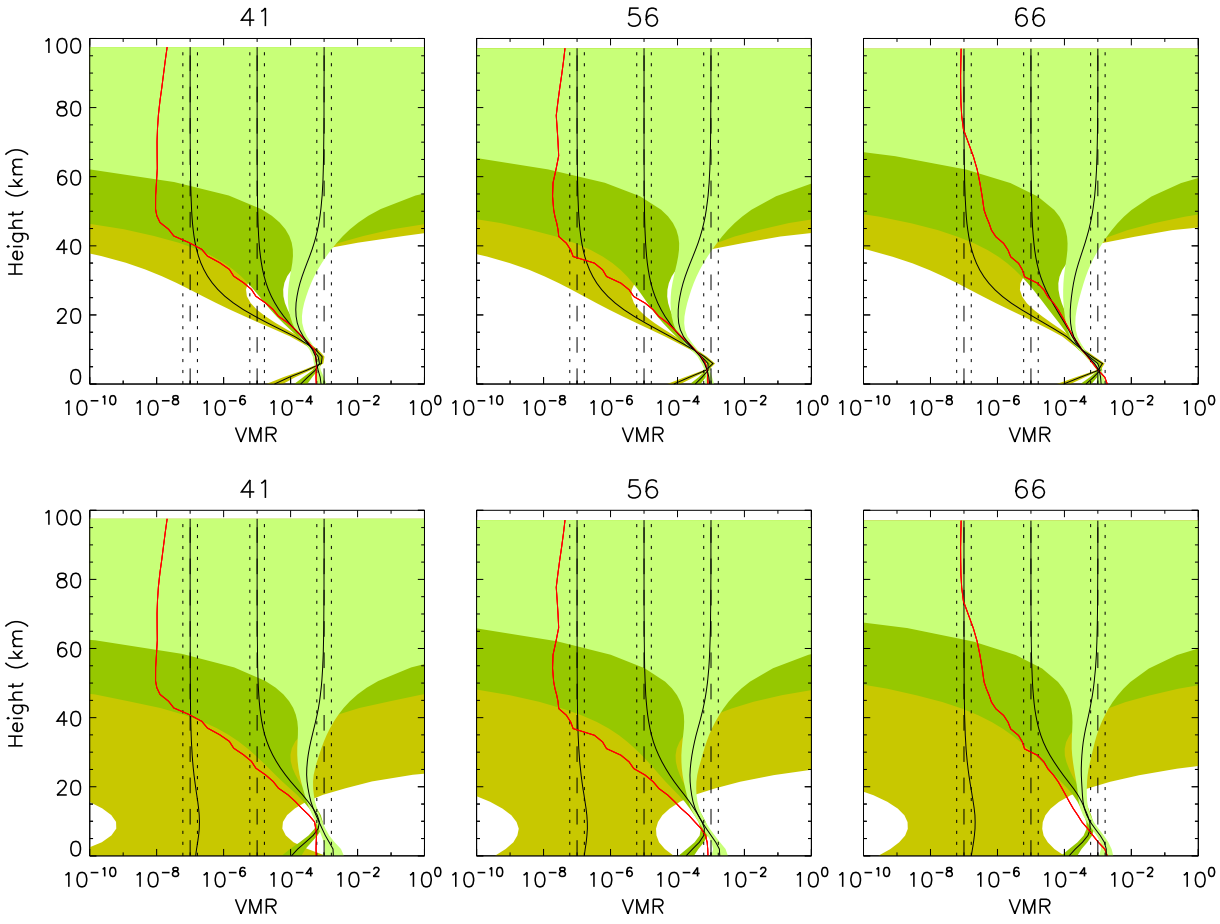


Figure 6.4 | Bracket water retrievals for r_{eff}=2.4 µm cases: (**Top**) τ_{A5}=0.01 (**Bottom**) τ_{A5}=0.1. All retrieved assuming r_{eff}=1.06 µm. Key: *A priori* (dashed line), *A priori error* (dotted lines), retrieved profile (black line), retrieval error (green shading), synthetic measurement profile (red line).

It can be seen that for the τ_{A5}=0.01 case the retrievals all converge on the true profile in the 5–25 km region. For the high opacity case, τ_{A5}=0.1, the results are still good, with only the left bracket failing to move towards the model water profile. The reduced information content from the high optical depth is the probable cause. This affects the left bracket profile the most as the radiance from water vapour will be the smallest due to it having the lowest VMR. For this case, the radiance in the channel will be dominated by radiance due to dust and hence the functional derivative for water (see §4.6.3) will be very small, i.e. low retrieval sensitivity to water vapour.

Fig. 6.4 shows the retrievals for the model mode, r_{eff}=2.4 µm, retrieving with the wrong mode (r_{eff}=1.06 µm), the furthest possible from the model mode. For the τ_{A5}=0.01 case the retrieval suffers little from the use of the wrong mode, giving a good fit like for the correct mode retrieval discussed above. As the opacity increases the effect of using the wrong mode becomes evident. Initially the results look similar to those τ_{A5}=0.1 retrievals above where the retrieval and model mode are the same. A similar behaviour is seen of centre and right profiles

converging in the 5–25 km range, with failure of the left bracket. Closer scrutiny reveals that though the centre and right profiles converge, they are offset from the true profile. The impact of the using the wrong dust mode is that the extinction cross-section at B2 is larger than it should be, resulting in extra radiance in B2 which is then misinterpreted by the retrieval as additional water vapour.

A clear trend has emerged, increasing opacity or increasing the difference in r_{eff}, between the modelled and retrieved dust modes, leads to poorer retrieval accuracy. Increasing both together produces the most erroneous results. To investigate further we now perform a numerical-based comparison between the different cases. This is a complex problem, but a simple metric can be created by which to evaluate the retrieval accuracy of models to the first order. The fractional difference between the modelled and retrieved values is given by

$$\mathbf{d_x}\% = \frac{|\mathbf{x_b} - \mathbf{x_0}|}{\mathbf{x_0}} \cdot 100\%, \tag{6.8}$$

where $\mathbf{d_x}$ gives percentage difference between the retrieved bracket profile, $\mathbf{x_b}$ and the model $\mathbf{x_0}$; these values are all vectors. Then for each bracket, the mean over height of the 5–25 km values, $\overline{\mathbf{d_x}}\%$, is calculated to produce a single-number metric. This range is chosen as it is the region of highest information content in the retrieval (as seen in the figures above). As retrieval inaccuracy increases $\overline{\mathbf{d_x}}\%$ increases.

This metric can then be used to create bracket difference plots, Figs 6.5–6.7, showing how retrieval accuracy fares over a changes in opacity and dust mode for the three different atmospheric models: 41, 56 and 66. The plots consist of four panels, with the model atmosphere given in the panel title. One panel for each of the retrieval 'brackets', left, centre and right as defined in the previous section. One additional panel the 'All Bracket' contains the mean values of $\overline{\mathbf{d_x}}$ over the three bracket points to give an overall picture of all the water retrievals for that atmospheric model. Within each panel the modelled (synthetic measurement) dust mode is given by the X-axis and the retrieval difference, $\overline{\mathbf{d_x}}\%$ on the Y-axis. Results for differing modelled dust modes are grouped by τ_{A5}, represented by a line linking the results. The optical depth is indicated by the line colour, e.g. red lines give results where τ_{A5}=0.1

When looking at the 'All Bracket' results (and most of the others) for all models, the same trend as observed above is seen. Increasing the opacity or the model-retrieval r_{eff} difference independently leads to lower accuracy. Increasing both leads to the most inaccurate results.

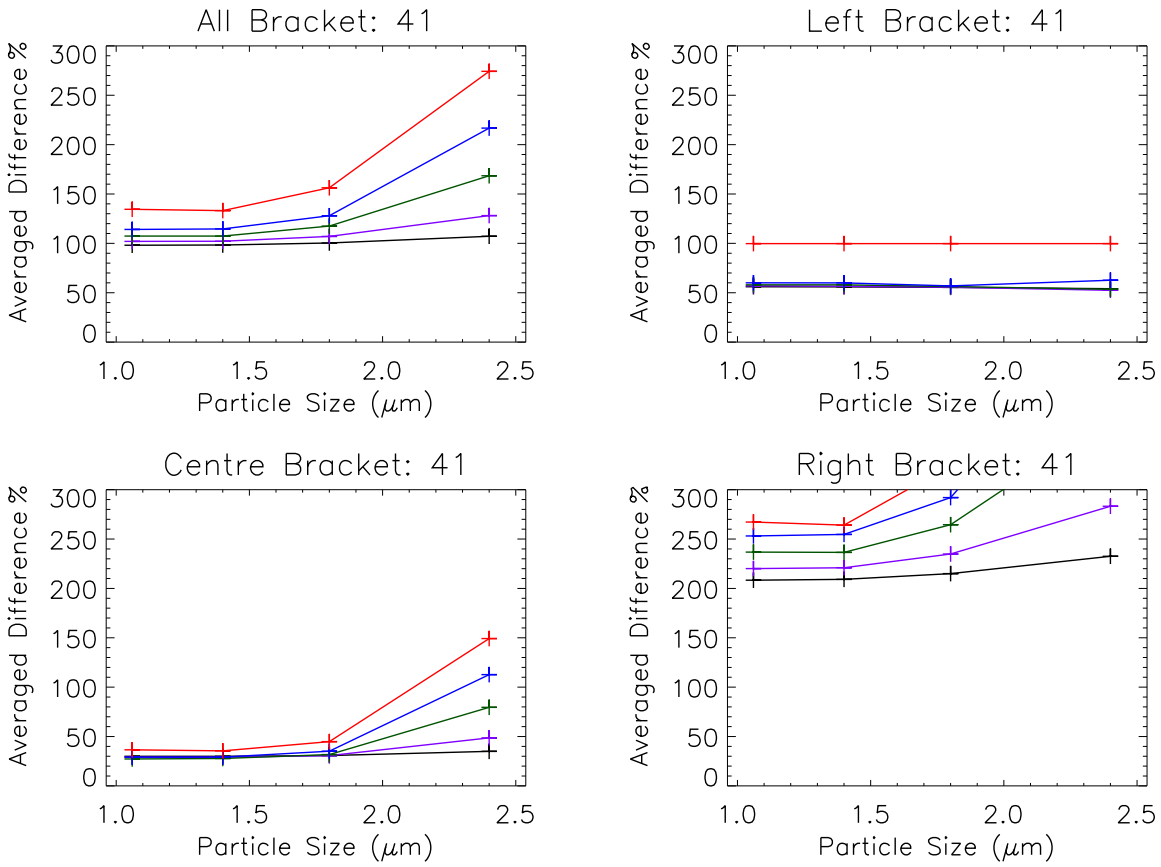


Figure 6.5 | Bracket difference ($\overline{\mathbf{d_x}}\%$) plots for dust series model 41. Lines coloured by τ_{A5} opacity: 0.01 (black), 0.025 (purple), 0.05 (green), 0.075 (blue), 0.1 (red).

By examining the individual bracket difference profiles it can be seen that the overall retrieval accuracy varies from bracket to bracket. The left bracket results tend to be the poorest followed by the right bracket, with the centre bracket as the most accurate. In addition the left brackets are least likely to follow the overall pattern, e.g. left bracket 56 results. The right bracket is better, but the values of $\overline{\mathbf{d_x}}\%$ are much worse, up to ten times the centre bracket values (right bracket 41). These results point to the fact the initial choice of APR (and error) has some importance, as the best results are achieved when the APR is closest to the final answer, viz. the centre profile. This is tempered by the fact that the brackets used cover four orders of magnitude (10^{-7}–10^{-3}) in VMR—the study is testing extremes. For real retrievals the APR profiles are likely to be much closer to the actual water vapour abundances and so less problematic.

The left bracket retrievals tend to be the most inaccurate due to being the 'least sensitive', as discussed earlier. The low water sensitivity helps explain the odd results seen in the left bracket plots of 66 where many of the τ_{A5} results for the 0.025–0.075 results appear to give better results than the low opacity 0.01 case. For these cases the higher dust opacity gives

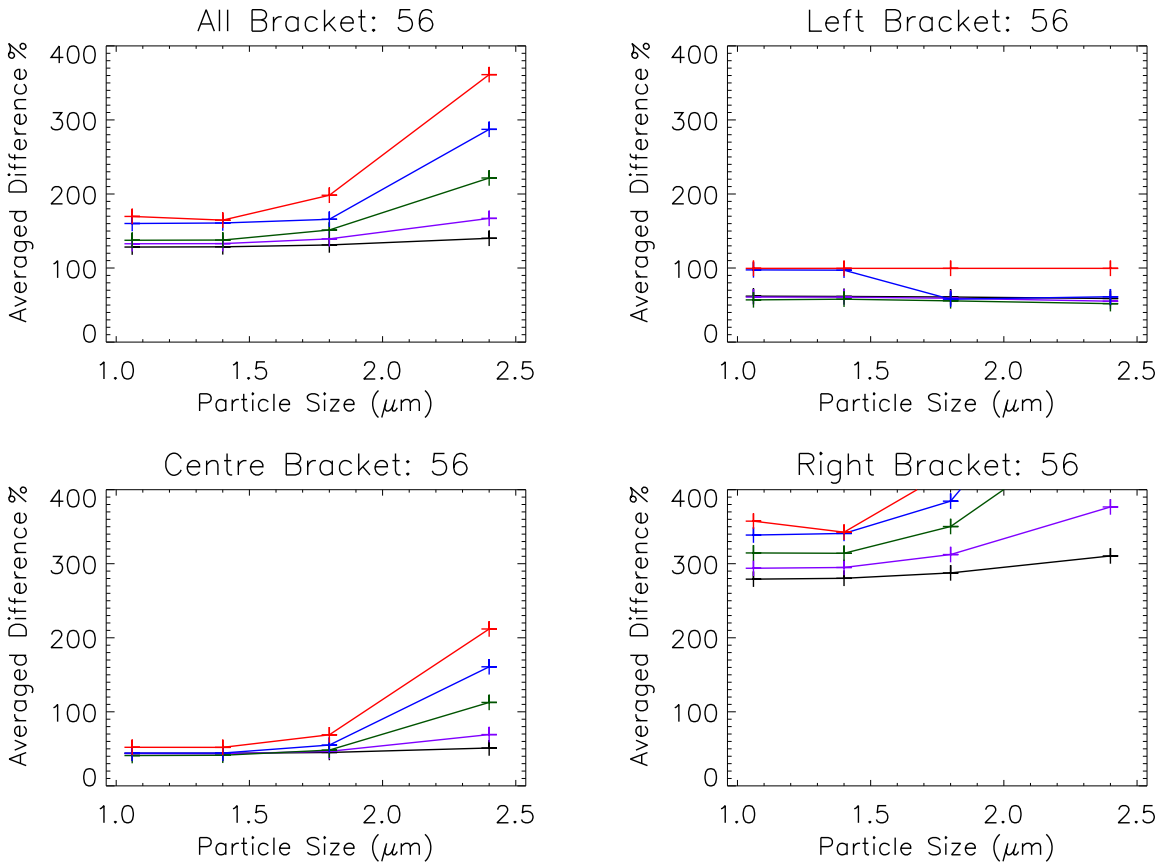


Figure 6.6 | As Fig. 6.5 for dust series model 56.

more radiance in B2, and the retrieval mistakes this for additional water vapour (as dust and water are co-located in height). The effect becoming more pronounced as the model dust mode becomes larger. The larger the model dust mode, the larger the false signal, because of the larger corresponding B2 cross-section value. As the left bracket is on the side of less water than the model, this effect pushes the retrieval in the right direction, for the wrong reason, giving the impression of increased accuracy. Unfortunately there is no simple way of using our simple metric, $\overline{\mathbf{d_x}}\%$, to isolate such cases.

6.2.3 Water Ice Series: First Stage

For this series the ice cross-sections at A4 for r_{eff} model modes 1.0–4.0 μm were normalized to the value from r_{eff}=1.41 μm. This distribution is then used for the retrievals of all modes and all opacities, with τ_{A4} ranging from 0.01 to 0.1. Dust was modelled with τ_{A5}=0.025 and was modelled and retrieved using the r_{eff}=1.06 μm, i.e. assuming dust mode was known for the retrieval.

For the first stage retrievals the accuracy of the results follows the same pattern as for

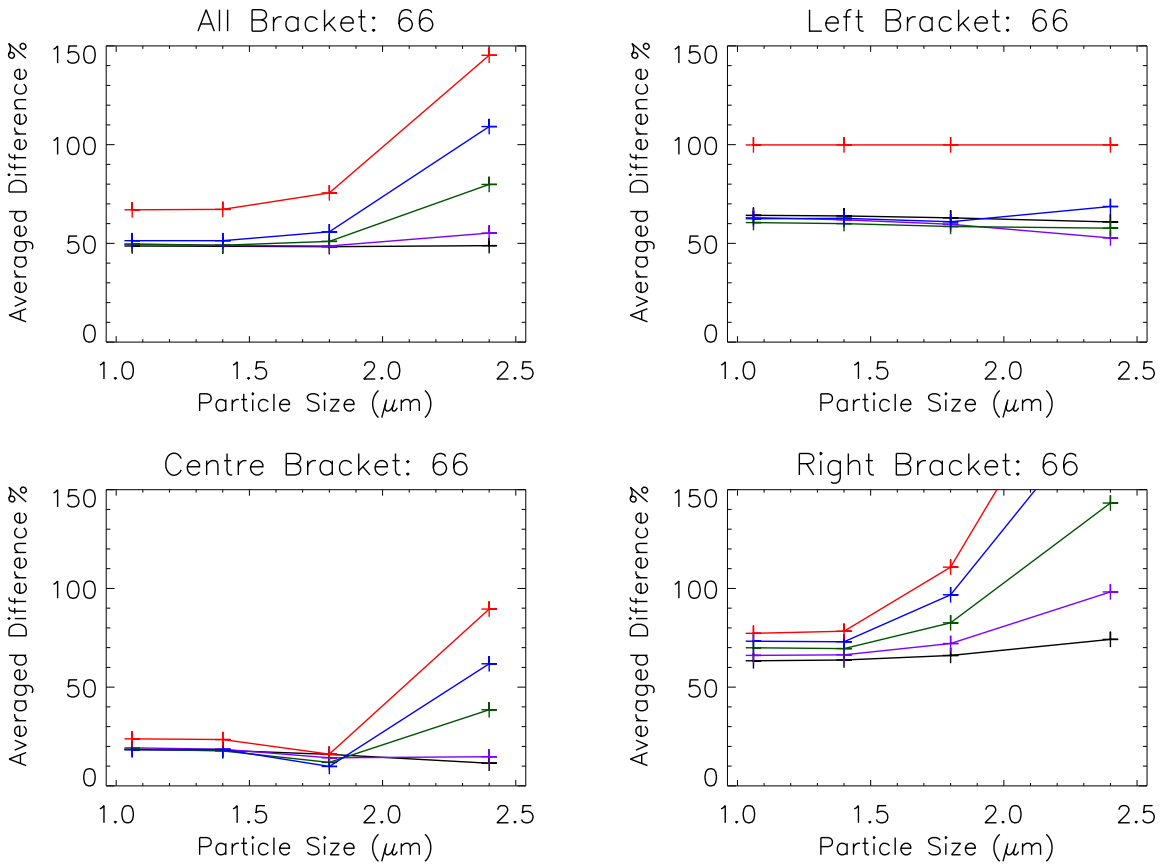


Figure 6.7 | As Fig. 6.5 for dust series model 66.

those of the dust series. Even for r_{eff}=4.0 μm mode, when the retrieval mode is the most incorrect, the retrieved temperature, dust and ice profiles have high accuracy. However, as the opacity increases the accuracy of the first stage retrievals suffers. Retrieval accuracy decreases even further as the difference between the model and retrieval ice modes increases combined with increasing opacity. This is demonstrated by the worst-case scenario in Fig. 6.8 showing the retrieved temperature, dust and ice profiles for the [r_{eff}=4.0 μm mode, $\tau_{A4} = 0.1$] case. Although the ice retrieval is a close match to the model profile, the temperature retrieval and dust retrieval have been significantly affected. The temperature profile underestimates by about 10 K in the 5–20 km region while dust overestimates by a factor of more than three at 20 km. The problems shown become significant at $\tau_{A4} = 0.05$.

Part of the problem is that ice extinction cross-sections are larger than equivalent dust values at most wavelengths. This is not normally a big problem as the ice optical depths tend to be lower. Another problem are the extra degrees of freedom added to the retrieval by retrieving both dust and ice. The different APRs and proportional errors used (see §6.1.2) result in differing retrieval sensitivities to dust and ice, which may become imbalanced at the higher opacities and

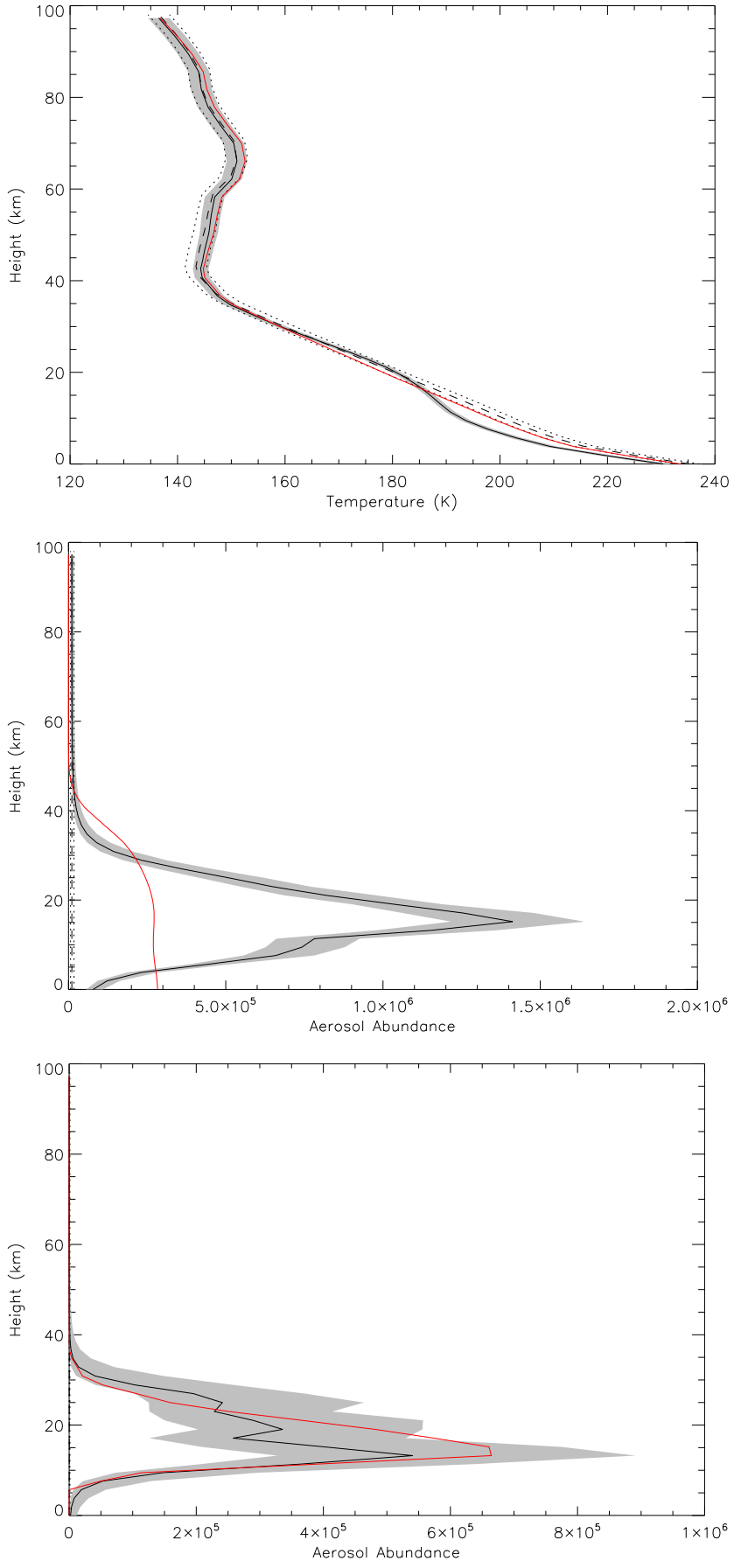


Figure 6.8 | Retrieved profiles for [r_{eff}=4.0 μm, τ_{A4}=0.1, Model 41] case: (**Top**) Temperature, (**Middle**) Dust (particles g^{-1}), (**Bottom**) Ice (particles g^{-1}). It was retrieved assuming r_{eff}=1.41 μm. Key: *A priori* (dashed line), *A priori error* (dotted lines), retrieved profile (black line), retrieval error (grey shading), synthetic measurement profile (red line).

larger incorrect ice modes.

6.2.4 Water Ice Series: Second Stage (Water)

To gauge a general trend in the ice series behaviour we start by visual inspections of retrieval profiles, showing sample cases here. Fig. 6.9 shows the retrievals for the model mode, r_{eff}=1.41 μm, retrieving with the correct mode. Results are shown for the lowest optical depth case, τ_{A4}=0.01, and the highest, τ_{A4}=0.1. It can be seen that for the τ_{A4}=0.01 case the retrievals all converge on the true profile in the 5–25 km region. For the high opacity case, τ_{A4}=0.1, the results are significantly affected, much more so than for the equivalent dust series case. For all brackets in the model 41 and 56 cases the retrievals do not match well, significantly underestimating. Only for the 66 case do the centre and right brackets match well. The failure of theses cases is likely due to reduced information content in B2 due to the high ice opacity, with the problem compounded by the presence of dust as well. The reason for the difference in 66 is likely due to the difference in the ice layer distribution for this case compared with the other two models (see ice panel of Fig. 6.1). For the other two models the ice is concentrated in a single peak layer with high specific densities concentrated in that region. This leads to high optical depths in the limb paths at the peak regions. For the 66 model the ice layer is spread out over a larger altitude range with lower peak ice abundances, leading to lower optical limb depths, and more information content in B2 for water vapour.

Fig. 6.10 shows the retrievals for the model mode, r_{eff}=1.0 μm, retrieving with the wrong mode (r_{eff}=1.41 μm). For the τ_{A4}=0.01 case the retrieval suffers little from the use of the wrong mode, giving a good match like for the correct mode retrieval discussed above, with a slight overestimate at 5 km. As the opacity increases the effect of using the wrong mode becomes significant. For the model 41, the centre and right brackets converge, but with a significant offset below the true profile abundances, while the left retrieval barely moves. For the model 56 results there is some loose convergence of the three brackets, but they oscillate about the true profile, overestimating offsets below 10 km and underestimating above. For the 66 case the right and centre brackets provide a decent match to to the true profile. This is probably due to the spread of the ice layer as described for the previous figure, meaning the impact of the ice layer is reduced on B2 limb paths. As for the dust series, the offsets are due to the difference in B2 extinction cross-section between the retrieval and model modes and their consequent impact on B2 radiances.

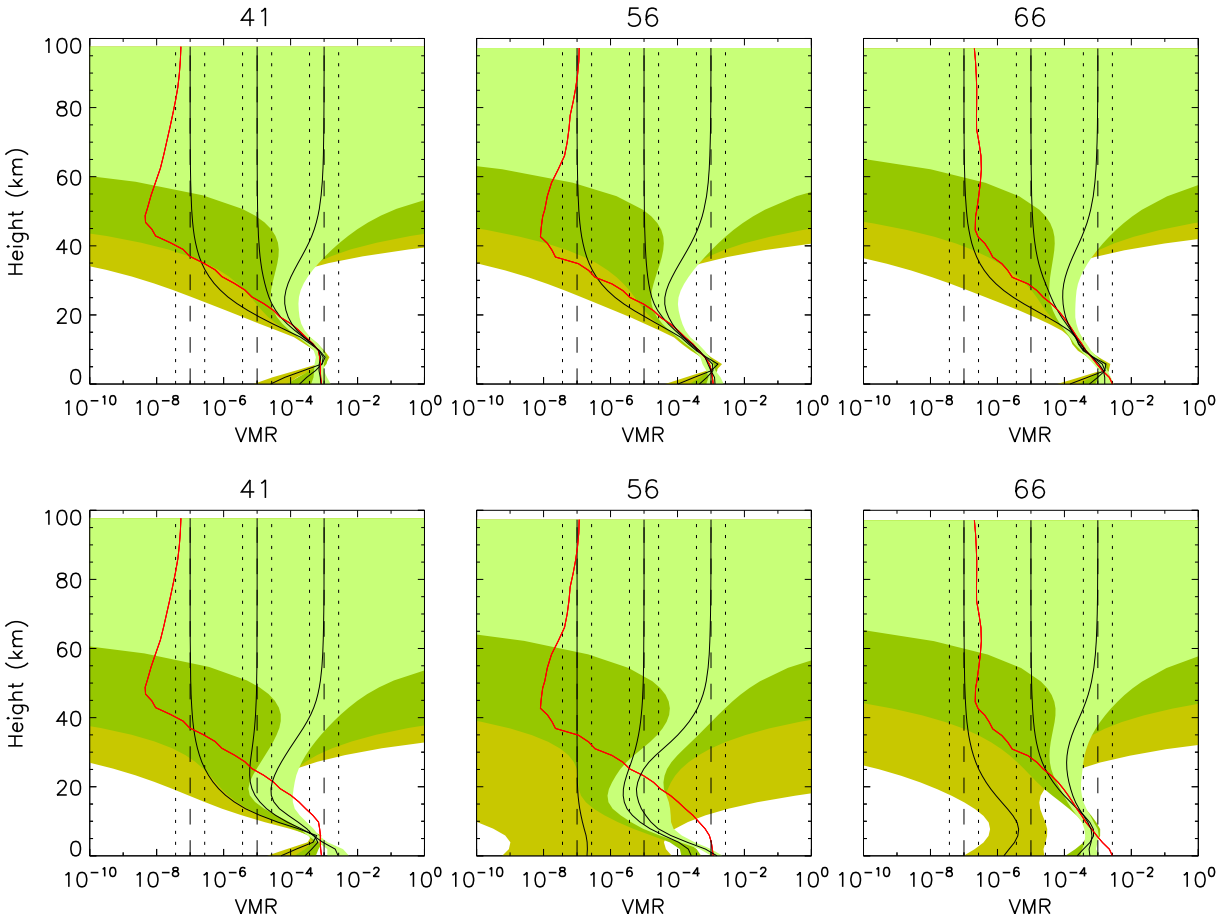


Figure 6.9 | Bracket water retrievals for r_{eff}=1.41 µm cases: (**Top**) τ_{A4}=0.01 (**Bottom**) τ_{A4}=0.1. All retrieved assuming r_{eff}=1.41 µm. Key: *A priori* (dashed line), *A priori error* (dotted lines), retrieved profile (black line), retrieval error (green shading), synthetic measurement profile (red line).

Fig. 6.11 shows the retrievals for the model mode, r_{eff}=4.0 µm, retrieving with the wrong mode (r_{eff}=1.41 µm). For the τ_{A4}=0.01 case the retrieval suffers little from the use of the wrong mode, giving results like those of the equivalent r_{eff}=1.0 µm case. For higher optical depths the impact on the retrievals is severe. For the model 41 case the three bracket profiles converge with a significant positive offset. For the model 56 case the centre bracket matches reasonably, while the right bracket has a positive offset and the left bracket does not move much. For the 66 case the impact is most severe with only the right profile actually changing from the APR and even then with a significant negative offset.

Numerical analysis plots for the second stage water retrievals are given in Figs 6.12–6.14 which shows plots of the difference metric, $\overline{\mathbf{d_x}}$%, where higher values indicate poorer retrieval accuracy. Results are grouped and coloured by opacity as for the dust series. Panel titles give the atmospheric model number (41, 56 or 66).

Similarly to the dust series results, higher ice optical depths, or model ice modes further

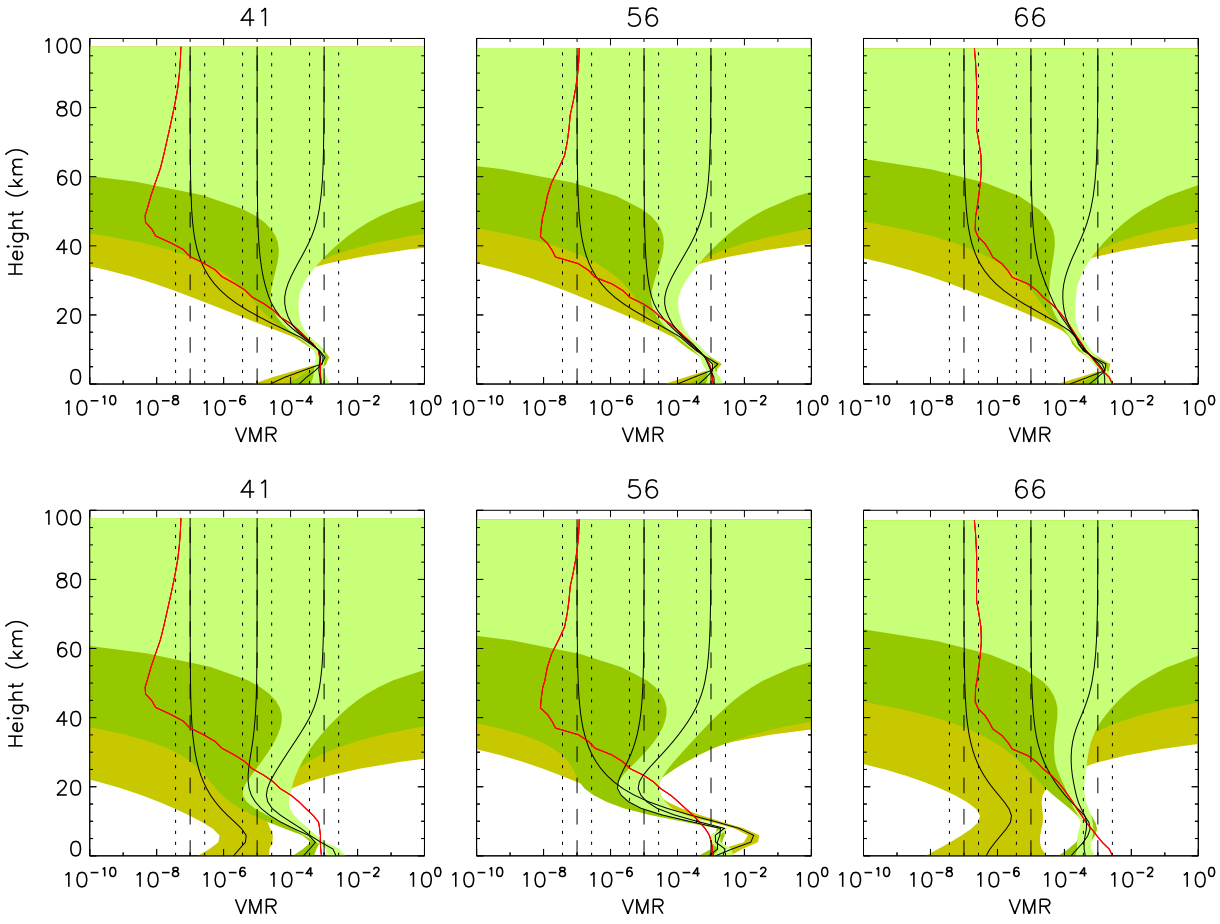


Figure 6.10 | Bracket water retrievals for r_{eff}=1.0 µm cases: (**Top**) τ_{A4}=0.01 (**Bottom**) τ_{A4}=0.1. All retrieved assuming r_{eff}=1.41 µm. Key: *A priori* (dashed line), *A priori error* (dotted lines), retrieved profile (black line), retrieval error (green shading), synthetic measurement profile (red line).

from the retrieval mode will generally result in higher values of $\overline{\mathbf{d_x}}\%$ corresponding to reduced retrieval accuracy. The pattern is most plain for the 'All Bracket' and Centre panels of 41 in Fig. 6.12. For the other models, 56 and 66, the results are less strict in following the pattern. One reason for this is likely due to first stage retrieval errors described earlier cascading into the water stage, but to differing degrees causing a less predictable result. Secondly, is a failure of the difference metric, $\overline{\mathbf{d_x}}\%$, by the way the averaging is done. This is because when differences span over many orders of magnitude there is a bias towards lower values of $\overline{\mathbf{d_x}}\%$ in the averaging because it is calculated with the absolute value of the difference. This is illustrated by looking at the the difference in LOG10 space. Here, overestimating by a factor of 10 (i.e. retrieving 10 times the true abundance) would be the same as underestimating by a factor of 10, giving the same difference, i.e. $|\log_{10}(\mathbf{x_b}) - \log_{10}(\mathbf{x_0})|$, whereas $\overline{\mathbf{d_x}}\%$ as calculated does not. In other words, consistent underestimating in normal space provides lower values of $\overline{\mathbf{d_x}}\%$.

As for the dust series the overall retrieval accuracy varies from bracket to bracket, with the

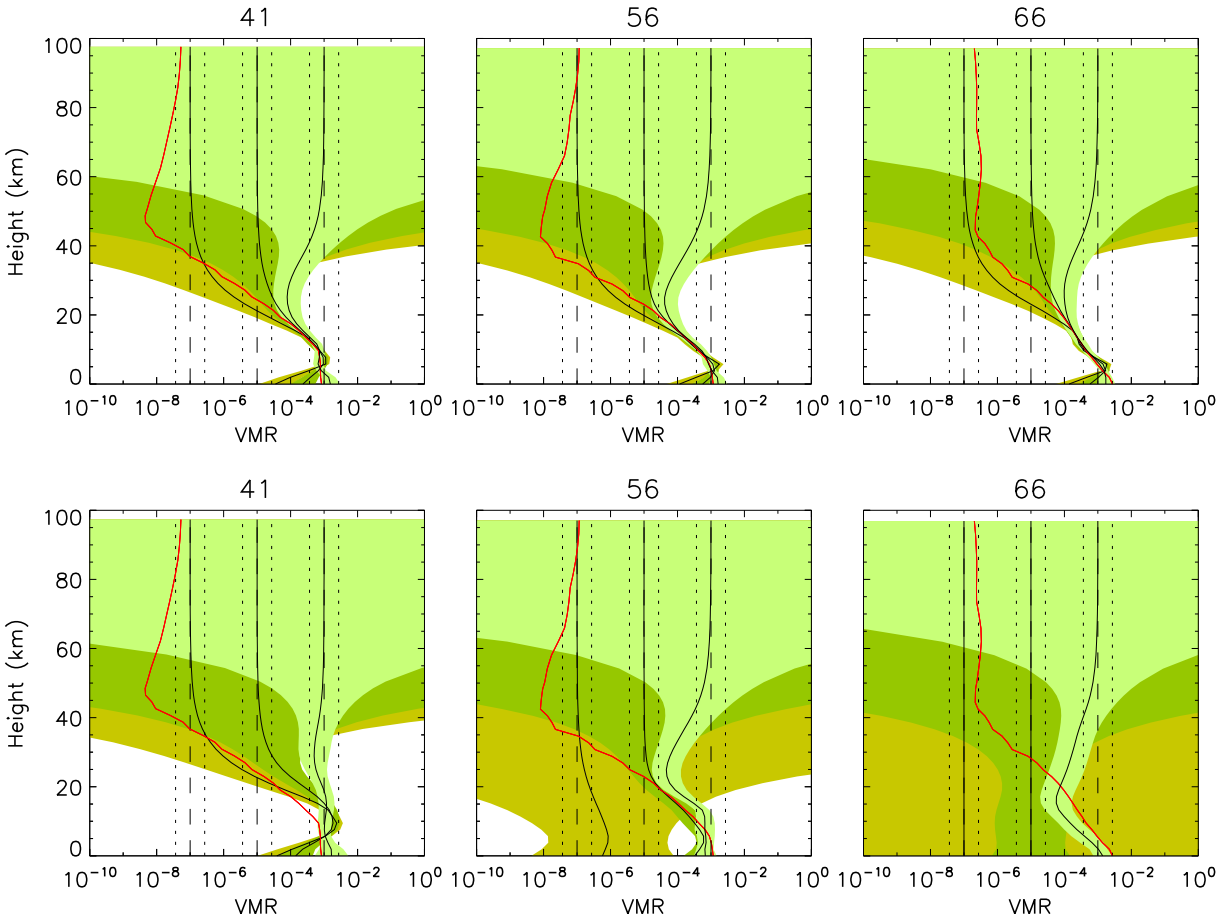


Figure 6.11 | Bracket water retrievals for r_{eff}=4.0 µm cases: (**Top**) τ_{A4}=0.01 (**Bottom**) τ_{A4}=0.1. All retrieved assuming r_{eff}=1.41 µm. Key: *A priori* (dashed line), *A priori error* (dotted lines), retrieved profile (black line), retrieval error (green shading), synthetic measurement profile (red line).

highest accuracy coming from the centre profiles followed by the right and then the left. The initial choice of APR is again shown to have an impact, as for the dust series and for the same reasons. As for the left bracket result at higher opacities in the dust series, the effect of ice radiance in B2 giving false water radiance is seen, 'pushing' the retrieval in the right direction towards the model curve for the wrong reason.

The results from the high opacities in the water ice series are unpredictable in their specific behaviour with regards to the retrieved profiles, not behaving consistently with changes in model ice mode or opacity. Sometimes they are underestimating, sometimes overestimating and sometimes they are completely insensitive, leaving the APR profile unchanged. The inconsistencies are attributed to two explanations: firstly, the differences in ice layer distribution between the models. Secondly, the issues discussed in regard to the first stage retrievals of increased degrees of freedom with multiple aerosols errors cascading into the second stage. The one pattern that does emerge is that increasing either opacity or increasing the difference between the retrieval

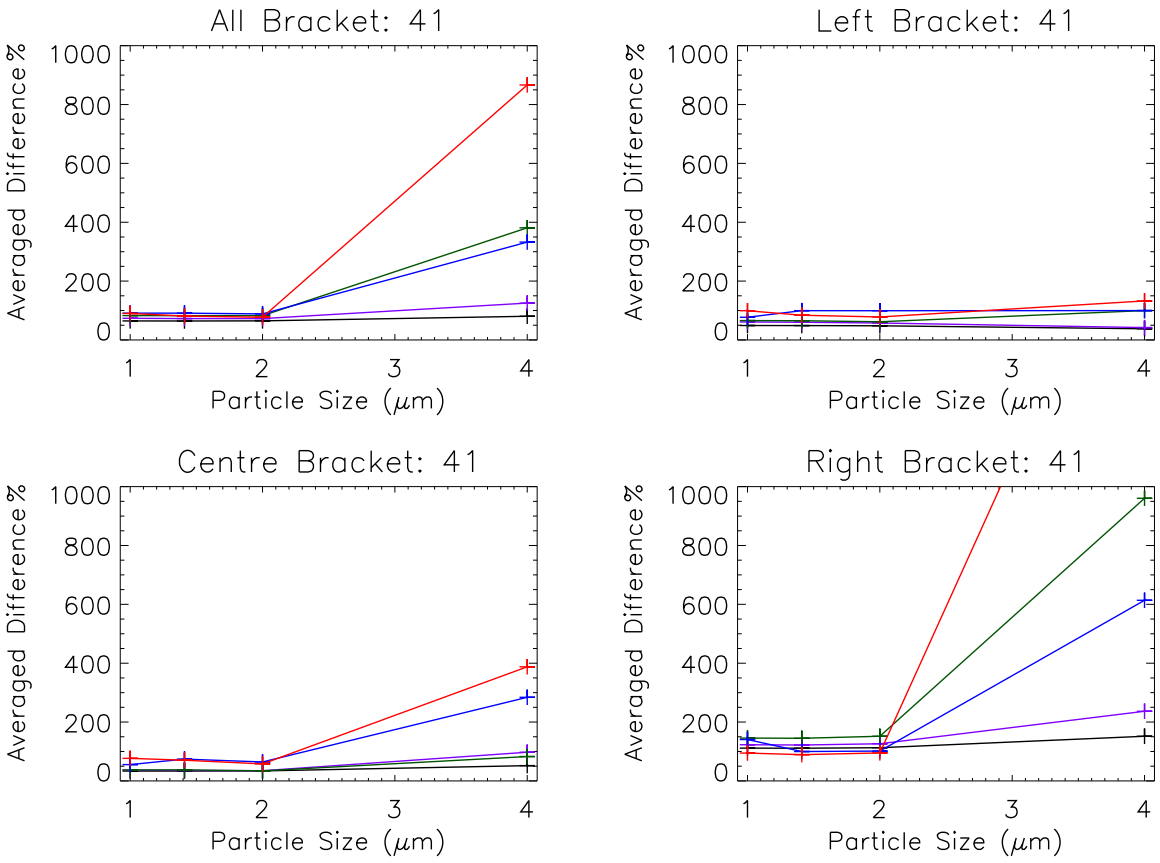


Figure 6.12 | Bracket difference ($\overline{\mathbf{d_x}}\%$) plots for ice series model 41. Lines coloured by τ_{A4} opacity: 0.01 (black), 0.025 (purple), 0.05 (green), 0.075 (blue), 0.1 (red).

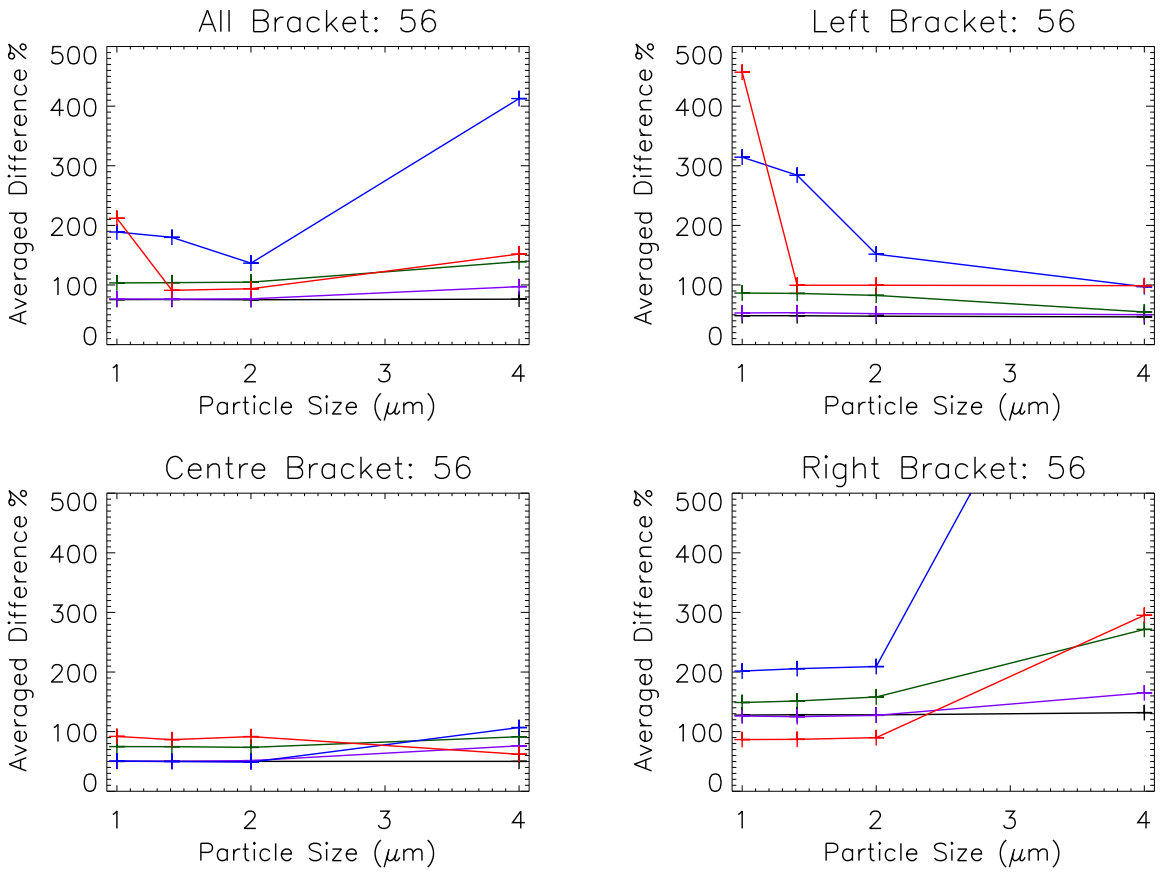


Figure 6.13 | As Fig. 6.12 for ice series model 56.

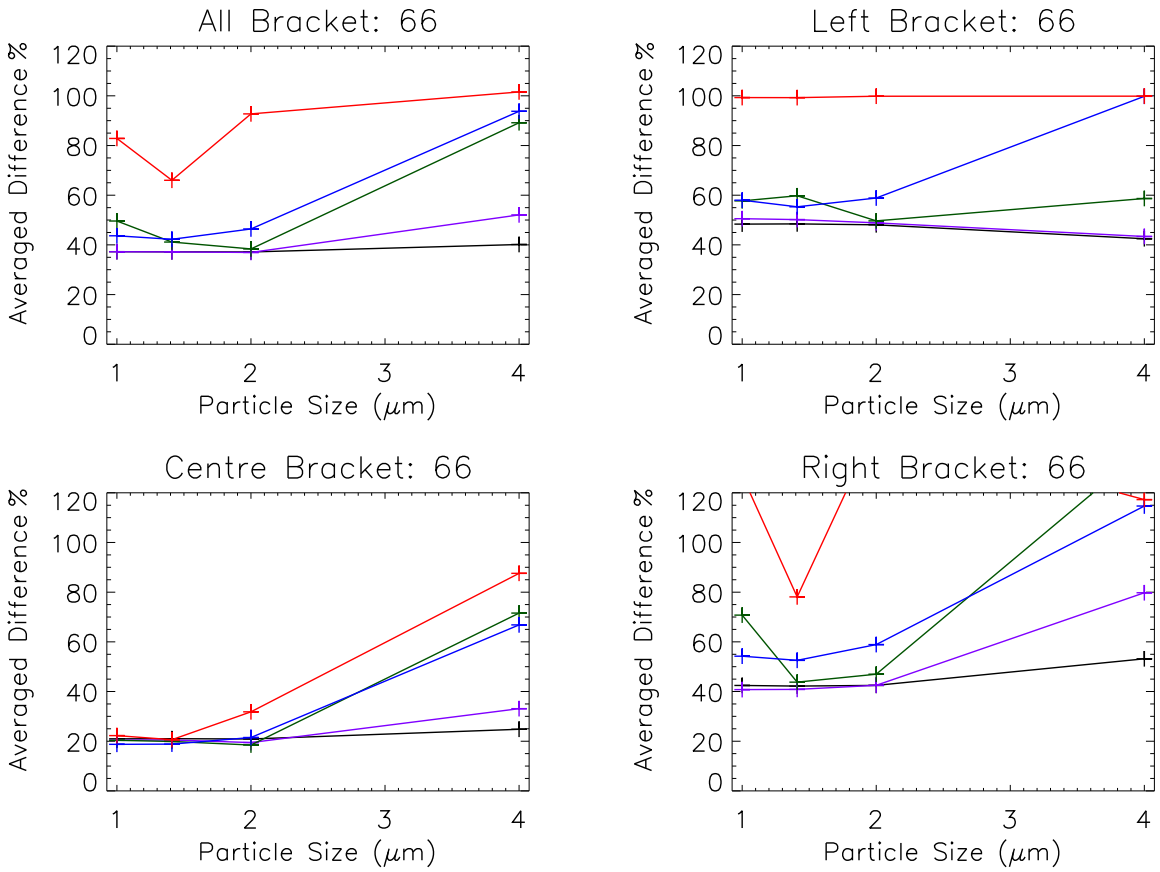


Figure 6.14 | As Fig. 6.12 for ice series model 66.

and model ice modes results in less accurate retrievals.

6.3 Using Covariance Matrices to Assess Aerosol Size Sensitivity

In Chapter 4, it was established that linear optimal estimation provides a number of intrinsic diagnostics for assessing retrievals. Covariance matrices provide a way of assessing correlation between elements of the state vector using their off-diagonal values. Ideally, assuming well chosen spectral regions that are uniquely sensitive to the retrieved atmospheric variable, we would assume little to no correlation. This corresponds to zero or near-zero off-diagonals. However, if there is a significant correlation then the opposite is true. This provides another way of investigating the aerosol-water interaction seen so far in the results, i.e. to see if the relationship with aerosol size is also revealed here.

There is a significant problem in that because of the two-stage nature of the retrieval, this covariance analysis cannot be done directly. Instead, retrievals need to be repeated on an all-in-one stage basis to allow comparison of the relevant matrix elements. As has already been

established in previous chapters the B2 channel has dual sensitivity to dust and water, this was the reason for splitting the retrieval into two stages. The point of this analysis is to see whether the sensitivity to aerosol size seen here is also seen in the covariance matrices. Necessarily, then this can only be used for a qualitative comparison, and the main methodology used in this chapter provides the only way to perform a quantitative analysis.

One-stage retrievals were performed for two cases from the dust-only (see §6.2.2) analyses that presented obvious differences (observed offset in water vapour VMR). These were for the 66 atmospheric model with r_{eff}=1.06 μm and 2.4 μm cases and τ_{A5}=0.1. Retrieval parameters were identical except for the fact that the retrieval was performed in one stage. Using, $\mathbf{C_m}$, a scaled version of, $\mathbf{S_m}$ (Eq. 4.39), the contribution of the measurement error covariance matrix to the final error in the retrieved state vector, correlation can be assessed. Elements are scaled as

$$\mathbf{C_m}(i,j) = \frac{\mathbf{S_m}(i,j)}{\sqrt{\mathbf{S_m}(i,i) \cdot \mathbf{S_m}(j,j)}}, \tag{6.9}$$

giving values in the range −1 to 1. This scaling is done to to make any correlation more visible. This matrix was then imaged by assigning colours to each element. The results are presented in Fig. 6.15. In the figure each matrix has been divided using a grid to show regions of related retrieved variables. The diagonals correspond to a specific variable (e.g. temperature at a certain height) being correlated with itself, so these are equal to 1 (see Eq. 6.9). Though the matrices have been divided into three grid boxes along each side, it should technically be four, as surface temperature is also retrieved in this case (bottom left corner). However, the corresponding regions are very small and not of interest in this test and so are left unlabelled. Within the three diagonal grid boxes the correlation of the variable with elements from neighbouring heights is seen in the off-diagonal elements. The remaining grid boxes indicate correlation between the values at a given height of one variable with the value at a height (not necessarily the same) in another, e.g. the D-W and W-D boxes show the correlation between dust and water. The diagonal elements of these grid boxes show the correlation at the same height between dust and water, the off-diagonals the impact of neighbouring heights. Elements within each grid box correspond to height in a pattern that runs from bottom left, 0 km, to top right, 100 km for the diagonals. The off-diagonals show how the height of one element corresponds to another e.g. top left element of D-W would should correlation from dust at 0 km and water at 100 km.

Comparing the one and two-stage retrievals reveals the problems of attempting to do the

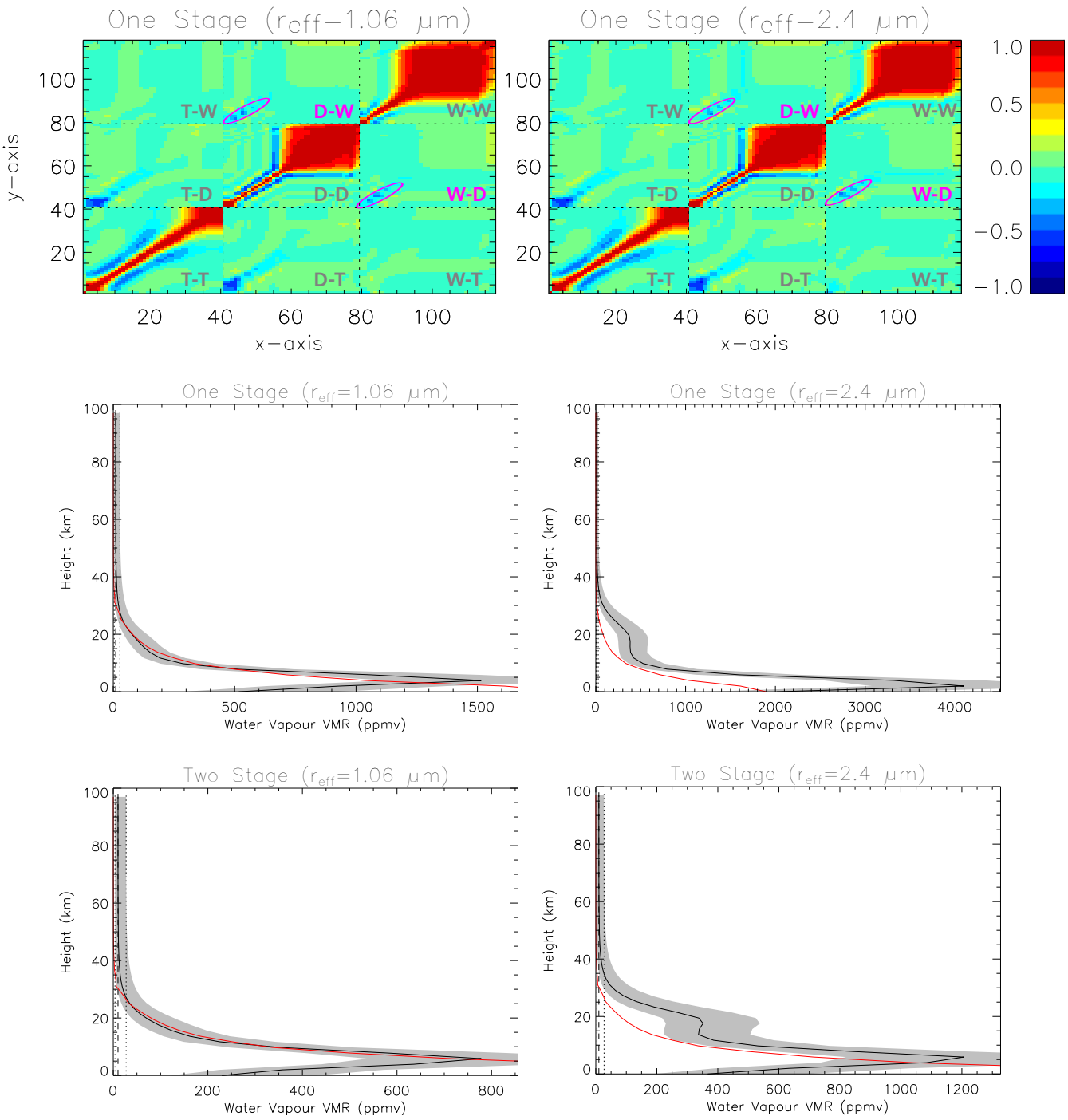


Figure 6.15 | (**Top Row**) Scaled covariance matrices image, $\mathrm{C_m}$, for one-stage retrieval for r_{eff} as indicated with τ_{A5}=0.1. Grid indicates division by related retrieved variables where text indicates the related variables: (T) temperature, (D) dust specific density and (W) water vapour VMR. Dust-water regions and observed correlation are highlighted in pink. Note that surface temperature regions are not labelled. (**Middle Row**) Retrieved water vapour profiles for one-stage retrieval. Key: *A priori* (dashed line), *A priori error* (dotted lines), retrieved profile (black line), retrieval error (grey shading), synthetic measurement profile (red line). (**Bottom Row**) Retrieved profile from two-stage retrieval for reference.

retrieval this way. Due to the dual sensitivity the retrieval heavily overestimates water vapour VMR in the one-stage cases. As with the two-stage cases, retrieving using the correct size mode (r_{eff}=1.06) gives better results, with a smaller superabundance in this case.

In the resulting covariance matrices, correlations are seen between neighbouring heights in T-T, D-D and W-W. For D-D and W-W large correlations are seen at higher altitudes. These correspond to regions where there is little to no dust/water and the radiance level is at the noise level, and so can be safely ignored. A genuine correlation between dust and water is also seen. These regions are ringed in pink on the figure. This is expected due to the dual dust-water sensitivity of B2. Despite the observed differences between the retrieved water vapour profiles for the r_{eff}=1.06 μm and 2.4 μm cases, in both one and two-stage retrievals, no corresponding difference is seen in the observed dust-water correlation. Therefore, the analysis as performed in this chapter is deemed the only way to detect and quantify the aerosol size mode dependency for water vapour retrievals.

6.4 Conclusions

Two-stage retrieval simulations for water vapour were performed to assess the impact of using the wrong aerosol mode (particle size distribution) and the choice of APR profile on water vapour retrieval accuracy. This was done for two series of models, one containing dust and one containing water ice plus dust. For the water ice series the dust was retrieved with the correct mode.

- The 5–25 km region of the water vapour retrieval was found to be the most sensitive region. This corresponds to the locations of highest water vapour abundance.
- These simulations also functioned as test of the effect of choice of APR profile on the water vapour retrieval. The left bracket results tend to be the poorest followed by the right bracket, with the centre brackets as the most accurate. These results point to the fact the initial choice of APR (and error) has some importance, as the best results are achieved when the APR is closest to the final answer, viz. the centre profile. This is tempered by the fact that the brackets used cover four orders of magnitude (10^{-7}–10^{-3}) in VMR as the study is testing extremes. For real retrievals the APR profiles are likely to be much closer (within an order of magnitude) to the actual water vapour abundances, using MCD profiles as the APR, and so less problematic.

- At lower optical depths, mismatches between the retrieval and model aerosol modes are not significant and water vapour retrievals still provide a good match. As optical depths increase retrieval accuracy starts to decrease. When optical depths are high enough they lead to reduced information content in B2 for water vapour, leading to retrievals which do not vary much from the APR.

- When there is a mismatch between retrieval/model aerosol modes this can manifest itself with a systematic offset of the retrieved profile from the true model profile, the effect becoming more prominent as the difference between the retrieval and model aerosol modes increases. This is due to additional/missing aerosol radiance in B2 because of the difference in extinction cross-section between the model/retrieval modes at B2, which is misinterpreted by the retrieval as extra/less water vapour.

- The problems caused by either mismatched retrieval/model aerosol mode or higher opacities become significantly worse when combined.

- When both dust and water ice are retrieved (instead of just dust) extra degrees of freedom are introduced to the retrieval. The different APRs and proportional errors used (see §6.1.2) result in differing retrieval sensitivities to dust and ice, which may become imbalanced at the higher opacities and larger incorrect ice modes. These cause unpredictable effects on the water vapour retrieval in terms of mapping specific behaviours. However, the general trend of reduced retrieval accuracy caused by increasing opacity or mismatching retrieval/model aerosol modes still holds.

- Covariance matrix tests were not able to detect the aerosol size mode dependency and showed that the bracket analysis is the only way to detect and quantitatively analyse the problem.

- Implications for retrievals on real MCS data are discussed in the next session.

6.5 Sensitivity Summary: Implications for Water Vapour Retrievals

The tests and simulations in Chapter 5 have shown that the intended procedure for retrievals of water vapour with MCS, using the B3/B2 detector radiance ratio, is not possible. As designed, the channels would have had similar sensitivities to aerosol and different sensitivities to water vapour. Using the B3/B2 ratio would then allow simultaneous retrieval of water vapour and

aerosol. Unfortunately, because the B2 and B3 spectral bandpasses are wider than originally specified both channels have similar sensitivities to dust and water and thus the B3/B2 ratio is useless. Hence, a two-stage retrieval methodology is necessary where water is retrieved in the second stage using B2 alone. This creates additional difficulties as aerosol must be accurately modelled and retrieved in the first stage to ensure accurate water vapour retrievals.

The sensitivity tests culminated in this chapter where the effect on water vapour retrieval accuracy of aerosol opacity and the incorrect choice of aerosol size distribution, i.e. wrong extinction cross-section at B2, were tested for northern hemisphere summer dayside conditions. Analysis by visual inspection of the profiles and values of the difference metric, $\overline{\mathbf{d_x}}\%$, yielded the following conclusions. For cases tested where only dust is present, when retrieved with a dust mode of r_{eff}=1.06 μm, good results were obtained for dust opacities up to τ_{A5}=0.075. This held true when the model dust mode was varied (i.e. retrieving with wrong mode) up to r_{eff}=1.8 μm. For cases of $\tau_{A5} \leq$0.025, the effect of the dust mode is less important. For the ice series tests, atmospheres were modelled with both dust and ice present; dust was held fixed at τ_{A5}=0.025. When retrieved with an ice mode of r_{eff}=1.41 μm good results were obtained for ice opacities up to τ_{A4}=0.05. This continued to hold when varying mode ice mode from r_{eff}=1.0 μm up to r_{eff}=2.0 μm. For cases of $\tau_{A4} \leq$0.025, the effect of the ice mode is less important.

L2 dataset results for northern hemisphere summer indicate that outside equatorial regions dust column opacities, τ_{A5}, are generally below 0.075. For water ice the highest opacities were near the equator in the aphelion cloud belt region and at the poles. Most column opacities, τ_{A4}, are generally below 0.025 for dayside observations. For nightside observations this increases to 0.05. Assuming our tests were representative this indicates a good chance of success in our water vapour retrieval attempts on the dayside allowing for a margin of error in choice of aerosol size mode. Unfortunately, we were unable to also simulate nightside or southern hemisphere observations due to time and complexity constraints. The lower nightside temperatures will lead to lower water vapour emission in B2. When combined with the higher ice opacities this is likely to lead to poorer quality retrievals for the nightside. Additionally, the low water abundances and low temperatures of the southern winter hemisphere are likely to lead to lower retrieval accuracy in this region as well.

7

Characterizing the Spectral Passband of B3

To further understand the wider-than-expected nature of the B3 filter (see §2.3.1) it was decided to undertake a series of measurements of the B3 spectral response, using a Fourier Transform Infrared (FTIR) spectrometer in conjunction with a pyroelectric detector, with custom electronics (see Thomas, 2011) and a purpose-built jig to hold the filter material at specific distances from the detector.

The B mesh filters of MCS use two-dimensional copper grids mounted on polypropylene substrates. The grids have specifically chosen widths and spacings in order to select the desired bandpass. They function by reflecting out-of-bandpass radiation while also acting as resonant meshes for in-bandpass radiation allowing transmission of the desired wavelengths. The B filters in MCS are composed by stacking a number of such meshes in order to produce the final required channel bandpass.

In the testing stages of their manufacture the filter layers were tested individually by Cardiff University in a FTIR spectrometer and all met their required specifications. They were not tested as a complete stack. After the integration of the filters into MCS the spectral response of the complete filter stacks were measured during pre-flight testing and calibration using a monochromator at JPL (McCleese et al., 2007). After these tests it was found that channel filter response of the B2 and B3 channels did not meet specification and were significantly wider,

with broadening observed on the shorter wavelengths side of the filter peaks. For B3 this was an increase in FWHM of 50% from 14 to 21 cm^{-1} as shown in Fig. 2.10.

It was thought that random forward scattering of out-of-bandpass radiation by the mesh filter may be the cause of the widening. At shorter wavelengths the meshes start to act like randomly orientated transmission diffraction gratings and this would cause some forward scattering of the light (Bowles 2007, personal communication). The broadening effect would increase as the distance between the filter and detector is decreased, as more of this scattered radiation will hit the detector. In MCS the filter-detector distance is very small, of the order of ∼100 µm and so this would cause significant broadening. At large distances the effect would likely to be too small to be noticed. It is a possibility that the broadening was not observed by Cardiff because their mesh layer-detector distances were orders of magnitude bigger and hence the broadening effect would be too small to be seen. Alternatively the scattering may only arise when a full filter stack is used and as Cardiff did not test this, the effect was not seen. It may also be a combination of both effects.

The proposed mechanism is illustrated in Fig. 7.1. The diagram shows two filter detector scenarios with filter-detector distance l_d. The filter response for each scenario is shown at the right hand side of the diagram. The difference in set-up between the scenarios is the filter-detector distance, with l_{d1} for scenario (A) and l_{d2} for scenario (B) where $l_{d1} > l_{d2}$. In each scenario the beam of unfiltered wavelengths, λ_{ALL} (yellow line), proceeds towards the filter. At the filter the desired in-bandpass wavelengths, λ_{IB} (green line), pass straight through hitting the detector. Some out-of-bandpass wavelengths, λ_{SC} (red line), are scattered forwards by the filter at angle θ. In the long-distance scenario, (A), the scattered radiation, λ_{SC}, passes by the detector without hitting it, giving the expected narrow filter response (white solid curve at right hand side of figure). In the short-distance scenario, (B), the distance is too small for the scattered radiation to miss the detector and so λ_{SC} and λ_{IB} hit the detector resulting in a broadened profile (white solid curve at right hand side of diagram, where the narrower dotted peak shows the unbroadened response). It can be seen then that as the distance is decreased larger values of θ are required for λ_{SC} to miss the detector and so more out-of-bandpass radiation will be detected leading to increased broadening.

In order to systematically test for this hypothesis an experimental set-up was required that mimics the optical configuration of MCS and provides a variable filter-detector distance. This would allow the the B3 filter FWHM to be measured at several distances, observing if any

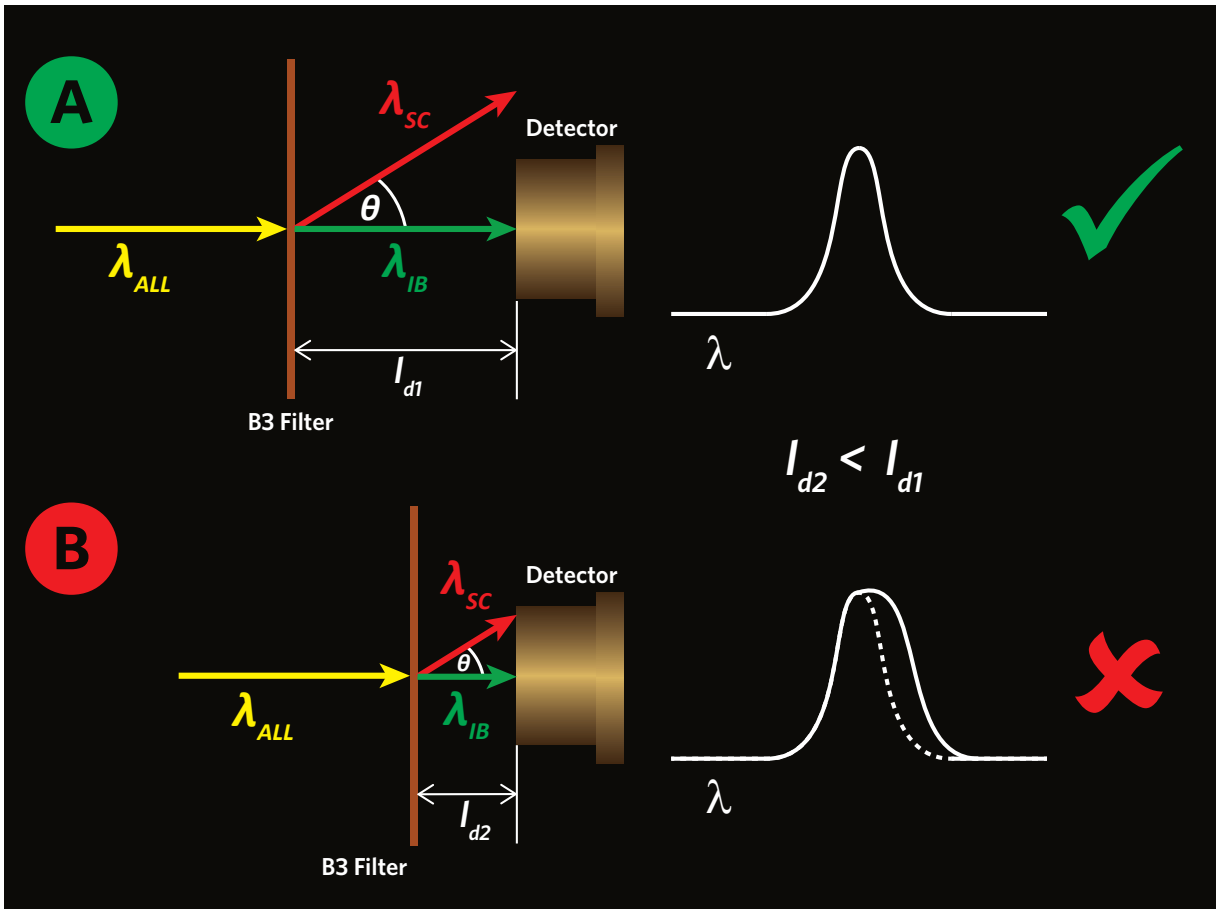


Figure 7.1 | Filter-detector scenarios, (A) and (B), for two different filter-detector distances, l_d, where $l_{d1} > l_{d2}$. The yellow arrows indicate an unfiltered light (λ_{ALL}) beam while the red and green arrows show the path of light taken by in-, λ_{IB}, and out-of-bandpass light, λ_{SC}, scattered by angle θ after being filtered. As the filter-detector distance is reduced the filter response appears to widen letting unwanted wavelengths reach the detector, represented by the white curves on the right. For (B) the unbroadened response is shown by the dashed line.

broadening occurs. If there is no broadening then

$$\mathrm{FWHM}(l_{\mathrm{SHORT}}) = \mathrm{FWHM}(l_{\mathrm{LONG}}) \tag{7.1}$$

where l is the filter-detector distance and $l_{\mathrm{LONG}} > l_{\mathrm{SHORT}}$. This would produce an horizontal line (constant value) on a plot of FWHM vs l_d (filter-detector distance). If broadening is observed then

$$\mathrm{FWHM}(l_{\mathrm{SHORT}}) > \mathrm{FWHM}(l_{\mathrm{LONG}}) \tag{7.2}$$

and we would expect a function that is not an horizontal line and where FWHM decreases as l_d increases.

An almost identical experiment was carried out in Thomas (2011) for the Diviner instrument

on board Lunar Reconnaissance Orbiter. As Diviner has an identical optical bench (but different filters), there was concern that its far infrared channels may also suffer from spectral broadening. Using the same set-up as for this experiment (see §7.1) tests were carried out for the Diviner channels (bandpass given in brackets): B1 (25–41 microns µm), B2 (50–100 µm) and B3 (100–400 µm). These filters are much wider than their MCS equivalents. Results found no significant broadening for any of the channels, which was confirmed by later detector response linearity testing. The channels were found to have met their design specifications.

7.1 Experimental Set-Up & Strategy

The experiment was performed inside an evacuated (∼6 mB) Bruker IFS66V FTIR spectrometer in conjunction with a purpose-built optical bench and detector jig. More information about the spectrometer and electronics used can be found in Thomas (2011) who conducted an almost identical experiment using the same equipment but with flight-spare filter material from Diviner (see above).

A schematic of the experimental set-up is given in Fig. 7.2, a top-down photo in Fig. 7.3 with detailed views of the detector jig and optical bench in Figs 7.4 and 7.5.

The spectrometer far infrared (Globar) source was used for the experiment producing an $f/4.7$ beam in the sample compartment, much slower than the final focal ratio of $f/1.7$ in MCS. In order to change the focal ratio, an off-axis paraboloid mirror (marked as 'mirror' in diagrams) was used on the optical bench with a convergence of $f/1.4$ to focus the beam onto the pyroelectric detector through the filter material. The mirror had a focal length of 25.4 mm and produced a spot size at focus narrower than the 2 mm detector width. This was the closest approximation that was possible with the equipment available. The effect of using a different focal ratio from that in MCS would likely change the measured FWHM from that measured in the instrument but should not diminish the effect of broadening due to scattering, it could even increase the effect because of the steeper beam cone angle. As we were only trying to ascertain the presence of a broadening effect and not make an accurate measurement of the spectral response as would be seen in MCS, this was deemed acceptable. At the detector the signal was recorded, where the shielded electronics box powered the detector, pre-amplified the signal and passed it to the spectrometer via its analogue-to-digital converter.

Flight-spare MCS B3 filter material was used and held in place using a custom-made filter

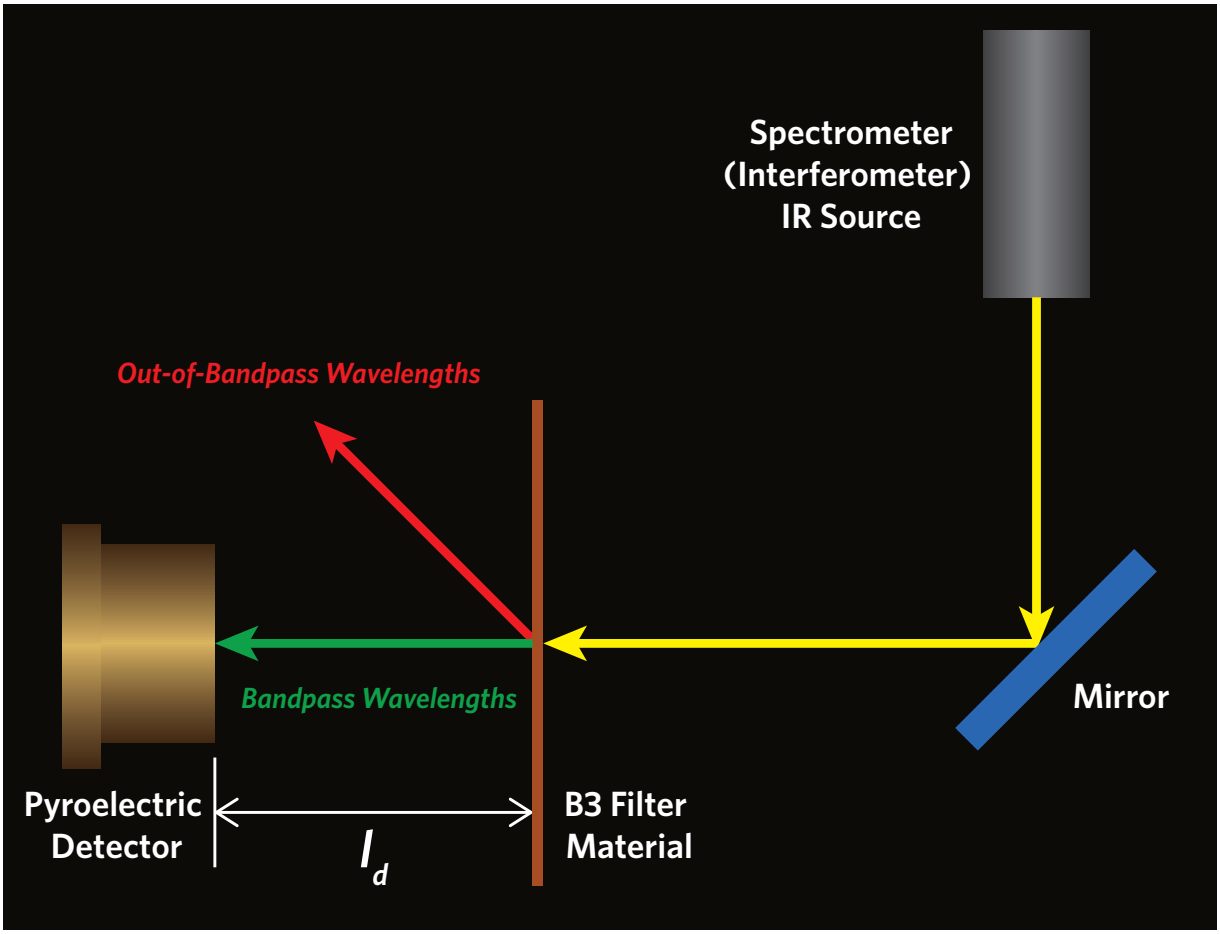


Figure 7.2 | Diagram of experimental set-up. The yellow arrows indicate the unfiltered far infrared beam from the spectrometer while the red and green arrows show the path of light taken by in- and out-of-bandpass light after being filtered.

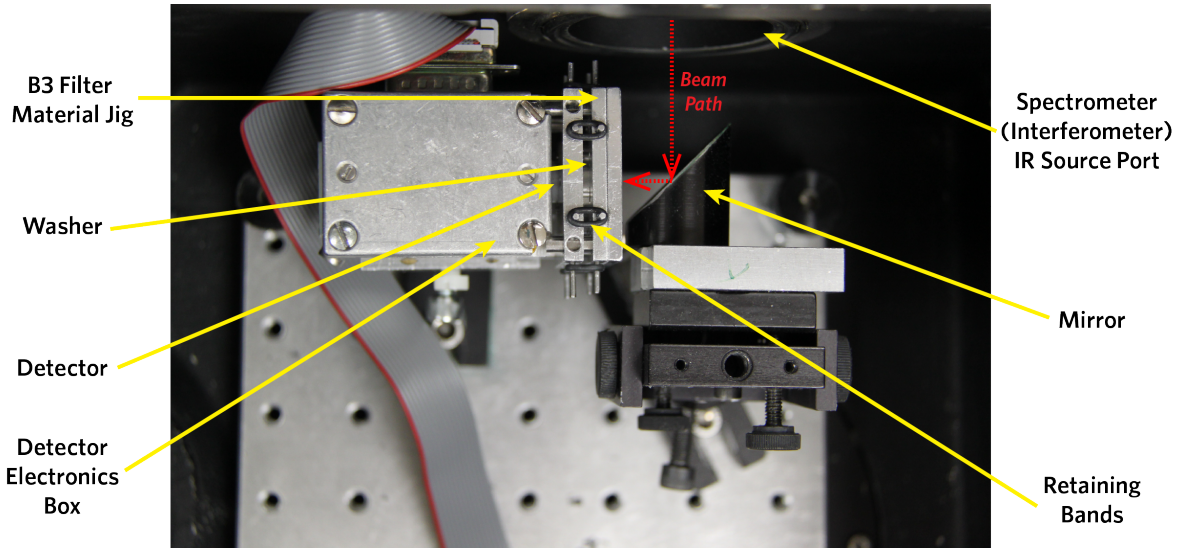


Figure 7.3 | A top-down view of the optical bench placed inside the spectrometer sample compartment. The red-dotted arrows show the path taken by the far infrared beam to the filter jig.

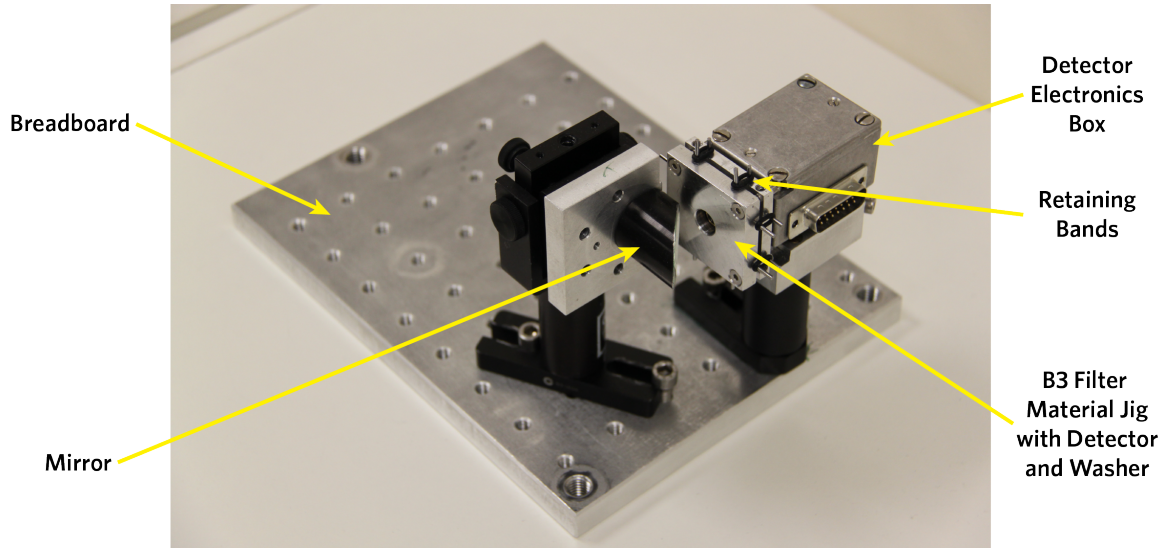


Figure 7.4 | Isometric perspective photograph of the optical bench outside the spectrometer compartment to allow for better viewing of components.

jig as shown Fig.7.5. The jig consisted of a frame for holding the filter, a back plate on which the detector was mounted (via two screws) and a washer-shim placed in between that set the filter-detector distance. The filter material was mounted in a frame made of two plates screwed together. The filter was held in place using screws in each corner with a circular array of grub screws in the centre. The corner screws were attached to runners which protruded through the back of the filter frame which could then be placed in corresponding holes on the fixed detector back plate allowing a variable distance to be set in conjunction with a washer-shim. The frame was held in place by the use of elastic retaining bands* attached to rods protruding from the filter frame and detector plate.

A coordinate measuring machine (CMM) was used to accurately assess the relative distance between the front of the detector element and back plate onto which it was mounted. The element was found to be sufficiently flat at an angle of 0.67±0.05°, corresponding to an error of 23±2 µm across the width of the detector. Using information from the CMM the distance between the front of the detector and the plate where filter was attached was found to be -1090±10 µm i.e. with no shim in place the detector would protrude through the filter by this distance. Given the MCS filter-detector distance of ∼100 µm it was determined to test at filter-detector distances of 50, 100, 200, 500 and 1000 µm, as this ought to show up any broadening. In order to accurately set the filter-detector distance to the chosen values, custom-made washer-shims of

*Testing revealed no effect, due to outgassing from the retaining bands, in the wavelength range used in this experiment.

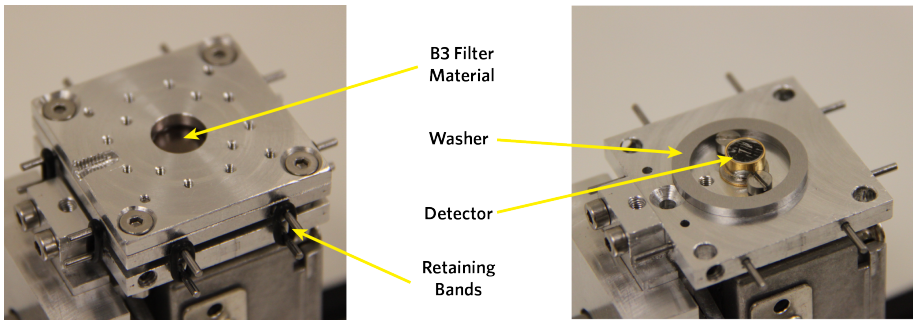


Figure 7.5 | A close-up of the filter jig before and after assembly. **(Left)** Fully assembled jig. Small holes on surrounding detector hole are for grub screws that were added after *Series 1* measurements. **(Right)** Filter and holding-frame removed revealing detector and washer shim for setting filter-detector distance.

mild steel were produced at thicknesses of 1140, 1190, 1290, 1590 and 2090 µm. Unfortunately, it was not possible to use the 1140 µm (l_d=50 µm) washer, as a gold wire attached to the detector protruded and was in danger of touching the filter at such a short distance. Initially the washers were machined to within a 100 µm tolerance and then ground to within ±10 µm with a surface grinder. The uncertainty in plate width was also ±10 µm. Adding in quadrature gives a combined uncertainty of $(23^2 + 10^2 + 10^2)^{\frac{1}{2}} = 27$ µm.

The pyroelectric IR detectors used were the Infratec LIE-332f model, where the detector window and housing had been removed with a lathe (a process dubbed 'decanning'). This was necessary as the detector windows do not operate in the required wavelength range for the measurements and the housing obstructed the close filter-detector distances needed. This detector was chosen as with 'decanning' it allowed the close values of l_d needed and had a reasonable response at the high FTIR scan frequencies (ruling out thermopile types as used in MCS). Unfortunately, once 'decanned' the detectors were very fragile and hygroscopic and their detection ability degraded over time. To minimise this effect detectors were kept in a nitrogen-purged dessicated container, only being exposed to air during the set up for a run. As a result of these problems multiple detectors had to be used over the course of the experiment as signal-to-noise performance reduced so severely, from gradual degradation or direct damage, that the results were useless.

The assembled optical bench was placed and screwed down into the spectrometer sample compartment and beam alignment onto the detector was performed, using the near infrared (quartz-halogen) source and KBr beam splitter to enable visual inspection that the beam was on target. This was done by manually aligning the mirror to ensure that beam was focused onto the

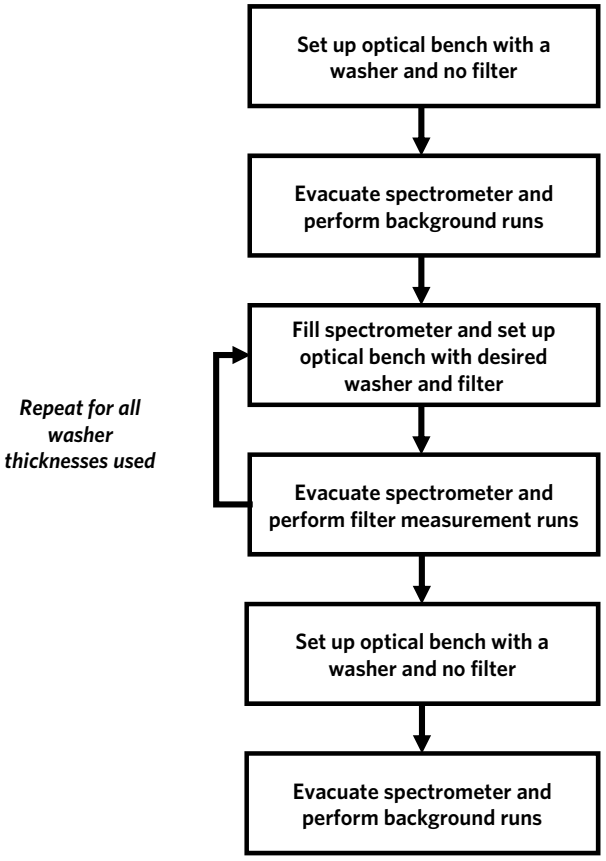


Figure 7.6 | A flowchart indicating the procedure of the experiment. The terms 'Evacuate' and 'Fill' refer to removing air or pressurising the spectrometer.

detector in the jig with no filter. Once the visual alignment was finished the KBr beam splitter was replaced with a mylar one and the source was switched to the far infrared. Fine-tuning of the alignment was then performed by maximising the interferogram signal on the detector. The spectrometer was then sealed and evacuated, ready for either a background measurement run (no filter in frame) or a B3 measurement run when adding the filter. When using the filter in the jig, the jig was first cleaned with acetone and dried in order to keep the filter material pristine. The mesh layers were then carefully stacked and mounted in the right order in the jig. The spectrometer was run with a 2 cm^{-1} resolution, 5 mm aperture and 1.6 kHz scanner velocity.

The experiment was performed five times, each instance referred to as a 'Series' (ranging from I to V). Each series consisted of multiple background measurement runs and multiple filter measurement runs using different thickness washer shims. Each series was performed over the course of two to five days, with long periods between each series (due to lab availability). The procedure for the runs in a given series is shown in the flowchart in Fig. 7.6. Parameters and dates for each series are given in Tbl. 7.1 where the 'Detector' column indicates when a detector was replaced identifying each detector by number, the first being 'Pyro-1', the second 'Pyro-2' and so on. The entry 'Pyro-3a' is the same detector as 'Pyro-3' but damaged as some of the gold black had been removed due to handling and the fragile nature of the 'decanned' detectors. Due to lab availability or the failure of a detector, the number of runs is not always consistent within a series. In the early series background runs were performed with different thickness washer shims, but it became apparent that this caused no difference in the resulting background spectrum, so for later series only one washer shim was used for background measurements.

7.2 Data Treatment & Uncertainties

To calculate B3 FWHMs requires the calculation of the filter transmission profile. This is achieved by dividing filtered radiance by the background radiance over the wavenumber range of interest

$$\mathcal{T}(\nu, l_d) = \frac{R_{\text{fil}}(\nu, l_d)}{R_{\text{bg}}(\nu, l_d)}, \tag{7.3}$$

where $\mathcal{T}(\nu, l_d)$ is the filter transmission at wavenumber, ν, for distance, l_d, and $R_{\text{fil}}(\nu, l_d)$ is the the filtered radiance with, $R_{\text{bg}}(\nu, l_d)$, the background radiance.

To calculate the transmission profile for a given filter-detector distance, l_d, the corresponding background spectra were first scaled to the maximum radiance seen at 258.41 cm^{-1} (an area clear of absorption/emission lines) and then averaged. The relevant filtered spectra for the value of l_d were scaled to the maximum peak radiance (corresponding to the filter peak transmission) and then divided by the averaged background spectrum to give the transmission profile from which the FWHM was calculated. A mean filter profile was also calculated using the average of the filter spectra, which was then divided by the averaged background spectrum. This is given in Tbl. 7.1 as the 'Intra-Series Mean FWHM'. All of these calculations were done on an intra-series basis. In addition a trans-series mean FWHM was then calculated by taking an average of the filter widths over all observations in all series at l_d, given as the red line in Fig. 7.7.

Sources of uncertainty within the experiment can be broken down into the following categories:

Position Uncertainties that affect the filter-detector distance, l_d. This includes the accuracy of the washer-shim thickness and detector back-plate flatness given as 27 µm (see 7.1 for more information).

Alignment Related to the above are uncertainties in alignment of the relative positions of the beam, mirror and filter. These are due to the fact that beam had to be manually aligned onto the detector (maximising the interferogram) and parts of the optical bench had to be moved between individual runs and series. More changes to the set-up were performed between series than between individual runs as the optical bench had to be partially disassembled after a series (for storage) and then reassembled when used for the next series. Variations between runs/series led to slightly different alignments and potentially, slight differences in B3 spectral response (e.g. due to different angle of incidence of the

light beam onto filter). The main effect seems to be difference in signal amplitude (up to 10%). This was dealt with by scaling background and filter spectra before calculating filter transmission (see above).

Detectors & Noise Uncertainties due to detectors include changing detectors (due to failure), performance drift due to the hygroscopic nature of detectors or other damage (e.g. removal of gold black coating). These detector uncertainties were addressed as the filter transmission was calculated by dividing the filter spectrum by the series averaged background spectrum, cancelling out the effects of detector drift. The main consequence then will be a decrease in the signal-to-noise ratio. Another source of uncertainty was noise from the detector, electronics and spectrometer.

In order to assess impact of the uncertainties on the data, two types of error have been calculated: the intra-series error, σ_{int}, looking at the uncertainty in FWHM within a series of results and the trans-series error, σ_{trans}, looking at the uncertainty across all results in all series. This allows us to assess repeatability within and across all series.

To calculate σ_{int} we first require the error in the intra-series mean filter transmission response at a given l_d, σ_{resp}:

$$\sigma_{\text{resp}}(\nu, l_d) = \bar{\mathcal{T}}(\nu, l_d)\sqrt{\left(\frac{\sigma_{\text{fil}}(\nu, l_d)}{\bar{R}_{\text{fil}}(\nu, l_d)}\right)^2 + \left(\frac{\sigma_{\text{bg}}(\nu, l_d)}{\bar{R}_{\text{bg}}(\nu, l_d)}\right)^2} \tag{7.4}$$

where $\sigma_{\text{fil}}(\nu, l_d)$ and $\sigma_{\text{bg}}(\nu, l_d)$ are the standard deviation of the scaled filter and background spectra at ν respectively, $\bar{R}_{\text{fil}}(\nu, l_d)$ and $\bar{R}_{\text{bg}}(\nu, l_d)$ are the intra-series mean radiance of the filter and background spectra at ν and $\bar{\mathcal{T}}(\nu, l_d)$ is the intra-series mean normalized filter transmission at ν. The intra-series error in the FWHM, σ_{int}, is then:

$$\sigma_{\text{int}}(l_d) = \sqrt{\left(\frac{d\nu}{d\bar{\mathcal{T}}}\right)^2_{\nu_1} \sigma^2_{\text{resp}}(\nu_1, l_d) + \left(\frac{d\nu}{d\bar{\mathcal{T}}}\right)^2_{\nu_2} \sigma^2_{\text{resp}}(\nu_2, l_d)} \tag{7.5}$$

where the derivatives and response errors are evaluated for $\bar{\mathcal{T}}(\nu, l_d)$ at ν_1 and ν_2, with

$$\bar{\mathcal{T}}(\nu_1) = \bar{\mathcal{T}}(\nu_2) = \frac{\bar{\mathcal{T}}_{\text{max}}}{2} \tag{7.6}$$

$$\text{FWHM} = \nu_2 - \nu_1 \tag{7.7}$$

where $\bar{\mathcal{T}}_{\text{max}}$ is the peak transmission of mean normalized filter response.

Table 7.1 | This table gives the parameters used during the B3 filter measurements (where l_d is filter-detector distance) and the calculated intra-series mean FWHMs and corresponding errors. Values with 'N/A' in the error column indicate a series where there is only one measured filter profile at the given l_d, where the FWHM of that profile is given instead of the mean.

l_d µm	Series	Date	Detector	Number of Runs	Acquisition Mode	Number of Scans	Intra-Series Mean FWHM cm^{-1}	Intra-Series FWHM Error, σ_{int} cm^{-1}
100	Series I	2–3 Mar 2009	Pyro-1	4	SINGLESIDED	400	18.94	1.02
200	Series I	3 Mar 2009	Pyro-1	1	SINGLESIDED	400	19.41	N/A
500	Series I	27 Feb, 2 Mar 2009	Pyro-1	3	SINGLESIDED	400	20.39	2.29
1000	Series I	27 Feb, 4 Mar 2009	Pyro-1	2	SINGLESIDED	400	19.34	1.12
100	Series II	16–17 Jun 2009	Pyro-1	3	SINGLESIDED	400	18.77	0.66
200	Series II	16–18 Jun 2009	Pyro-1	3	SINGLESIDED	400	17.59	0.97
500	Series II	16–17 Jun 2009	Pyro-1	2	SINGLESIDED	400	18.15	0.25
1000	Series II	15–16 Jun 2009	Pyro-1	3	SINGLESIDED	400	17.65	0.20
500	Series III	27 Jun 2009	Pyro-2	1	SINGLESIDED	400	18.47	N/A
1000	Series III	27 Jun 2009	Pyro-2	1	SINGLESIDED	800	17.33	N/A
100	Series IV	30 Jun, 1–2 Jul 2009	Pyro-3	4	SINGLESIDED	400	17.74	0.63
200	Series IV	30 Jun, 1–2 Jul 2009	Pyro-3	4	SINGLESIDED	400	17.97	0.38
500	Series IV	30 Jun, 1–2 Jul 2009	Pyro-3	4	SINGLESIDED	400	18.08	0.31
1000	Series IV	30 Jun, 1–2 Jul 2009	Pyro-3	4	SINGLESIDED	400	17.91	0.37
100	Series V	9–10 Feb 2010	Pyro-3a	4	DOUBLESIDED	200	16.54	0.20
200	Series V	9–10 Feb 2010	Pyro-3a	4	DOUBLESIDED	200	16.27	0.23
500	Series V	9–10 Feb 2010	Pyro-3a	4	DOUBLESIDED	200	16.29	0.28
1000	Series V	9–10 Feb 2010	Pyro-3a	4	DOUBLESIDED	200	16.33	0.31

The trans-series error, σ_{trans}, is calculated as the standard deviation across all FWHMs over all series for a given l_d, shown by the grey-shaded areas in Fig. 7.7.

7.3 Results

The calculated filter widths from the measurements are given in Tbl. 7.1 and Fig. 7.7. Normalized filter profiles for *Series IV* and *V* are given in Figs 7.8 & 7.9. The table summarizes the results for each series at a given l_d, giving the intra-series mean FWHM and corresponding intra-series error, σ_{int}, when available. In series where only a single run was performed for a given value of l_d, the FWHM for that run is given (instead of the mean FWHM) with 'N/A' given in the error column.

The chart in Fig. 7.7 plots all the filter widths for all runs for each series. The trans-series mean FWHM, the mean FWHM across all results and all series, at each l_d are plotted as a red line. The semi-transparent shaded grey area (given as 'Std Dev' in the legend) gives the trans-series error, the standard deviation of results from all series at a given l_d.

The main trend of the results indicates that there is no systematic change in FWHM over the tested range of l_d, especially when compared to the 50% (7 cm^{-1}) broadening seen in the JPL measurements. The low values for the intra-series error, σ_{int}, (<1 cm^{-1}) indicate there is little spread in results over the range within a series. The notable exception here is *Series I*

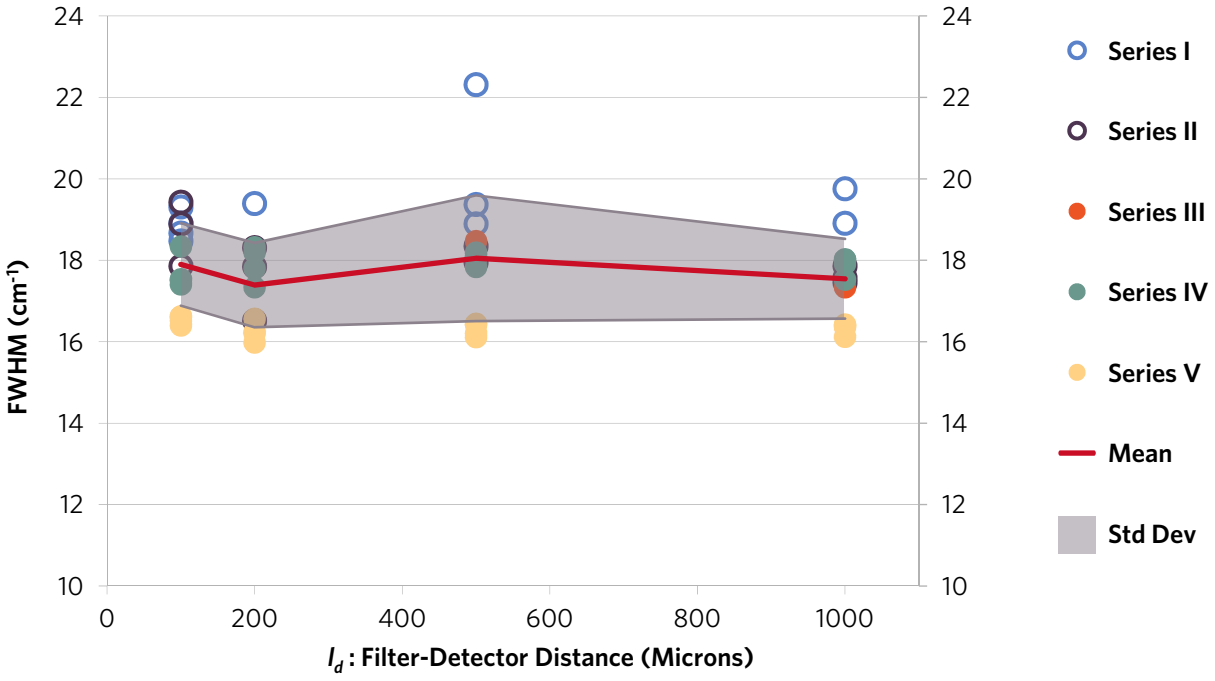


Figure 7.7 | Results for FWHM for all runs across all series for different values of filter-detector distance, l_d. FWHMs from each series are represented by different symbols listed in the legend. The trans-series mean (given as 'Mean' in the legend) is given by the red line and the trans-series error (standard deviation, given as 'Std Dev' in the legend) is represented by the semi-transparent grey shaded area.

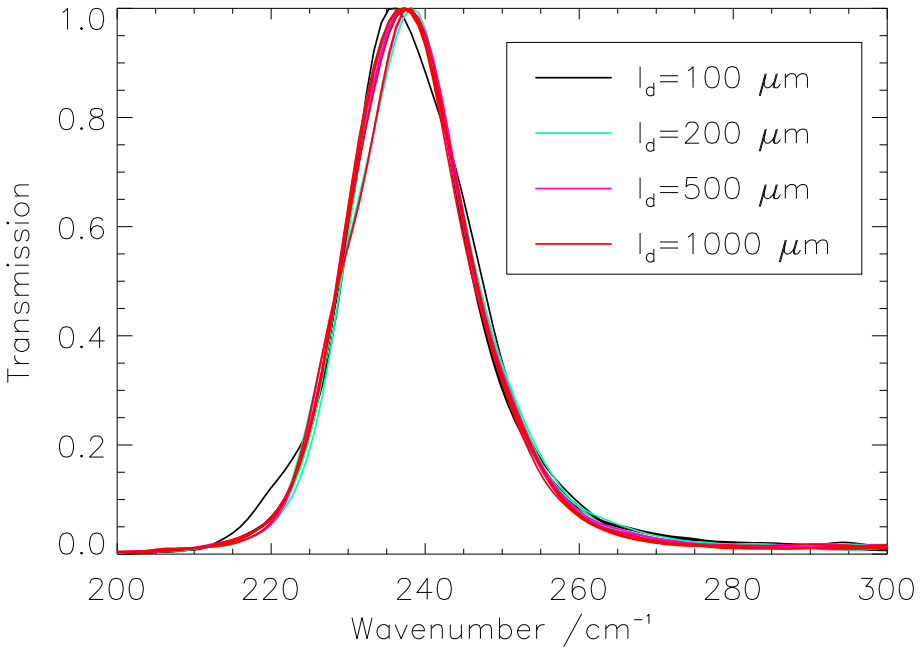


Figure 7.8 | A plot of all the normalized filter transmission profiles for *Series IV*. Profiles are coloured according to l_d, where the value is given in the legend. Note that there is significant overlap between profiles.

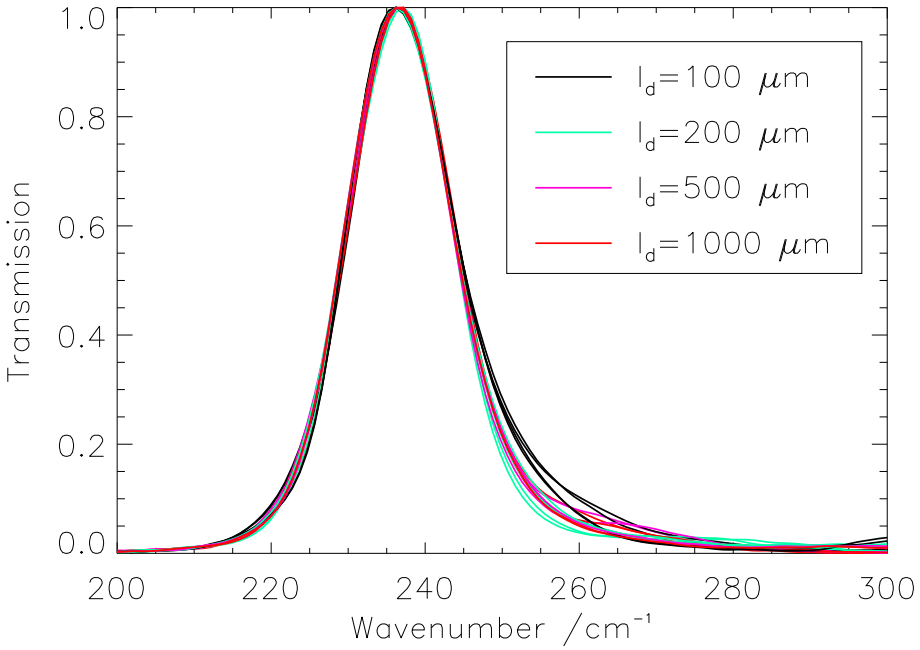


Figure 7.9 | Same as Fig.7.8 for *Series V*.

with correspondingly higher values of σ_{int} (>1 cm^{-1}). There is a greater spread in the results between series shown by the values of the trans-series error, σ_{trans}, which are generally bigger (>1 cm^{-1}) than their σ_{int} equivalents. It is probable that the spread between results is a systematic error induced by the slight differences in optical alignment, differences in conditions and/or spectrometer parameters at the time of each series (see §7.2 and Table. 7.1 for details).

The highly spread values of *Series I* were conducted over a wider time span than the other series. *Series II–V* were conducted over two to three days while *Series I* was conducted over five days. Consequently, alignment errors and detector degradation are likely to have had a larger impact on these measurements. There was more time for the detector to degrade outside of the vacuum or protective storage and the optical bench had to be disassembled and reassembled more frequently than for the other series. Additionally, the detector used for this series had been used in previous experiments and had been 'decanned' for a longer period of time, allowing for further degradation than the other detectors.

Despite no systematic broadening being measured, some other anomalies were seen in *Series IV* and *V*. These are visible in Figs 7.8 & 7.9 where normalized filter profiles have been given and are colour-coded according to l_d. For *Series IV* we see a small shift in the peak wavenumber of the filter profile between observations (this is also seen in *Series I* and *II* which are not shown). In addition for one case at l_d=100 µm (black) we see a larger peak shift and a small enlargement

in the wing at 215–220 cm^{-1}. For *Series V* we see no peak shifting but see enlargements in the filter wing at 250–270 cm^{-1} for some of the l_d=100 µm and one of the l_d=1000 µm (red) profiles. Given that these anomalies do not arise consistently across all series and are much smaller than the JPL-observed B3 broadening, they are likely to be artefacts due to slight alignment differences between measurements, rather than observations of any genuine broadening effect.

7.4 Discussions & Conclusions

Over the range of filter-detector distances (l_d) tested, no systematic change in FWHM was observed. Therefore it seems that the proposed random forward scattering with rapid fall-off theory is incorrect and another explanation must be sought to explain the broadening. The set-up used for this experiment is not an exact replication of the MCS focal plane array so it may be that the observed broadening is due to another effect not present in this set-up but present in the MCS focal-plane. This could be some form of optical interaction between the baffles (not modelled in our set-up) and the mesh filters, e.g. scattering. It would therefore be highly prudent for an accurate retesting of the MCS focal-plane set-up to be performed to investigate this.

Another possibility was that that the filter-broadening effect that was observed by JPL's pre-flight MCS testing (McCleese et al., 2007) was caused by an artefact of their monochromator testing, such as spectral leaks in the order sorting filters used. This seems unlikely given our results from the B3/B2 scatter plot testing in §5.2. In those tests MCS observed radiances were compared with simulated ones. The results supported a reduced sensitivity of the B3/B2 ratio to water independent of assumed filter profile. Therefore the optical interaction theory discussed above is the more likely culprit. Retesting of the MCS focal-plane set-up could verify this.

8

Retrievals

Results from Chapter 5 demonstrated that the original method of using the B3:B2 radiance ratio to retrieve water independently of aerosol is untenable. Consequently, a two-stage retrieval process has been developed using only the B2 channel. This was tested with a B2 residuals retrieval of real MCS data and a series of retrievals on synthetic measurements testing the effects of aerosol model choice. Presented here are the results of the two-stage retrieval on real MCS observations for L_s=111–173° (September 2006–January 2007), during the northern hemisphere summer of MY28. This encompasses the period of nominal MCS observations from the start of the mission, just after Mars orbital insertion and aerobraking, to just prior to the elevation actuator slewing problems (see Chapter 2).

Results for water vapour column abundances are compared to nadir retrievals of TES (Smith, 2004), SPICAM (Trokhimovskiy et al., 2015) and ground-based observations (Krasnopolsky et al., 2015). Retrieved vertical profiles are compared to limb retrieval data of CRISM (Clancy et al., 2017) and SPICAM (Maltagliati et al., 2011a, 2013).

8.1 Observations

MCS data used comes from the observations starting with the beginning of the mission on 24 September 2006 (L_s=111°) and extending to the 27 January 2007 (L_s=173°), during northern hemisphere summer MY28 on Mars. This includes dayside and nightside observations, mostly

at local surface times (LST) of 03h and 15h because of MRO's polar orbit. There is a larger spread in local times when close to the poles. The observations have been split into two seasonal blocks, L_s=111–140° and L_s=140–173°. These will be referred to as 'early summer' and 'late summer'. This was done to allow easy comparison with binned CRISM data and also to observe seasonal variation. These seasonal blocks were further divided into dayside (09–21h LST) and nightside (21h–09h LST) observations. This data was taken before MCS suffered its elevation slew impairment (see Chapter 2) and hence includes fully calibrated nadir and limb data. Where available, limb observations were combined with local nadir observations <1° away in latitude and longitude. Observation averaging is as described in §2.4.

8.2 Method

8.2.1 A Priori

The *a priori* (APR) model atmospheres are constructed following the procedure discussed in §3.4. For each observation, data from the corresponding time and location are found in the MCD (MY24 scenario). Information is also obtained from the L2 dataset (comprised of MCS retrieval results performed by Kleinböhl et al., 2009)—the equivalent retrieval data performed with the same observation. The MCD is used to provide volume mixing ratio (VMR) profiles for CO_2, N_2 and water vapour. Temperature, pressure, dust and water ice profiles along with surface temperature values are provided by the L2 dataset. Values from missing altitudes are extrapolated (using MCD data) and used to construct the relevant profiles and values ready for NEMESIS to use in the retrieval. Aerosol parameters for dust and ice are as given in §3.3.1 (particle size distributions and complex refractive index data).

8.2.2 Retrieval Procedure

Retrievals of MCS observations were performed with NEMESIS in two stages. Following the procedure outlined below:

Stage One: Using the APR model a retrieval is performed for temperature, pressure, dust, water ice and surface temperature using channels A1–A5 and B1 as a dummy channel (this is discussed in the next section). Continuous profiles are retrieved for temperature and aerosols with l_c=1.0 (correlation length, see Eq. 4.38). The pressure retrieval is performed for pressure at a single altitude which is then used to scale the rest of the pressure profile accordingly. The

altitude used is that from the equivalent pressure retrieval in the L2 data, with the APR error set to the error in the retrieved L2 value. The APR errors for other first stage retrieval parameters are as follows: 2 K for temperature profile and surface temperature, 50% of the specific particle density (particles per gram of atmosphere) at each height for the dust profile and 50% for the water ice profile. Dust and ice are modelled as non-scattering (absorption-only, for more information and testing of this assumption see §3.3.1 and 3.3.4). Aerosol size distributions are modelled using the modified gamma distributions, giving complex refractive indices as described in §3.3.1. The modified gamma distribution is characterised by the three parameters a, b and c as defined in §3.3.1, but also supplies values for r_{eff} and v_{eff}. For dust these are r_{eff}=1.06 µm and v_{eff}=0.3, where a=2.24, b=8.04 and c=0.647. For water ice, r_{eff}=1.41 µm and v_{eff}=0.15, where a=12.6, b=31.4, c=0.436. These values are taken from Kleinböhl et al. (2009, 2011). A forward measurement error of 0.25 mW/m^2/sr/cm^{-1} is used for channels A1–A5, while for the dummy channel, B1, a value of 2 mW/m^2/sr/cm^{-1} is used.

Stage Two: The retrieved values from the first stage are used to set the atmospheric state for the water retrieval. The MCD water vapour data are used as the APR profile with an APR error of 50% in the VMR at each height. A continuous profile retrieval is performed for water vapour using the B2 channel with l_c=1.0 and a forward model error of 0.25 mW/m^2/sr/cm^{-1}.

8.2.3 Detector Selection and Dummy B1

Information content for limb paths with MCS observations varies significantly with altitude. This means that often there are detectors, particularly at lower tangent heights with strong absorption that contribute little to no useful information as the channel becomes optically thick. In the worst cases these lower retrieval accuracy and so it becomes necessary to remove these detectors from the retrieval. For the channels used in the first stage of the retrieval not all limb detectors are used, though generally all nadir detectors are, but as channel-averaged radiances. As nadir paths are shorter the chances of the channel becoming optically thick are much lower.

For A1–A5 the retrieval uses the same detectors as those used in L2 data. Firstly, the bottom pixels in each channel are removed where the ground is overly present in the detector FOV. Secondly, pixels are removed that have exceeded limb opacity thresholds for the relevant channel. A brief description is given here, but full details are given in Kleinböhl et al. (2009). It is important to note that L2-based detector selections are based on the selections in the L2 results database and are not altered during the course of this retrieval. The criteria described

below were applied at the time when these retrievals were made and are deemed valid for use in this retrieval as there is no good reason to think that our first stage retrievals will vary significantly from the L2 profiles.

The main channels for temperature profile retrieval are A1, A2 and A3, located in the CO_2 absorption band, with A3 in the band centre corresponding to the highest altitudes (i.e. region of most absorption) and A1 located away from the centre corresponding to the lowest heights (region of lowest absorption). When the CO_2 line-of-sight (LOS) opacity exceeded 2.0, there was a switch to A2 detectors and then to A1 when A2 LOS opacity exceeded the limit. The lowest A1 detector used was required to have a FOV surface contribution less than 20% when the atmospheric limb path was still transparent. Alternatively, in cases where the limb path was opaque close to the ground, only the LOS opacity threshold was applied in determining the lowest detector.

For dust detectors (A5) the lowest detector was required to have a LOS opacity less than 2.5 and a FOV surface contribution of less than 10%. The opacity criterion is to prevent analysis of radiances that contain little to no useful information. To reduce errors due to extended FOV-wing contributions the top A5 detector used was required to have a radiance of at least 5% of the channel's maximum individual detector radiance.

For water ice detectors (A4) the lowest detector had the same LOS opacity and FOV surface contribution criteria applied. In addition, the bottom A4 pixel used is coupled to the lowest A5 detector selected such that A4 and A5 shared the lower bound. The top pixel used was not linked to A5 and was required to have at least 1–3% of the channel's maximum individual detector radiance.

In the second stage only the B2 channel is used. Channel-averaged values of the nadir detectors are used and limb detectors with an altitude below 1 km are removed to minimise errors due to FOV-wing surface contributions.

In the first stage of the retrieval the channels A1–A5 with B1 as a 'dummy channel' are used. The B1 channel is predominantly used by NEMESIS to identify which detector is which. It is present for all limb heights used after detector selection, i.e. B1 is selected if there is any other channel detector present for that limb tangent height. It has an artificially enlarged forward measurement error of 2 $mW/m^2/sr/cm^{-1}$ (c.f. normal measurement error of 0.25 $mW/m^2/sr/cm^{-1}$) to lessen contribution to and loosen its constraint on final retrieved profiles. It was found that if A4, A5 and B1 are used simultaneously and weighted equally (with equal forward measurement

errors) that the retrieval quality and radiance fitting was poor. When the retrieval tried to fit B1 radiances it led to much larger residuals in both the A4 and A5 channels, which then fitted very poorly. This suggests errors in the extinction cross-sections in the far infrared. These could be caused by either the wrong choice of particle size distribution or errors in the complex refractive index data at these wavelengths. Consequently, as seen from the synthetic retrievals in Chapter 6 this is likely to lead to problems at higher aerosol opacities. For this retrieval we have followed the same procedure as Kleinböhl et al. (2009) and retrieved dust and water ice using A4 and A5.

8.3 Results

8.3.1 Retrieval Quality and Coverage

A key signifier of retrieval quality is the χ^2/n_y value which is provided in the output of the NEMESIS retrieval, where χ^2 is as defined in Eq. 4.12 and n_y is the number of points in the measurement vector. The χ^2 cost function describes the closeness of fit of the measured radiances to the calculated ones and is part of the optimal estimation cost function, ϕ (Eq. 4.35). It is important to note that, though very similar in form, this statistic is not the reduced chi-squared, χ^2/n_f, where n_f is the number of degrees of freedom. This is because there are not n_y independent data (degrees of freedom), i.e. $n_y \neq n_f$. The χ^2/n_y statistic is useful for analysing the fit quality for the manual quality control process described here. Under normal circumstances it is $\mathcal{O}(1)$ (i.e. within an order of magnitude) for a realistic converged solution.

A χ^2/n_y=1 threshold was set for all first stage retrievals while for the second stage retrievals a χ^2/n_y=3 value was used for the dayside observations and χ^2/n_y=1 for the nightside results. The thresholds for first stage and second stage are linked, so that results have to pass both thresholds in order to be included (e.g. a dayside first stage retrieval that had χ^2/n_y=0.9 with corresponding second stage χ^2/n_y=5 would not be included). The distributions of χ^2/n_y for the early summer (L_s=111–140°) block are given in Fig. 8.1.

For northern hemisphere dayside observations, i.e. those with the highest water abundances, it was impossible to get values lower than 2–3. For dayside observations, testing by inspection with small subsets of data showed that this gave good radiance fits and a large fraction of non-spurious results. An example dayside retrieval is shown in Fig. 8.2. In the nightside results, for the equivalent northern hemisphere high water abundance region, many retrieved profiles

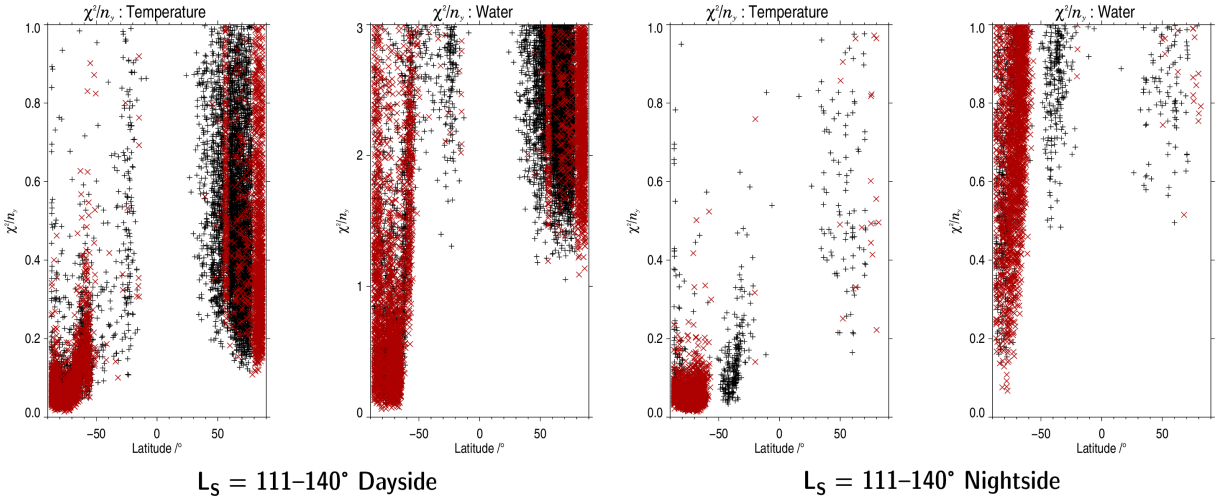


Figure 8.1 | Plot of zonal distribution of χ^2/n_y values for dayside and nightside retrievals in early summer (L_s=111–140°) block. Black points indicate retrievals performed on a combination of limb and nadir radiances, red points indicate limb radiance only retrievals. Results are similar for the late summer block. Results were thresholded, see text for details.

were found to have χ^2/n_y<1. Initially, the same χ^2/n_y=3 threshold was tried as for the dayside results, but this led to the inclusion of a large fraction of spurious retrievals.

Unfortunately filtering results by χ^2/n_y alone is not sufficient to guarantee the removal of spurious retrievals. Spurious retrievals are present in both the dayside and nightside results. Curiously, the problem is much more severe for the nightside results despite generally having lower values of χ^2/n_y. These spurious retrievals take the form of unrealistically exaggerated and oversaturated (by factors of 100 or more) water vapour layers. They are normally co-located in altitude with dust or water ice layers. It is thought that these spurious layers are due to aerosol radiance contribution in B2 being misinterpreted by the retrieval as water vapour. This is the same behaviour as seen in simulated retrievals in Chapter 6 testing the affect of retrieving with the incorrect aerosol mode and discussed in the previous section on B1 as a dummy channel. It is likely there are errors in the far infrared aerosol extinction cross-sections at B2.

In the simulated retrievals (see Chapter 6) the degree of error varied with opacity, so that at low dust and ice opacities it was negligible. Consequently, an additional threshold was tried using the column optical depth data for dust at A5, τ_{A5}, and ice at A4, τ_{A4}, from the L2 dataset. This was tested for conservative values of 0.025 and 0.01 for both τ_{A5} and τ_{A4}. These values were chosen as the effects of aerosol on water retrievals were shown to be less important at these values (see §6.5). These thresholds were ultimately not helpful as they tended to remove all or most retrievals from the northern hemisphere, including those that look realistic, and even then

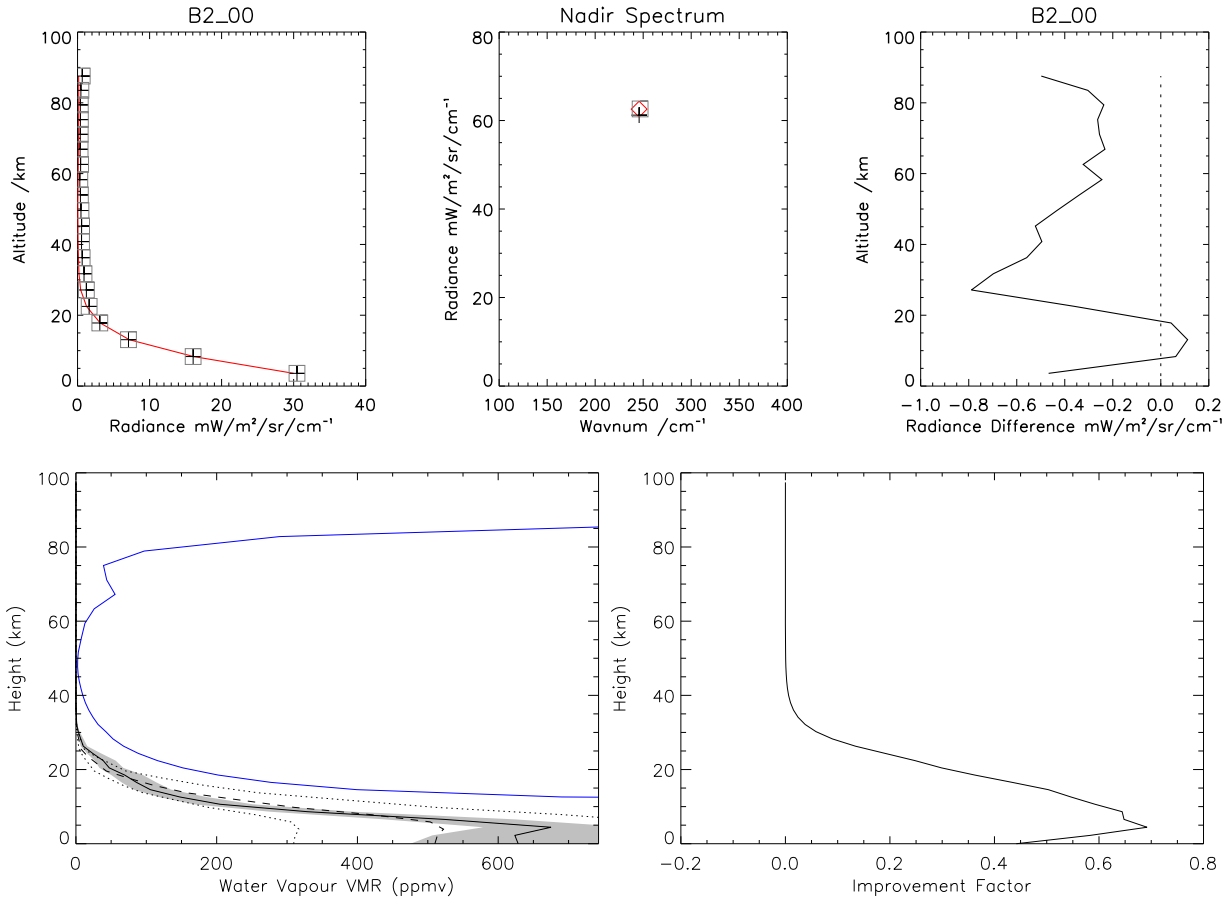


Figure 8.2 | Radiance Fits & Retrieval for N. Mid-Latitude Dayside Water Retrieval:**(Top Left)** Limb radiance fits where the red line corresponds to retrieved radiances and the black crosses in grey squares indicate observed radiances, **(Top Middle)** nadir fit. **(Top Right)** difference between observed and retrieved limb radiances. **(Bottom Left)** Retrieved water vapour profile as black solid line with grey shaded error. The APR profile and error are the dashed and dotted lines respectively and the blue line is the saturation VMR. **(Bottom Right)** improvement factor.

some spurious retrievals were still left in the filtered data.

Retrieval coverage for each block is given in Fig. 8.3. Coverage for dayside results is much better than for nightside results, due to harsher thresholds in χ^2/n_y required for the nightside results. In the dayside results, coverage is good between the mid-latitudes and poles for both hemispheres, with better northern hemisphere coverage for the early summer dayside results. For the nightside results, northern hemisphere coverage is considerably lower than for the southern hemisphere, with the early summer block having better overall coverage than the late summer block.

The large gap in the equatorial and northern tropics for all blocks is mirrored in the χ^2/n_y distribution (Fig. 8.1). High aerosol opacities in this region prevent good retrievals from being performed here. For dust this is due to the high equatorial opacities and for water ice high opacities in the equator and northern tropics.

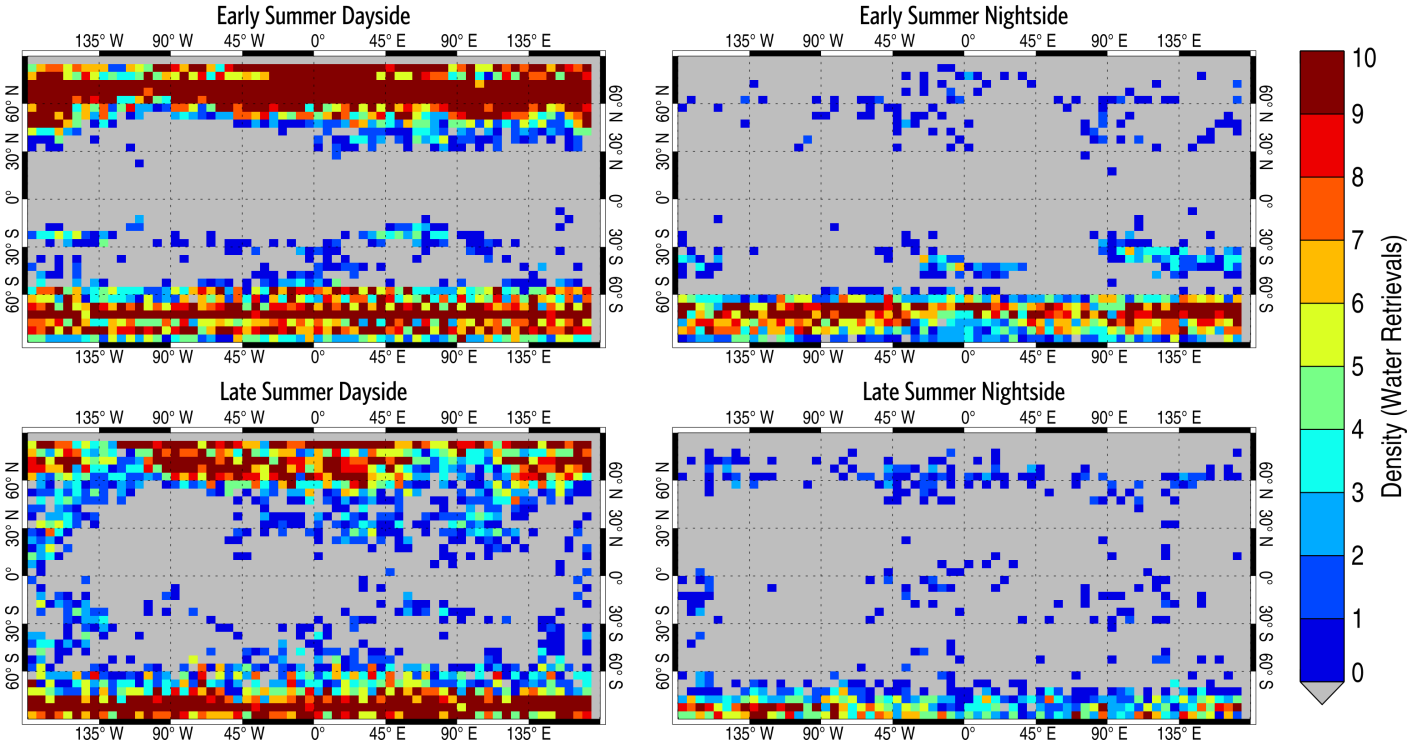


Figure 8.3 | Number of retrievals per bin for early/late summer dayside and nightside result blocks. Dark red bins have ≥10 retrievals.

For zonal average plots and histogram map plots retrieved profiles were binned in bins of 5° latitude and 6.25° longitude and 5 km in height. For the zonal average line profile plots the retrievals were binned in bins of 10° latitude. For the line plots a mean profile and the standard deviation were calculated for all of the retrievals in the bin.

8.3.2 First Stage Retrieval Results

As water vapour is the main focus of this work, retrievals of temperature and aerosol will only be discussed briefly. Zonal averages for temperature, surface temperature and aerosol are given in Figs 8.4–8.9. These are compared with the MCS retrieval results of McCleese et al. (2010). In their paper they present seasonal average retrievals of temperature and aerosols. In comparing the respective datasets some important differences need to be taken into account. The results plots used from McCleese et al. (2010) for the comparison are bins centred at L_s=90°, 135° and 180°. They are the average of a Martian year and half's worth observations (MY28 & MY29). Our observations blocks are centred at L_s=126° (111–140°, early summer) and 157° (140–173°, late summer) and are for MY28 only. Consequently, our retrieval bins are temporally in-between the results for comparison. Additionally, fewer observations are available for averaging especially when accounting for the χ^2/n_y selection criteria, with the problem being worse for nightside

results. Our selection criteria will inevitably lead to sampling bias likely preferring lower opacity aerosol results, as these are more conducive to successful water vapour retrievals. However, as acknowledged in McCleese et al. (2010) this is already a problem with their MCS retrievals though to a lesser extent.

In our retrievals we use height above the surface as our vertical coordinate, whereas McCleese et al. (2010) use pressure as their main vertical coordinate. Our choice to use height is based on the fact that in the literature vertical profiles of water vapour are generally presented in this manner (including those for comparison later in this chapter). This then allows simple cross-referencing between our first stage results and water results. This makes comparisons with McCleese et al. (2010) slightly more difficult, but not impossible. They provide areoid (Mars equipotential surface) heights for their temperature results. These are a reasonable approximation to surface height. Areoid equivalent heights are provided in the captions for dust and water ice opacity.

For temperature the thermal structure from our retrievals is a good match to those of McCleese et al. (2010). In the early summer results the asymmetry in warmth is readily visible. Also seen is the so-called 'polar warming' in the middle atmosphere over the the colder southern polar vortex. The northern polar vortex is also visible as a weak temperature minimum at 40 km, with an overlying north polar warming (though less intense than its southern counterpart). Also seen in the nightside early summer results is a 155–160 K region stretching across from the edge of the southern polar warming feature towards the equator. McCleese et al. (2010) relate this to the thermal tide.

For the late summer the results are closer to the equinox results of McCleese et al. (2010) with a move towards a more symmetric structure in temperature about the equator. Strong middle atmospheric warmings of broad horizontal extent are present, overlying polar vortices that have similar temperatures.

For dust, our results compare reasonably well with those of McCleese et al. (2010). For the dayside, regions of moderate to high dust opacity are seen extending from the southern tropics towards the pole. In the early summer the dust opacity has a greater altitude extent in the tropics and polar regions, reaching to about 25 km. In late summer this drops to about 15 km. Highest opacities for early summer are seen at 60–80°N in our results. The early summer equatorial peak seen in their results is absent in ours. This is because we have empty bins at the equator, due to the low likelihood of retrieval success because of the high opacities present.

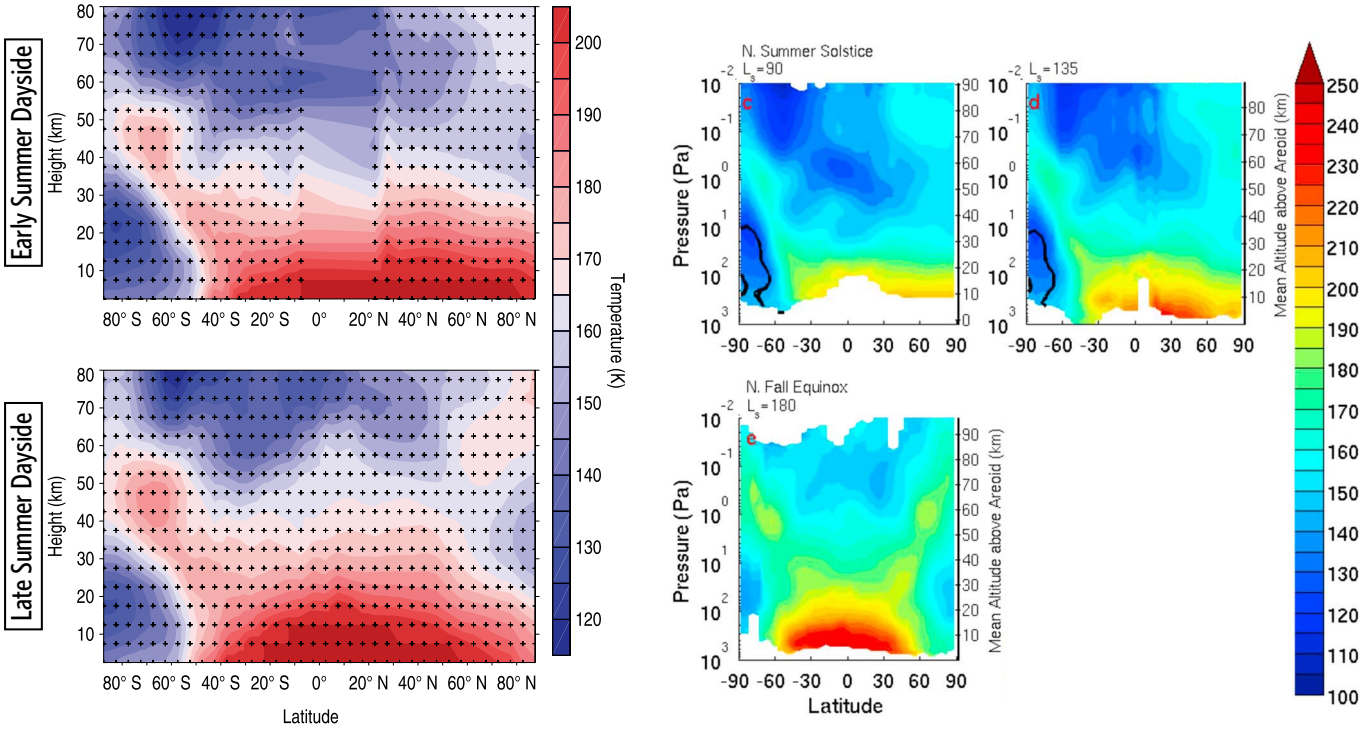


Figure 8.4 | Zonal average dayside temperature retrievals: **(Left Top)** early summer (bin centre: L_s=126°), **(Left Bottom)** late summer (bin centre: L_s=157°). Bins containing data marked with cross. **(Right)** Results from McCleese et al. (2010) for comparison for (L_s bin in title). Black contour indicates CO_2 frost point.

Credit: Reproduced from McCleese et al. (2010), 'Structure and dynamics of the Martian lower and middle atmosphere as observed by the Mars Climate Sounder: Seasonal variations in zonal mean temperature, dust, and water ice aerosols'. Journal of Geophysical Research (Planets), 115, E12016. Copyright 2010 by the American Geophysical Union (0148-0227/10/2010JE003677).

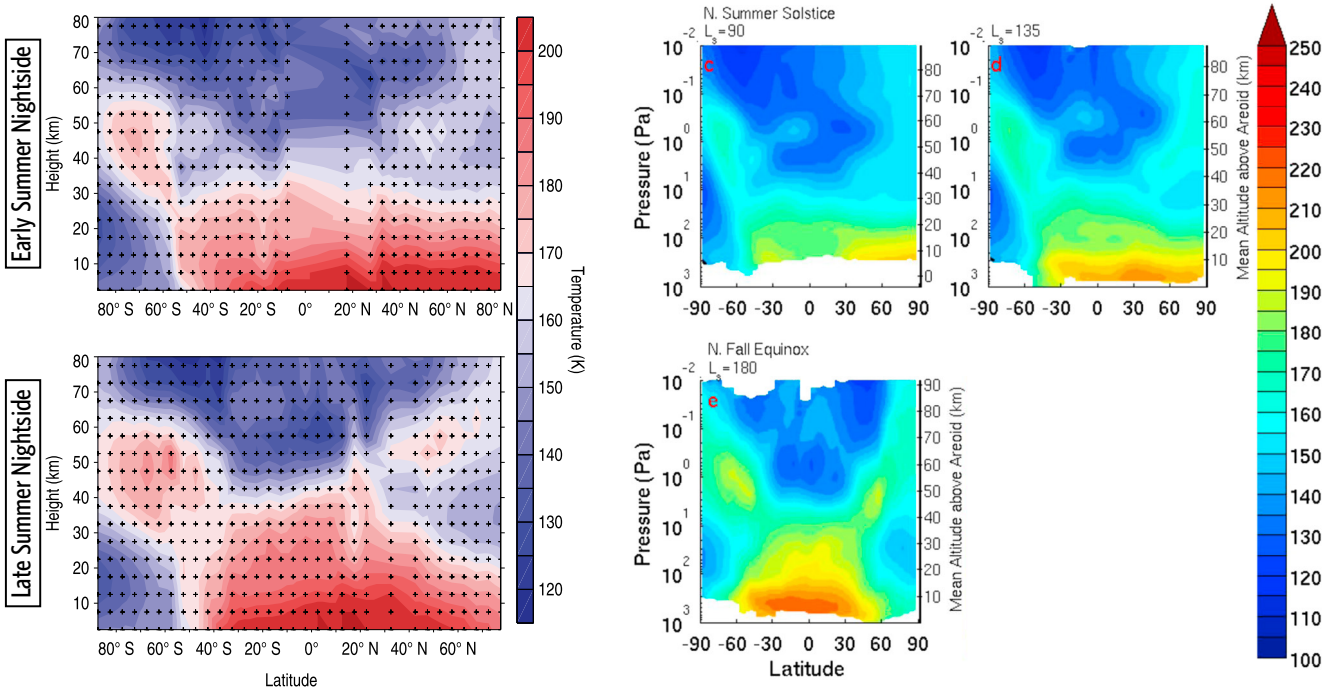


Figure 8.5 | Zonal average nightside temperature retrievals: **(Left Top)** early summer (bin centre: L_s=126°), **(Left Bottom)** late summer (bin centre: L_s=157°). Bins containing data marked with cross. **(Right)** Results from McCleese et al. (2010) for comparison for (L_s bin in title). Black contour indicates CO_2 frost point.

Credit: Reproduced from McCleese et al. (2010), 'Structure and dynamics of the Martian lower and middle atmosphere as observed by the Mars Climate Sounder: Seasonal variations in zonal mean temperature, dust, and water ice aerosols'. Journal of Geophysical Research (Planets), 115, E12016. Copyright 2010 by the American Geophysical Union (0148-0227/10/2010JE003677).

The late summer equatorial maximum is present in both datasets. Lower dust opacity regions seen in the southern mid-latitudes extend to near the pole. The southern polar maximum seen in their results is much stronger than ours. This is likely due to the low opacity bias (selection bias from the χ^2/n_y thresholds) mentioned earlier.

For the nightside dust opacity, the general shape of our results matches well with those of McCleese et al. (2010). A decrease is again seen in the vertical extent of dust moving from early to late summer. The southern polar maximum is absent in our results. The selection bias will have a bigger effect on nightside results because of the stricter χ^2/n_y thresholds required. The strong maxima right at the poles are likely interpolation errors, as these regions have no data indicated by the empty bins.

For water ice, our results are a good match where data are available. In both the early and late summer blocks a potential strong diurnal variation of tropical water ice can be seen, attributed to the diurnal thermal tide by McCleese et al. (2010). The strongest regions of ice opacity are confined to the equator on the dayside and more spread out on the nightside (and

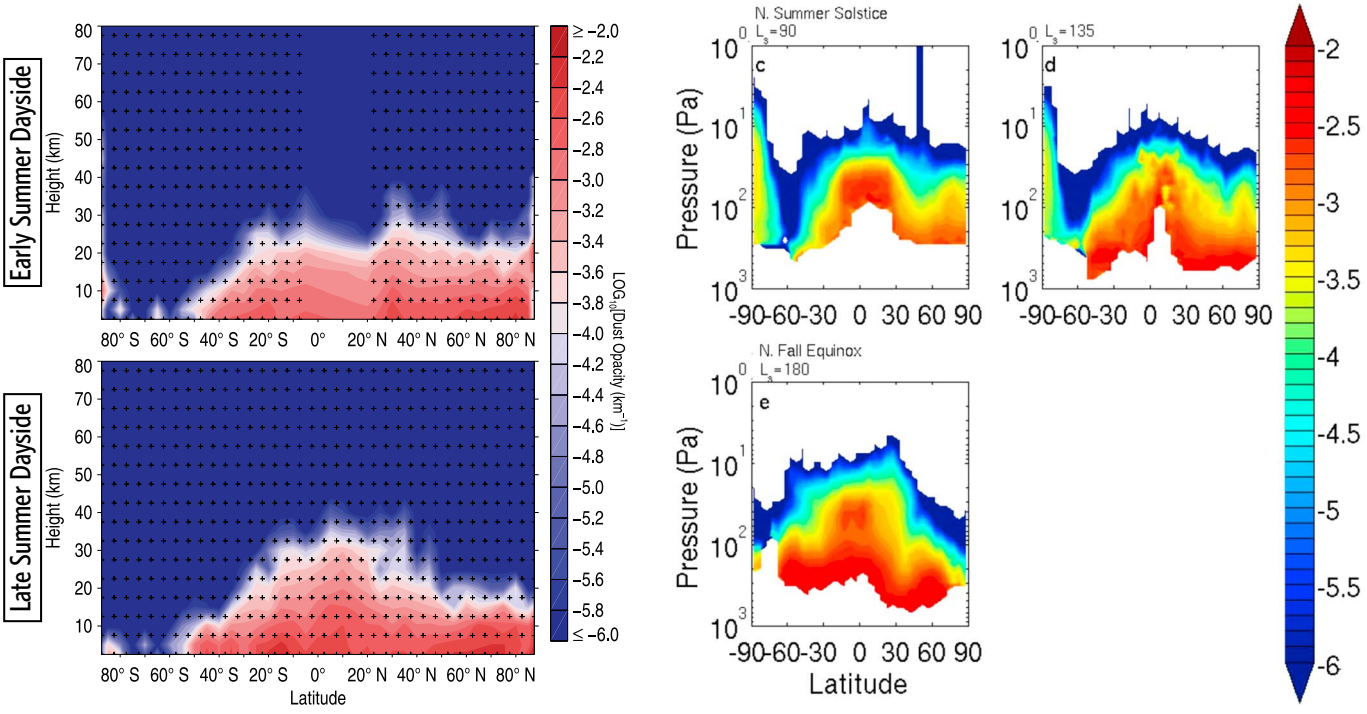


Figure 8.6 | Log_{10} of zonal average dust opacity (km^{-1}) dayside retrievals: **(Left Top)** early summer (bin centre: L_s=126°), **(Left Bottom)** late summer (bin centre: L_s=157°). Bins containing data marked with cross. **(Right)** Results from McCleese et al. (2010) for comparison for (L_s bin in title). Vertical coordinate is pressure (see text for details). Height-pressure equivalents: $h(p{=}10^3\ \mathrm{Pa}){\approx}0$ km and $h(p{=}10^0\ \mathrm{Pa}){\approx}50$ km.

Credit: Reproduced from McCleese et al. (2010), 'Structure and dynamics of the Martian lower and middle atmosphere as observed by the Mars Climate Sounder: Seasonal variations in zonal mean temperature, dust, and water ice aerosols'. Journal of Geophysical Research (Planets), 115, E12016. Copyright 2010 by the American Geophysical Union (0148-0227/10/2010JE003677).

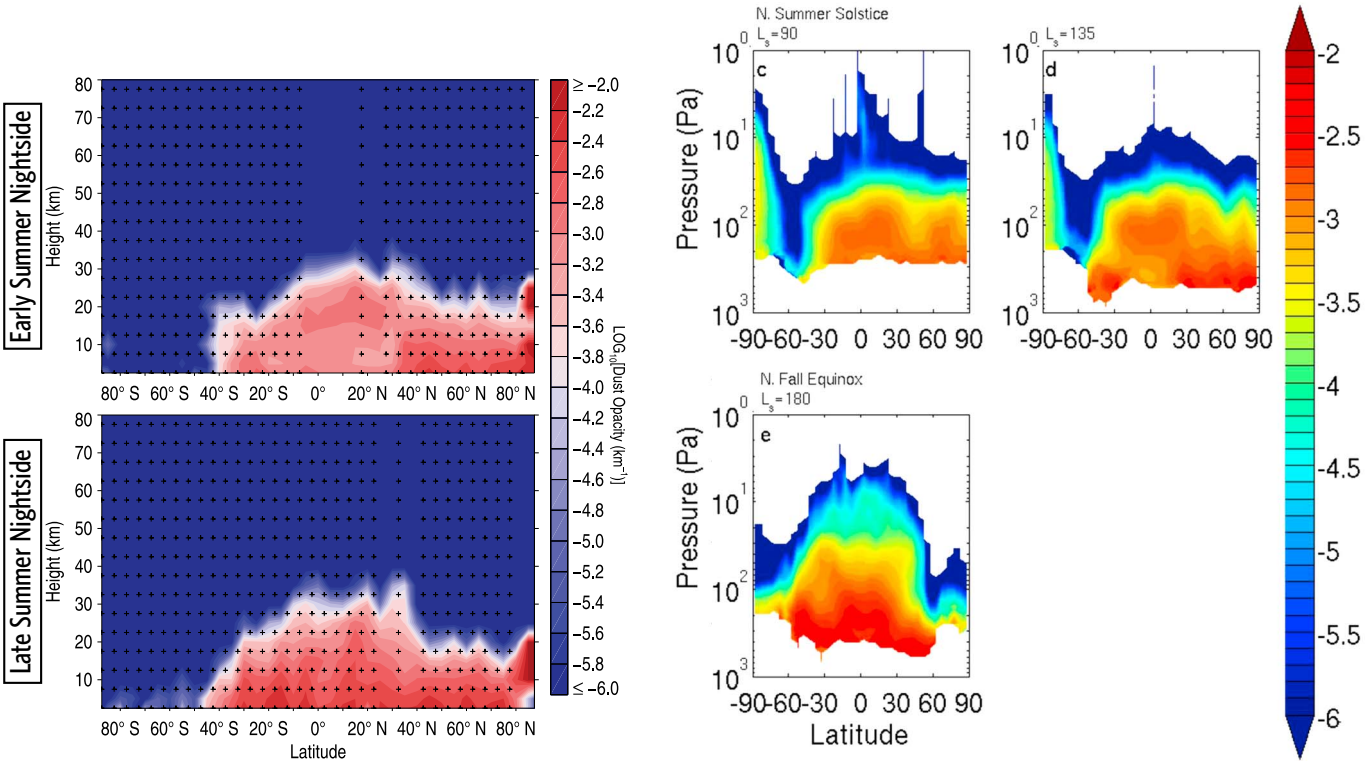


Figure 8.7 | Log_{10} of zonal average dust opacity (km^{-1}) nightside retrievals: **(Left Top)** early summer (bin centre: L_s=126°), **(Left Bottom)** late summer (bin centre: L_s=157°). Bins containing data marked with cross. **(Right)** Results from McCleese et al. (2010) for comparison for (L_s bin in title). Vertical coordinate is pressure (see text for details). Height-pressure equivalents: $h(p{=}10^3\ \text{Pa}){\approx}0$ km and $h(p{=}10^0\ \text{Pa}){\approx}50$ km.

Credit: Reproduced from McCleese et al. (2010), 'Structure and dynamics of the Martian lower and middle atmosphere as observed by the Mars Climate Sounder: Seasonal variations in zonal mean temperature, dust, and water ice aerosols'. Journal of Geophysical Research (Planets), 115, E12016. Copyright 2010 by the American Geophysical Union (0148-0227/10/2010JE003677).

reaching to lower altitudes), the 'aphelion cloud belt' seen in past observations. High equatorial ice opacity for early summer dayside results is implied by the empty bins in this region, and the elevated opacities on either side.

For the late summer multiple broad maxima are seen over the latitude range. Strong diurnal variation is also observed. For the dayside results a well-defined minimum is seen at 30°N tilting towards 60°N at 40 km. An additional minimum is seen for both dayside and nightside results at 30°S leaning towards 60°S at 40 km. Our results seems intermittent between that observed in their L_s=135° and L_s=180° bins. This is attributed to our results block being in between the two L_s bins of McCleese et al. (2010).

8.3.3 Second Stage Retrieval Results

8.3.4 Column Abundances

In Fig. 8.10 column abundances calculated with dayside results are compared with those of TES (Smith, 2004; Krasnopolsky et al., 2015), SPICAM (Trokhimovskiy et al., 2015; Krasnopolsky et al., 2015), ground-based observations and MCD observations (at the given longitude though this is fairly close to the zonal average; Krasnopolsky et al., 2015) at L_s=110° (close to our L_s=111–140° range). Most of these are presented in the third panel down, which is taken from Fig. 3 of Krasnopolsky et al. (2015) where the TES data has been averaged over three Martian years (also at the given longitude and also close to the zonal average) and the SPICAM (zonal average) data over five. In the bottom panel is a plot of zonal column abundance vs L_s also averaged over five Martian years (MY27–31). Local surface time for the TES observations is 1400, for SPICAM variable times around noon and for the MCD and ground-based results 0920. The nightside results have been left out of this section because the poor coverage gives undue weight to the spurious retrievals and outliers more prominent in those blocks, leaving little useful information to be gleaned.

Column abundances are given for both topography scaled (blue line) and unscaled (red line) cases. The scaled values account for differences in topography and are calculated according to (Smith et al., 2002):

$$d_{\text{scale}} = \frac{d}{(p_{\text{surf}}/6.1)}, \tag{8.1}$$

where d_{scale} is the topography scaled water vapour column abundance in pr. µm, d is the unscaled column abundance and p_{surf} is the surface pressure in mbar.

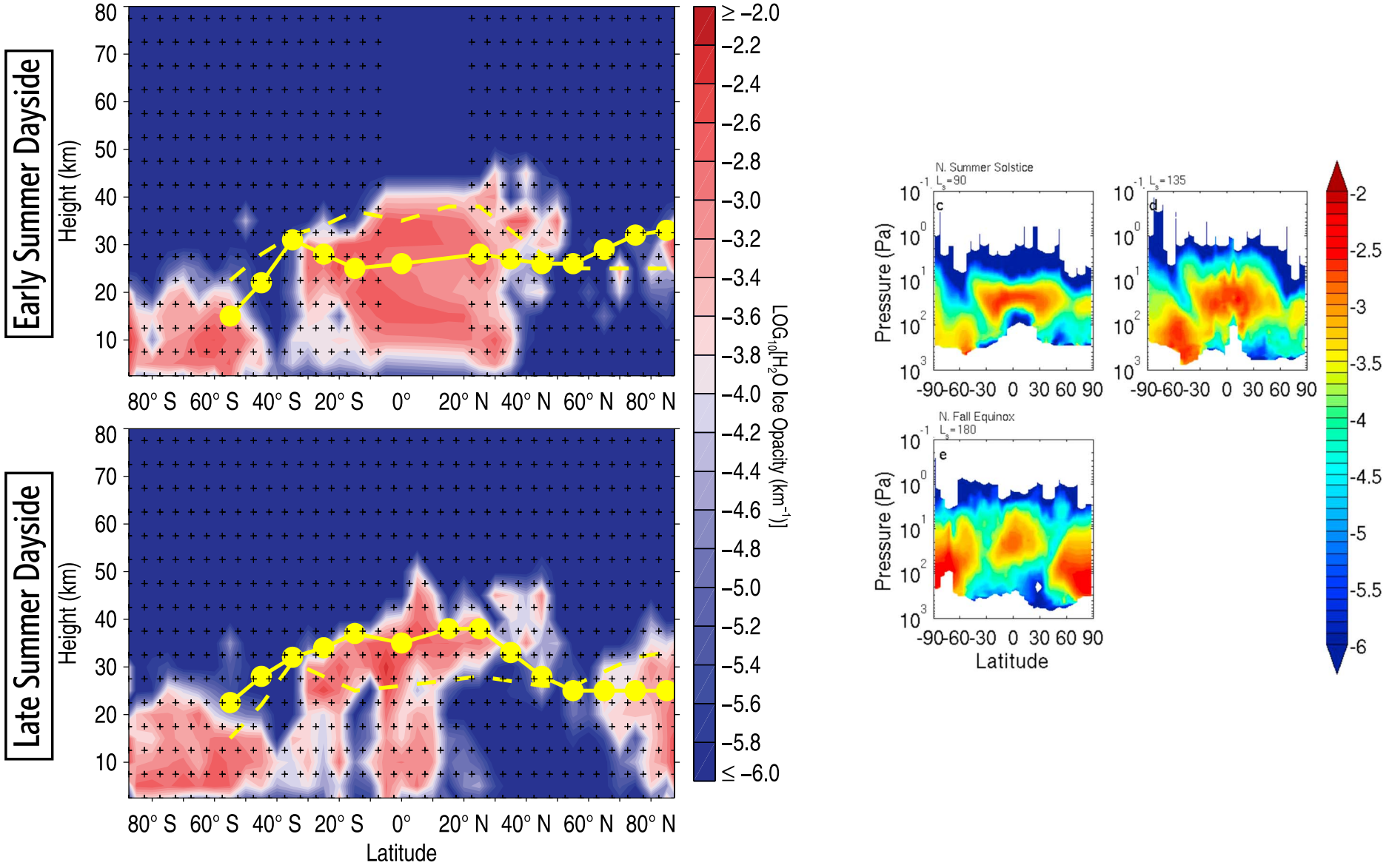


Figure 8.8 | Log_{10} of zonal average water ice opacity (km^{-1}) dayside retrievals: **(Left Top)** early summer (bin centre: L_s=126°), **(Left Bottom)** late summer (bin centre: L_s=157°). Bins containing data marked with cross. **(Right)** Results from McCleese et al. (2010) for comparison for (L_s bin in title). Vertical coordinate is pressure (see text for details). Height-pressure equivalents: $h(p=10^3\ \text{Pa})\approx 0$ km and $h(p=10^{-1}\ \text{Pa})\approx 70$ km. (**Yellow Lines**) These are overplotted on the retrievals on the left. They mark the 'profile top', a proxy for the condensation level, discussed in §8.3.5. The solid line gives the profile top for the season/plot that it is in. Circles show bin centres from line plots used to calculate profile top (see Fig. 8.12). The dashed line gives the value for the other season, for ease of comparison.

Credit: Reproduced from McCleese et al. (2010), 'Structure and dynamics of the Martian lower and middle atmosphere as observed by the Mars Climate Sounder: Seasonal variations in zonal mean temperature, dust, and water ice aerosols'. Journal of Geophysical Research (Planets), 115, E12016. Copyright 2010 by the American Geophysical Union (0148-0227/10/2010JE003677).

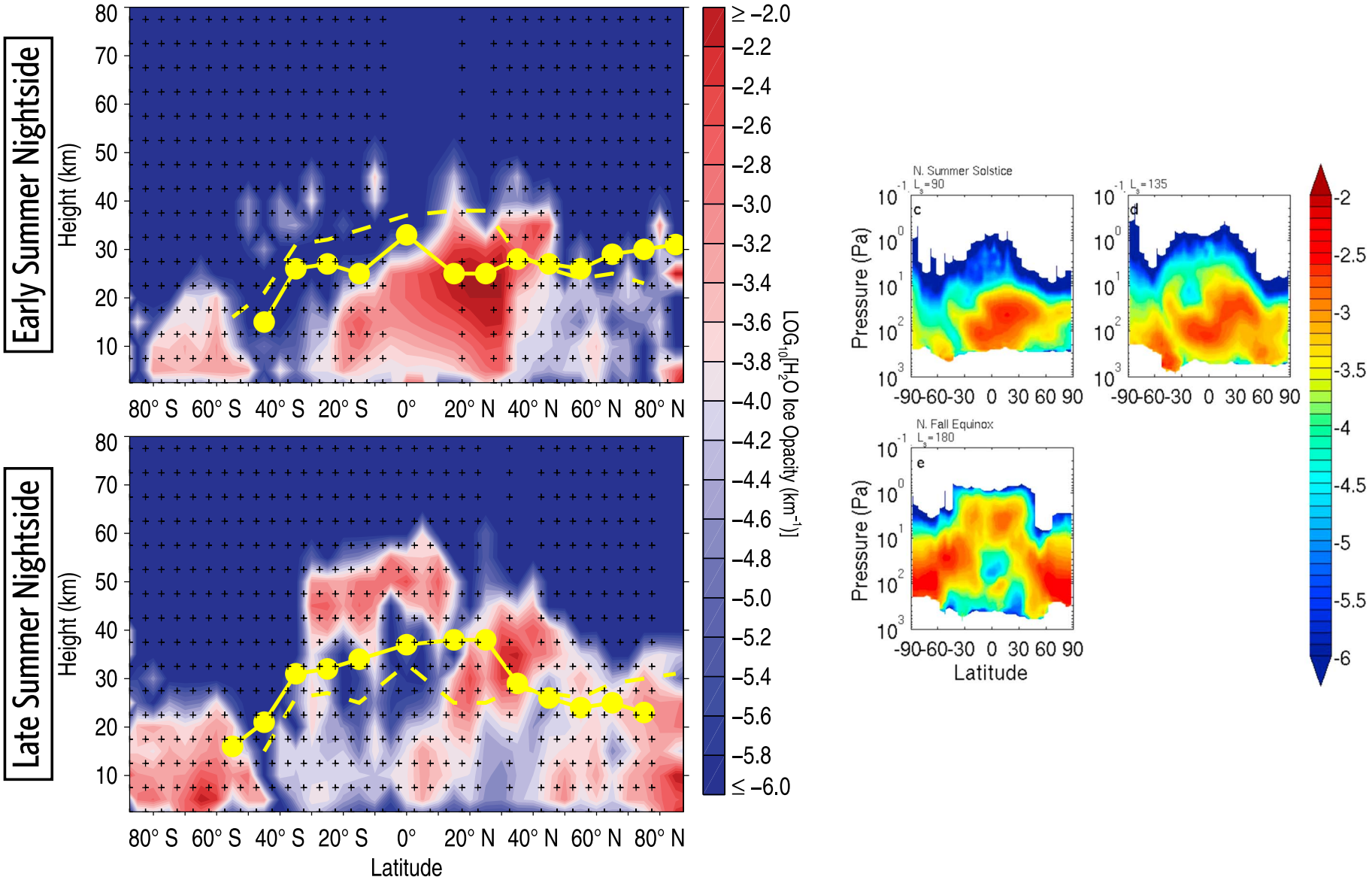


Figure 8.9 | Log_{10} of zonal average water ice opacity (km^{-1}) nightside retrievals: **(Left Top)** early summer (bin centre: L_s=126°), **(Left Bottom)** late summer (bin centre: L_s=157°). Bins containing data marked with cross. **(Right)** Results from McCleese et al. (2010) for comparison for (L_s bin in title). Vertical coordinate is pressure (see text for details). Height-pressure equivalents: $h(p{=}10^3\ \text{Pa}){\approx}0$ km and $h(p{=}10^{-1}\ \text{Pa}){\approx}70$ km. (**Yellow Lines**) These are overplotted on the retrievals on the left. They mark the 'profile top', a proxy for the condensation level, discussed in §8.3.5. The solid line gives the profile top for the season/plot that it is in. Circles show bin centres from line plots used to calculate profile top (see Fig. 8.13). The dashed line gives the value for the other season, for ease of comparison.

Credit: Reproduced from McCleese et al. (2010), 'Structure and dynamics of the Martian lower and middle atmosphere as observed by the Mars Climate Sounder: Seasonal variations in zonal mean temperature, dust, and water ice aerosols'. Journal of Geophysical Research (Planets), 115, E12016. Copyright 2010 by the American Geophysical Union (0148-0227/10/2010JE003677).

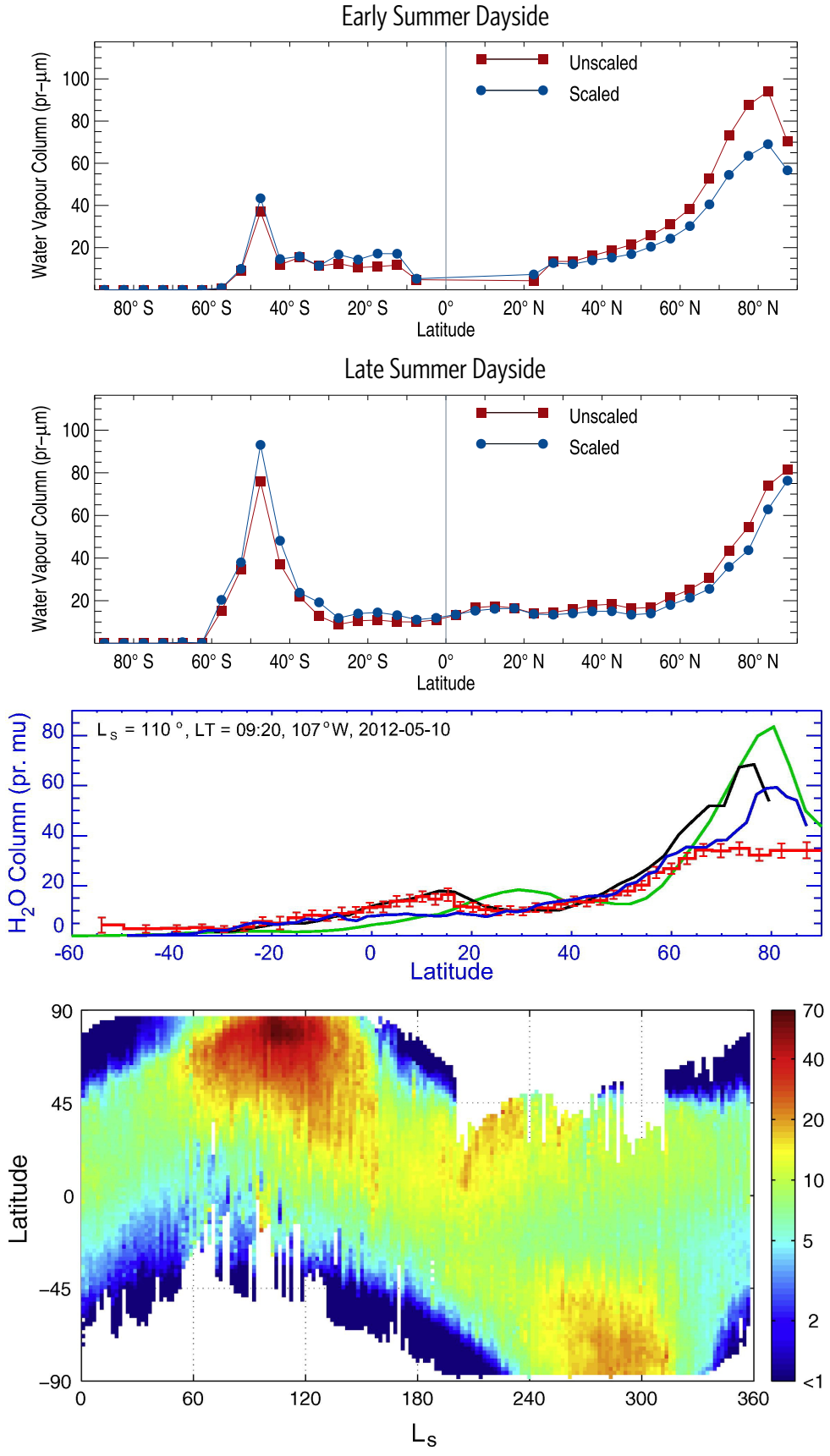


Figure 8.10 | Water vapour column abundances for dayside results: **(Top)** Early Summer (L_s=111–140°); **(Centre Top)** Late Summer (L_s=140–173°); **(Centre Bottom)** results from TES (black line), SPICAM (blue line), ground-based telescope (red line) and MCD (green line) and **(Bottom)** SPICAM zonal column abundance vs L_s.

Credit: (CB) Reprinted from Icarus, 257, Krasnopolsky (2015), 'Variations of the HDO/H_2O ratio in the martian atmosphere and loss of water from Mars', 377–386, Copyright (2015), with permission from Elsevier. (B) Reprinted from Icarus, 251, Krasnopolsky (2015), 'Mars' water vapor mapping by the SPICAM IR spectrometer: Five martian years of observations', 50–64, Copyright (2015), with permission from Elsevier.

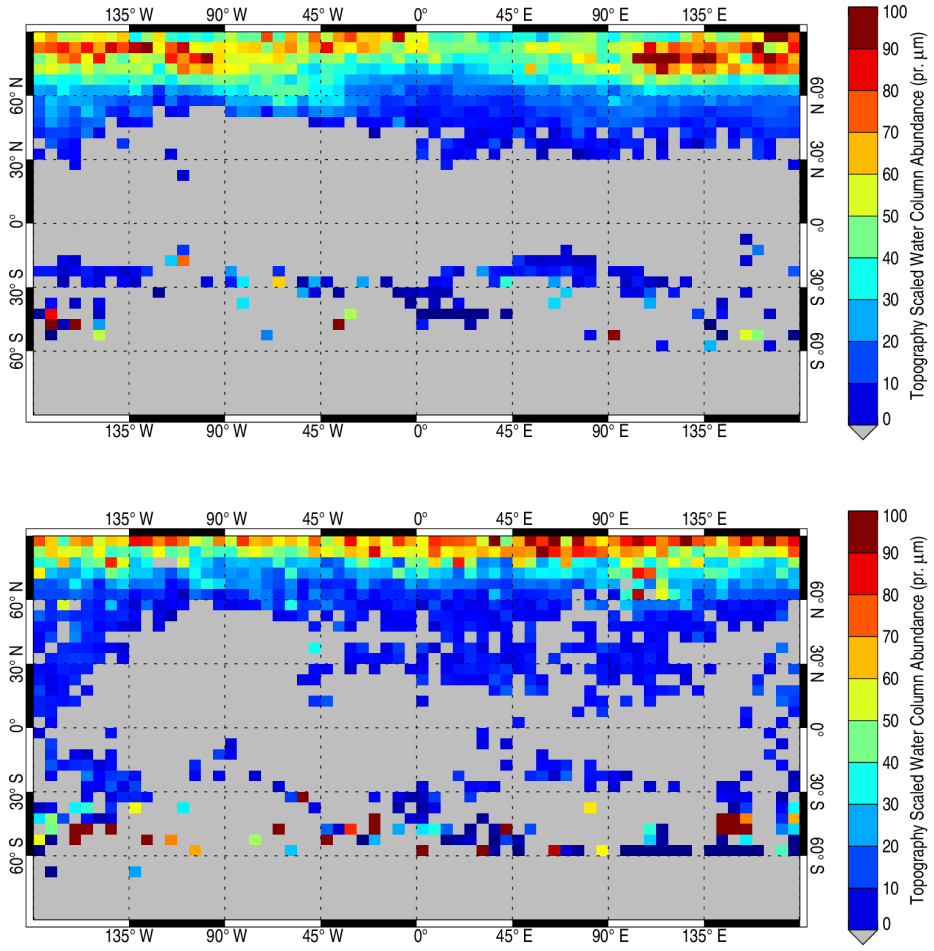


Figure 8.11 | Topography scaled water vapour column abundances for dayside results: **(Top)** Early Summer and **(Bottom)** Late Summer.

Dayside results for both early and late summer show an unrealistic large spike in the southern mid-latitudes. This is caused by the high number of spurious retrievals and outliers in this band. This can be seen when looking at the distribution for the same column abundances over latitude and longitude in Fig. 8.11. Also noticeable here is the dearth of equatorial and northern tropics results for the early summer results. However, for the late summer block there are some retrievals in this region, though relatively few in number. As explained earlier the reason for fewer retrievals here is that this is a region of high aerosol opacity making retrieval success unlikely.

Barring these problems we can see zonal average column abundances compare favourably with observations made by others in Fig. 8.10. For early summer the scaled peak values of 70 pr. µm compare well with the 60–80 pr. µm peaks of the other datasets. The peak location of 80°N matches well with the SPICAM and ground based-results, whereas for the TES results it

is a little further south. Good agreement with all datasets is seen in the 40–60°N band. In the 10–20°S band the value of 10 pr. µm seen matches reasonably well with the TES and ground-based observations. It is also important to remember that these observations come from slightly different L_s values and are for specific longitude whereas ours are a zonal average. Despite this good agreement has been achieved.

Late summer results are for higher L_s than most of the comparison datasets and so comparison with them is of little use. However, SPICAM values at this season are available in the bottom panel of Fig. 8.10 in the zonal average vs L_s plot. Good agreement with their results is found. The peak has moved further north and the drop-off to lower values in the northern hemisphere is much steeper. Relatively constant values of 20 pr. µm are seen up to the southern hemisphere spike with near-zero abundances near the pole.

Looking at the column abundance maps in Fig. 8.11 longitudinal changes in water abundance can also be seen between the early and late summer result. Notably in the early summer the high abundance regions at north polar latitudes are strongly separated in the early summer block, confined in two bands, one from 90°E–90°W and a second smaller band at 50°W–0°W. These match well with the OMEGA polar map results (L_s=111–115°) of Melchiorri et al. (2007).

8.3.5 Vertical Profiles & Comparison with CRISM Results

Shown in Figs 8.12 and 8.13 are the vertical profiles of volume mixing ratio (VMR) in parts per million by volume (ppmv) of the water vapour retrievals. Results have been presented in the same way as for the first stage, one figure for dayside results and one for nightside. Each figure includes both early and late summer blocks allowing for easy comparison of seasonal changes. Results south of 70°S have been omitted as retrieval information content is very low here and the abundances are near-zero so close to the pole.

Profiles for the improvement factor retrieval diagnostic (see Eq. 6.7), for selected latitude bands from early summer, for day and nightside retrievals, are presented in Fig. 8.14. They give an indication of where information is found in the retrieval. For sake of brevity, only selected latitude bands are presented in the figure, as these are representative of the surrounding bands and clearly show the relationship between information content and latitude. The same behaviour is seen in the late summer retrievals. Moving southwards, retrieval information content is higher and has a larger vertical extent in the warmer NH than in the colder SH, matching abundance and vertical extent of the water vapour profile. The information content is near-zero at latitudes

south of 60°S, due to the low water vapour content and low radiances (near the noise level), as a consequence of the lower temperatures here. The plots also clearly show how information content drops below 5 km and at high altitudes as the retrieval relaxes back towards the APR at all latitudes.

From looking at the water vapour profiles the reason behind the spuriously high column abundances becomes apparent. This is in the form of apparent detached water layers (DWL) with very high mixing ratios, often well in excess of the corresponding saturation VMR. The DWL are mostly present in areas of high aerosol opacity such as the tropics and equator (dust and ice) and polar regions (ice from the polar hood). It is likely that many of these are false retrievals where an additional radiance contribution in B2, from aerosol, has been misinterpreted as a water signal and led to false overly large abundances. This is probably due to the wrong choice of aerosol size distribution. As has been noted the problem is much more severe in the nightside results and this is likely to be due to the ice particles here being larger than previously thought (Kleinböhl et al., 2017).

Ignoring these for a moment, we can see that despite this the general expected trend of a very dry winter southern hemisphere (SH) with a much wetter northern hemisphere (NH) is seen. This is most notable in the polar regions at the caps where the bulk of the water is released and profiles increase to large amounts close to the surface. It can be identified in both the dayside and nightside results, with the vertical extension of the water vapour layer increasing in the NH. In the dayside, the expected results of a reasonably constant VMR down from the condensation level towards the ground can be seen until high northern latitudes, where very high VMRs are present at the seasonal caps. In the nightside results a similar pattern is seen, though the effects on the average profile of the high VMR DWL are more prevalent than on the dayside results.

In addition some inversion layers for water vapour close to the ground in the boundary layer can be seen northwards of the equator up to about 80°N. However, the reliability of the inversion layers result is debatable as they are in the region below about 5 km where the improvement factor (see Fig. 8.14) is decreasing rapidly and the retrieval will be relaxing back towards the APR which include inversion layers (see Fig. 8.2 for an example). Also, it is important to note that many of the L2 profiles used to create APR profiles for the first stage retrievals were incomplete in their altitude coverage and had to be extrapolated for our retrievals (see the Method section). This often means that where L2-based APR profiles were used, the bottom 5–10 km of aerosol profiles in particular are part of that extrapolated range. These may be

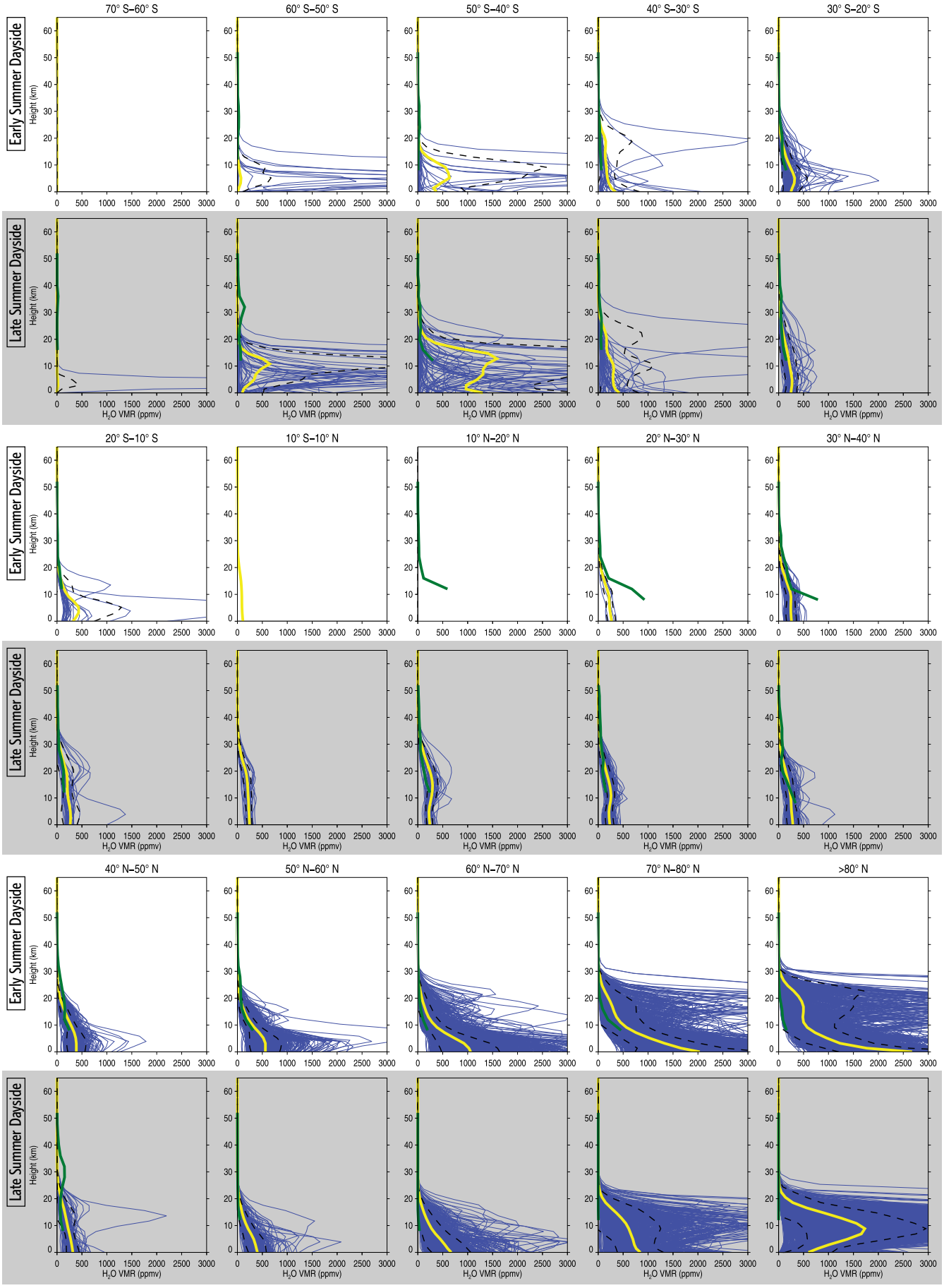


Figure 8.12 | Dayside water retrievals with latitude bins for early/late summer on top of each other as marked. Profiles (blue lines) have been overplotted with mean (yellow line) and standard deviation (black dashed line). Profiles have been height shifted to the areoid and are overplotted with the CRISM results (green line).

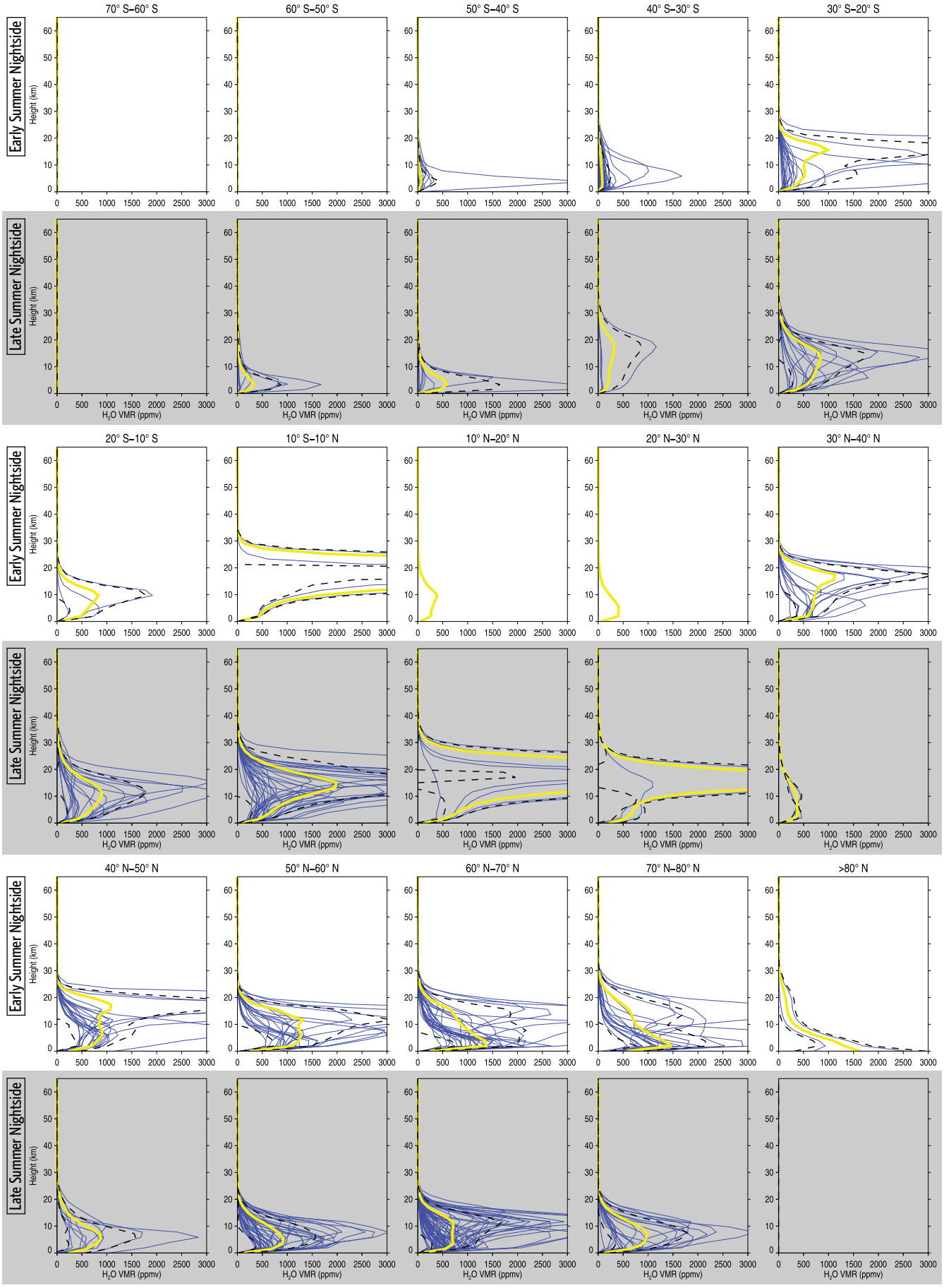


Figure 8.13 | Nightside water retrievals with latitude bins for early/late summer on top of each other as marked. Profiles (blue lines) have been overplotted with mean (yellow line) and standard deviation (black dashed line).

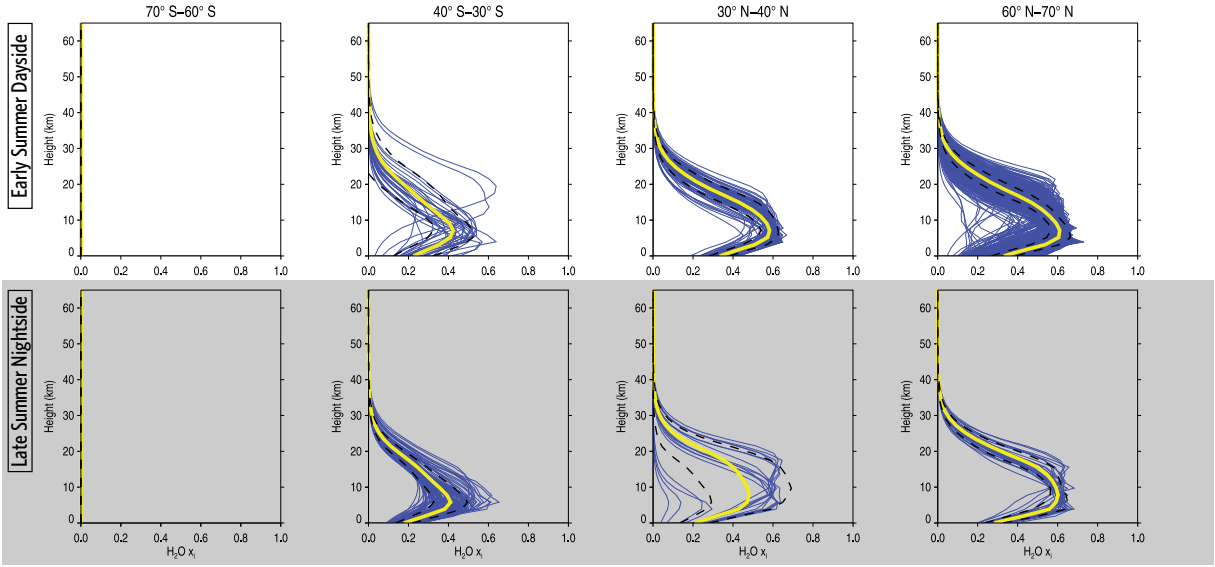


Figure 8.14 | Improvement factor for Dayside/Nightside water retrievals for selected latitude bins for early summer on top of each other as marked. Profiles (blue lines) have been overplotted with mean (yellow line) and standard deviation (black dashed line).

unreliable due to likely high limb path aerosol opacities seen this low in the atmosphere.

Assessing diurnal variation is hampered by the poorer coverage for nightside results and high numbers of spurious profiles. However, some comparison can be made by comparing the envelopes of the retrieved profiles in each latitude bin and looking for overlap. A high degree of overlap would suggest no significant variation between dayside and nightside results in that bin. For both early and late summer there is significant overlap between the profile envelopes in regions where aerosol opacity is lower and the water abundance (and hence water signal) is stronger. This can be seen for early and late summer results polewards of 30°N, and 40–20°S. Numerical calculations of the difference were made for bins where there is more than one profile for the equivalent dayside/nightside results of the same season. A selection of these results are given in Fig. 8.15 as these are representative of all the results. The difference was calculated as the difference between the average profiles of the bins in Figs. 8.12 & 8.13: $\mathrm{VMR_{diff}} = \mathrm{VMR_{night}} - \mathrm{VMR_{day}}$. The error in the difference was calculated by adding the standard deviations of the day/night average profiles in quadrature to calculate an RMS value. It can be clearly seen that the difference is almost exclusively smaller than the error except for a few cases near the surface. These differences are highly unlikely to be genuine as they are in the region where the retrieval is insensitive as it is relaxing back to the APR (see Fig. 8.14).

There may be some genuine variation near the equator, with a decrease in the condensation height on the nightside, perhaps seen as condensation increasing the opacity of the aphelion

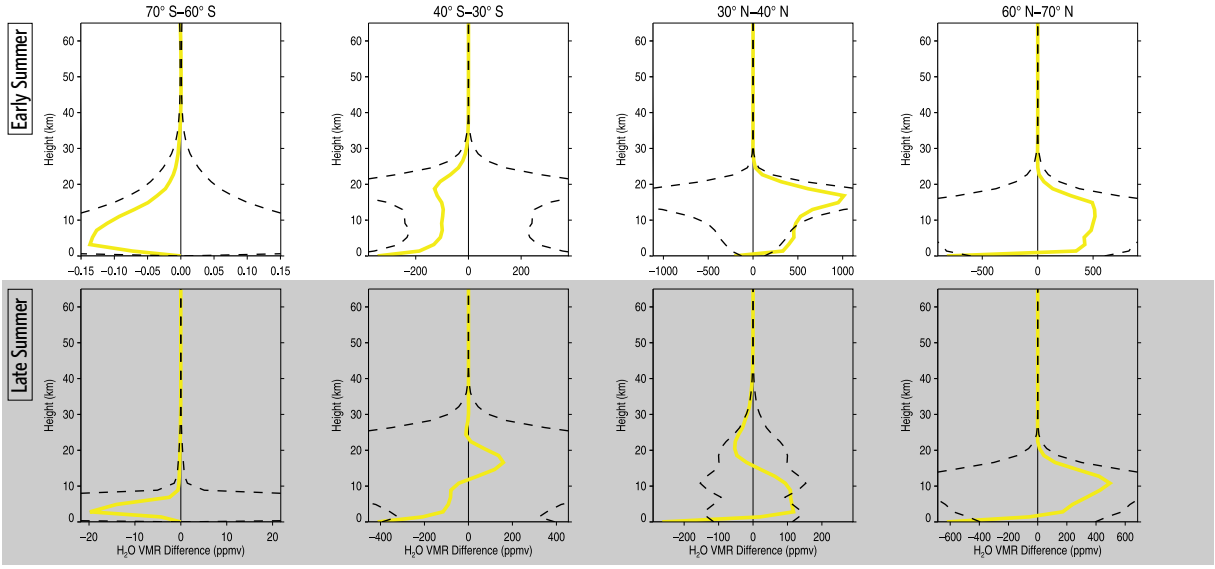


Figure 8.15 | Diurnal variation for selected latitude bins. Difference (yellow line) is calculated as $\mathrm{VMR_{diff}} = \mathrm{VMR_{night}} - \mathrm{VMR_{day}}$. Error (black dashed line) is the RMS of the standard deviations for the dayside and nightside profiles. Almost no diurnal variation can be seen outside of the error. For the regions where the difference is larger than error, near the surface, the retrieval is insensitive and relaxing back to the APR.

cloud belt at night as discussed earlier (see §8.3.2). Unfortunately, this is difficult to disentangle from errors caused by high aerosol opacity. Overall, these results suggest that for heights above 5 km (those MCS is able to probe effectively) there is little significant diurnal variation in regions of low aerosol opacity. The greatest variation is likely to lie in these problematic high opacity (due to aerosol-water interaction) areas or much closer to the surface driven by surface interactions such as regolith exchange or sublimation from the seasonal cap.

Using the results of Clancy et al. (2017) it is possible to perform validation of dayside retrievals, using their binned vertical profiles derived from CRISM retrievals of 1.27 µm $O_2(^1\Delta_g)$ dayglow over ≥8–80 km altitudes. These comparisons are particularly appropriate as CRISM is also on MRO and so observations will have the same local surface times and similar observation geometries. Their observations range from 2009–2016 (MY29–33). Seasonal averages were obtained from two of their bins, L_s=100–140° and 140–200°, which can be compared with the early summer and late summer blocks respectively. The CRISM profiles have been drawn as green lines on the dayside vertical profile plots in Fig. 8.12. To aid comparison water profiles in the figures have been mapped onto areoid heights rather than surface heights, the same as the CRISM data.

Evidence of seasonal variation is seen in the dayside results, in the form of variation of the

condensation level (vertical extent) of the water profiles. The early summer results have higher condensation levels at mid to high latitudes and these are greater also than the equivalent latitude range in the late summer. The condensation levels in early summer results then decrease towards the south pole. During the late summer we see the highest condensation levels in the equatorial regions and the tropics (mean profile reaching >30 km) with lower levels in northern mid to high latitudes. Late summer condensation levels are higher than their early summer equivalents in the southern tropics, equator and northern tropics. This matches the variation on condensation level from TES results seen in Fig. 1.7. Similar behaviour is seen in the CRISM results. The nightside results are somewhat noisier but the same pattern seems to be present.

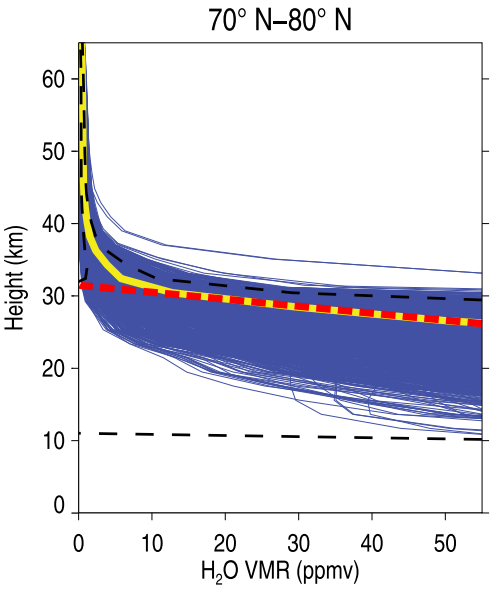


Figure 8.16 | Figure showing example extrapolation (red dashed line) used to calculate profile top for the 70–80°N bin of the early summer dayside retrievals. Profiles (blue lines) have been overplotted with mean (yellow line) and standard deviation (black dashed line).

To visualise this behaviour more easily, we created a quantity dubbed the 'profile top', to use a proxy for the condensation level. This is calculated by manually extrapolating the top 'flat' part of the average water profile from a latitude bin, to the axis, as demonstrated in Fig. 8.16. An error of ±2.5 km was estimated for the profile top due to the extrapolation. The profile top versus latitude was then overplotted on the ice opacity retrievals in Figs. 8.8 & 8.9. Due to the process of extrapolation there is likely to be a positive systematic offset between the profile top and the real condensation level, i.e. it is higher than the condensation level. An additional source of error comes from the water profiles themselves, as the profile top extrapolation uses the average profile which in turn will include some spurious high DWL results. Despite these caveats the behaviour discussed above is also seen on these plots. Also, visible is how the profile top tracks the bases of high ice opacity regions, though with a systematic offset above the base of high opacity ice levels. This verifies its reliability as a first-order approximation of the condensation level.

These seasonal difference results show the variation in vertical behaviour as water vapour is transported southward in the cross-equatorial Hadley cell, as seen in column abundance vs L_s plots, such as those in Figs. 1.4, 1.5 and 8.25. This variation in condensation level is tracked by the variation in the aphelion cloud belt strength and vertical extent (see Figs 8.8 & 8.9). When

the level is high, water reaches higher levels before condensing. The higher levels at the equator and tropics in late summer then make the aphelion cloud belt weaker in late summer than early summer.

For the early summer dayside results we see that at >80°N the CRISM profile fits within the profile envelope and 1σ. Moving southward an excellent match is seen between 80–50°N with the mean profile and the CRISM profile being on top of one another. From 50–20°N our profiles and the CRISM data start to diverge, though still matching within the profiles envelope in 10–20 km range. Raised CRISM VMRs at 20–30 km are not seen in our results. And from 30°N towards the equator much larger abundances are seen below 10 km in CRISM data. Close matches are again seen in the 10–40°S and then within the envelope for the remaining SH profiles. At 40–60°S we see matching within the envelope, with some water layers at 35 km in CRISM profiles, but not ours.

For late summer results we see close matches at altitudes >20 km in the >80–70°N range with matching within the profile envelope below this. Close matching is seen in the 70–10°N region below 30 km. Above 30 km in the 50–30°N region some layers of higher abundance are seen in the CRISM profiles, but not ours. In the SH close matches are seen from 10–30°S. A good match is again seen polewards of this for the regions where CRISM data are available.

Overall excellent agreement is found between our vertical retrievals and the CRISM dataset, particularly in the 80–50°N latitude band, where the water abundances are highest. Disagreements between the datasets come in three types: a) layers of water at ≥30 km which appear in the CRISM data but not ours b) regions where our retrievals have higher or lower abundances and match only within the profiles envelope and c) regions in the tropics where our retrievals have significantly lower abundances below 15 km.

These differences may be caused by a lack of sensitivity in our retrieval at higher altitudes or interannual variation as CRISM data are from MY29–33 and ours are from MY28. Lack of high altitude sensitivity is supported by Fig. 8.14, where at altitudes ≥30 km the improvement factor is near-zero. Regions where profiles only match within the profile envelope or in the tropics correspond to regions of high aerosol abundance and hence areas where spurious retrievals are more probable. The results are very encouraging.

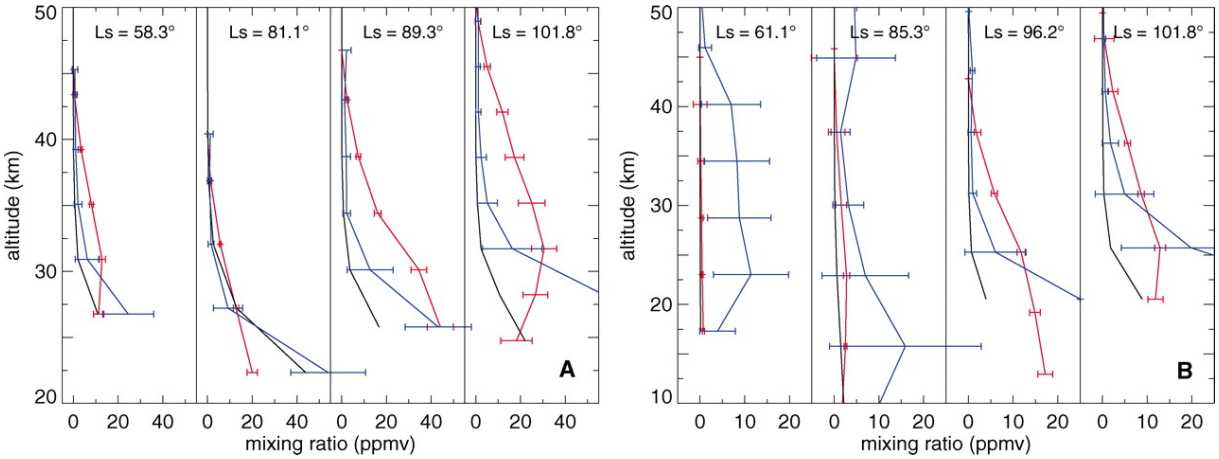


Figure 8.17 | Selection of typical water vapour volume–mixing ratio profiles in the (A) northern and (B) southern hemisphere. Black curve, modelled profile by the LMD-GCM; red curve, the retrieved SPICAM results; blue curve, saturation water vapour–mixing ratio. Supersaturation exists where the red values are greater than the blue ones.

Credit: Maltagliati et al. (2011a), Evidence of Water Vapor in Excess of Saturation in the Atmosphere of Mars'. Science, 333, 1868–1871. Reprinted with permission from AAAS.

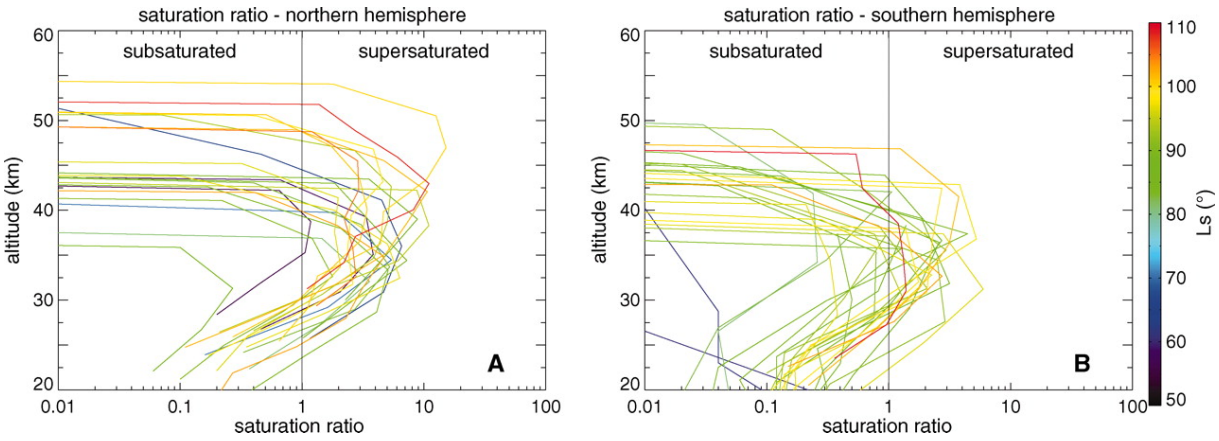


Figure 8.18 | Saturation ratio for all orbits of the campaign. (A) Northern hemisphere. (B) Southern hemisphere. The vertical line marks the value of 1, which corresponds to the saturated state.

Credit: Maltagliati et al. (2011a), Evidence of Water Vapor in Excess of Saturation in the Atmosphere of Mars'. Science, 333, 1868–1871. Reprinted with permission from AAAS.

8.3.6 Comparison with SPICAM Results

It is also possible to do vertical profile comparison with SPICAM data from Maltagliati et al. (2011a, 2013) for northern hemisphere summer observations from MY29. These can be compared with our early summer results. This is particularly pertinent with regard to detached water layer (DWL) observations as they observed supersaturation and DWL in their own data. Hence, though a lot of the DWL seen in our results are likely to be spurious, there is a possibility that some of the lower VMR cases could be genuine. Examples of supersaturation and some DWL are shown in Figs 8.17 & 8.18 (Figs 2 & 3 from their 2011a paper). However for supersaturation

to occur the atmosphere must be clear of dust, as the dust particles function as condensation nuclei for water vapour (Maltagliati et al., 2011a).

When looking at individual profiles in conjunction with the corresponding aerosol profile, for retrievals where some of the more extreme DWL occur, it can be seen that the extreme cases are most certainly spurious. This is because the peaks of the DWL line up exactly with the peak of high-opacity dust and/or water ice layers. It seems probable that with a dust/ice layer of high limb path opacity there will be significant aerosol emission or absorption in the B2 channel which is mistaken for water vapour by the retrieval. An example retrieval is shown in Fig. 8.19. Here there is a large DWL at around 20 km with co-located dust and ice peaks in specific density. Looking at the observed radiance profile it can be seen there is a radiance 'bump' at the location of the peak and this is likely due to dust radiance in the channel. The retrieval fails to match the bump and underestimates radiance here. Below the height of the DWL the water profile radiances fit well and are below saturation, indicating that the rest of this profile is more reliable.

Dust-Water Correlation

Despite these results the co-location of dust and water do not automatically entail false results. Maltagliati et al. (2013) frequently observed this correlation in their own results. Some examples from their SPICAM solar occultation retrieved profiles are given in Figs 8.20–8.23 for MY29. From their paper it can be seen that dust and water frequently appear together. Particularly pertinent examples from their paper are Figures 18c, 18f and 21b. These are closest to our results in L_s (Martian season) and can be used for comparison. They have been reproduced here alongside relevant dayside retrievals from our results. These show the water vapour mixing ratio in ppmv, allowing for direct comparison. Their dust opacities however are given as slant optical depth at around 1300 nm, so here qualitative comparisons with our results are best. Also, there is generally a big local time difference as solar occultation observations can only be performed during sunrise and sunset (c.f. MCS observations are mostly at 03h and 15h except for near the poles).

Comparing these results to the general trend of our results we start by comparing a NH mid-latitude result of theirs with similar latitude bands in our results in Fig. 8.20. In their results dust and water are co-located with a dust peak about 10 km above a water peak. In our results the overall trend is similar with the co-location of dust and water, but in the zonal plots

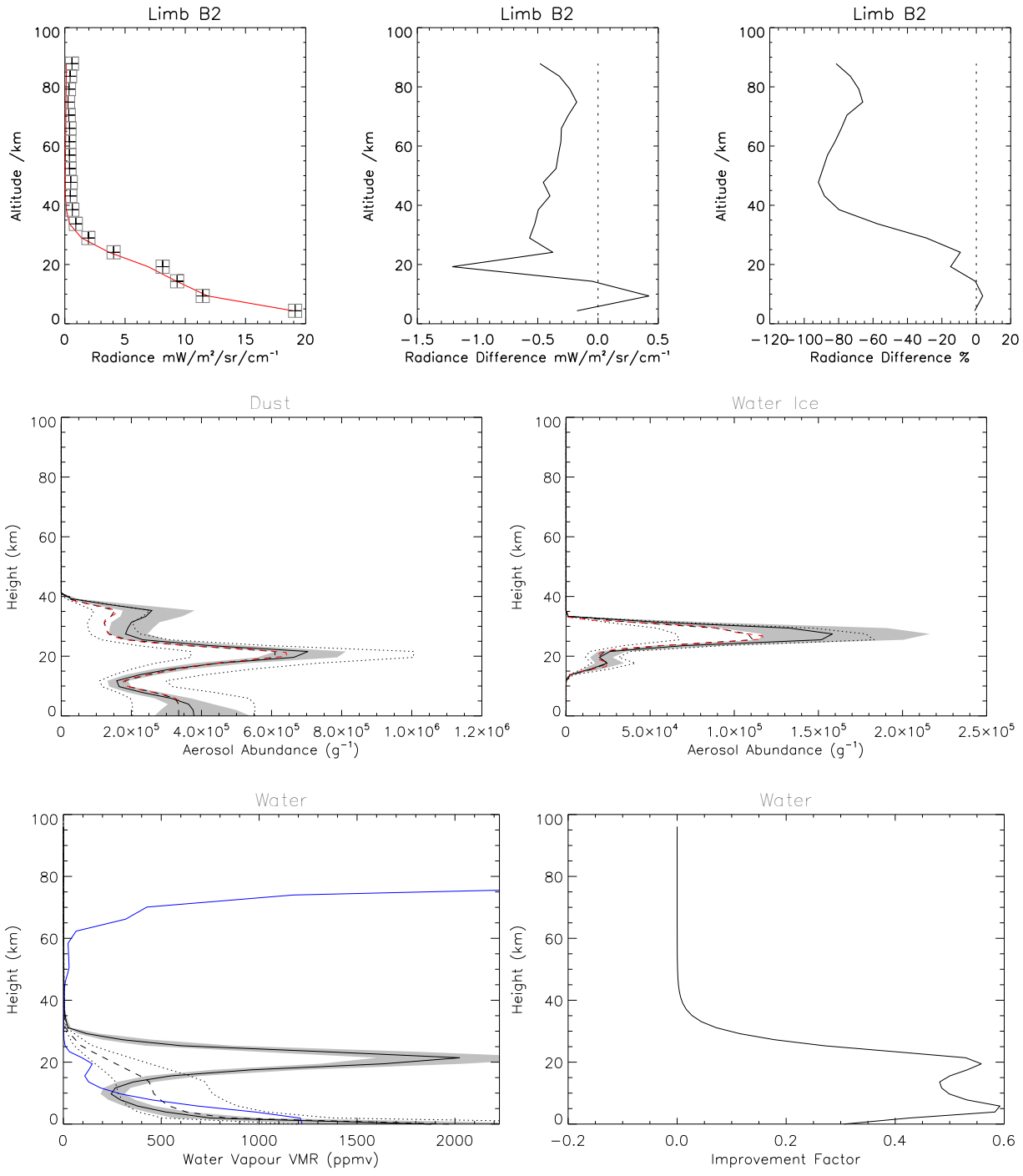


Figure 8.19 | Example of Spurious Retrieval: **(Top Left)** Limb radiance fits where the red line corresponds to retrieval radiances and the black crosses in grey squares indicate observed radiances, **(Top Middle)** difference between observed and retrieval radiances, **(Top Right)** percentage difference between observed and retrieval radiances, **(Middle Left)** dust abundance, **(Middle Right)** water ice abundance, **(Bottom Left)** retrieved water vapour profile and **(Bottom Right)** improvement factor. For plots retrieved profile is black solid line with grey shaded error. The APR profile and error are the dashed and dotted lines respectively and the blue line is the saturation VMR. Red lines are L2 profiles and errors. Observation is at L_s=114°, 86.583°N, 21.119°E at 1100 LST.

for dust and water, average line vertical profile peaks are smeared out (by the averaging). The main water ice peak is seen above both dust and water layers. This behaviour is as expected, as it is at the condensation level and is seen in the other comparison figures in this section. Looking at the results for individual retrievals (blue lines), peaks can be seen for both dust and water. Some detached dust peaks are seen, above all the water profiles at about 40 km. Additionally, in their results the water layer extends up to 50 km whereas in our results it only extends to 30–40 km.

An example from our results of a similar profile (but from 10° further north), dubbed *Retrieval A*, is given in Fig. 8.21. This contains the water profile in A(iii) along with the accompanying aerosol profiles from the first stage. From A(ii), the region seems to be free of water ice. An overlying detached dust layer is seen in A(i). This lies above both the water layer and another dust layer, though the higher peak for dust is around 30 km instead of 40 km and underlying water layer does not peak but exponentially increases towards the surface correlating closely with the dust profile.

Examining a SH mid-latitude profile in Fig 8.22 we see a more closely matched correlation with dust and water with matching layer heights and both increasing towards the surface. This is mirrored in our results, though as in the previous comparison the layer heights are higher in their results than ours, by about 5 km this time. Though some of our profiles have similar magnitude VMRs, these seem to be the 'driest' cases in our results (at the edge of the profiles envelope), as our average profile show much higher abundances. These results are more distant in L_s than the previous comparison (about 10° L_s), so differences could be due to the seasonal gap or local time. The water ice peak again caps the water and dust profiles, with a substantial secondary layer below.

The final dust-water case for comparison is a SH near-equatorial result in Fig. 8.23 which is the nearest to ours in season (L_s). Again there is a strong overlap between the dust and water layers, with the peak of the water layer lying around 2.5 km below the upper peak of the dust layer. Looking at the blue dust profiles, some detached peaks can be seen at 20 km overlying the water profiles. The vertical extent of our water retrievals is lower at 35 km compared to 50 km in their results. At lower altitudes there is a good match to the curve, but no peaks are seen in our profiles.

An example of an individual profile in this latitude band from our results, dubbed *Retrieval B*, is given in Fig. 8.24. The water profile is given in B(iii) alongside its corresponding aerosol

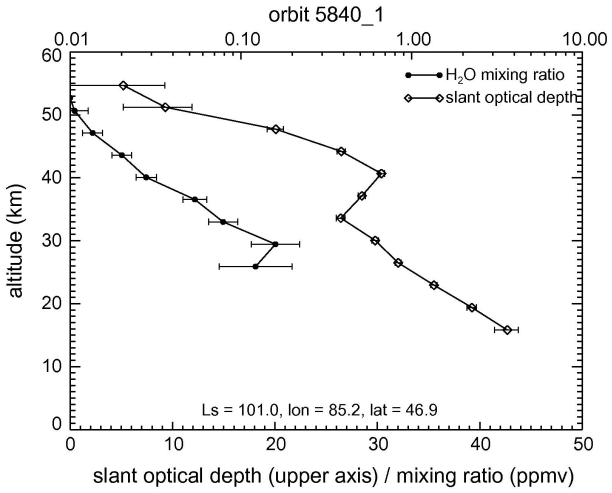
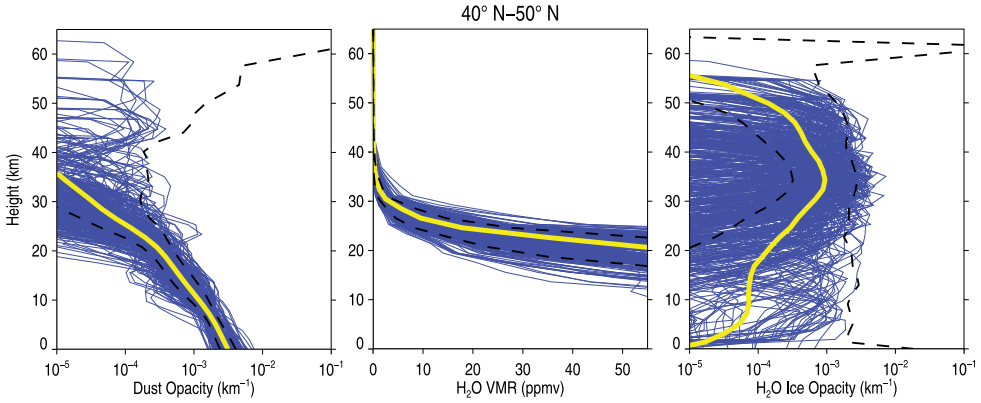


Figure 8.20 | Figure 18c from Maltagliati et al. (2013) compared with early summer 40°–50°N aerosol and water profiles. Profiles (blue lines) have been overplotted with mean (yellow line) and standard deviation (black dashed line).

Credit: Reprinted from Icarus, 223, Maltagliati et al. (2013), 'Annual survey of water vapor vertical distribution and water-aerosol coupling in the martian atmosphere observed by SPICAM/MEx solar occultations', 942–962, Copyright (2013), with permission from Elsevier.



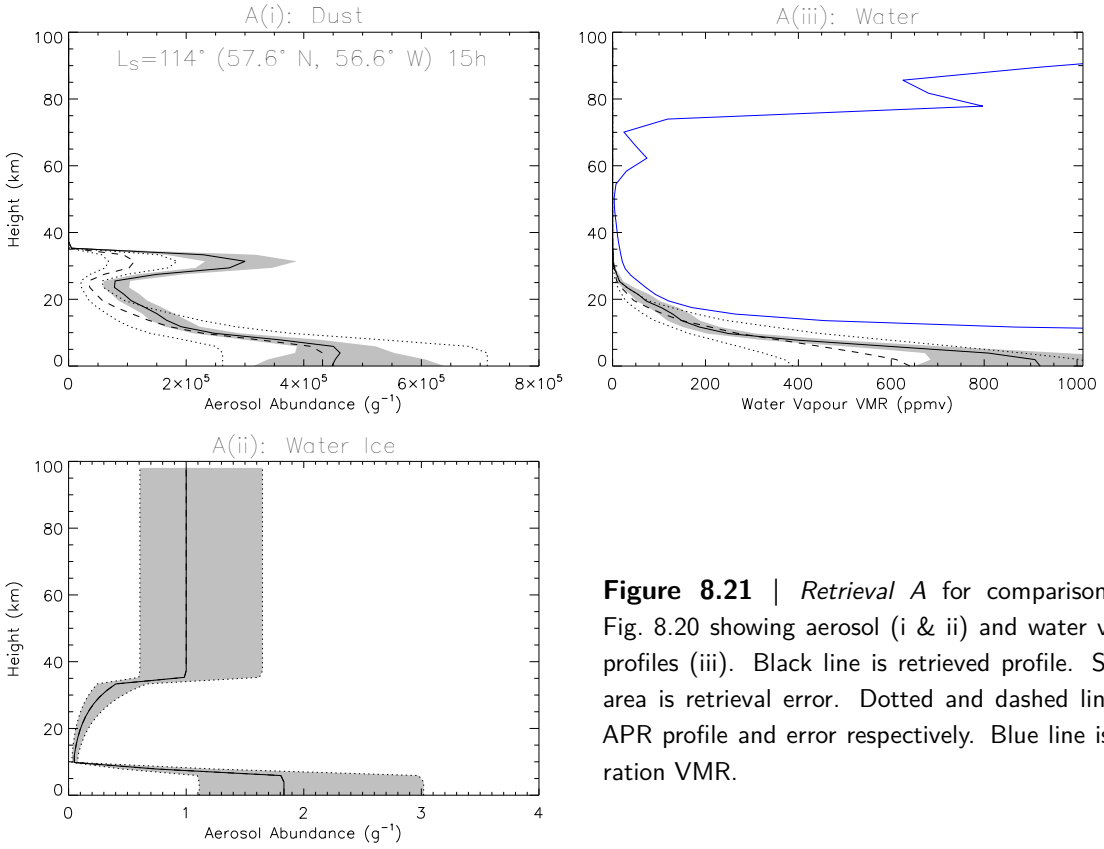


Figure 8.21 | *Retrieval A* for comparison with Fig. 8.20 showing aerosol (i & ii) and water vapour profiles (iii). Black line is retrieved profile. Shaded area is retrieval error. Dotted and dashed lines are APR profile and error respectively. Blue line is saturation VMR.

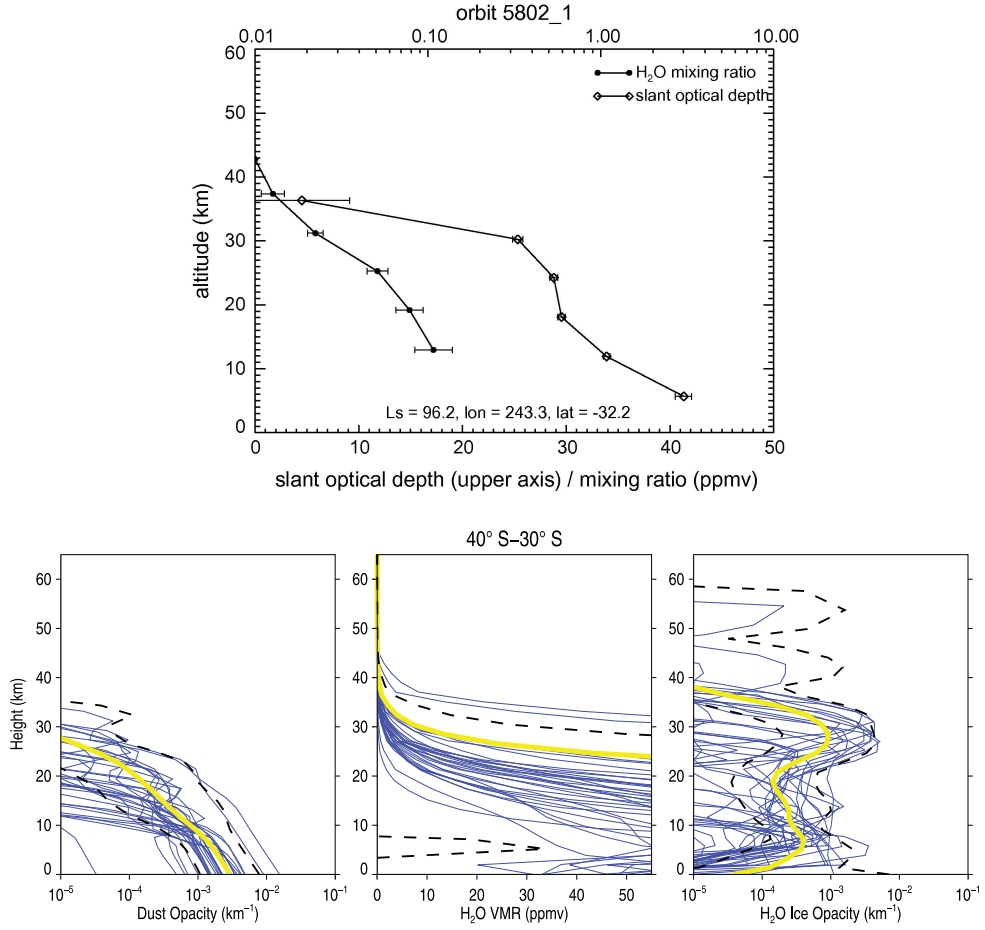


Figure 8.22 | Figure 18f from Maltagliati et al. (2013) compared with early summer 30°–40°S aerosol and water profiles. Profiles (blue lines) have been overplotted with mean (yellow line) and standard deviation (black dashed line).

Credit: Reprinted from Icarus, 223, Maltagliati et al. (2013), 'Annual survey of water vapor vertical distribution and water-aerosol coupling in the martian atmosphere observed by SPICAM/MEx solar occultations', 942–962, Copyright (2013), with permission from Elsevier.

profiles, B(i) & (ii). Three layers of dust are seen with two detached peaks at 20 and 35 km with ice layers on top of each at 25 km and 40 km, presumably having scavenged dust as condensation nuclei. Below the detached dust and ice layers the water layer is present, well below saturation and again correlating well with the bottom dust layer. There is a slight decrease just above the surface, but at these low altitudes there is likely to be little information (as the the low altitude detectors will have been removed in the selection process, see §8.2.3 & Fig. 8.14). In comparison with Fig. 8.23 we see the upper dust layer matches well in altitude. The peak in the water layer is also substantially lower than the the dust peak, with no upper peak or DWL as seen in their profile. The lack of a high water vapour peak may be due to the observed ice cloud formation at the these upper altitudes.

From our results a strong correlation is observed between dust and water vapour confirming what was seen by Maltagliati et al. (2013), in that there seems to be complex interaction between

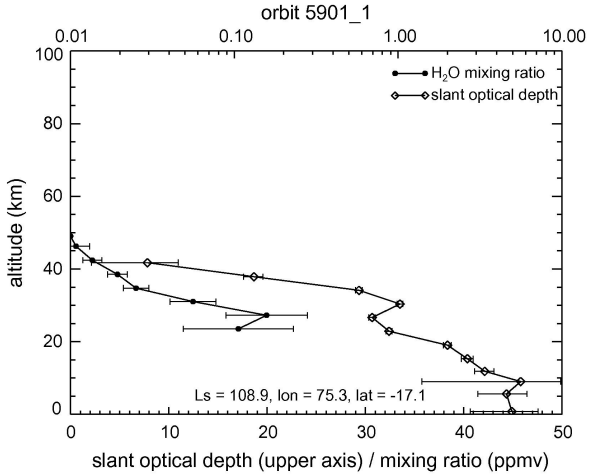
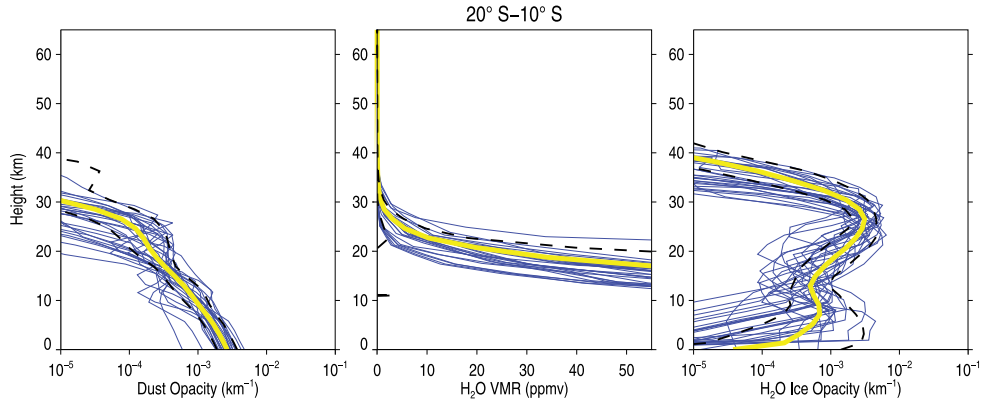


Figure 8.23 | Figure 21b from Maltagliati et al. (2013) compared with early summer 10°–20°S aerosol and water profiles. Profiles (blue lines) have been overplotted with mean (yellow line) and standard deviation (black dashed line).

Credit: Reprinted from Icarus, 223, Maltagliati et al. (2013), 'Annual survey of water vapor vertical distribution and water-aerosol coupling in the martian atmosphere observed by SPICAM/MEx solar occultations', 942–962, Copyright (2013), with permission from Elsevier.



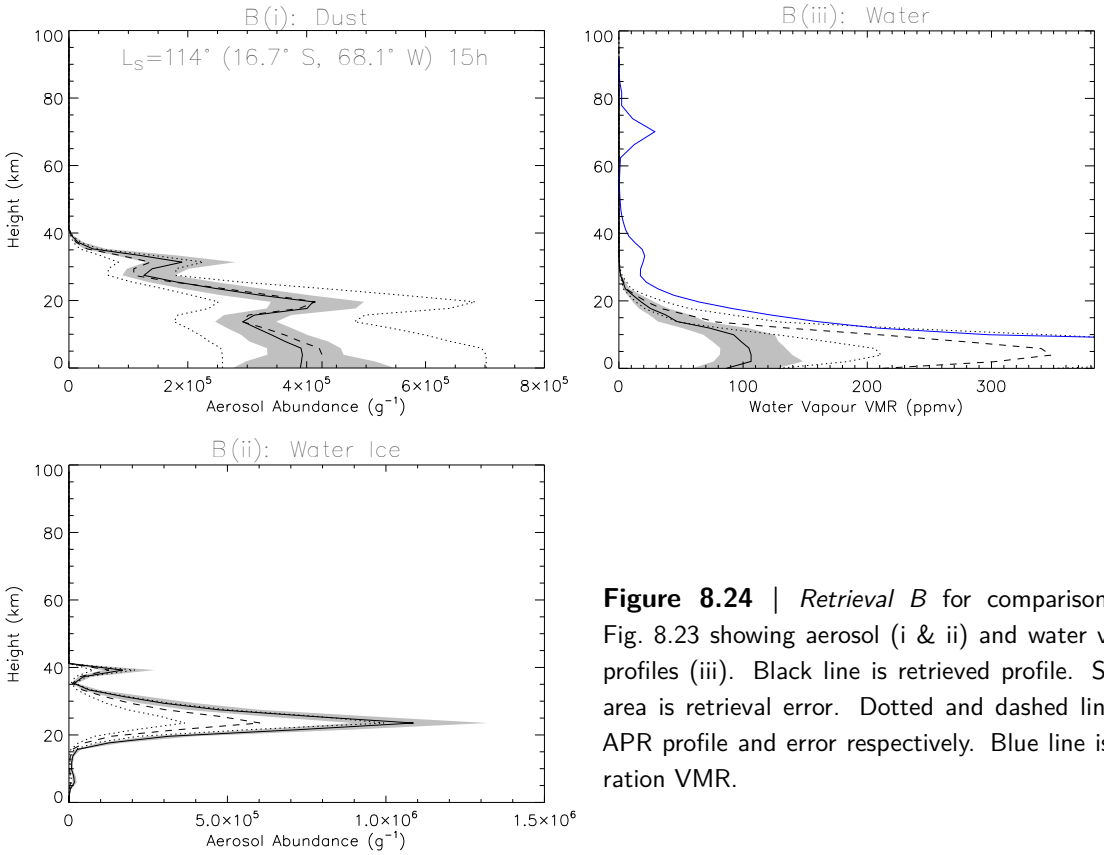


Figure 8.24 | *Retrieval B* for comparison with Fig. 8.23 showing aerosol (i & ii) and water vapour profiles (iii). Black line is retrieved profile. Shaded area is retrieval error. Dotted and dashed lines are APR profile and error respectively. Blue line is saturation VMR.

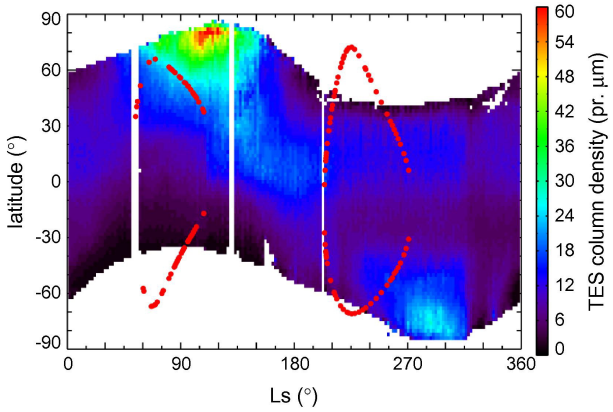


Figure 8.25 | Position of SPICAM profiles (red dots) as a function of L_s and latitude. The background illustrates the water column density in precipitable microns as measured by TES in MY26. The observations used for comparison are those from L_s=90–110°.

Credit: Reprinted from Icarus, 223, Maltagliati et al. (2013), 'Annual survey of water vapor vertical distribution and water-aerosol coupling in the martian atmosphere observed by SPICAM/MEx solar occultations', 942–962, Copyright (2013), with permission from Elsevier.

the two cycles. Additionally, water ice layers are frequently found above water layers and over or in between dust layers. The vertical extent of our water vapour profiles is frequently lower than theirs. Given that this behaviour has been seen in comparisons with both CRISM and SPICAM, it is likely that our retrievals are less sensitive to water vapour above 30 km, supported by our improvement factor profiles in Fig. 8.14.

General Comparison with Maltagliati et al. (2013)

In this section we will compare our results more generally to the vertical profiles of the first campaign from Maltagliati et al. (2013) during the period L_s=90–110°; the observation distribution over L_s and latitude is given in Fig. 8.25. In Figs. 8.26–8.29 our early summer results from similar latitude ranges are presented alongside theirs. Our profiles are limited to a similar ppmv range as their results to aid comparison. Our results start slightly later in season at L_s=111–140°, unfortunately no observations closer to ours in L_s were available.

When looking at all of these results together a number of conclusions can be drawn. Firstly, our profiles have consistently lower vertical extent with condensation levels generally about 10 km lower than theirs. This consistent difference in vertical extent between the datasets could be due to differences in local time of observation. The nature of solar occultation observations necessitates that the local time of observation will be sunrise/sunset with typically lower atmospheric temperatures than our dayside results at 15h LST. Clouds exhibit strong local time variations that will have corresponding variations in water vapour profiles, although these variations are not very specific to terminator local times (Clancy et al., 2017). However, as discussed

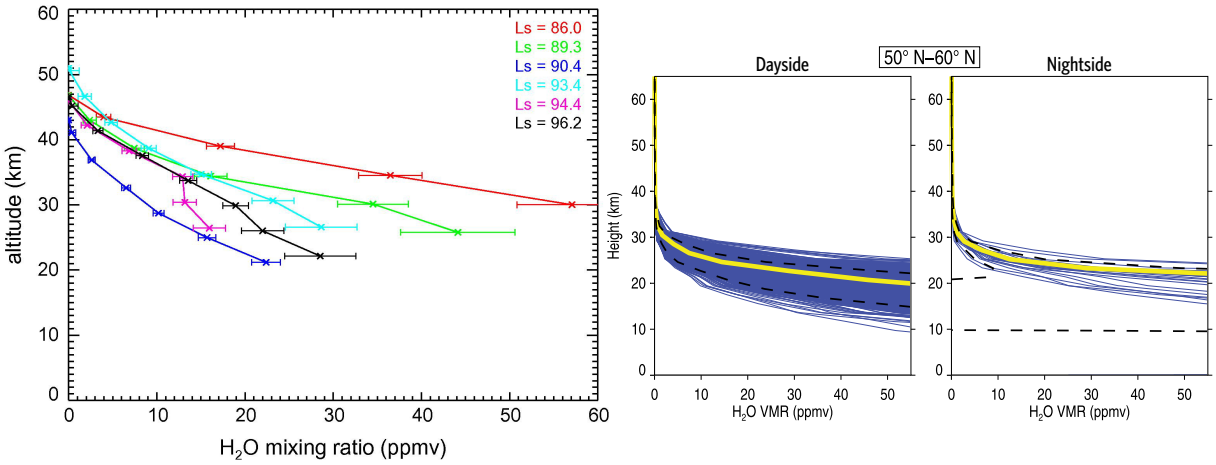


Figure 8.26 | Figure 8b from Maltagliati et al. (2013) compared with early summer 50°–60°N water profiles. Profiles (blue lines) have been overplotted with mean (yellow line) and standard deviation (black dashed line).

Credit: Reprinted from Icarus, 223, Maltagliati et al. (2013), 'Annual survey of water vapor vertical distribution and water-aerosol coupling in the martian atmosphere observed by SPICAM/MEx solar occultations', 942–962, Copyright (2013), with permission from Elsevier.

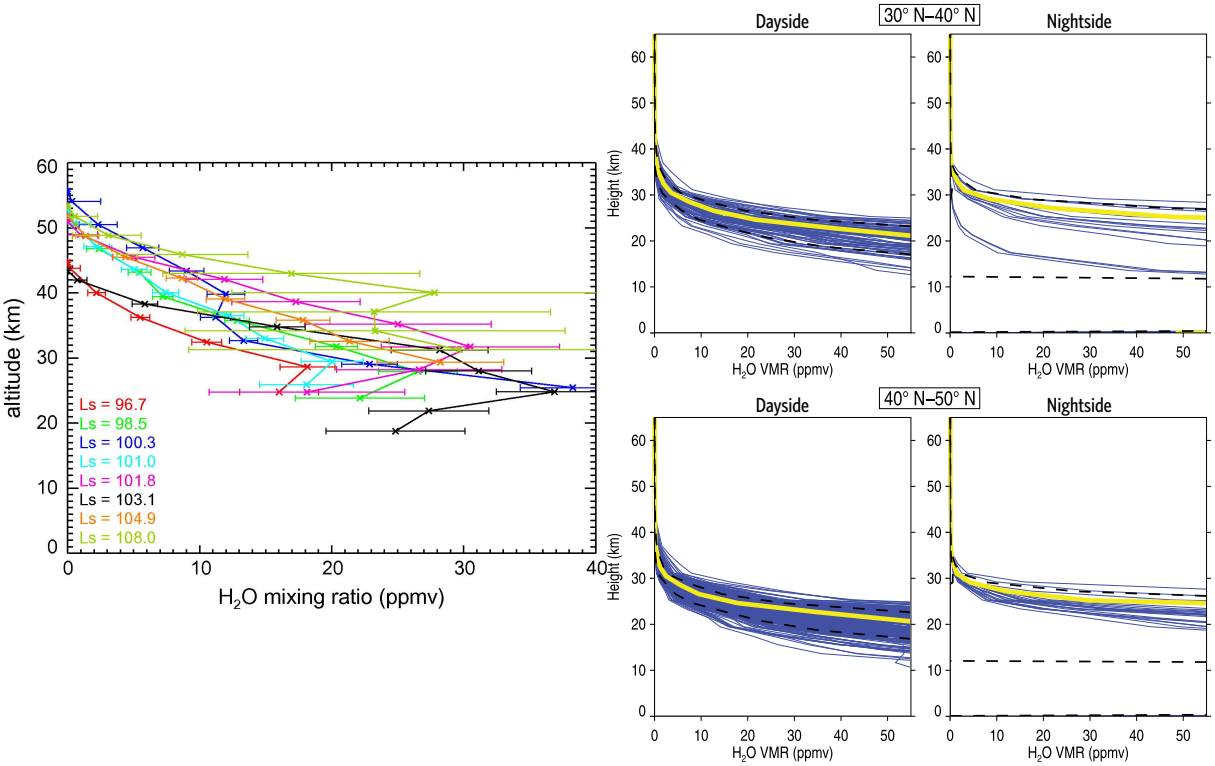


Figure 8.27 | Figure 8c from Maltagliati et al. (2013) compared with early summer 30°–50°N water profiles. Profiles (blue lines) have been overplotted with mean (yellow line) and standard deviation (black dashed line).

Credit: Reprinted from Icarus, 223, Maltagliati et al. (2013), 'Annual survey of water vapor vertical distribution and water-aerosol coupling in the martian atmosphere observed by SPICAM/MEx solar occultations', 942–962, Copyright (2013), with permission from Elsevier.

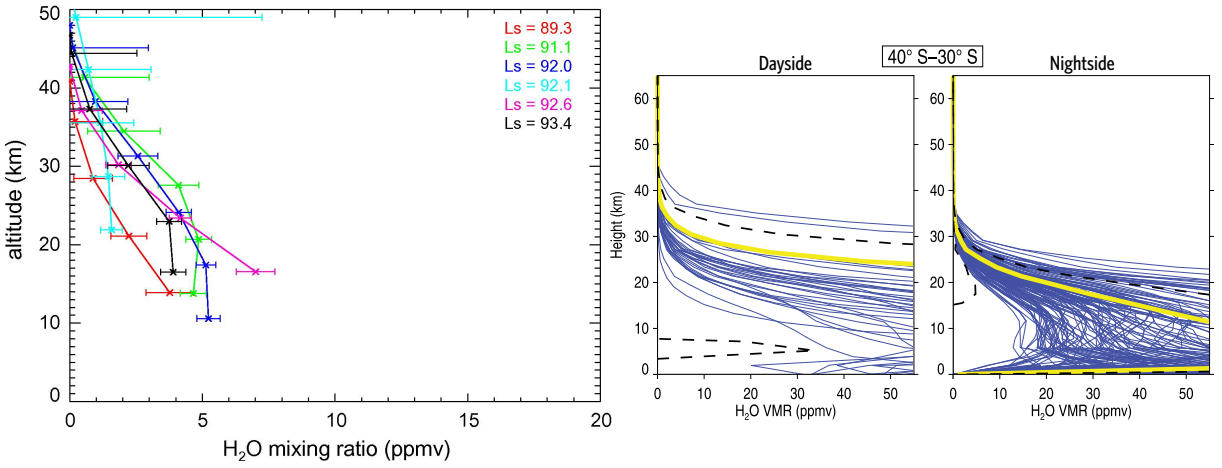


Figure 8.28 | Figure 8f from Maltagliati et al. (2013) compared with early summer 40°–30°S water profiles. Profiles (blue lines) have been overplotted with mean (yellow line) and standard deviation (black dashed line).

Credit: Reprinted from Icarus, 223, Maltagliati et al. (2013), 'Annual survey of water vapor vertical distribution and water-aerosol coupling in the martian atmosphere observed by SPICAM/MEx solar occultations', 942–962, Copyright (2013), with permission from Elsevier.

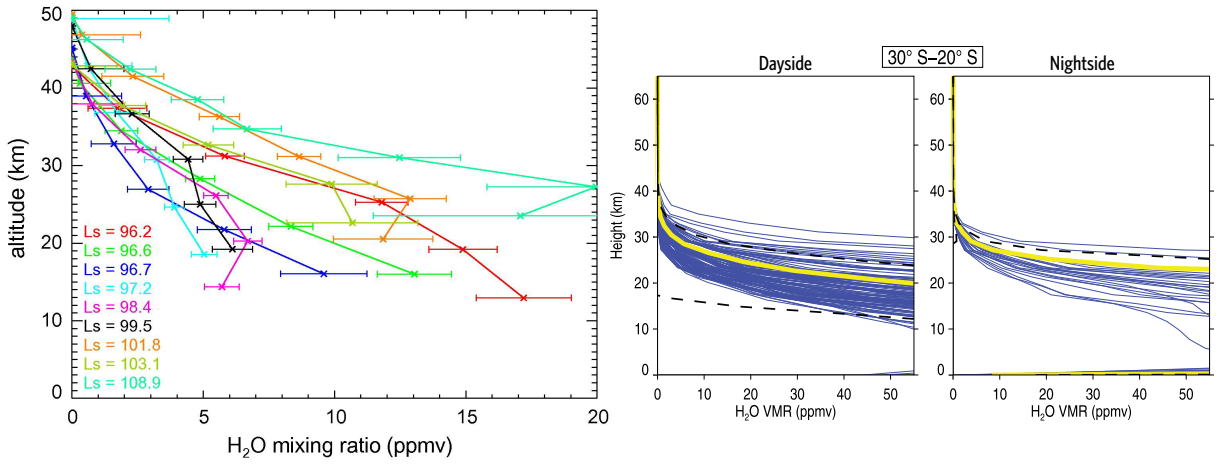


Figure 8.29 | Figure 8g from Maltagliati et al. (2013) compared with early summer 30°–20°S water profiles. Profiles (blue lines) have been overplotted with mean (yellow line) and standard deviation (black dashed line).

Credit: Reprinted from Icarus, 223, Maltagliati et al. (2013), 'Annual survey of water vapor vertical distribution and water-aerosol coupling in the martian atmosphere observed by SPICAM/MEx solar occultations', 942–962, Copyright (2013), with permission from Elsevier.

earlier, we saw no significant diurnal variation between our 03h/15h observations. Additionally, even if there is diurnal variation that we have not observed, it would be expected that with the higher dayside temperatures the water vapour would reach to at least the same vertical extent if not greater due to convection and higher saturation VMRs at higher altitudes. The most likely candidate then is a lack of sensitivity in our retrievals above 30 km as mentioned earlier. It is a possibility that our greater abundances lower down in the atmosphere could be due to some local time effect in combination with the difference in season (L_s).

Secondly, DWL are often seen in their results at about 30 km and above (see Figs. 8.27 & 8.29) but not ours. As these features were seen in CRISM results as well this provides more evidence for our lack of higher altitude sensitivity.

Thirdly, for SH cases (see Figs.8.28 & 8.29), our profiles generally have much higher abundances than theirs at altitudes of 20 km and below. This could be due to a difference in L_s, as our results are later and this will lead to higher abundances in the lower atmosphere. At the same time, the same pattern of lower abundances at higher altitudes is seen.

In their paper Maltagliati et al. (2013) compared their results to the those of the LMD Global Climate Model (see Fig. 8.30); this is the same model that generated the results for the MCD. In their paper they state that their profiles generally have higher abundances in the middle atmosphere than the GCM with a greater vertical extent and the appearance of DWL. In our results we similarly found that our abundances were often higher than equivalent MCD values, though our results did not have the greater vertical range, and apart from the spurious DWL results previously discussed do not replicate the high-altitude DWL seen in their results. Some potentially genuine DWL do appear in our results, though they seem less common (given that the average profiles seem to follow the more generally expected shape of a constant VMR up to condensation height) than in the Maltagliati et al. (2013) results and generally appear at lower altitudes.

8.4 Conclusions

Retrievals of water vapour were performed using observations from MCS during MY28 L_s=111–173° (NH summer) and split into early (111–140°) and late summer (140–173°) blocks. Despite difficulties and a limited number of nightside retrievals, there has been success in reproducing expected seasonal trends alongside some unexpected results. Discounting the contribution from

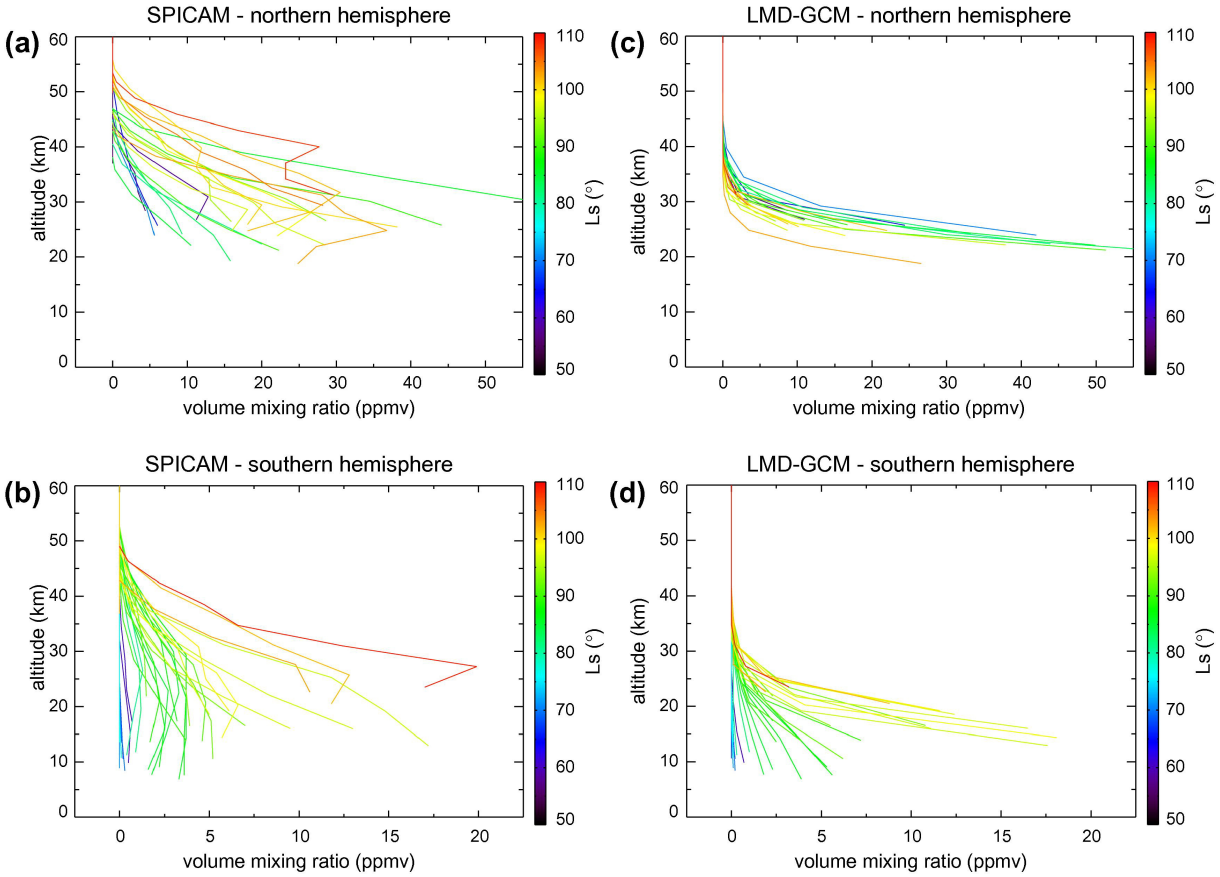


Figure 8.30 | Comparison between all the water profiles acquired by SPICAM (plots a and b) during the first occultation campaign and those predicted by the LMD-GCM (plots c and d). The northern hemisphere is shown in the upper part (plots a and c), and the southern one in the lower part (plots b and d). The colour indicates the L_s. Note that the x-axis scale is different for the two hemispheres.

Credit: Reprinted from Icarus, 223, Maltagliati et al. (2013), 'Annual survey of water vapor vertical distribution and water-aerosol coupling in the martian atmosphere observed by SPICAM/MEx solar occultations', 942–962, Copyright (2013), with permission from Elsevier.

spurious supersaturated DWL, column abundances match the expected pattern with greater abundances in the summer NH at the edge of the polar cap gradually decreasing southwards.

Seasonal variation in the vertical extent of water vapour has been observed following the seasonal changes in condensation level. This also shows the vertical aspect of behaviour, as water vapour is transported southward in the cross-equatorial Hadley cell. In conjunction with our ice retrievals this has allowed direct observation of vertical interaction/evolution between the transported water vapour and the aphelion cloud belt for the first time. Seasonal changes in the vertical extent are seen to have an impact on the cloud belt. When the condensation level is high water reaches higher levels before condensing. The higher levels at the equator and tropics in late summer then make the aphelion cloud belt weaker in late summer than early summer. This was supported by our use of the profile top metric as a a proxy for condensation level in Figs. 8.8 & 8.9.

Nightside vertical profiles of water vapour have been retrieved for the first time. Unfortunately, due to higher ice opacities at night, retrievals are noisier and the coverage is not as extensive as for the dayside. Having both dayside and nightside retrievals allows direct comparison for diurnal variation. No significant diurnal variation above error (profile envelope overlap or standard deviation) was observed in regions of lower aerosol opacity. Comparison in regions of higher aerosol opacity are frustrated by retrieval inaccuracy and poor coverage. Unfortunately, these regions are one of the most likely types to see variation due to aerosol-water interaction (e.g. cloud formation). Another potential region is at near-surface altitudes where surface interaction may be observed (e.g. adsorption). Here, MCS's extended detector FOV-wings along with higher opacities hamper effective retrievals.

Observations of a strong correlation between dust and water profiles suggest interaction between Mars' most variable cycles. This correlation is not straightforward, for as well as observing co-located dust and water layers we have also seen dust layers lying above water layers. Ice layers are also frequently seen over dust and water vapour layers.

A number of unphysical supersaturated DWL observations have been noted in our results and future work will require their identification and removal. The cause seems to be the false attribution by the retrieval of B2 radiances from aerosol as water for high dust and ice limb path opacities. Simple thresholds based on aerosol optical column depth were tested but did not help. Such profiles could potentially be identified through the use of a limb opacity per kilometre threshold in A5 for dust and A4 for ice, as high aerosol abundances are likely to produce unreliable water results.

Good agreement was found in comparisons to other datasets for water vapour column abundance (TES, SPICAM and ground-based). For vertical profiles good agreement was found with the CRISM vertical profile data of Clancy et al. (2017). Some disagreement was found at higher altitudes in the form of detached water layers and lower abundances above about 30 km. Agreement was found with SPICAM solar occultation results at lower heights in the atmosphere, though at higher altitudes abundances were higher than our results.

As lower abundances were found above 30 km in comparisons with both CRISM and SPICAM data, it is suggested that our retrievals suffer reduced sensitivity at higher altitudes. This was supported by our improvement factor profiles in Fig. 8.14. The radiometric errors induced by choice of aerosol size distribution have led to retrievals that require higher forward modelling errors, particularly the high B1 error (see §8.2.3). This provides lower radiance constraint

for the retrieval and has likely led to the reduced sensitivity of our water retrievals at higher altitudes where radiances are low. To resolve this in the future it would be best to develop a retrieval methodology where the aerosol extinction cross-section was also retrieved using an aerosol-sensitive far infrared channel such as B1 (which is still transparent in regions where the mid-infrared channels A4 and A5 would be opaque). As B1 (31.7 µm) is much closer in wavelength to B2 (41.7 µm) than A4 (11.8 µm) or A5 (22.2 µm) this could then be used to extrapolate to the extinction cross-section at B2. This should eliminate spurious radiance contributions in B2 from aerosols and would allow tighter radiance constraints (lower forward modelling errors) increasing high altitude sensitivity. In conjunction with a first stage retrieval using a far infrared channel such as B1, it would also allow the retrieval of water to lower altitudes in regions of higher limb opacity than previously possible. This could potentially allow examination of the boundary layer and surface interaction.

Overall, it can be concluded that retrievals from MCS have provided some new limits on diurnal variation and insight into the current state of the Martian water cycle in its interaction with the aphelion cloud belt. However, without the additional retrieval of aerosol extinction cross-section it is unlikely that the full potential of MCS's abilities for vertical water profile retrievals will be realised.

9

Conclusions and Future Work

Chapters 5 to 8 give the results of our investigation into the ability of MCS to effectively retrieve vertical profiles of water vapour. This is broken into three sections. First, looking at the sensitivity of the B2 and B3 channels to water and other atmospheric parameters, seeing how their wider-than-expected spectral passbands affect the radiances in these channels and retrieval performance. Second, investigating the B3 mesh filter material with laboratory experiments in order to understand why the B-channels failed to meet their specified spectral bandwidths. Third, using the information gained from the sensitivity studies to conduct a retrieval campaign on real MCS observations during the Martian summer of MY28 (September 2006–January 2007). This final chapter summarises key results from these chapters suggesting further work and improvements for future analysis.

9.1 Conclusions

Presented here are the main results obtained from this work.

9.1.1 Sensitivity Studies

It was originally envisioned that MCS would use the B2 and B3 channels together, using their radiance ratio, to perform the retrievals of water vapour by isolating it from the effects of aerosol

(see §2.3.1). Both channels failed to meet their original specifications and have spectral band-passes that are significantly wider than designed. A number of simulation tests were performed to gauge the sensitivity of the wider channels to see if they could still be used together or if a different retrieval methodology ought to be sought.

Simulations of individual detector pair ratios found no detectable change in ratio above noise, as the amount of water vapour in the atmosphere was varied for a northern hemisphere summer profile (§5.1). This was over a range of 1–100 pr. µm, representing the full range of water vapour abundances on Mars. Reduced B3/B2 ratio sensitivity was confirmed for scatter plots of B3-B2 radiance from a 4 h block of MCS results when compared with an equivalent simulation of MCS performing nominally, i.e. filters with no broadening (§5.2). Further simulations tested the affect on the ratio of changing temperature and dust in comparison with changes in water vapour abundance (§5.3). It was found that low temperatures and more importantly dust opacity both acted to reduce sensitivity of the ratio. For a northern summer equatorial scenario (water column abundance 11 pr. µm) with a typical dust value of τ_{1075}=0.1 (optical depth at 1075 cm^{-1}) the reduction in ratio was significant. Increasing the opacity to τ_{1075}=1.8 decreased ratio sensitivity to near-zero. The results of these tests showed that the use of the B3/B2 ratio for water vapour retrievals independent of aerosol is not feasible.

As a consequence of the above the B2 channel must be used on its own in a two-stage water vapour retrieval. This is challenging as B2 is sensitive to both aerosol and water vapour. This fact was suggested by B2 radiance residual tests which sought to gauge the sensitivity of the channel to water vapour (§5.4). Subsequent simulations of the effect of dust and ice on B2 radiance confirmed that the channel has significant radiance contributions from aerosol when present.

A final set of simulations were used to establish the affect on water vapour retrieval accuracy of aerosol opacity and the incorrect choice of aerosol size distribution, i.e. wrong extinction cross-section at B2 (see Chapter 6). The tests were conducted for a range of opacities and aerosol size modes. These opacities are representative of condition on Mars during the northern hemisphere summer season. Sets of dust/ice particle size distributions were chosen to reflect a range of conditions on Mars based on the work of Wolff & Clancy (2003), Wolff et al. (2006) and Kleinböhl et al. (2009, 2011). Northern hemisphere dayside atmospheres during summer were modelled as this season and region corresponds to the highest water abundances on Mars and so those most readily detectable. Also, the retrievals performed on real MCS data in Chapter 8

were for this season. These tests gave a benchmark to give an idea of the conditions under which retrievals would succeed. It was found that increasing either aerosol opacity or the difference between the retrieved and modelled aerosol size mode reduced retrieval accuracy. Combinations of high opacity and high model-retrieval size mode difference gave the worst results.

For cases tested where only dust is present, when retrieved with a dust mode of r_{eff}=1.06 μm, good results were obtained for dust opacities up to τ_{A5}=0.075. This held true when the model dust mode was varied (i.e. retrieving with wrong mode) up to r_{eff}=1.8 μm. For cases of $\tau_{A5} \leq$0.025, the effect of the dust mode is less important. For the ice series tests, atmospheres were modelled with both dust and ice present; dust was held fixed at τ_{A5}=0.025. When retrieved with an ice mode of r_{eff}=1.41 μm good results were obtained for ice opacities up to τ_{A4}=0.075. This continued to hold when varying mode ice mode from r_{eff}=1.0 μm up to r_{eff}=2.0 μm. For cases of $\tau_{A4} \leq$0.025, the effect of the ice mode is less important. When compared with typical L2 dataset values for this season, it was found that most dust and water ice column opacities for dayside measurements fell within the 'good results' range implying a good chance of retrieval success with real data.

9.1.2 Characterizing the Spectral Passband of B3

It was proposed that random forward scattering by the B2 and B3 mesh filters may be the mechanism behind the observed broadening in their spectral bandpasses. It was believed that this process would scatter out-of-bandpass light into the detector at short filter-detector distances, such as that in MCS, which is ∼100 μm. It was believed this effect would have a rapid fall-off as the filter-detector distance, l_d, was increased. To test this hypothesis measurements of the B3 filter spectral response were conducted using an FTIR spectrometer and custom-built filter jig. This jig allowed measurements of the B3 filter response to be taken while l_d was varied in the range 100–1000 μm. In conjunction with background measurements these were used to calculate the FWHM of B3. No systematic change in FWHM was observed over the range of l_d tested. Hence, it seems that the proposed random forward scattering with rapid fall-off theory is incorrect and another explanation must be sought to explain the broadening. However, the set-up used for this experiment was not an exact replication of the MCS focal plane array so it may be that the observed broadening is due to another effect not present in this set-up but present in the MCS focal-plane. This could be some form of optical interaction between the baffles (not modelled in our set-up) and the mesh filters, e.g. scattering.

Another possibility was that that the filter-broadening effect that was observed by JPL's pre-flight MCS testing (McCleese et al., 2007) was caused by an artefact of their monochromator testing, such as spectral leaks in the order sorting filters used. This seems unlikely given our results from the B3/B2 scatter plot testing in §5.2. In those tests MCS observed radiances were compared with simulated ones. The results supported a reduced sensitivity of the B3/B2 ratio to water independent of assumed filter profile. Therefore the optical interaction theory discussed above is the more likely culprit.

9.1.3 Retrievals

Using the results of the sensitivity studies a two-stage retrieval for water vapour was developed and used on MCS data with observations from the Martian northern hemisphere summer of MY28, L_s=111–173°. The results were split into early (111–140°) and late summer (140–173°) blocks to allow monitoring of seasonal differences and further split into dayside and nightside sub-blocks for assessment of diurnal variation. In the first stage vertical profiles for temperature, pressure, dust and water ice along with surface temperature were retrieved using channels A1–A5 and B1 as a dummy channel. In the second stage water vapour was retrieved using B2, with the results of the first stage setting the atmospheric state. There were fewer successful nightside retrievals than dayside leading to poorer coverage on the nightside.

First Stage Retrievals

Though not the main focus for this study the atmospheric parameters retrieved in the first stage were nevertheless an essential step in the two-stage retrieval process of water vapour. Our results were compared with those of McCleese et al. (2010). This was complicated by their different seasonal binning (comparison bins used were at L_s values of 90°, 135° and 180°) and choice of pressure as the vertical coordinate rather surface height as in our results. Despite this a good match was found between our results and theirs in seasonal and diurnal behaviour for temperature, dust and water ice.

For temperature our early summer results yielded the expected asymmetry with warmer northern hemisphere (NH) temperatures and a cooler southern hemisphere (SH) reproducing the main features seen in McCleese et al. (2010) data, such as the polar warming. For the late summer results a move towards a more symmetric thermal structure was seen as the season approached the equinox.

For dust on the dayside, regions of moderate to high dust opacity were seen extending from the southern tropics towards the north pole. In the early summer the dust opacity had a greater altitude extent in the tropics and north polar regions, reaching to about 25 km. In late summer this dropped to about 15 km. A high opacity equatorial maximum seen in the McCleese et al. (2010) results was implied in our early summer results by the lack of successful retrievals in this region. An equatorial maximum was observed in the late summer block. Lower dust opacity regions seen in the southern mid-latitudes extend to near the south pole. The southern polar maximum seen in their results is much stronger than ours. This was likely due to a low opacity bias (selection bias from the χ^2/n_y thresholds). On the nightside, the general shape of our results matched well with those of McCleese et al. (2010). A decrease was again seen in the vertical extent of dust moving from early to late summer. The southern polar maximum was absent in our results, this was likely due to the aforementioned selection bias.

For water ice, our results were a good match where data was available. In both the early and late summer blocks a potential strong diurnal variation of tropical water ice was seen, attributed to the diurnal thermal tide by McCleese et al. (2010). The strongest regions of ice opacity are confined to the equator on the dayside and more spread out on the nightside (and reaching to lower altitudes), the 'aphelion cloud belt' seen in past observations. High equatorial ice opacity for early summer dayside results was implied by the empty bins in this region, and the elevated opacities adjacent to this region. For the late summer multiple broad maxima were seen over the latitude range. Strong diurnal variation was also observed.

Second Stage Retrievals: Water Vapour

Despite difficulties and a limited number of retrievals for the nightside, there was success in reproducing expected seasonal trends alongside some unexpected results. Discounting the contribution from spurious supersaturated detached water layers (DWL), column abundances matched the expected spatial distribution with greater abundances in the northern summer hemisphere at the edge of the polar cap gradually decreasing southwards.

Seasonal variation in the vertical extent of water vapour was observed following the seasonal changes in condensation level. This also showed the vertical aspect of behaviour, as water vapour is transported southward in the cross-equatorial Hadley cell. In conjunction with our ice retrievals this allowed direct observation of vertical interaction/evolution between the transported water vapour and the aphelion cloud belt for the first time. Seasonal changes in the

vertical extent are seen to have an impact on the cloud belt. When the condensation level is high water reaches higher levels before condensing. The higher levels at the equator and tropics in late summer then make the aphelion cloud belt weaker than it is in early summer. This was supported by our use of the 'profile top' metric as a a proxy for condensation level.

Nightside vertical profiles of water vapour have been retrieved for the first time. Unfortunately, due to the higher ice opacities at night, retrievals were noisier and the coverage was not as extensive as for the dayside. Having both dayside and nightside retrievals allowed direct comparison for determining diurnal variation. No significant diurnal variation above error (profile envelope overlap or standard deviation) was observed in regions of lower aerosol opacity. Comparisons in regions of higher aerosol opacity were frustrated by retrieval inaccuracy and poor coverage. Unfortunately, these regions are one of the most likely types to see variation due to aerosol-water interaction (e.g. cloud formation). Another potential region is at near-surface altitudes where surface interaction may be observed (e.g. adsorption). Here, MCS's extended detector FOV-wings along with higher opacities hampered effective retrievals.

Observations of a strong correlation between dust and water profiles suggest interaction between Mars' most variable cycles. This correlation is not straightforward, for as well as observing co-located dust and water layers we also saw dust layers lying above water layers. Ice layers were also frequently seen over dust and water vapour layers.

A number of unphysical supersaturated DWL observations were noted in our results and future work will require their identification and removal. The cause seemed to be the false attribution by the retrieval of B2 radiances from aerosol as water for high dust and/or ice limb path opacities. Simple thresholds based on aerosol optical column depth were tested but did not help. Such profiles could potentially be identified through the use of a limb opacity per kilometre threshold in A5 for dust and A4 for ice, as high aerosol abundances are likely to produce unreliable water results.

Good agreement was found in comparisons to other datasets for water vapour column abundance (TES, SPICAM and ground-based). For vertical profiles good agreement was found with the CRISM vertical profile data of Clancy et al. (2017). Some disagreement was found at higher altitudes in the form of detached water layers and lower abundances above about 30 km. Agreement was found with SPICAM solar occultation results at lower heights in the atmosphere, though at higher altitudes abundances were higher than our results.

As lower abundances were found above 30 km in comparisons with both CRISM and SPICAM

data, it is believed that our retrievals suffered from reduced sensitivity at higher altitudes. This was supported by our improvement factor profiles. The radiometric errors induced by choice of aerosol size distribution led to retrievals that required higher forward modelling errors, particularly the high B1 error (see §8.2.3). This provided lower radiance constraint for the retrieval and likely led to the reduced sensitivity of our water retrievals at higher altitudes where radiances were low. This lack of radiance constraint also causes problems for retrievals at near-surface altitudes due to the high limb path aerosol opacities seen here.

9.2 Future Work

There are options for the future development and improvement of vertical water vapour profile retrieval methodology and analysis. There is also a need for work to be done regarding laboratory measurements of filter transmission profiles of the B2 and B3 channels. These are discussed below.

9.2.1 Sensitivity Studies

As mentioned above, the current retrieval process seems to suffer from reduced sensitivity at altitudes above 30 km and near-surface altitudes. This situation could be improved upon by the retrieval of aerosol extinction cross-sections. This will be discussed below. This new retrieval scheme will then need a series of sensitivity studies similar to those carried in this thesis in order to gauge improvements. This would need to focus on high and near-surface altitudes, with a focus on whether the retrieval can successfully resolve detached water layers.

9.2.2 Characterizing the Spectral Passband of B3

The results of the B3 filter response measurements raises questions, given that it was not possible to recreate the MCS B-channel broadening effect as observed in the JPL monochromator tests. As discussed earlier the set-up used for our experiment was not an exact replication of the MCS focal plane array. It may be that the broadening is due to an effect not duplicated in our set-up. This could be some form of optical interaction between the baffles and the mesh filters, e.g. scattering. It would therefore be highly prudent for an accurate retesting of the MCS focal-plane set-up to be performed to investigate this.

9.2.3 Retrievals of Water Vapour

Retrieval of Aerosol Extinction Cross-Section

It has become apparent that for MCS water vapour retrievals to improve, with greater sensitivity at higher and lower altitudes, the retrieval scheme needs to include aerosol extinction cross-section as a retrieved parameter. This would need to be done with a far infrared channel such as B1 (which is still transparent in regions where the mid-infrared channels A4 and A5 would be opaque). As B1 (31.7 µm) is much closer in wavelength to B2 (41.7 µm) than A4 (11.8 µm) or A5 (22.2 µm) this could then be used to extrapolate to the extinction cross-section at B2. This should eliminate spurious radiance contributions in B2 from aerosols and would allow tighter radiance constraints (lower forward modelling errors), increasing high altitude sensitivity. In conjunction with a first stage retrieval using a far infrared channel such as B1, it would also allow the retrieval of water to lower altitudes in regions of higher limb opacity than previously possible.

Increase in high altitude sensitivity would allow for the successful retrieval of detached water layers while a near-surface sensitivity increase could potentially allow examination of the boundary layer and surface interaction. Additionally, successful retrievals under high opacity conditions would extend spatial and temporal coverage, particularly for the northern summer equatorial regions and also for nightside observations. An increase in the coverage and altitude extent of dayside and nightside observations would allow for a more rigorous test of diurnal variation sensitive to smaller changes in atmospheric water vapour content. It would also allow observations of the vertical behaviour of water vapour in challenging high opacity conditions such as dust storms or the the more opaque regions of the aphelion cloud belt.

Preliminary work on an extinction cross-section retrieval has been done by Kleinböhl et al. (2017, 2018). They calculated empirically derived extinction efficiency ratios using two far infrared channels of MCS: B1 for dust and B2 for water ice. To calculate an empirical extinction, k_{meas}, for the aerosol and channel of interest, they used radiance ratios of R_{meas}, the measured radiance (from MCS observations) and calculated radiance, R_{calc} (from their radiative transfer calculations). From Kleinböhl et al. (2017) the radiances can be defined as

$$R_x = B(\nu, T_{\text{eff}}) \cdot e^{-k_x \cdot U}, \tag{9.1}$$

where x indicates either the measured or calculated case, B is the Planck function at effective wavenumber ν and the effective limb temperature T_{eff}, k is the extinction coefficient and U is the aerosol amount. Assuming an optically thin atmosphere, the desired extinction coefficient is then derived by

$$k_{\text{meas}} = k_{\text{calc}} \cdot \frac{R_{\text{meas}}}{R_{\text{calc}}}. \tag{9.2}$$

Using this procedure they derived empirical extinction coefficients for dust at B1 in regions where dust is the main absorber. They repeated the method for water ice at B2 in regions where ice dominates. For water ice they found that their values of k_{meas} varied. Different values for k_{meas} were obtained for dayside and nightside water ice in the equatorial belt region (location of the aphelion cloud belt), implying different particle size distributions.

It may be possible to use this method to calculate an empirical aerosol extinction coefficient and then extrapolate to get a better value at B2. This ought to work reasonably well for dust extinction at B1. However, using B2 to get values for water ice could be problematic as it will be hard to disentangle the effects of water ice from water vapour. Suitable observations with high water ice and low water vapour will have to be found that are spatially and temporally near target water vapour retrievals, given the observed variation in k_{meas}.

Radiative Transfer Improvements

Several approximations were used in this thesis in order to allow retrievals within a reasonable time frame. These include the correlated-k approximations and the neglect of scattering. With anticipated future improvements in computing power it could be possible to discard these approximations, instead using line-by-line models and including full multiple scattering. Some work along these lines could be done now, but only for a small subset of observations given the great computational expense. Additionally, two or three dimensional retrievals could be performed on the data given that slant and limb paths sample the atmosphere at several different altitudes, latitudes and longitudes.

Short Timescale Evolution of Water Vapour Vertical Profile and Aerosol Interaction

Comparisons were made in this thesis to explore diurnal variation, but because of the paucity of nightside results and spurious results induced by high aerosol opacity this was fairly coarse. If improved extinction coefficients can be calculated this opens the door to investigating smaller-scale diurnal variation and daily variation. This becomes particularly relevant for exploring the

short timescale evolution (days) of water vapour, particularly with regard to vertical extent, detached water layers and aerosol interaction. Furthermore, if altitude sensitivity can be extended, it allows the observation of water vapour that is transported to high altitudes, seen in the results from Fedorova et al. (2018) with SPICAM and Vandaele et al. (2019) with NOMAD/ACS. This water may then be a source of extra hydrogen escape after photodissociation by near-UV sunlight, as suggested by Fedorova et al. (2018).

Spatial, Seasonal and Interannual Variation

The retrievals performed in this thesis represent only a small subset of the full MCS dataset which now extends over six Martian years (MY28–34). A great deal of information can be gleaned by extending the retrievals over a larger temporal range. This would allow for extensive seasonal and interannual variation to investigated. Potential challenges in doing this may arise because of the MCS elevator slewing problems discussed in Chapter 2. As a consequence of this problem the instrument no longer performs nadir observations and is limited to off-nadir views with surface incidence angles of 60–70° in data after 9 October 2007. The impact of this on water vapour retrievals will need to studied. Additionally, it could be fruitful to use the MCS dataset to explore regional and small-scale localised phenomena to explore spatial variation on Mars, as well as focusing on the global picture.

Validation and Opportunities with ExoMars Trace Gas Orbiter

ExoMars TGO provides a new opportunity for independent validation of MCS water retrieval results, using results from the NOMAD and ACS instruments. Additionally, if MCS retrieval altitude range can be extended with aerosol extinction retrievals as discussed above, a number of opportunities are opened up. One of these would include increased temporal coverage for exploring diurnal variation, as MCS has 03h/15h LST observation times, while those of NOMAD and ACS are at 06h/18h (as they are solar occultation instruments). Another opportunity would be having two instruments that can explore high altitude water variation, increasing the opportunities of capturing related transient phenomena.

9.3 Summary

Overall, it can be concluded that retrievals from MCS have provided some new limits on diurnal variation and insight into the current state of the Martian water cycle in its interaction with the water ice aphelion cloud belt. They have also compared well with existing datasets from other instruments. These results provide a useful contribution to the Martian remote sensing community for exploring the complex and dynamic processes of water vapour in the Martian atmosphere. Unfortunately, without the additional retrieval of aerosol extinction cross-section it is unlikely that the full potential of MCS's abilities for vertical water profile retrievals will be realised. Laboratory testing has also revealed a need for further measurements of the filter transmission profiles of the B2 and B3 channels in the MCS focal plane array.

Bibliography

καὶ ὑπομονὴν ἔχεις, καὶ ἐβάστασας διὰ τὸ ὄνομά μου, καὶ οὐ κεκοπίακες.

You have persevered and have endured hardships for my name, and have not grown weary.

—THE BIBLE, *Revelation 2:3* (NIV)

Adlen, S. J. M., 2004: *Remote Sounding of the Martian Atmosphere with Mars Climate Sounder*. Ph.D. thesis, University of Oxford.

Andrews, D. G., 2000: *An Introduction to Atmospheric Physics*. Cambridge University Press.

Andrews-Hanna, J. C., R. J. Phillips, and M. T. Zuber, 2007: Meridiani Planum and the global hydrology of Mars. *Nature*, **446**, 163–166, doi:10.1038/nature05594.

Anonymous, 2007: Mars's uphill ocean explained. *New Scientist*, **194(2608)**, 23–+.

Baker, V. R., 1982: *The Channels of Mars*. Research supported by NASA, NSF, and Australian-American Educational Foundation Austin, TX, University of Texas Press, 1982. 204 p.

— 2001: Water and the martian landscape. *Nature*, **412**, 228–236.

— 2005: Planetary science: Picturing a recently active Mars. *Nature*, **434**, 280–283, doi:10.1038/434280a.

— 2007: Planetary science: Water cycling on Mars. *Nature*, **446**, 150–151, doi:10.1038/446150b.

Baker, V. R., R. G. Strom, V. C. Gulick, J. S. Kargel, and G. Komatsu, 1991: Ancient oceans, ice sheets and the hydrological cycle on Mars. *Nature*, **352**, 589–594, doi:10.1038/352589a0.

Bandfield, J. L., 2007: High-resolution subsurface water-ice distributions on Mars. *Nature*, **447**, 64–67, doi:10.1038/nature05781.

Barker, E. S., 1976: Martian atmospheric water vapor observations - 1972-74 apparition. *Icarus*, **28**, 247–268.

Barker, E. S., R. A. Schorn, A. Woszczyk, R. G. Tull, and S. J. Little, 1970: Mars: Detection of atmospheric water vapor during the southern hemisphere spring and summer season. *Science*, **170**, 1308–1310.

Beish, J. D., 2007: http://www.tnni.net/∼dustymars/. Observing the Planet Mars.
URL http://www.tnni.net/$\sim$dustymars/

Bibring, J.-P., Y. Langevin, F. Poulet, A. Gendrin, B. Gondet, M. Berthé, A. Soufflot, P. Drossart, M. Combes, G. Bellucci, V. Moroz, N. Mangold, B. Schmitt, OMEGA Team, S. Erard, O. Forni, N. Manaud, G. Poulleau, T. Encrenaz, T. Fouchet, R. Melchiorri, F. Altieri, V. Formisano, G. Bonello, S. Fonti, F. Capaccioni, P. Cerroni, A. Coradini, V. Kottsov, N. Ignatiev, D. Titov, L. Zasova, P. Pinet, C. Sotin, E. Hauber, H. Hoffman, R. Jaumann, U. Keller, R. Arvidson, J. Mustard, T. Duxbury, and F. Forget, 2004: Perennial water ice identified in the south polar cap of Mars. *Nature*, **428**, 627–630, doi:10.1038/nature02461.

Bibring, J.-P., Y. Langevin, A. Soufflot, C. Combes, and C. Cara, 1989: Results from the ISM experiment. *Nature*, **341**, 591–593, doi:10.1038/341591a0.

Biver, N., A. Lecacheux, T. Encrenaz, E. Lellouch, P. Baron, J. Crovisier, U. Frisk, Å. Hjalmarson, M. Olberg, A. Sandqvist, and S. Kwok, 2005: Wide-band observations of the 557 GHz water line in Mars with Odin. *A&A*, **435**, 765–772, doi:10.1051/0004-6361:20042247.

Böttger, H. M., 2003: *Modelling the Water Cycle on Mars*. Ph.D. thesis, University of Oxford.

Böttger, H. M., S. R. Lewis, P. L. Read, and F. Forget, 2005: The effects of the martian regolith on GCM water cycle simulations. *Icarus*, **177**, 174–189, doi:10.1016/j.icarus.2005.02.024.

Bowles, N., 2007: Private Communication.

Boynton, W. V., W. C. Feldman, S. W. Squyres, T. H. Prettyman, J. Brückner, L. G. Evans, R. C. Reedy, R. Starr, J. R. Arnold, D. M. Drake, P. A. J. Englert, A. E. Metzger, I. Mitrofanov, J. I. Trombka, C. d'Uston, H. Wänke, O. Gasnault, D. K. Hamara, D. M. Janes, R. L. Marcialis, S. Maurice, I. Mikheeva, G. J. Taylor, R. Tokar, and C. Shinohara, 2002: Distribution of Hydrogen in the Near Surface of Mars: Evidence for Subsurface Ice Deposits. *Science*, **297**, 81–85, doi:10.1126/science.1073722.

Brothers, T. C. and J. W. Holt, 2016: Three-dimensional structure and origin of a 1.8 km thick ice dome within Korolev Crater, Mars. *Geophysical Research Letters*, **43**, 1443–1449, doi:10.1002/2015GL066440.

Brown, L. R., C. M. Humphrey, and R. R. Gamache, 2007: CO_2-broadened water in the pure rotation and ν_2 fundamental regions. *Journal of Molecular Spectroscopy*, **246**, 1–21, doi:10.1016/j.jms.2007.07.010.

Burch, D. E., D. A. Gryvnak, R. R. Patty, and C. E. Bartky, 1969: Absorption of Infrared Radiant Energy by CO2O and H2O. IV. Shapes of Collision-Broadened CO2 Lines. *Journal of the Optical Society of America (1917-1983)*, **59**, 267–+.

Byrne, S., C. M. Dundas, M. R. Kennedy, M. T. Mellon, A. S. McEwen, S. C. Cull, I. J. Daubar, D. E. Shean, K. D. Seelos, S. L. Murchie, B. A. Cantor, R. E. Arvidson, K. S. Edgett, A. Reufer, N. Thomas, T. N. Harrison, L. V. Posiolova, and F. P. Seelos, 2009: Distribution of Mid-Latitude Ground Ice on Mars from New Impact Craters. *Science*, **325**, 1674–, doi:10.1126/science.1175307.

Byrne, S. and A. P. Ingersoll, 2003: A Sublimation Model for Martian South Polar Ice Features. *Science*, **299**, 1051–1053, doi:10.1126/science.1080148.

Cabrol, N. A. and E. A. Grin, 2010: *Lakes on Mars*.

Carr, M. H., 1995: The Martain drainage system and the origin of valley networks and fretted channels. *Journal of Geophysical Research*, **100**, 7479–7507.

— 1996: *Water on Mars*. New York: Oxford University Press, |c1996.

Carr, M. H. and J. W. Head, 2003: Oceans on Mars: An assessment of the observational evidence and possible fate. *Journal of Geophysical Research (Planets)*, **108**, 8–1, doi:10.1029/2002JE001963.

Chaffin, M. S., J.-Y. Chaufray, I. Stewart, F. Montmessin, N. M. Schneider, and J.-L. Bertaux, 2014: Unexpected variability of Martian hydrogen escape. *Geophysical Research Letters*, **41**, 314–320, doi:10.1002/2013GL058578.

Chahine, M. T., 1970: Inverse Problems in Radiative Transfer: Determination of Atmospheric Parameters. *Journal of Atmospheric Sciences*, **27**, 960–967, doi:10.1175/1520-0469(1970)027<0960:IPIRTD>2.0.CO;2.

— 1972: A General Relaxation Method for Inverse Solution of the Full Radiative Transfer Equation. *Journal of Atmospheric Sciences*, **29**, 741–747, doi:10.1175/1520-0469(1972)029<0741:AGRMFI>2.0.CO;2.

Christensen, P. R., D. L. Anderson, S. C. Chase, R. N. Clark, H. H. Kieffer, M. C. Malin, J. C. Pearl, J. Carpenter, N. Bandiera, and F. G. Brown, 1992: Thermal emission spectrometer experiment - Mars Observer mission. *Journal of Geophysical Research*, **97**, 7719–7734.

Clancy, R. T., A. W. Grossman, M. J. Wolff, P. B. James, D. J. Rudy, Y. N. Billawala, B. J. Sandor, S. W. Lee, and D. O. Muhleman, 1996: Water vapor saturation at low altitudes around Mars aphelion: A key to Mars climate? *Icarus*, **122**, 36–62, doi:10.1006/icar.1996.0108.

Clancy, R. T., B. J. Sandor, M. J. Wolff, P. R. Christensen, M. D. Smith, J. C. Pearl, B. J. Conrath, and R. J. Wilson, 2000: An intercomparison of ground-based millimeter, MGS TES, and Viking atmospheric temperature measurements: Seasonal and interannual variability of temperatures and dust loading in the global Mars atmosphere. *Journal of Geophysical Research*, **105**, 9553–9572, doi:10.1029/1999JE001089.

Clancy, R. T., M. D. Smith, F. Lefèvre, T. H. McConnochie, B. J. Sandor, M. J. Wolff, S. W. Lee, S. L. Murchie, A. D. Toigo, H. Nair, and T. Navarro, 2017: Vertical profiles of Mars 1.27 μm O_2 dayglow from MRO CRISM limb spectra: Seasonal/global behaviors, comparisons to LMDGCM simulations, and a global definition for Mars water vapor profiles. *Icarus*, **293**, 132–156, doi:10.1016/j.icarus.2017.04.011.

Clancy, R. T., M. J. Wolff, and P. R. Christensen, 2003: Mars aerosol studies with the MGS TES emission phase function observations: Optical depths, particle sizes, and ice cloud types versus latitude and solar longitude. *Journal of Geophysical Research (Planets)*, **108**, 2–1, doi:10.1029/2003JE002058.

Clarke, J. T., J.-L. Bertaux, J.-Y. Chaufray, G. R. Gladstone, E. Quemerais, J. K. Wilson, and D. Bhattacharyya, 2014: A rapid decrease of the hydrogen corona of Mars. *Geophysical Research Letters*, **41**, 8013–8020, doi:10.1002/2014GL061803.

Clifford, S. M. and T. J. Parker, 2001: The Evolution of the Martian Hydrosphere: Implications for the Fate of a Primordial Ocean and the Current State of the Northern Plains. *Icarus*, **154**, 40–79, doi:10.1006/icar.2001.6671.

Conrath, B. J., 1975: Thermal structure of the Martian atmosphere during the dissipation of the dust storm of 1971. *Icarus*, **24**, 36–46.

Crisp, J. A., M. Adler, J. R. Matijevic, S. W. Squyres, R. E. Arvidson, and D. M. Kass, 2003: Mars Exploration Rover mission. *Journal of Geophysical Research (Planets)*, **108**, 2–1, doi:10.1029/2002JE002038.

Curran, R. J., B. J. Conrath, R. A. Hanel, V. G. Kunde, and J. C. Pearl, 1973: Mars: Mariner 9 Spectroscopic Evidence for H_2O Ice Clouds. *Science*, **182**, 381–383.

de Kok, R., 2005: Oxygen compunds in Titan's stratosphere: First Year Report—August 2005, AOPP First Year DPhil Report.

— 2007: *Oxygen compunds, aerosols and condensate clouds in Titan's stratosphere*. Ph.D. thesis, University of Oxford.

de Kok, R., P. G. J. Irwin, N. A. Teanby, E. Lellouch, B. Bézard, S. Vinatier, C. A. Nixon, L. Fletcher, C. Howett, S. B. Calcutt, N. E. Bowles, F. M. Flasar, and F. W. Taylor, 2007a: Oxygen compounds in Titan's stratosphere as observed by Cassini CIRS. *Icarus*, **186**, 354–363, doi:10.1016/j.icarus.2006.09.016.

de Kok, R., P. G. J. Irwin, N. A. Teanby, C. A. Nixon, D. E. Jennings, L. Fletcher, C. Howett, S. B. Calcutt, N. E. Bowles, F. M. Flasar, and F. W. Taylor, 2007b: Characteristics of Titan's stratospheric aerosols and condensate clouds from Cassini CIRS far-infrared spectra. *Icarus*, **191**, 223–235, doi:10.1016/j.icarus.2007.04.003.

di Achille, G. and B. M. Hynek, 2010: Ancient ocean on Mars supported by global distribution of deltas and valleys. *Nature Geoscience*, **3**, 459–463, doi:10.1038/ngeo891.

Encrenaz, T., B. Bézard, T. Owen, S. Lebonnois, F. Lefèvre, T. Greathouse, M. Richter, J. Lacy, S. Atreya, A. S. Wong, and F. Forget, 2005a: Infrared imaging spectroscopy of Mars: H_2O mapping and determination of CO_2 isotopic ratios. *Icarus*, **179**, 43–54, doi:10.1016/j.icarus.2005.06.022.

Encrenaz, T., T. Fouchet, R. Melchiorri, P. Drossart, B. Gondet, Y. Langevin, J.-P. Bibring, F. Forget, L. Maltagliati, D. Titov, and V. Formisano, 2008a: A study of the Martian water vapor over Hellas using OMEGA and PFS aboard Mars Express. *A&A*, **484**, 547–553, doi:10.1051/0004-6361:20079288.

Encrenaz, T., T. K. Greathouse, M. J. Richter, B. Bézard, T. Fouchet, F. Lefèvre, F. Montmessin, F. Forget, S. Lebonnois, and S. K. Atreya, 2008b: Simultaneous mapping of H_2O and H_2O_2 on Mars from infrared high-resolution imaging spectroscopy. *Icarus*, **195**, 547–556, doi:10.1016/j.icarus.2008.01.022.

Encrenaz, T., R. Melchiorri, T. Fouchet, P. Drossart, E. Lellouch, B. Gondet, J.-P. Bibring, Y. Langevin, D. Titov, N. Ignatiev, and F. Forget, 2005b: A mapping of martian water sublimation during early northern summer using OMEGA/Mars Express. *A&A*, **441**, L9–L12, doi:10.1051/0004-6361:200500171.

Evans, J. E. and E. W. Maunder, 1903: Experiments as to the actuality of the "Canals" observed on Mars. *Monthly Notices of the Royal Astronomical Society*, **63**, 488–499, doi:10.1093/mnras/63.8.488.

Farmer, C. B. and D. D. Laporte, 1972: The Detection and Mapping of Water Vapor in the Martian Atmosphere, The Viking Mars Orbiter. *Icarus*, **16**, 34–46.

Fedorova, A., J.-L. Bertaux, D. Betsis, F. Montmessin, O. Korablev, L. Maltagliati, and J. Clarke, 2018: Water vapor in the middle atmosphere of Mars during the 2007 global dust storm. *Icarus*, **300**, 440–457, doi:10.1016/j.icarus.2017.09.025.

Fedorova, A., O. Korablev, J.-L. Bertaux, A. Rodin, A. Kiselev, and S. Perrier, 2006a: Mars water vapor abundance from SPICAM IR spectrometer: Seasonal and geographic distributions. *Journal of Geophysical Research (Planets)*, **111**, 9–+, doi:10.1029/2006JE002695.

Fedorova, A. A., O. I. Korablev, J. L. Bertaux, A. V. Rodin, F. Montmessin, D. A. Belyaev, and A. Reberac, 2009: Solar infrared occultation observations by SPICAM experiment on Mars-Express: Simultaneous measurements of the vertical distributions of H $_2$O, CO $_2$ and aerosol. *Icarus*, **200**, 96–117, doi:10.1016/j.icarus.2008.11.006.

Fedorova, A. A., O. I. Korablev, S. Perrier, J.-L. Bertaux, F. Lefevre, A. Rodin, and A. Kiselev, 2006b: Exploration of Mars in the SPICAM-IR experiment onboard the Mars-Express spacecraft: 2. Nadir observations: Simultaneous observations of water vapor and O_2 glow in the Martian atmosphere. *Cosmic Research*, **44**, 294–304, doi:10.1134/S0010952506040034.

Fedorova, A. A., A. V. Rodin, and I. V. Baklanova, 2004: MAWD observations revisited: seasonal behavior of water vapor in the martian atmosphere. *Icarus*, **171**, 54–67, doi:10.1016/j.icarus.2004.04.017.

Fletcher, L., 2005: Saturn's Upper Troposhere form Cassini/CIRS Ground-Based Observations: First Year Report—August 2005, AOPP First Year DPhil Report.

— 2007: *Saturn's Atmosphere: Structure and Composition from Cassini/CIRS*. Ph.D. thesis, University of Oxford.

Forget, F., K. Dassas, Y. Wanherdrick, S. R. Lewis, S. J. Collins, and S. J. Bingham, 2005: Mars Climate Database v4.1 User Manual.

Forget, F., E. Millour, S. Lebonnois, L. Montabone, K. Dassas, S. R. Lewis, P. L. Read, M. A. López-Valverde, F. González-Galindo, F. Montmessin, F. Lefèvre, M.-C. Desjean, and J.-P. Huot, 2006: The new Mars climate database. *Mars Atmosphere Modelling and Observations*, F. Forget, M. A. Lopez-Valverde, M. C. Desjean, J. P. Huot, F. Lefevre, S. Lebonnois, S. R. Lewis, E. Millour, P. L. Read, and R. J. Wilson, eds., 128–+.

Formisano, V., D. Grassi, N. I. Ignatiev, and L. Zasova, 2001: IRIS Mariner 9 data revisited: water and dust daily cycles. *Planetary and Space Science*, **49**, 1331–1346.

Fouchet, T., E. Lellouch, N. I. Ignatiev, F. Forget, D. V. Titov, M. Tschimmel, F. Montmessin, V. Formisano, M. Giuranna, A. Maturilli, and T. Encrenaz, 2007: Martian water vapor: Mars Express PFS/LW observations. *Icarus*, **190**, 32–49, doi:10.1016/j.icarus.2007.03.003.

Goody, R. M. and Y. L. Yung, 1989: *Atmospheric radiation : theoretical basis*. New York: Oxford University Press, |1989.

Grotzinger, J. P., S. Gupta, M. C. Malin, D. M. Rubin, J. Schieber, K. Siebach, D. Y. Sumner, K. M. Stack, A. R. Vasavada, R. E. Arvidson, F. Calef, L. Edgar, W. F. Fischer, J. A. Grant, J. Griffes, L. C. Kah, M. P. Lamb, K. W. Lewis, N. Mangold, M. E. Minitti, M. Palucis, M. Rice, R. M. E. Williams, R. A. Yingst, D. Blake, D. Blaney, P. Conrad, J. Crisp, W. E. Dietrich, G. Dromart, K. S. Edgett, R. C. Ewing, R. Gellert, J. A. Hurowitz, G. Kocurek, P. Mahaffy, M. J. McBride, S. M. McLennan, M. Mischna, D. Ming, R. Milliken, H. Newsom, D. Oehler, T. J. Parker, D. Vaniman, R. C. Wiens, and S. A. Wilson, 2015: Deposition, exhumation, and paleoclimate of an ancient lake deposit, Gale crater, Mars. *Science*, **350**, doi:10.1126/science.aac7575.

Haberle, R. M., R. T. Clancy, F. Forget, M. D. Smith, and R. W. Zurek, 2017: *The atmosphere and climate of Mars*. Cambridge University Press.

Haberle, R. M. and B. M. Jakosky, 1990: Sublimation and transport of water from the north residual polar CAP on Mars. *Journal of Geophysical Research*, **95**, 1423–1437.

Haberle, R. M., C. P. McKay, J. Schaeffer, N. A. Cabrol, E. A. Grin, A. P. Zent, and R. Quinn, 2001: On the possibility of liquid water on present-day Mars. *Journal of Geophysical Research*, **106**, 23317–23326, doi:10.1029/2000JE001360.

Hanel, R. A., B. J. Conrath, D. E. Jennings, and R. E. Samuelson, 2003: *Exploration of the Solar System by Infrared Remote Sensing: Second Edition*. Exploration of the Solar System by Infrared Remote Sensing, by R. A. Hanel and B. J. Conrath and D. E. Jennings and R. E. Samuelson, pp. 534. ISBN 0521818974. Cambridge, UK: Cambridge University Press, April 2003.

Hansen, J. E. and L. D. Travis, 1974: Light scattering in planetary atmospheres. *Space Science Reviews*, **16**, 527–610.

Harri, A.-M., M. Genzer, O. Kemppinen, J. Gomez-Elvira, R. Haberle, J. Polkko, H. Savijärvi, N. Rennó, J. A. Rodriguez-Manfredi, W. Schmidt, M. Richardson, T. Siili, M. Paton, M. D. L. Torre-Juarez, T. Mäkinen, C. Newman, S. Rafkin, M. Mischna, S. Merikallio, H. Haukka, J. Martin-Torres, M. Komu, M.-P. Zorzano, V. Peinado, L. Vazquez, and R. Urqui, 2014: Mars Science Laboratory relative humidity observations: Initial results. *Journal of Geophysical Research (Planets)*, **119**, 2132–2147, doi:10.1002/2013JE004514.

Harris, L., R. T. McGinnies, and B. M. Siegel, 1948: Preparation and optical properties of gold blacks. *Journal of the Optical Society of America (1917-1983)*, **38**, 582.

Head, J. W., H. Hiesinger, M. A. Ivanov, M. A. Kreslavsky, S. Pratt, and B. J. Thomson, 1999: Possible Ancient Oceans on Mars: Evidence from Mars Orbiter Laser Altimeter Data. *Science*, **286**, 2134–2137, doi:10.1126/science.286.5447.2134.

Henyey, L. G. and J. L. Greenstein, 1941: Diffuse radiation in the Galaxy. *Astrophysical Journal*, **93**, 70–83, doi:10.1086/144246.

Hiesinger, H. and J. W. Head, III, 2002: Topography and morphology of the Argyre Basin, Mars: implications for its geologic and hydrologic history. *Planetary and Space Science*, **50**, 939–981, doi:10.1016/S0032-0633(02)00054-5.

Holt, J. W., A. Safaeinili, J. J. Plaut, J. W. Head, R. J. Phillips, R. Seu, S. D. Kempf, P. Choudhary, D. A. Young, N. E. Putzig, D. Biccari, and Y. Gim, 2008: Radar Sounding Evidence for Buried Glaciers in the Southern Mid-Latitudes of Mars. *Science*, **322**, 1235–, doi:10.1126/science.1164246.

Houben, H., 1999: The Martian diurnal water cycle. *Advances in Space Research*, **23**, 1587–1590.

Houghton, J. T., F. W. Taylor, and C. D. Rodgers, 1984: *Remote sounding of atmospheres*. Cambridge Planetary Science Series, Cambridge: University Press, 1984.

Howett, C. J. A., 2005: *Laboratory Measurements of Ammonia Ice and Ammonium Hydrosulphide Ice for use in Jovian Radiative Transfer Models*. Ph.D. thesis, University of Oxford.

Ignatiev, N. I., L. V. Zasova, V. Formisano, D. Grassi, and A. Maturilli, 2002: Water vapour abundance in Martian atmosphere from revised Mariner 9 IRIS data. *Advances in Space Research*, **29**, 157–162.

Irwin, P. G. J., 1991: *Remote Sounding of the Martian Atmosphere*. Ph.D. thesis, University of Oxford.

— 2004: Oxford Planetary Group RADTRANS User Manual 3.0.

— 2009: *Giant Planets of Our Solar System: Atmospheres, Composition, and Structure, 2nd ed.*. Springer Praxis Books, Volume ISBN 978-3-540-85157-8. Springer Berlin Heidelberg, 2009.

Irwin, P. G. J., P. Parrish, T. Fouchet, S. B. Calcutt, F. W. Taylor, A. A. Simon-Miller, and C. A. Nixon, 2004: Retrievals of jovian tropospheric phosphine from Cassini/CIRS. *Icarus*, **172**, 37–49, doi:10.1016/j.icarus.2003.09.027.

Irwin, P. G. J., N. A. Teanby, R. de Kok, L. N. Fletcher, C. J. A. Howett, C. C. C. Tsang, C. F. Wilson, S. B. Calcutt, C. A. Nixon, and P. D. Parrish, 2008: The NEMESIS planetary atmosphere radiative transfer and retrieval tool. *Journal of Quantitative Spectroscopy and Radiative Transfer*, **109**, 1136–1150, doi:10.1016/j.jqsrt.2007.11.006.

Irwin, R. P., A. D. Howard, R. A. Craddock, and J. M. Moore, 2005: An intense terminal epoch of widespread fluvial activity on early Mars: 2. Increased runoff and paleolake development. *Journal of Geophysical Research (Planets)*, **110**, E12S15, doi:10.1029/2005JE002460.

Jakosky, B. M. and C. B. Farmer, 1982: The seasonal and global behavior of water vapor in the Mars atmosphere - Complete global results of the Viking atmospheric water detector experiment. *Journal of Geophysical Research*, **87**, 2999–3019.

Jakosky, B. M., M. Slipski, M. Benna, P. Mahaffy, M. Elrod, R. Yelle, S. Stone, and N. Alsaeed, 2017: Mars' atmospheric history derived from upper-atmosphere measurements of $^{38}Ar/^{36}Ar$. *Science*, **355**, 1408–1410, doi:10.1126/science.aai7721.

James, P. B., B. P. Bonev, and M. J. Wolff, 2005: Visible albedo of Mars' south polar cap: 2003 HST observations. *Icarus*, **174**, 596–599, doi:10.1016/j.icarus.2004.08.024.

James, P. B., P. C. Thomas, M. J. Wolff, and B. P. Bonev, 2007: MOC observations of four Mars year variations in the south polar residual cap of Mars. *Icarus*, **192**, 318–326, doi:10.1016/j.icarus.2007.07.014.

Jay, V. J., 2000: *Remote Sounding of the Atmosphere by High-Resolution Spectroscopy*. Ph.D. thesis, University of Oxford.

Kieffer, H. H., T. Z. Martin, S. C. Chase, Jr., E. D. Miner, and F. D. Palluconi, 1976: Martian north pole summer temperatures - Dirty water ice. *Science*, **194**, 1341–1344.

Kleinböhl, A., L. Chen, and J. T. Schofield, 2017: Far Infrared Spectroscopic Parameters of Mars Atmospheric Aerosols and their Application to MCS Retrievals in High Aerosol Conditions. *The Mars Atmosphere: Modelling and observation*, F. Forget and M. Millour, eds., 2230.

Kleinböhl, A., J. Schofield, and D. Kass, 2018: Water ice cloud profiles during the aphelion season on Mars retrieved from Mars Climate Sounder far-infrared radiance measurements. *42nd COSPAR Scientific Assembly*, volume 42 of *COSPAR Meeting*, B4.1–32–18.

Kleinböhl, A., J. T. Schofield, W. A. Abdou, P. G. J. Irwin, and R. J. de Kok, 2011: A single-scattering approximation for infrared radiative transfer in limb geometry in the Martian atmosphere. *Journal of Quantitative Spectroscopy and Radiative Transfer*, **112**, 1568–1580, doi:10.1016/j.jqsrt.2011.03.006.

Kleinböhl, A., J. T. Schofield, D. M. Kass, W. A. Abdou, C. R. Backus, B. Sen, J. H. Shirley, W. G. Lawson, M. I. Richardson, F. W. Taylor, N. A. Teanby, and D. J. McCleese, 2009: Mars Climate Sounder limb profile retrieval of atmospheric temperature, pressure, and dust and water ice opacity. *Journal of Geophysical Research (Planets)*, **114**, 10006–+, doi:10.1029/2009JE003358.

Korablev, O., N. Ignatiev, A. Fedorova, A. Rodin, L. Zasova, J. L. Bertaux, F. Montmessin, T. Encrenaz, E. Lellouch, T. Fouchet, V. Formisano, M. D. Smith, D. Titov, M. Tschimmel, L. Maltagliati, R. T. Clancy, and A. Sprague, 2006: Water in Mars atmosphere: comparison of recent data sets. *Mars Atmosphere Modelling and Observations*, F. Forget, M. A. Lopez-Valverde, M. C. Desjean, J. P. Huot, F. Lefevre, S. Lebonnois, S. R. Lewis, E. Millour, P. L. Read, and R. J. Wilson, eds., 244–+.

Krasnopolsky, V. A., 2002: Mars' upper atmosphere and ionosphere at low, medium, and high solar activities: Implications for evolution of water. *Journal of Geophysical Research (Planets)*, **107**, 11–1, doi:10.1029/2001JE001809.

— 2015: Variations of the HDO/H_2O ratio in the martian atmosphere and loss of water from Mars. *Icarus*, **257**, 377–386, doi:10.1016/j.icarus.2015.05.021.

Krasnopolsky, V. A., G. L. Bjoraker, M. J. Mumma, and D. E. Jennings, 1997: High-resolution spectroscopy of Mars at 3.7 and 8 μm: A sensitive search for H_2O_2, H_2CO, HCl, and CH_4, and detection of HDO. *Journal of Geophysical Research*, **102**, 6525–6534, doi:10.1029/96JE03766.

Krasnopolsky, V. A., O. I. Korablev, V. I. Moroz, A. A. Krysko, J. E. Blamont, and E. Chassefiere, 1991: Infrared solar occultation sounding of the Martian atmosphere by the Phobos spacecraft. *Icarus*, **94**, 32–44, doi:10.1016/0019-1035(91)90139-K.

Lacis, A. A. and V. Oinas, 1991: A description of the correlated-k distribution method for modelling nongray gaseous absorption, thermal emission, and multiple scattering in vertically inhomogeneous atmospheres. *Journal of Geophysical Research*, **96**, 9027–9064.

Leighton, R. R. and B. C. Murray, 1966: Behavior of carbon dioxide and other volatiles on Mars. *Science*, **153**, 136–144.

Lellouch, E., T. Encrenaz, T. de Graauw, S. Erard, P. Morris, J. Crovisier, H. Feuchtgruber, T. Girard, and M. Burgdorf, 2000: The 2.4-45μm spectrum of Mars observed with the infrared space observatory. *Planetary and Space Science*, **48**, 1393–1405.

Lévy, A., N. Lacome, and C. Chackerian, Jr., 1992: Collisional line mixing. *Spectroscopy of the Earth's Atmosphere and Interstellar Medium*, K. N. Rao & A. Weber, ed., 261–337.

Liou, K. N., 2002: *An Introduction to Atmospheric Radiation., 2nd ed.*. International Geophysics Series, Vol. 84, Academic Press.

Lolachi, R., 2007: Water Vapour in the Martian Atmosphere: First Year Report—Summer 2007, AOPP First Year DPhil Report.

Luo, W. and T. F. Stepinski, 2009: Computer-generated global map of valley networks on Mars. *Journal of Geophysical Research (Planets)*, **114**, E11010, doi:10.1029/2009JE003357.

Malin, M. C., K. S. Edgett, B. A. Cantor, M. A. Caplinger, G. E. Danielson, E. H. Jensen, M. A. Ravine, J. L. Sandoval, and K. D. Supulver, 2010: An overview of the 1985-2006 Mars Orbiter Camera science investigation. *International Journal of Mars Science and Exploration*, **5**, 1–60, doi:10.1555/mars.2010.0001.

Maltagliati, L., F. Montmessin, A. Fedorova, O. Korablev, F. Forget, and J.-L. Bertaux, 2011a: Evidence of Water Vapor in Excess of Saturation in the Atmosphere of Mars. *Science*, **333**, 1868–1871, doi:10.1126/science.1207957.

Maltagliati, L., F. Montmessin, O. Korablev, A. Fedorova, F. Forget, A. Määttänen, F. Lefèvre, and J.-L. Bertaux, 2013: Annual survey of water vapor vertical distribution and water-aerosol coupling in the martian atmosphere observed by SPICAM/MEx solar occultations. *Icarus*, **223**, 942–962, doi:10.1016/j.icarus.2012.12.012.

Maltagliati, L., D. V. Titov, T. Encrenaz, R. Melchiorri, F. Forget, M. Garcia-Comas, H. U. Keller, Y. Langevin, and J.-P. Bibring, 2008: Observations of atmospheric water vapor above the Tharsis volcanoes on Mars with the OMEGA/MEx imaging spectrometer. *Icarus*, **194**, 53–64, doi:10.1016/j.icarus.2007.09.027.

Maltagliati, L., D. V. Titov, T. Encrenaz, R. Melchiorri, F. Forget, H. U. Keller, and J.-P. Bibring, 2011b: Annual survey of water vapor behavior from the OMEGA mapping spectrometer onboard Mars Express. *Icarus*, **213**, 480–495, doi:10.1016/j.icarus.2011.03.030.

McCleese, D. J., N. G. Heavens, J. T. Schofield, W. A. Abdou, J. L. Bandfield, S. B. Calcutt, P. G. J. Irwin, D. M. Kass, A. Kleinböhl, S. R. Lewis, D. A. Paige, P. L. Read, M. I. Richardson, J. H. Shirley, F. W. Taylor, N. Teanby, and R. W. Zurek, 2010: Structure and dynamics of the Martian lower and middle atmosphere as observed by the Mars Climate Sounder: Seasonal variations in zonal mean temperature, dust, and water ice aerosols. *Journal of Geophysical Research (Planets)*, **115**, 12016, doi:10.1029/2010JE003677.

McCleese, D. J., J. T. Schofield, F. W. Taylor, W. A. Abdou, O. Aharonson, D. Banfield, S. B. Calcutt, N. G. Heavens, P. G. J. Irwin, D. M. Kass, A. Kleinböhl, W. G. Lawson, C. B. Leovy, S. R. Lewis, D. A. Paige, P. L. Read, M. I. Richardson, N. Teanby, and R. W. Zurek, 2008: Intense polar temperature inversion in the middle atmosphere on Mars. *Nature Geoscience*, **1**, 745–749, doi:10.1038/ngeo332.

McCleese, D. J., J. T. Schofield, F. W. Taylor, S. B. Calcutt, M. C. Foote, D. M. Kass, C. B. Leovy, D. A. Paige, P. L. Read, and R. W. Zurek, 2007: Mars Climate Sounder: An investigation of thermal and water vapor structure, dust and condensate distributions in the atmosphere, and energy balance of the polar regions. *Journal of Geophysical Research*, **112**, doi:10.1029/2006JE002790.

McConnochie, T. H., M. D. Smith, M. J. Wolff, S. Bender, M. Lemmon, R. C. Wiens, S. Maurice, O. Gasnault, J. Lasue, P.-Y. Meslin, A.-M. Harri, M. Genzer, O. Kemppinen, G. M. Martínez, L. DeFlores, D. Blaney, J. R. Johnson, and J. F. Bell, 2018: Retrieval of water vapor column abundance and aerosol properties from ChemCam passive sky spectroscopy. *Icarus*, **307**, 294–326, doi:10.1016/j.icarus.2017.10.043.

Melchiorri, R., T. Encrenaz, P. Drossart, T. Fouchet, F. Forget, D. Titov, L. Maltagliati, F. Altieri, M. Vincendon, Y. Langevin, and J. P. Bibring, 2009: OMEGA/Mars Express: South Pole Region, water vapor daily variability. *Icarus*, **201**, 102–112, doi:10.1016/j.icarus.2008.12.018.

Melchiorri, R., T. Encrenaz, T. Fouchet, P. Drossart, E. Lellouch, B. Gondet, J.-P. Bibring, Y. Langevin, B. Schmitt, D. Titov, and N. Ignatiev, 2007: Water vapor mapping on Mars using OMEGA/Mars Express. *Planetary and Space Science*, **55**, 333–342, doi:10.1016/j.pss.2006.05.040.

Michalski, J. R., E. Z. N. Dobrea, P. B. Niles, and J. Cuadros, 2017: Ancient hydrothermal seafloor deposits in Eridania basin on Mars. *Nature Communications*, **8**, 15978, doi:10.1038/ncomms15978.

Montabone, L., F. Forget, E. Millour, R. J. Wilson, S. R. Lewis, B. Cantor, D. Kass, A. Kleinböhl, M. T. Lemmon, M. D. Smith, and M. J. Wolff, 2015: Eight-year climatology of dust optical depth on Mars. *Icarus*, **251**, 65–95, doi:10.1016/j.icarus.2014.12.034.

Montmessin, F., O. Korablev, F. Lefèvre, J.-L. Bertaux, A. Fedorova, A. Trokhimovskiy, J. Y. Chaufray, G. Lacombe, A. Reberac, L. Maltagliati, Y. Willame, S. Guslyakova, J.-C. Gérard, A. Stiepen, D. Fussen, N. Mateshvili, A. Määttänen, F. Forget, O. Witasse, F. Leblanc, A. C. Vandaele, E. Marcq, B. Sandel, B. Gondet, N. Schneider, M. Chaffin, and N. Chapron, 2017:

SPICAM on Mars Express: A 10 year in-depth survey of the Martian atmosphere. *Icarus*, **297**, 195–216, doi:10.1016/j.icarus.2017.06.022.

Morgan, A. M., A. D. Howard, D. E. J. Hobley, J. M. Moore, W. E. Dietrich, R. M. E. Williams, D. M. Burr, J. A. Grant, S. A. Wilson, and Y. Matsubara, 2014: Sedimentology and climatic environment of alluvial fans in the martian Saheki crater and a comparison with terrestrial fans in the Atacama Desert. *Icarus*, **229**, 131–156, doi:10.1016/j.icarus.2013.11.007.

Mouginot, J., A. Pommerol, P. Beck, W. Kofman, and S. M. Clifford, 2012: Dielectric map of the Martian northern hemisphere and the nature of plain filling materials. *Geophysical Research Letters*, **39**, L02202, doi:10.1029/2011GL050286.

Murchie, S. L., J. F. Mustard, B. L. Ehlmann, R. E. Milliken, J. L. Bishop, N. K. McKeown, E. Z. Noe Dobrea, F. P. Seelos, D. L. Buczkowski, S. M. Wiseman, R. E. Arvidson, J. J. Wray, G. Swayze, R. N. Clark, D. J. Des Marais, A. S. McEwen, and J.-P. Bibring, 2009: A synthesis of Martian aqueous mineralogy after 1 Mars year of observations from the Mars Reconnaissance Orbiter. *Journal of Geophysical Research (Planets)*, **114**, E00D06, doi:10.1029/2009JE003342.

Murray, J. B., J.-P. Muller, G. Neukum, S. C. Werner, S. van Gasselt, E. Hauber, W. J. Markiewicz, J. W. Head, B. H. Foing, D. Page, K. L. Mitchell, G. Portyankina, and T. H. Co-Investigator Team, 2005: Evidence from the Mars Express High Resolution Stereo Camera for a frozen sea close to Mars' equator. *Nature*, **434**, 352–356, doi:10.1038/nature03379.

NASA/JPL-Caltech, 2007: http://photojournal.jpl.nasa.gov/. Observing the Planet Mars.
URL `http://photojournal.jpl.nasa.gov/`

NASA/MSL, 2011: http://science.nasa.gov/missions/msl/. Missions – Mars Science Laboratory – NASA Science.
URL `http://science.nasa.gov/missions/msl/`

Newsom, H. E., N. L. Lanza, A. M. Ollila, S. M. Wiseman, T. L. Roush, G. A. Marzo, L. L. Tornabene, C. H. Okubo, M. M. Osterloo, V. E. Hamilton, and L. S. Crumpler, 2010: Inverted channel deposits on the floor of Miyamoto crater, Mars. *Icarus*, **205**, 64–72, doi:10.1016/j.icarus.2009.03.030.

Orosei, R., S. E. Lauro, E. Pettinelli, A. Cicchetti, M. Coradini, B. Cosciotti, F. Di Paolo, E. Flamini, E. Mattei, M. Pajola, F. Soldovieri, M. Cartacci, F. Cassenti, A. Frigeri, S. Giuppi, R. Martufi, A. Masdea, G. Mitri, C. Nenna, R. Noschese, M. Restano, and R. Seu, 2018: Radar evidence of subglacial liquid water on Mars. *Science*, **361**, 490–493, doi:10.1126/science.aar7268.

Pankine, A. A. and L. K. Tamppari, 2015: Constraints on water vapor vertical distribution at the Phoenix landing site during summer from MGS TES day and night observations. *Icarus*, **252**, 107–120, doi:10.1016/j.icarus.2015.01.008.

Parker, T. J., D. S. Gorsline, R. S. Saunders, D. C. Pieri, and D. M. Schneeberger, 1993: Coastal geomorphology of the Martian northern plains. *Journal of Geophysical Research*, **98**, 11061–+.

Parker, T. J., R. S. Saunders, and D. M. Schneeberger, 1989: Transitional morphology in west Deuteronilus Mensae, Mars - Implications for modification of the lowland/upland boundary. *Icarus*, **82**, 111–145, doi:10.1016/0019-1035(89)90027-4.

Perron, J. T., J. X. Mitrovica, M. Manga, I. Matsuyama, and M. A. Richards, 2007: Evidence for an ancient martian ocean in the topography of deformed shorelines. *Nature*, **447**, 840–843, doi:10.1038/nature05873.

Picardi, G., J. J. Plaut, D. Biccari, O. Bombaci, D. Calabrese, M. Cartacci, A. Cicchetti, S. M. Clifford, P. Edenhofer, W. M. Farrell, C. Federico, A. Frigeri, D. A. Gurnett, T. Hagfors, E. Heggy, A. Herique, R. L. Huff, A. B. Ivanov, W. T. K. Johnson, R. L. Jordan, D. L. Kirchner, W. Kofman, C. J. Leuschen, E. Nielsen, R. Orosei, E. Pettinelli, R. J. Phillips, D. Plettemeier, A. Safaeinili, R. Seu, E. R. Stofan, G. Vannaroni, T. R. Watters, and E. Zampolini, 2005: Radar Soundings of the Subsurface of Mars. *Science*, **310**, 1925–1928, doi:10.1126/science.1122165.

Plaut, J. J., G. Picardi, A. Safaeinili, A. B. Ivanov, S. M. Milkovich, A. Cicchetti, W. Kofman, J. Mouginot, W. M. Farrell, R. J. Phillips, S. M. Clifford, A. Frigeri, R. Orosei, C. Federico, I. P. Williams, D. A. Gurnett, E. Nielsen, T. Hagfors, E. Heggy, E. R. Stofan, D. Plettemeier, T. R. Watters, C. J. Leuschen, and P. Edenhofer, 2007: Subsurface Radar Sounding of the South Polar Layered Deposits of Mars. *Science*, **316**, 92, doi:10.1126/science.1139672.

Plaut, J. J., A. Safaeinili, J. W. Holt, R. J. Phillips, J. W. Head, R. Seu, N. E. Putzig, and A. Frigeri, 2009: Radar evidence for ice in lobate debris aprons in the mid-northern latitudes of Mars. *Geophysical Research Letters*, **36**, L02203, doi:10.1029/2008GL036379.

Pompea, S. M. and R. P. Breault, 1995: Black surfaces for Optical Systems. *Handbook of Optics Volume II Devices, Measurements, and Properties 2nd edition*, M. Bass, E. W. V. Stryland, D. R. Williams, and W. L. Wolfe, eds., McGraw-Hill, INC., New York, NY, chapter 37, 37.1–37.70.

Puliafito, E., R. Bevilacqua, J. Olivero, and W. Degenhardt, 1995: Retrieval error comparison for several inversion techniques used in limb-scanning millimeter-wave spectroscopy. *Journal of Geophysical Research*, **100**, 14,257–14,267, doi:10.1029/95JD00212.

Putzig, N. E., R. J. Phillips, B. A. Campbell, J. W. Holt, J. J. Plaut, L. M. Carter, A. F. Egan, F. Bernardini, A. Safaeinili, and R. Seu, 2009: Subsurface structure of Planum Boreum from Mars Reconnaissance Orbiter Shallow Radar soundings. *Icarus*, **204**, 443–457, doi:10.1016/j.icarus.2009.07.034.

Read, P. and S. Lewis, 2004: *The Martian Climate Revisited: Atmosphere and Environment of a Desert Planet*. UK: Springer-Praxis.

Richardson, M. I. and R. J. Wilson, 2002: Investigation of the nature and stability of the Martian seasonal water cycle with a general circulation model. *Journal of Geophysical Research (Planets)*, **107**, 5031, doi:10.1029/2001JE001536.

Rodgers, C. D., 1976: Retrieval of Atmospheric Temperature and Composition From Remote Measurements of Thermal Radiation. *Reviews of Geophysics and Space Physics*, **14**, 609–+.

— 2000: *Inverse Methods for Atmospheric Sounding: Theory and Practice; Series on Atmospheric, Oceanic and Planetary Physics Vol. 2*. World Scientific.

Rodin, A. V., O. I. Korablev, and V. I. Moroz, 1997: Vertical Distribution of Water in the Near-Equatorial Troposphere of Mars: Water Vapor and Clouds. *Icarus*, **125**, 212–229, doi:10.1006/icar.1996.5602.

Rodriguez, J. A. P., A. G. Fairén, K. L. Tanaka, M. Zarroca, R. Linares, T. Platz, G. Komatsu, H. Miyamoto, J. S. Kargel, J. Yan, V. Gulick, K. Higuchi, V. R. Baker, and N. Glines, 2016: Tsunami waves extensively resurfaced the shorelines of an early Martian ocean. *Scientific Reports*, **6**, 25106, doi:10.1038/srep25106.

Rosenqvist, J., P. Drossart, M. Combes, T. Encrenaz, E. Lellouch, J. P. Bibring, S. Erard, Y. Langevin, and E. Chassefière, 1992: Minor constituents in the Martian atmosphere from the ISM/Phobos experiment. *Icarus*, **98**, 254–270, doi:10.1016/0019-1035(92)90094-N.

Rothman, L. S., A. Barbe, D. C. Benner, L. R. Brown, C. Camy-Peyret, M. R. Carleer, K. Chance, C. Clerbaux, V. Dana, V. M. Devi, A. Fayt, J.-M. Flaud, R. R. Gamache, A. Goldman, D. Jacquemart, K. W. Jucks, W. J. Lafferty, J.-Y. Mandin, S. T. Massie, V. Nemtchinov, D. A. Newnham, A. Perrin, C. P. Rinsland, J. Schroeder, K. M. Smith, M. A. H. Smith, K. Tang, R. A. Toth, J. Vander Auwera, P. Varanasi, and K. Yoshino, 2003: The HITRAN molecular spectroscopic database: edition of 2000 including updates through 2001. *Journal of Quantitative Spectroscopy and Radiative Transfer*, **82**, 5–44.

Rothman, L. S., D. Jacquemart, A. Barbe, D. Chris Benner, M. Birk, L. R. Brown, M. R. Carleer, C. Chackerian, K. Chance, L. H. Coudert, V. Dana, V. M. Devi, J. Flaud, R. R. Gamache, A. Goldman, J. Hartmann, K. W. Jucks, A. G. Maki, J. Mandin, S. T. Massie, J. Orphal, A. Perrin, C. P. Rinsland, M. A. H. Smith, J. Tennyson, R. N. Tolchenov, R. A. Toth, J. Vander Auwera, P. Varanasi, and G. Wagner, 2005: The HITRAN 2004 molecular spectroscopic database. *Journal of Quantitative Spectroscopy and Radiative Transfer*, **96**, 139–204, doi:10.1016/j.jqsrt.2004.10.008.

Savijärvi, H., A.-M. Harri, and O. Kemppinen, 2016: The diurnal water cycle at Curiosity: Role of exchange with the regolith. *Icarus*, **265**, 63–69, doi:10.1016/j.icarus.2015.10.008.

Schorn, R. A., C. B. Farmer, and S. J. Little, 1969: High-Dispersion Spectroscopic Studies of Mars. III. Preliminary Results of 1968-69 Water-Vapor Studies. *Icarus*, **11**, 283–+.

Sheehan, W., 1996: *The Planet Mars: A History of Observation and Discovery*. Tucson: University of Arizona Press.

Smith, M. D., 2002: The annual cycle of water vapor on Mars as observed by the Thermal Emission Spectrometer. *Journal of Geophysical Research (Planets)*, **107**, 25–1, doi:10.1029/2001JE001522.

— 2004: Interannual variability in TES atmospheric observations of Mars during 1999-2003. *Icarus*, **167**, 148–165, doi:10.1016/S0019-1035(03)00287-2.

— 2006: TES atmospheric temperature, aerosol optical depth, and water vapor observations 1999-2004. *Mars Atmosphere Modelling and Observations*, F. Forget, M. A. Lopez-Valverde, M. C. Desjean, J. P. Huot, F. Lefevre, S. Lebonnois, S. R. Lewis, E. Millour, P. L. Read, and R. J. Wilson, eds., 211–+.

— 2008: Spacecraft Observations of the Martian Atmosphere. *Annual Review of Earth and Planetary Sciences*, **36**, 191–219, doi:10.1146/annurev.earth.36.031207.124334.

Smith, M. D., F. Daerden, L. Neary, and A. Khayat, 2018: The climatology of carbon monoxide and water vapor on Mars as observed by CRISM and modeled by the GEM-Mars general circulation model. *Icarus*, **301**, 117–131, doi:10.1016/j.icarus.2017.09.027.

Smith, M. D., M. J. Wolff, R. T. Clancy, and S. L. Murchie, 2009a: Compact Reconnaissance Imaging Spectrometer observations of water vapor and carbon monoxide. *Journal of Geophysical Research (Planets)*, **114**, E00D03, doi:10.1029/2008JE003288.

Smith, M. D., M. J. Wolff, N. Spanovich, A. Ghosh, D. Banfield, P. R. Christensen, G. A. Landis, and S. W. Squyres, 2006: One Martian year of atmospheric observations using MER Mini-TES. *Journal of Geophysical Research (Planets)*, **111**, 12–+, doi:10.1029/2006JE002770.

Smith, P. H., L. K. Tamppari, R. E. Arvidson, D. Bass, D. Blaney, W. V. Boynton, A. Carswell, D. C. Catling, B. C. Clark, T. Duck, E. DeJong, D. Fisher, W. Goetz, H. P. Gunnlaugsson, M. H. Hecht, V. Hipkin, J. Hoffman, S. F. Hviid, H. U. Keller, S. P. Kounaves, C. F. Lange,

M. T. Lemmon, M. B. Madsen, W. J. Markiewicz, J. Marshall, C. P. McKay, M. T. Mellon, D. W. Ming, R. V. Morris, W. T. Pike, N. Renno, U. Staufer, C. Stoker, P. Taylor, J. A. Whiteway, and A. P. Zent, 2009b: H_2O at the Phoenix Landing Site. *Science*, **325**, 58–, doi:10.1126/science.1172339.

Spinrad, H., G. Münch, and L. D. Kaplan, 1963: Letter to the Editor: the Detection of Water Vapor on Mars. *Astrophysical Journal*, **137**, 1319–+, doi:10.1086/147613.

Sprague, A. L., D. M. Hunten, L. R. Doose, R. E. Hill, W. V. Boynton, M. D. Smith, and J. C. Pearl, 2006: Mars atmospheric water vapor abundance: 1991 1999, emphasis 1998 1999. *Icarus*, **184**, 372–400, doi:10.1016/j.icarus.2006.05.021.

Sprague, A. L., D. M. Hunten, R. E. Hill, B. Rizk, and W. K. Wells, 1996: Martian water vapor, 1988-1995. *Journal of Geophysical Research*, **101**, 23229–23254, doi:10.1029/96JE02265.

Squyres, S. W., J. P. Grotzinger, R. E. Arvidson, J. F. Bell, W. Calvin, P. R. Christensen, B. C. Clark, J. A. Crisp, W. H. Farrand, K. E. Herkenhoff, J. R. Johnson, G. Klingelhöfer, A. H. Knoll, S. M. McLennan, H. Y. McSween, R. V. Morris, J. W. Rice, R. Rieder, and L. A. Soderblom, 2004: In Situ Evidence for an Ancient Aqueous Environment at Meridiani Planum, Mars. *Science*, **306**, 1709–1714, doi:10.1126/science.1104559.

Squyres, S. W., A. H. Knoll, R. E. Arvidson, B. C. Clark, J. P. Grotzinger, B. L. Jolliff, S. M. McLennan, N. Tosca, J. F. Bell, W. M. Calvin, W. H. Farrand, T. D. Glotch, M. P. Golombek, K. E. Herkenhoff, J. R. Johnson, G. Klingelhöfer, H. Y. McSween, and A. S. Yen, 2006: Two Years at Meridiani Planum: Results from the Opportunity Rover. *Science*, **313**, 1403–1407, doi:10.1126/science.1130890.

Summerhayes, C. and P. Beeching, 2007: Hitler's Antarctic base: the myth and the reality. *Polar Record*, **43**, 1–21, doi:10.1017/S003224740600578X.

Tamppari, L. K., D. Bass, B. Cantor, I. Daubar, C. Dickinson, D. Fisher, K. Fujii, H. P. Gunnlauggson, T. L. Hudson, D. Kass, A. Kleinböhl, L. Komguem, M. T. Lemmon, M. Mellon, J. Moores, A. Pankine, J. Pathak, M. Searls, F. Seelos, M. D. Smith, S. Smrekar, P. Taylor, C. Holstein-Rathlou, W. Weng, J. Whiteway, and M. Wolff, 2010: Phoenix and MRO coordinated atmospheric measurements. *Journal of Geophysical Research (Planets)*, **115**, E00E17, doi:10.1029/2009JE003415.

Thomas, I., 2011: *Measurement of Properties of the Lunar Surface Using the Diviner Lunar Radiometer Experiment on the NASA Lunar Reconnaissance Orbiter*. Ph.D. thesis, University of Oxford.

Titov, D. V., 2002: Water vapour in the atmosphere of Mars. *Advances in Space Research*, **29**, 183–191.

Titov, D. V., W. J. Markiewicz, N. Thomas, H. U. Keller, R. M. Sablotny, M. G. Tomasko, M. T. Lemmon, and P. H. Smith, 1999: Measurements of the atmospheric water vapor on Mars by the Imager for Mars Pathfinder. *Journal of Geophysical Research*, **104**, 9019–9026, doi:10.1029/1998JE900046.

Titus, T. N., 2004: Mars: Water, water everywhere. *Nature*, **428**, 610–611, doi:10.1038/nature02482.

Titus, T. N., H. H. Kieffer, and P. R. Christensen, 2003: Exposed Water Ice Discovered near the South Pole of Mars. *Science*, **299**, 1048–1051, doi:10.1126/science.1080497.

Toigo, A. D., M. D. Smith, F. P. Seelos, and S. L. Murchie, 2013: High spatial and temporal resolution sampling of Martian gas abundances from CRISM spectra. *Journal of Geophysical Research (Planets)*, **118**, 89–104, doi:10.1029/2012JE004147.

Trokhimovskiy, A., A. Fedorova, O. Korablev, F. Montmessin, J.-L. Bertaux, A. Rodin, and M. D. Smith, 2015: Mars' water vapor mapping by the SPICAM IR spectrometer: Five martian years of observations. *Icarus*, **251**, 50–64, doi:10.1016/j.icarus.2014.10.007.

Tschimmel, M., N. I. Ignatiev, D. V. Titov, E. Lellouch, T. Fouchet, M. Giuranna, and V. Formisano, 2008: Investigation of water vapor on Mars with PFS/SW of Mars Express. *Icarus*, **195**, 557–575, doi:10.1016/j.icarus.2008.01.018.

Tull, R. G., 1970: High-Dispersion Spectroscopic Observations of Mars. IV. The Latitude Distribution of Atmospheric Water Vapor. *Icarus*, **13**, 43–+.

Vandaele, A. C., O. Korablev, F. Daerden, S. Aoki, I. R. Thomas, F. Altieri, M. López-Valverde, G. Villanueva, G. Liuzzi, M. D. Smith, J. T. Erwin, L. Trompet, A. A. Fedorova, F. Montmessin, A. Trokhimovskiy, D. A. Belyaev, N. I. Ignatiev, M. Luginin, K. S. Olsen, L. Baggio, J. Alday, J.-L. Bertaux, D. Betsis, D. Bolsée, R. T. Clancy, E. Cloutis, C. Depiesse, B. Funke, M. Garcia-Comas, J.-C. Gérard, M. Giuranna, F. Gonzalez-Galindo, A. V. Grigoriev, Y. S. Ivanov, J. Kaminski, O. Karatekin, F. Lefèvre, S. Lewis, M. López-Puertas, A. Mahieux, I. Maslov, J. Mason, M. J. Mumma, L. Neary, E. Neefs, A. Patrakeev, D. Patsaev, B. Ristic, S. Robert, F. Schmidt, A. Shakun, N. A. Teanby, S. Viscardy, Y. Willame, J. Whiteway, V. Wilquet, M. J. Wolff, G. Bellucci, M. R. Patel, J.-J. López-Moreno, F. Forget, C. F. Wilson, R. Young, H. Svedhem, J. L. Vago, D. Rodionov, NOMAD Science Team, and ACS Science Team, 2019: Martian dust storm impact on atmospheric H_2O and D/H observed by ExoMars Trace Gas Orbiter. *Nature*, **568**, 521–525, doi:10.1038/s41586-019-1097-3.

Villanueva, G. L., M. J. Mumma, R. E. Novak, H. U. Käufl, P. Hartogh, T. Encrenaz, A. Tokunaga, A. Khayat, and M. D. Smith, 2015: Strong water isotopic anomalies in the martian atmosphere: Probing current and ancient reservoirs. *Science*, **348**, 218–221, doi:10.1126/science.aaa3630.

Warren, S. G., 1984: Optical constants of ice from the ultraviolet to the microwave. *Applied Optics*, **23**, 1206–1225.

Warren, S. G. and R. E. Brandt, 2008: Optical constants of ice from the ultraviolet to the microwave: A revised compilation. *Journal of Geophysical Research (Atmospheres)*, **113**, 14220, doi:10.1029/2007JD009744.

White, O. L., E. R. Stofan, J. J. Plaut, A. Safaeinili, Y. Gim, G. Picardi, and Marsis Team, 2007: MARSIS Radar Sounder Observations in the Vicinity of Ma'adim Vallis. *Lunar and Planetary Institute Conference Abstracts*, volume 38 of *Lunar and Planetary Inst. Technical Report*, 1541–+.

Whiteway, J. A., L. Komguem, C. Dickinson, C. Cook, M. Illnicki, J. Seabrook, V. Popovici, T. J. Duck, R. Davy, P. A. Taylor, J. Pathak, D. Fisher, A. I. Carswell, M. Daly, V. Hipkin, A. P. Zent, M. H. Hecht, S. E. Wood, L. K. Tamppari, N. Renno, J. E. Moores, M. T. Lemmon, F. Daerden, and P. H. Smith, 2009: Mars Water-Ice Clouds and Precipitation. *Science*, **325**, 68–, doi:10.1126/science.1172344.

Wikipedia, Accessed 2011-06-07: Mars Reconnaissance Orbiter.
URL `http://en.wikipedia.org/wiki/Mars_Reconnaissance_Orbiter`

Wilson, R. J., M. D. Smith, and G. Neumann, 2006: The diurnal variation and radiative influence of martian water ice clouds. *Mars Atmosphere Modelling and Observations*, F. Forget, M. A. Lopez-Valverde, M. C. Desjean, J. P. Huot, F. Lefevre, S. Lebonnois, S. R. Lewis, E. Millour, P. L. Read, and R. J. Wilson, eds., 262–+.

Wolff, M. J. and R. T. Clancy, 2003: Constraints on the size of Martian aerosols from Thermal Emission Spectrometer observations. *Journal of Geophysical Research (Planets)*, **108**, 1–1, doi:10.1029/2003JE002057.

Wolff, M. J., M. D. Smith, R. T. Clancy, N. Spanovich, B. A. Whitney, M. T. Lemmon, J. L. Bandfield, D. Banfield, A. Ghosh, G. Landis, P. R. Christensen, J. F. Bell, and S. W. Squyres, 2006: Constraints on dust aerosols from the Mars Exploration Rovers using MGS overflights and Mini-TES. *Journal of Geophysical Research (Planets)*, **111**, 12–+, doi:10.1029/2006JE002786.

Yamamoto, G., 1969: Estimation of rotational line widths of carbon dioxide bands. *Journal of Quantitative Spectroscopy and Radiative Transfer*, **9**, 371–382, doi:10.1016/0022-4073(69)90032-6.

Zent, A. P., R. M. Haberle, H. C. Houben, and B. M. Jakosky, 1993: A coupled subsurface-boundary layer model of water on Mars. *Journal of Geophysical Research*, **98**, 3319–3337.

Zent, A. P., M. H. Hecht, T. L. Hudson, S. E. Wood, and V. F. Chevrier, 2016: A revised calibration function and results for the Phoenix mission TECP relative humidity sensor. *Journal of Geophysical Research (Planets)*, **121**, 626–651, doi:10.1002/2015JE004933.

Zuber, M. T., 2007: Planetary science: Mars at the tipping point. *Nature*, **447**, 785–786, doi:10.1038/447785a.

Zuber, M. T., D. E. Smith, S. C. Solomon, J. B. Abshire, R. S. Afzal, O. Aharonson, K. Fishbaugh, P. G. Ford, H. V. Frey, J. B. Garvin, J. W. Head, A. B. Ivanov, C. L. Johnson, D. O. Muhleman, G. A. Neumann, G. H. Pettengill, R. J. Phillips, X. Sun, H. J. Zwally, W. B. Banerdt, and T. C. Duxbury, 1998: Observations of the North Polar Region of Mars from the Mars Orbiter Laser Altimeter. *Science*, **282**, 2053–+.

Zurek, R. W. and S. E. Smrekar, 2007: An overview of the Mars Reconnaissance Orbiter (MRO) science mission. *Journal of Geophysical Research (Planets)*, **112**, E05S01, doi:10.1029/2006JE002701.